Forschungsbericht 2018-13

# Design Concept of a Highly-Integral Grid-Structure for Composite Airframes

Steffen Niemann

Deutsches Zentrum für Luft- und Raumfahrt
Institut für Faserverbundleichtbau und
Adaptronik
Braunschweig

DLR Deutsches Zentrum
für Luft- und Raumfahrt

ISSN 1434-8454

ISRN DLR-FB—2018-13

*Bauweise, Flugzeugrumpf, Anisogrid, Faserverbundwerkstoff*

(Publiziert in englischer Sprache)

Steffen NIEMANN
Institut für Faserverbundleichtbau und Adaptronik des DLR, Braunschweig

**Bauweisenkonzept einer hochintegralen Grid-Struktur für den Flugzeugbau aus Faserverbundwerkstoff**

*Dissertation Technische Universität Carolo-Wilhelmina zu Braunschweig*
*DLR-Forschungsbericht 2018-13, 2018, 161 Seiten, 97 Bilder, 7 Tabellen, 98 Literaturstellen, 35,00 € zzgl. MwSt.*

Die Vorteile von Faserverbunden, wie die Anpassbarkeit an Bauteillasten, ihr hoher Integrationsgrad bei der Herstellung oder auch die Möglichkeiten zur Funktionsintegration, scheinen Grid-Architekturen vereinen zu können. In der vorliegenden Dissertation wird ein Anisogrid-Struktur-Konzept unter den Gesichtspunkten für zivile Flugzeugrumpfstrukturen entwickelt, analysiert und getestet.

Das Konzept besteht aus integral gefertigten Rippen unterschiedlicher Orientierungen (spiral und radial), einer lasttragenden Haut und speziellen Interface-Lagen, welche die Rippenstruktur und die Haut verbinden. Als Fertigungskonzept ist ein voll automatisierter Prozess zur Verarbeitung von Prepreg-Halbzeugen erarbeitet worden, welcher die hohen Qualitätsansprüche berücksichtigt.

Da für die spezielle Struktur der sich kreuzenden Rippen und dem angedachten Fertigungsprozess nur begrenzte Materialuntersuchungen bekannt sind, werden statische Druck- und Zugtests auf Element-Ebene durchgeführt und Steifigkeit- wie auch Festigkeitskennwerte sowie das generelle Versagensverhalten bestimmt.

Darauf bezugnehmend erfolgt ein Vergleich der dreieckigen Anisogrid- mit der aktuellen rechteckigen Versteifungs-Architektur auf Paneel-Ebene. Diese strukturmechanische Untersuchung wird gezielt auf den Einfluss der Schrägstellung der Steifen reduziert und Paneele unter axialem Druck, reinem Schub und Druck-Schub-Kombinationen ausgelegt.

Mit einem Paneeltest unter Axialdruck kann die Funktionstüchtigkeit des Strukturkonzeptes, die erarbeiteten Materialeigenschaften sowie das spezielle Nachbeulverhalten einer Anisogridstruktur bestätigt werden. Abschließend wird unter Berücksichtigung einer Konzept-Weiterentwicklung eine Perspektive der grundlegenden Bauweise aufgezeigt.

*Airframe structure, Design, Composite, Grid Structure, Anisogrid*

Steffen NIEMANN
Institute of Composite Structures and Adaptive Systems (DLR), Braunschweig

**Design Concept of a Highly-Integral Grid-Structure for Composite Airframes**

*Doctoral Thesis Technische Universität Carolo-Wilhelmina zu Braunschweig*
*DLR-Forschungsbericht 2018-13, 2018, 161 pages, 97 figs., 7 tabs., 98 refs., 35,00 €*

The advantages of composite materials, with their specific load adaptable properties and their high degree of integration in terms of one-shot manufacturing and function integration; grid structures seem to combine all of these. In this dissertation, an Anisogrid structure concept is developed, analysed and tested under consideration of the requirements for civil primary airframe structures.

The developed Anisogrid structure concept consists of intersecting integral manufactured ribs with different orientations (helical, circumferential), a load-bearing skin and a special interface, connecting the grid structure and the skin. The manufacturing approach is based on prepreg material under consideration of full automation and high-quality assurance demands (Advanced Fibre Placement).

In order to overcome the lack of available material properties in the special intersecting rib design, static compression and tension tests are performed and analysed to characterise the stiffness and strength properties as well as basic structural failure behaviour.

In the next step, the triangular stiffened grid architecture is compared to the conventional rectangular stiffened structure in terms of minimum weight on panel level. In this structural-mechanical investigation, the focus is deliberately placed on the isolated effect of the skew of the stiffeners and performed under uniaxial compression, pure shear and the combination of both.

Subsequently, the observed different buckling behaviour and the functionality of interface layers between the skin and the grid are validated by means of a compression panel test. With these test results, a perspective for this integral structural design concept is presented considering a specific further development step.

Forschungsbericht 2018-13

# Design Concept of a Highly-Integral Grid-Structure For Composite Airframes

Steffen Niemann

Deutsches Zentrum für Luft- und Raumfahrt
Institut für Faserverbundleichtbau und
Adaptronik
Braunschweig

| | |
|---|---|
| 161 | Seiten |
| 97 | Bilder |
| 7 | Tabellen |
| 98 | Literaturstellen |

DLR Deutsches Zentrum
für Luft- und Raumfahrt

# Design Concept of a Highly-Integral Grid-Structure for Composite Airframes

Bauweisenkonzept einer hochintegralen Grid-Struktur für den Flugzeugbau aus Faserverbundwerkstoff

Von der Fakultät für Maschinenbau
der Technischen Universität Carolo-Wilhelmina zu Braunschweig

zur Erlangung der Würde
eines Doktor-Ingenieurs (Dr.-Ing.)

genehmigte Dissertation

| | |
|---|---|
| von: | Dipl.-Ing. (FH) Steffen Niemann M.Sc. |
| aus (Geburtsort): | Demmin |
| | |
| eingereicht am: | 09.08.2017 |
| mündliche Prüfung am: | 11.12.2017 |
| | |
| Gutachter: | Prof. Dr.-Ing. Michael Sinapius |
| | Prof. Dr.-Ing. Peter Horst |

2018

# Abstract

Composite materials, with their specific load adaptable properties, and their high degree of integration in terms of one-shot manufacturing and function integration. Grid structures seem to combine all these advantages. In this dissertation, an Anisogrid structure concept is developed, analysed and tested under consideration of the requirements for civil primary airframe structures.

The developed Anisogrid structure concept consists of intersecting integral manufactured ribs with different orientations (helical, circumferential), a load-bearing skin and a special interface, connecting the grid structure and the skin. The manufacturing approach is based on prepreg material under consideration of full automation and high-quality assurance demands (Advanced Fibre Placement).

In order to overcome the lack of available material properties in the special intersecting rib design, static compression and tension tests are performed and analysed to characterise the stiffness and strength properties as well as basic structural failure behaviour.

In the next step, the triangular stiffened grid architecture is compared to the conventional rectangular stiffened structure in terms of minimum weight on panel level. In this structural-mechanical investigation, the focus is deliberately placed on the isolated effect of the skew of the stiffeners and performed under uniaxial compression, pure shear and the combination of both.

Subsequently, the observed different buckling behaviour and the functionality of interface layers between the skin and the grid are validated by means of a compression panel test. With these test results, a perspective for this integral structural design concept is presented considering a specific further development step.

# Kurzfassung

Die Vorteile von Faserverbunden, wie die Anpassbarkeit an Bauteillasten, ihr hoher Integrationsgrad bei der Herstellung oder auch die Möglichkeiten zur Funktionsintegration, scheinen Grid-Architekturen vereinen zu können. In der vorliegenden Dissertation wird ein Anisogrid-Struktur-Konzept unter den Gesichtspunkten für zivile Flugzeugrumpfstrukturen entwickelt, analysiert und getestet.

Das Konzept besteht aus integral gefertigten Rippen unterschiedlicher Orientierungen (spiral und radial), einer lasttragenden Haut und speziellen Interface-Lagen, welche die Rippenstruktur und die Haut verbinden. Als Fertigungskonzept ist ein voll automatisierter Prozess zur Verarbeitung von Prepreg-Halbzeugen erarbeitet worden, welcher die hohen Qualitätsansprüche berücksichtigt.

Da für die spezielle Struktur der sich kreuzenden Rippen und dem angedachten Fertigungsprozess nur begrenzte Materialuntersuchungen bekannt sind, werden statische Druck- und Zugtests auf Element-Ebene durchgeführt und Steifigkeit- wie auch Festigkeitskennwerte sowie das generelle Versagensverhalten bestimmt.

Darauf bezugnehmend erfolgt ein Vergleich der dreieckigen Anisogrid- mit der aktuellen rechteckigen Versteifungs-Architektur auf Paneel-Ebene. Diese strukturmechanische Untersuchung wird gezielt auf den Einfluss der Schrägstellung der Steifen reduziert und Paneele unter axialem Druck, reinem Schub und Druck-Schub-Kombinationen ausgelegt.

Mit einem Paneeltest unter Axialdruck kann die Funktionstüchtigkeit des Strukturkonzeptes, die erarbeiteten Materialeigenschaften sowie das spezielle Nachbeulverhalten einer Anisogridstruktur bestätigt werden. Abschließend wird unter Berücksichtigung einer Konzept-Weiterentwicklung eine Perspektive der grundlegenden Bauweise aufgezeigt.

## Danksagung / Acknowledgements

Ein besonderes Dankeschön möchte ich an Prof. Dr.-Ing. Michael Sinapius richten, der die Betreuung meiner Promotion angenommen hat. Wir haben über die Jahre so einige Promotionsgespräche gehabt, in denen er mir stets wertvolle Hinweise zum Inhalt und zur Bearbeitung gegeben, und mich in meinem Vorhaben bestärkt hat. Zudem möchte ich herzlich Prof. Dr.-Ing. Peter Horst für das Koreferat meiner Dissertation danken, der mich durch seine Expertise und Arbeiten insbesondere auf dem Gebiet der Grid-Strukturen weiterführend beeinflusste.

Weiterhin gilt ein besonderer Dank meinem Abteilungsleiter Prof. Dr.-Ing. Christian Hühne, der mir exzellente Rahmenbedingungen geschaffen hat und mit dem ich in den internationalen Projekten ausgiebig über die Thematik und die Dissertation diskutieren konnte. Dankenswerterweise übernimmt er auch den Prüfungsvorsitz.

Insgesamt möchte ich auch meinen Kolleginnen und Kollegen am Institut für Faserverbundleichtbau und Adaptronik für das feine Arbeitsumfeld danken. Die offenen Bürotüren und konstruktiven Diskussionen haben einen großen Anteil an dem Gelingen solch einer Arbeit. Insbesondere möchte ich meinem Bürokollegen Henrik Borgwardt, Ronald Wagner, Matthias Beerhorst und Olaf Mierheim sowie auch meinen Studenten für die anregenden Gespräche danken.

Last but not least gilt mein Dank auch meinen Eltern, die mich seit mehreren Dekaden tatkräftig unterstützen, und natürlich meiner Ehefrau Juliane, die mich seit vielen Jahren ganz wesentlich in meinem Tun bestärkt.

A special thank you I’d like to say to Prof. Dr-Ing Michael Sinapius, who has taken care of my doctorate. Over the years we had many discussions, in which he has always given me valuable advices on the content and the treatment, and motivation for the work. I would also like to thank Prof. Dr-Ing Peter Horst for the second review of my dissertation, who influenced me with his work and expertise especially in the field of grid structures.

Furthermore a special thanks to my department head Prof. Dr-Ing Christian Hühne, who has provided me with excellent working conditions and with whom I was able to discuss extensively the topic and the dissertation in the international projects, and who also chairs the examination committee.

I would also like to thank my colleagues at the Institute Composite Structures and Adaptive Systems for the kind work environment. The culture of open office doors and constructive discussions have a large part in the success of the work. In particular, I like to express my thanks to my office colleague Henrik Borgwardt, Ronald Wagner, Matthias Beerhorst and Olaf Mierheim and also my students for the fruitful discussions.

Last but not least I convey my thanks to my parents, who support me my whole life, and of course to my wife Juliane, who is tremendously strengthening me all the years.

*“Do not fear failure but rather fear not trying.”*

Roy T. Bennett

# Contents

# Abbreviations and Symbols

*Abbreviations*

| | |
|---|---|
| AFP | advanced fibre placement |
| ATL | advanced tape laying |
| CC | cut-complexity (relates to the cutting of the tape at grid knot) |
| CIRA | Italian Aerospace Research Centre |
| CRISM | Institute for Special Machinery (Russian Federation) |
| DIC | digital image correlation |
| FE | finite element |
| FEM | finite element model |
| FVR | fibre volume content |
| IATA | International Air Transport Association |
| ICCI | Isogrid Composite Canada Inc. |
| LCM | liquid composite moulding |
| LL | limit load |
| MoS | margin of safety |
| SD | standard deviation |
| UL | ultimate load |

*Symbols*

| | |
|---|---|
| $(\ )_a$ | referring to *axial* |
| $(\ )_c$ | referring to *circumferential* |
| $(\ )_h$ | referring to *helical* |
| $(\ )_s$ | referring to *skin* |
| $(\ )_I$ | referring to *Interface layer* |
| $\varphi$ | helical or diagonal angle to the curvature axis |
| $\sigma_{Bten}$ | fracture strength tension |
| $\sigma_{Bcom}$ | fracture strength compression |

| | |
|---|---|
| a | panel length |
| b | panel width |
| d | stiffener distance |
| h | height |
| t | thickness |
| L | interface layer feet length |
| P | load |
| R | radius |
| $E_{ten}$ | elasticity modulus for tension |
| $E_{com}$ | elasticity modulus for compression |
| $G_{IIc}$ | energy release rate – Mode II (in-plane shear) |

*Units*

| | |
|---|---|
| mm | |
| ( )° | angle in degree |
| kN | kilo newton |
| kg/m$^2$ | normalized weight to the area |
| N/mm | load per unit length (line load) |
| µm/m | strain value used for composite materials |
| GPa | material stiffness |
| MPa | material strength |
| J/m$^2$ | energy release rate |

# 1 Introduction

For flying in airy heights, the development of aircraft has always depended on a maximum of lightweight designs. The continuing improvement of structural efficiency leads not only to better aircraft performance but also to cost savings in terms of fuel consumption and emissions. Particularly the environmental demands continue to become much stricter due to the climatic impact of the use of fossil fuels.

The *International Air Transport Association* (IATA) committed in 2009 to reduce its carbon emissions of $CO_2$ to 50% (2005) by 2050. This massive reduction should be realised through aircraft technology, economic measures, biofuels and radically new technologies. This strategy additionally has to face a still-growing airplane market (see Figure 1 left). Under consideration of today's production of 50 airplanes per month, Airbus needs an increase in the airplane production rate to over 80 airplanes per month to satisfy the market [2] (see Figure 1 right).

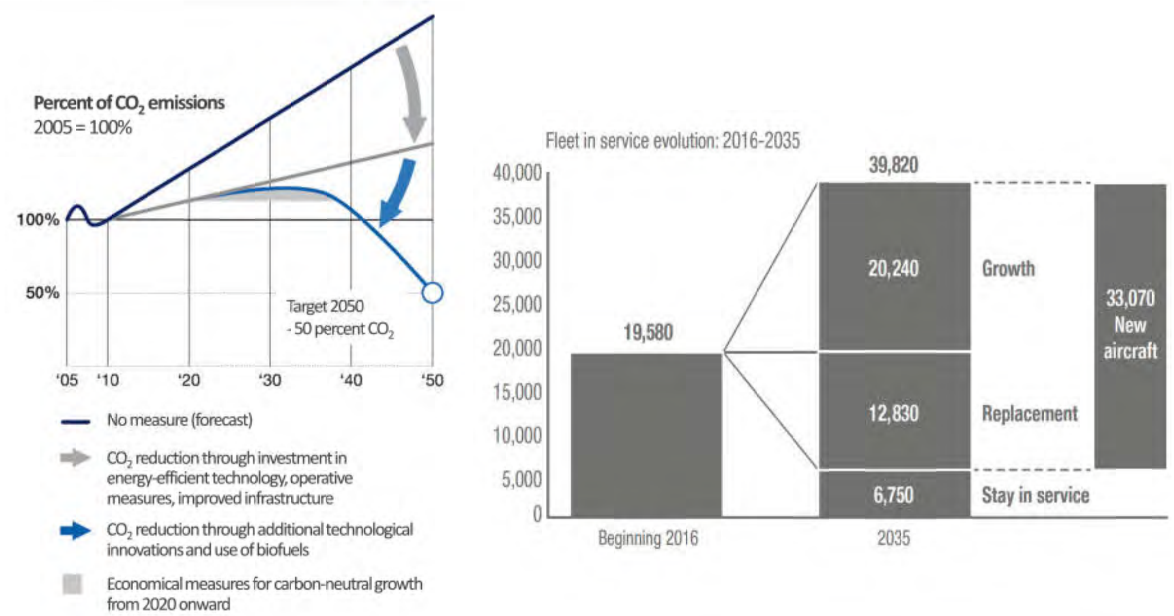

*Figure 1: left: IATA emission roadmap [35] figure after [18]; right: AIRBUS aircraft growth forecast [2]*

Various ways are available to reach these goals, whereby the use of materials with higher performance is one of these. Composites can be called the third major material era in aviation after the use of wood and aluminium. With each material, the basic design of the aircraft also changed. The first airplane fuselages made from wood were trusses with longitudinal and transverse/vertical stiffeners which were braced by wires. With rising flight speeds and heights, metal trusses were used and finally replaced by monocoque and semi-monocoque structures (stressed skins) made from aluminium alloys.

With the change from the metal fuselage structure to the composite fuselage these days, mainly a material substitution has been realised. Current composite fuselages are still semi-monocoque structures with a differentially manufactured and assembled load-bearing skin, stringers in longitudinal and frames in circumferential direction. Since this is certainly comprehensible to the risk of the new material, design methods and production processes, the combination of material and material-compatible lightweight design represents the goal in the structural development.

In space applications, carbon composites have been used for decades due to their extreme lightweight performance. Cylindrical structures like the airplane fuselage are found in similar size and also load, for example in shell structures or the interstages of big carrier rockets such as the Ariane, Proton or the Saturn. These shell structures are typically much more integrally manufactured and with the use of composites, a different kind of architecture, the so-called *lattice structure*, was invented in the US and Russia. Lattice or grid structures consist of a framework of stiffeners, called ribs, which intersect each other due to their different orientation. The high lightweight characteristics in combination with the high degree of integration and resultant low-cost manufacturing process also make the grid structures very interesting for airframes.

# 2 Research Hypotheses and Outline

As the grid architecture is used successfully for aerospace structures, the main hypothesis is facing that such a concept is also intended to have high lightweight potential for airframe structures. One of the main challenges is the adaptation of such a concept to current laminate rules, which would significantly simplify needed certification processes.

- Thesis 1: *An Anisogrid concept with variable helical angle, interface layers and laminate stacking of cut and uncut layers combines the advantages of grid structures and fulfils main laminate requirements for airframes.*

As visualised in Figure 2, this concept builds the basis for the thesis and is developed and described in detail in Chapter 4. The structural mechanical potential of the stiffening architecture is of crucial interest. Out of literature sources, a number of examples are present showing the lightweight potential. This bias is proven for the concept with skin. To do so, suitable material properties are needed.

Due to the specific concept design of cut and uncut layers in the intersections of the grid structure and resulting different laminate stackings in the plain rib and the knot area, the question arises as to which material properties need to be used for analysis in terms of stiffness and strength. In the literature, only limited results can be found and consequently, pure rib and knot element specimens are tested statically under tension and compression in Chapter 5.

- Thesis 2: *The material properties of the knot specimen are significantly reduced by the cutting concept in terms of stiffness and strength.*

For the potential analysis, the effect of skewing the stiffeners shall be investigated with respect to the minimum panel weight under given load cases. Motivated by the question of whether the Anisogrid stiffened panel design has an inherent, design based weight benefit, in Chapter 6 the concept is compared to a conventional Orthogrid stiffened panel design. To investigate the skewing effect separately, both stiffened panel designs will be analysed considering the same stiffener geometry, material and manufacturing concept.

- Thesis-3: *The triangular stiffened Anisogrid concept has an inherent weight benefit in comparison to the Orthogrid concept.*

The validation of the main concept features is based on a panel compression test and the results are described in Chapter 7. The aim is to validate fundamentally the functionality of the interface layers and the post-buckling behaviour of the triangular skin-bays.

- Thesis 4: *Anisogrid structures with interface layers are able to generate a reliable connection of the grid and skin, even during a deep buckling state.*
- Thesis 5: *Anisogrid structures with triangular skin-bays show a post-buckling behaviour without mode-switches which is different to stiffened panels with rectangular skin-bays.*

As a result of these investigations, the advantages and drawback of the concept are listed and a perspective for the proposed design concept is given in Chapter 8. In the last chapter of this thesis, the results are summarised and next steps are formulated.

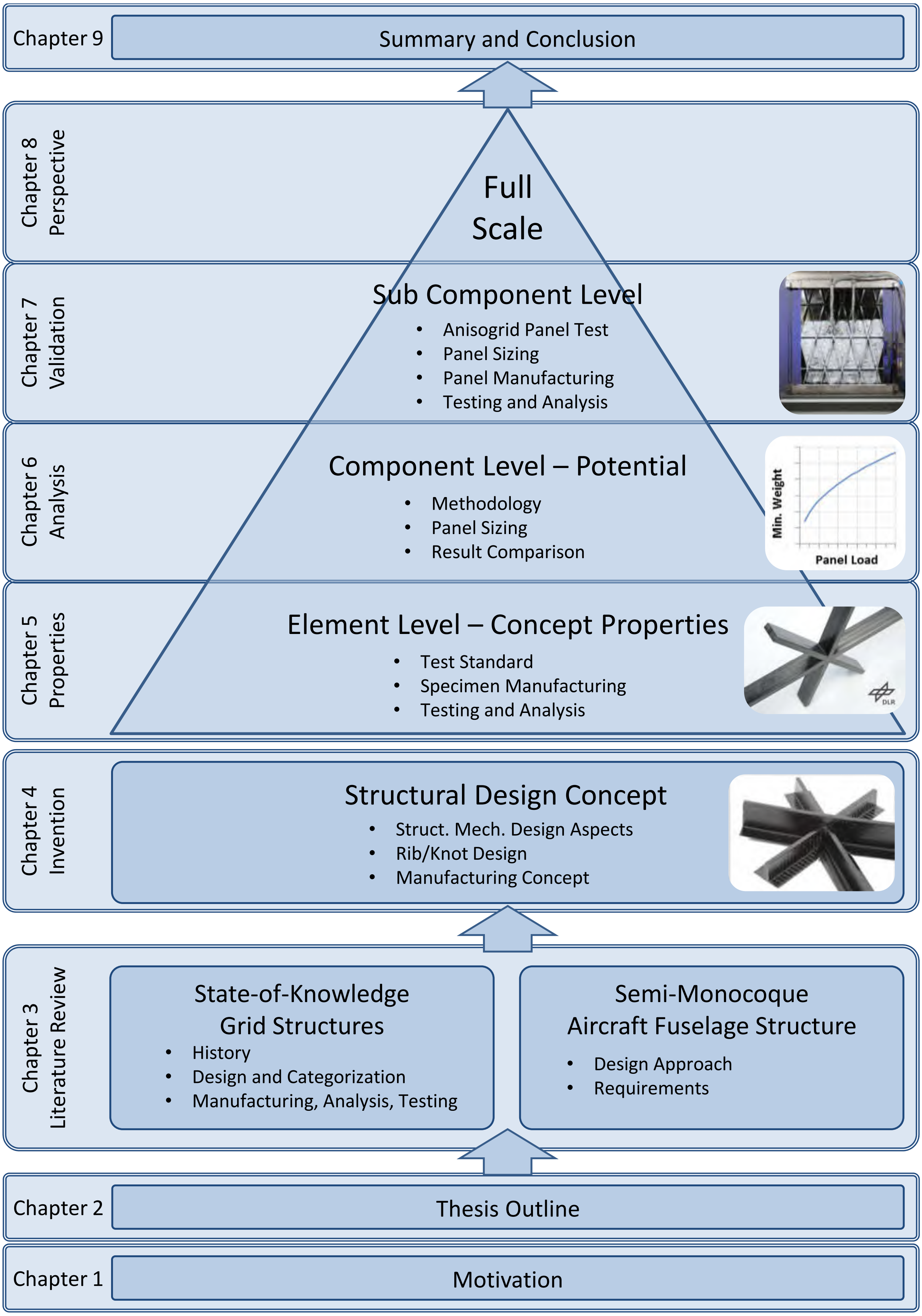

*Figure 2: Thesis structure*

# 3 State-of-Knowledge – Anisogrid-Design

In the history of the lattice structures, it can be seen that the researchers and designers developed this structure in a very evolutionary way. This means that new concepts were based strongly on current state-of-the-art designs. As a result, this chapter is structured quite chronologically. In Section 3.1, the origins of the lattice structures are presented and following this, the development of this structural concept is compiled for the United States, Russia and other countries, such as Japan. In the focused Sections 3.2-3.4, the development level is summarised for the manufacturing process, the analysis and the testing of the structure. In the last Section 3.5, today's semi-monocoque structure is explained including the requirements for the new fuselage concept.

## 3.1 Historic Sources

The first lattice towers were invented and built by Vladimir G. Shukhov (patented in 1896) within the framework of the 16th All-Russia industrial and art exhibition in Nizhny Novgorod in 1896 [77]. The towers consist of different hyperbolic segments, which are built from open metal profiles. The stiffeners connect the bottom and top of a segment at an angle, creating a lattice of intersecting stiffeners. In the intersection points, the stiffeners are simply riveted with one or two bolts. At specific distances, additional circumferential rings complete the framework structure. The hyperbolic shape of a segment results from the usage of straight stiffener profiles and the two angled stiffener directions. The Shukhov water towers are known as extremely weight- and economically-efficient constructions. This can be seen by comparing the original plan of the Sabovka tower (350 m height, approx. 2200 tons) with the Eiffel tower (305 m, 8850 tons) or the Tokyo radio tower (330 m, 4000 tons) designed at the same time [77]. Shukhov's lattice towers found wide application as water, light and radio towers, not only on land but also as ship masts (lattice or cage masts – on Russian and US battleships) (see Figure 3).

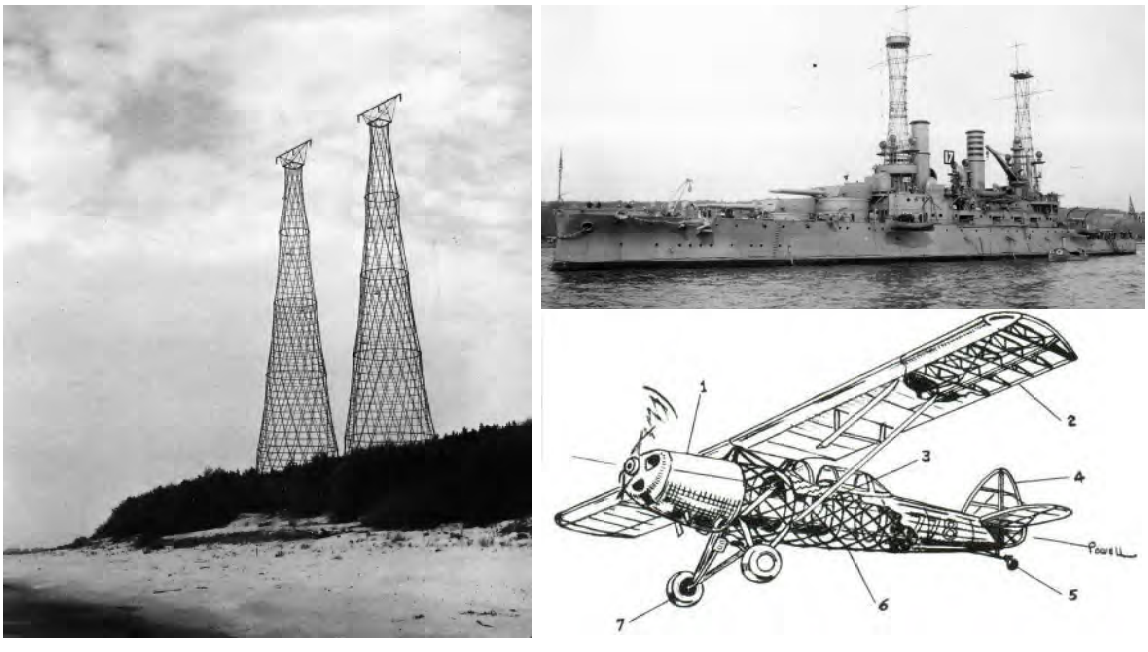

*Figure 3: left: Shukhov radio towers in Nizhny Novgorod region (still in service)*
*right, above: battleship, USS Michigan, with lattice radio towers*
*below: Earl Player's "The Player" with lattice plywood fuselage [63]*

For airframes George Yates from Beaverton, Oregon, worked on first fuselage and wing structures for home-built aircraft such as his “Stiper” in late 1920’s [63]. The former Navy man was inspired by the lattice masts on World-War-I battleships like USS Michigan or USS Arizona. Yates, Player and Thalman later built fully plywood airplanes with stripes wound around bulkheads and circumferential formers/frames (see Figure 3). Although this structure was titled as very lightweight and especially cheap to manufacture [63], the design kept “a kind of footnote in American aviation design” [7]. The first patent on a geodetic airframe fuselage welded out of metal stripes was claimed by Harvey C. Mummert in 1929 [51], whether no direct connection to Yates, Player or Thalman can be observed today.

A much further step Sir Barnes Wallis made at the company Vickers in the same time in Great Britain. He developed and built the first geodetic airplane fuselage structure for the prototype G.4/31, which had his first flight in 1934 [52]. Sir Barnes Wallis collected wide experience with mathematics of geodetic structures with the design of airships, particularly the Vickers R.100. The so-called retaining mesh wires of the gas bags follow geodesic lines, producing a rigid curvilinear shell structure. The well-known Vickers Wellington bomber was invented in the following years with geodesic fuselage and also wings and had its first flight in 1936 [52] (see Figure 4, left). The Wellington fuselage structure consists of full metal left and right handed helical struts which are torsionally fixed by a pair of so-called fish plates at the intersecting points (see Figure 4, right).

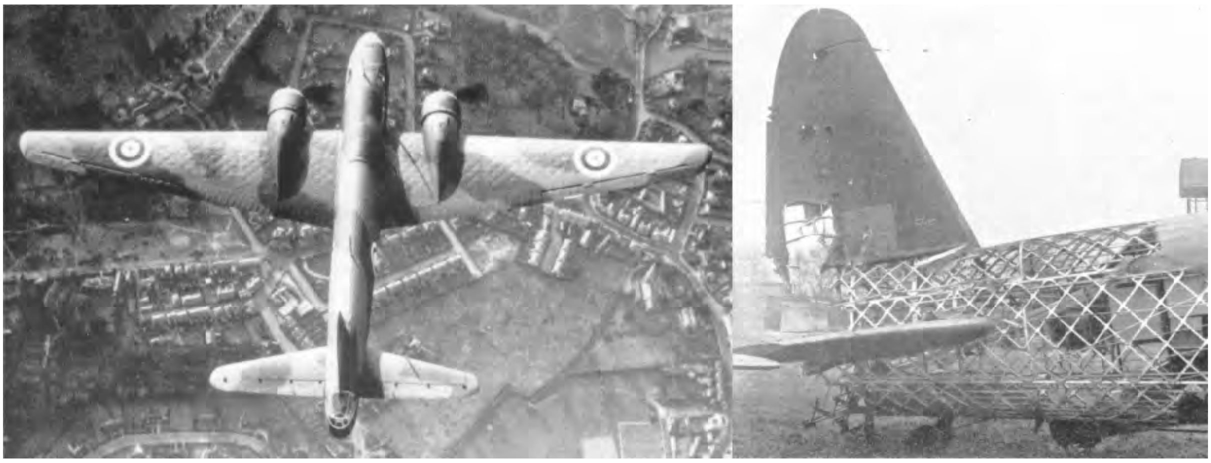

*Figure 4: left: Wellington bomber in flight [52]*
*right: Wellington visible structure due to massive damage [52]*

The Wellington bomber was attested as very lightweight bomber with high cargo capacity and mainly as very robust aircraft. There were lots of cases that the bombers still came back home even with major structural damage. Nevertheless after the second World-War the ‘Wellington’ design was not developed further because of the relatively complex helical strut design and the high assembly costs of the structure [52].

After first geodesic structures were realised for aircraft, the design has been caught up again for aerospace structures in the middle of the twentieth century.

### 3.1.1 Development of Grid Structures in the United States

The Isogrid stiffening concept as metallic integral structure was developed by R. Meyer under contract of McDonnell Douglas for space launchers such as the Delta [46, 53, 64]. The panels contained a load-bearing skin and ribs forming equilateral triangles, machined from aluminium plates (see Figure 5, left). In the 1970s, first designs with CFRP-reinforced Isogrid aluminium structures were patented by Paul Slysh [73–75].

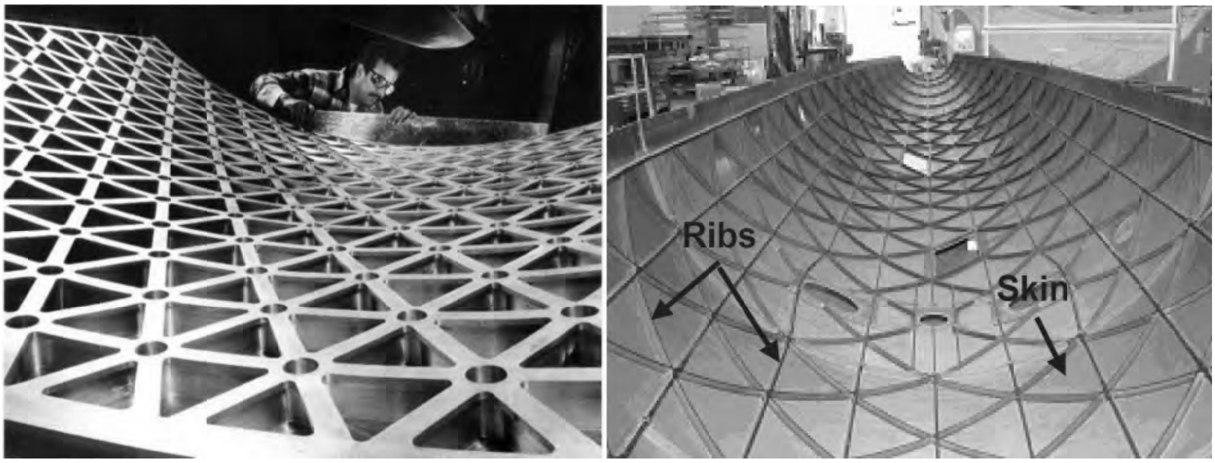

*Figure 5: left: Aluminium Isogrid panel [4];*
*right: Advanced Isogrid Structure (AGS) on Minotaur fairing [9]*

In the late seventies and early eighties Rehfield and Reddy made great progress in terms of analysis and also manufacturing concepts of Isogrid structures [66–69]. In these studies, the authors kept more or less to the equilateral Isogrid concept, which is much easier to analyse due to the isotropic properties of the grid. In 1985, Reddy mentioned that they varied the angle of the grid and also the angle of the skin but the Isogrid was the best configuration [65].

From the mid-nineties Huybrechts, Tsai and Meink analysed, manufactured and tested grid stiffened structures in a wide extent. Notably due to the new capabilities of computational calculations, Huybrechts and Tsai analysed the grids not only as Isogrid but also as, named by them, “Advanced Isogrid Structures” (AGS), where the triangles were not fixed to equilateral triangles anymore [13, 31, 34]. Huybrechts and Meink focused on the manufacturing concept of so-called “Hybrid Tooling manufacturing method” [32] for wet-winding, out of which Wegner et al. developed later the so-called “Expansion block” method [33]. The author’s results showed the potential for the AGS particularly for the development of aerospace shroud structures [95], wherein Wegner, Higgins and Biskner developed the Minotaur fairing [9, 28, 29] (see Figure 5, right).

### 3.1.2 Development of Grid Structures in Russia

One of the first lattice structure made from composite material was developed, manufactured and tested in Russia in 1981 in terms of a rocket interstage [87]. As a consequence to the promising results, a research campaign was initiated at the Central Institute of Special Machinery (CRISM). Interstage structures as well as a first aircraft fuselage barrel section were manufactured in 1985 and 1986 [87] (see Figure 6). The lattice interstage concept was further developed and went into service for the Proton M rocket as highly weight efficient shell structure in the 2000’s [89, 91]. The entire rib structure including reinforcing elements for cut-outs and end rings for connection are manufactured in a one-shot wet-filament winding process [6, 88].

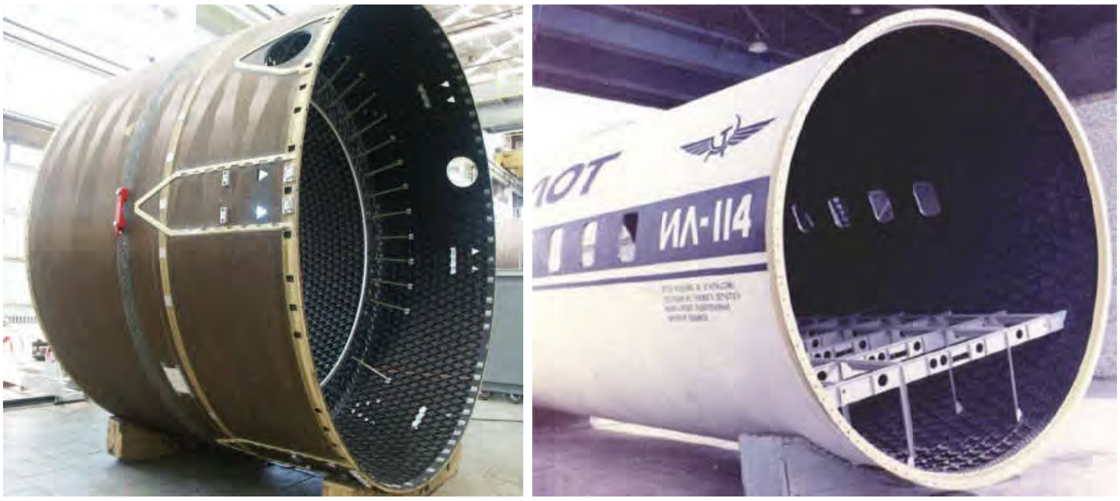

*Figure 6: left: lattice interstage structure [88]; right: lattice fuselage demonstrator [92]*

Since beginning of the new millennium, Prof. Vasiliev et al. are frequently publishing their research and application results, getting involved in several international research projects [92].

### 3.1.3 Development of Grid Structures in Other Countries

In the middle of the 1980s not only in the US and Russia the grid structures were part of research but also in Japan for the design of aerospace structures by e.g. Mori, Hosomura et al. [30]. The main question for these researchers was also the design, analysis and manufacturing of lattice structures [26, 60]. Very impressive is that on the Japanese space launcher Mu-SII-1 a composite lattice structure (without skin) was successfully used as the 3rd interstage in 1985, which might be the first flown composite lattice space structure [61] (see Figure 7).

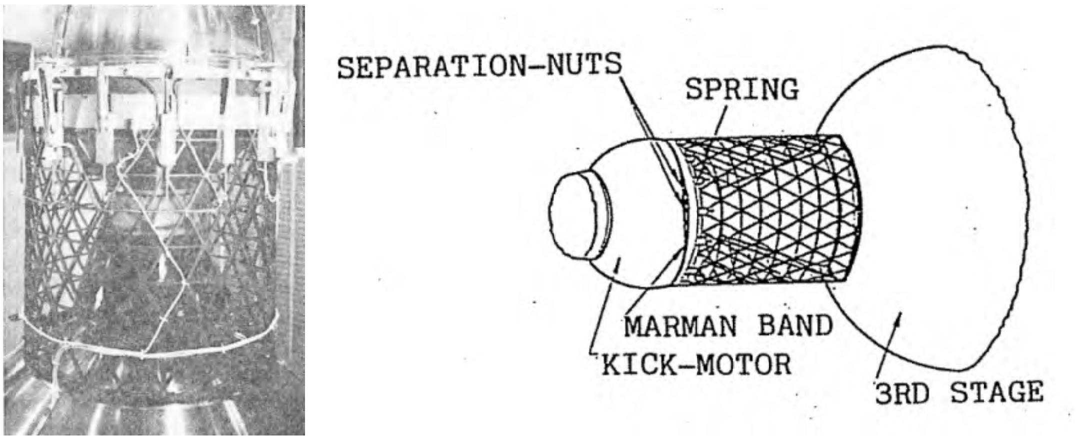

*Figure 7: Composite lattice structure on Japanese Mu-3SII rocket 1985 [61]*

In Canada the company ICCI, Isogrid Composite Canada Inc., produces plates and shells with AGS grid in an own patented automated fibre placement process, since 2003. The company produces e.g. floor panels for different applications such as helicopters or cargo containers [37].

In his dissertation, supervised by Prof. Vasiliev, Giovanni Totaro works on the design, analysis, manufacturing and testing of lattice structures at the Italian Aerospace Research Centre CIRA [80]. Starting with optimisation of lattice structures globally [86] and analysing local buckling capabilities [81, 82], the manufacturing of lattice structures with dry-fibre placement is quite special [83] which Totaro and his colleagues are focussing on.

In recent years the EADS CASA group in Spain also works on lattice structures for aerospace applications [17]. They investigate the design and the Advanced Fibre Placement manufacturing process.

At the Technical University of Delft, fibre steering technique with the Automated Fibre Placement (AFP) process has been tested and analysed for grid structures. The fibre tows are steered by its half width around the intersection knot keeping a constant rib height and enabling usage of high fibre-volume-ratio. In view of these investigations and in cooperation, the NLR is also performing manufacturing trials and design concepts on panel level [10].

### 3.1.4 Categorisation of Grid Terms and Definitions

As a result of the literature review, the common definition of a grid structure and also categorisation of different grid types shall be summarised.

A *grid structure* is typically understood as a global highly integrally manufactured stiffened structure. The most important point is that stiffeners of different orientation are present and that they intersect each other in some way, thereby building a stiff self-carrying and loadable plate or shell structure. The number of stiffener orientations can vary between two and four. The cross-section of the stiffeners can be monolithic, then typically called ribs, or of other shape. A skin can also be combined on one or both sides with the grid, whereby an open grid structure without skin is also typical in use.

The categorisation of the grid structures in literature is carried out according to the quantity of stiffeners and, most of the time, by the angle at which the stiffener directions intersect each other. Typical grid structures are symmetrical, which means that e.g. equilateral or equal-sided triangles are formed for tri-directional grids. The following definitions are used quite commonly in literature (for illustration see Figure 8):

- "*Axial-/ Radial-grid*": is seen to be beneficial to define in particular for the tri-directional grid types. Axial-grid means that the third rib direction (e.g. basis of the equal-sided triangle) is oriented along the main load or e.g. along the axis of a curved shell structure. Radial-grid means that the third rib direction is transverse oriented to the curvature of a shell.
- "*Orthogrid*": is a two-directional grid structure, in which the stiffeners are oriented in 0°/90° direction and a quadratic or rectangular cell is resulting.
- "*Isogrid*": is a tri-directional grid structure, whereby the triangular cell is equilateral, resulting in a stiffener angle of 60°. The isotropic in-plane properties leads to the "iso"-prefix [32].
- "*Anisogrid*": is a tri-directional grid structure. In contrast to the Isogrid the angle of the helical ribs is adaptable between 0° and 90°. The term is used e.g. by Totaro [84] and De Nicola [15]. Particularly in this thesis, Anisogrid describes a radial-grid.
- "*Advanced Isogrid Structure*" or "AGS": is a tri-directional grid structure, in which the angle is variable and the triangular cell is typically equal-sided. The AGS term was introduced in the United States. AGS are mostly used as axial-grids.
- "*Lattice Structure*": this expression is mainly coined by Prof. Vasiliev and is related to tri-directional grid structures. The angle is variable. A triangular cell is also equal-sided, whether typically for lattice structures the circumferential ribs are split and diamond shaped cells result. Lattice structures are typically radial-grids and in some cases axial ribs are added.

- *"Wafflegrid"*: is a grid with four rib directions, whereby the wafflegrid has a fix helical angle of +/-45°. It is not very common as manufactured structure, but often used in design comparisons.

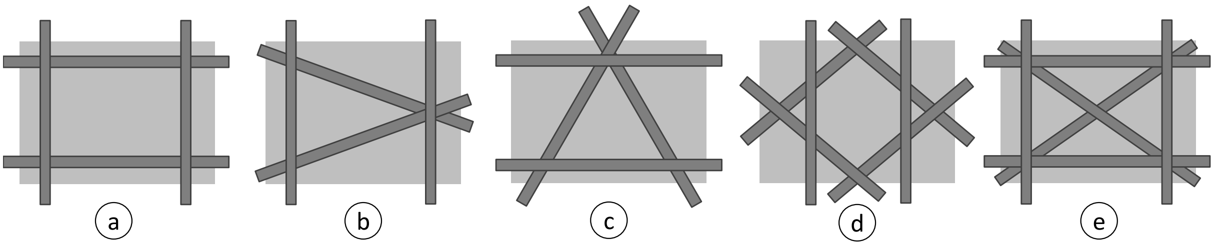

*Figure 8: Common grid types: Orthogrid (a), Radialgrid/Anisogrid (b), Axialgrid/AGS (c), Lattice Structure (d), Wafflegrid (e)*

## 3.2 Manufacturing of Grid Structures

A well-proven manufacturing process is the wet-filament winding used by CRISM. Very large 4 m diameter barrel structures as well as thin-walled beam structures are fabricated successfully and are in service today [89]. For the wet-winding process, dry fibre tows (glass, carbon or aramid) are pulled through a resin bath, impregnating the fibre tow with the matrix, and then wound on a mandrel. For the lattice structures, CRISM enhanced this process with silicone moulds containing the grooves for the ribs which is placed on the barrel-tool and wound around. Special developed resins enable, with their viscosity and pot life properties, that even large barrel sections can be wound, which is due to the size a time consuming process. As the whole section is wound with an endless fibre tow, the fibres are over-pressed at the rib intersections (the knots). The process reflects a real one-shot manufacturing meaning that barrel end rings, reinforcements for cut-outs or load introductions are fabricated in the same time within the rib structure. Due to the low costs of the raw materials and the high degree of automation it is a very cost efficient process.

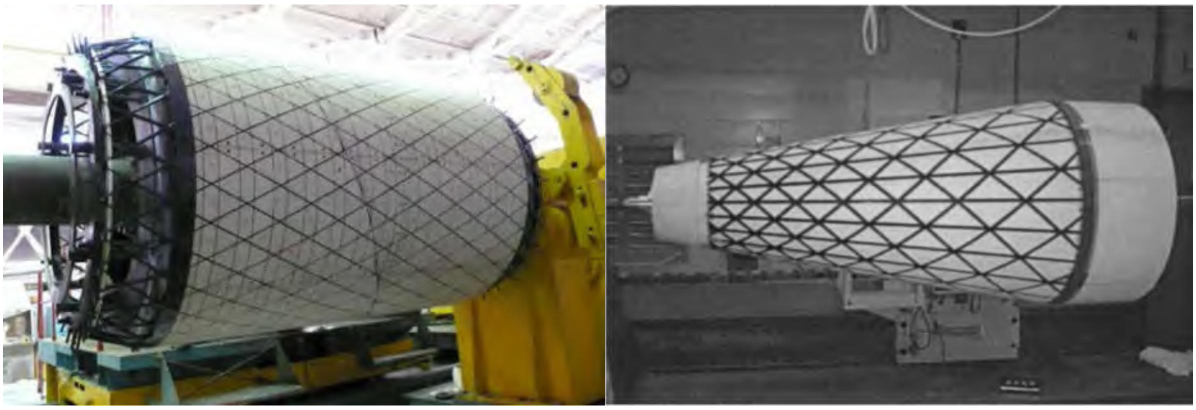

*Figure 9: left: Wet-filament winding [88]; right: Prepreg winding Hybrid Tooling [33]*

Besides the wet-filament, a winding process with pre-impregnated tows (prepreg tows, typically called slit tapes today) was used in the United States for the manufacturing of rocket shrouds by Huybrechts et al. [32]. They developed different kinds of tools for this process such as the *Hybrid Tooling* and the *Expansion Block* process. In both tooling concepts, silicon rubber is also used as expansion material for compaction of the rib laminate but in a different amount for better control of the compaction forces. A similar process is used by the ICCI Company in Canada.

An AFP process with prepreg slit tapes, EADS CASA investigates in their studies. A difference is that they work with a high fibre volume content which why no over-pressing in the knot is suitable. Different variants for the intersections were investigated and as a compromise of manufacturing and structural mechanical reasons a thickening at the knot was chosen [17].

Totaro and De Nicola developed in recent years a dry-fibre placement process in combination with infusion at CIRA [15]. A multi-axis robot is used for fibre placement and resin infusion for matrix infiltration in combination with an out-of-autoclave approach, reducing the process costs. The mandrel is covered with a grooved silicon-rubber carpet in which is wound. With this process, an interstage structure including end rings and local reinforcement frames for cut-outs has been successfully wound and infused, resulting in satisfying and promising material properties [85].

## 3.3 Analysis Methods

The analysis of grid structures can be divided into the analytical/semi-analytical methods (smeared stiffeners) and the numerical-based methods (discrete stiffeners). With the help of increasing calculation performance, the numerical methods are being used more and more, even in detailed models for optimisation purposes with multi-parameter problems. Classical, but highly efficient, are the analytical and semi-analytical-based methods for the sizing and optimisation of large design spaces and different architectures. The main sizing criteria are the global stability of the shell or the cylinder, the local stability of the stiffeners and, if applicable, the skin, and the strength in all elements.

### 3.3.1 Smeared Methods for Stiffeners and Optionally a Skin

The global description of the deformation and stability behaviour of a grid structure is carried out in many ways with the help of smeared approaches. In general, the smearing of the stiffeners into an unstiffened plate with uniform thickness is a suitable method shown by different researchers. The computation of the equivalent orthotropic plate stiffnesses enables efficiently the consideration of stiffeners with any orientation or grid pattern. With these equivalent stiffnesses, typically, a Rayleigh-Ritz energy based method as approximation procedure is used to calculate the global buckling loads of the panel.

The basic smearing approach for Isogrid structures optionally with skin is described in the NASA Handbook from 1973 [53]. On the one hand the Isogrid is limited to equilateral triangles (60° stiffener angle) but also flanged ribs are considered, due to the focus to metallic structures.

In 1984, Stroud et al. showed the evaluation of buckling load estimation with a smeared stiffness approach in comparison with finite element models in a NASA report [76] for uniaxial compression. He observed in some cases high overestimation of the smearing approach and concluded only limited utilisation of their smearing method.

In 1986, Onoda used a sizing and optimisation approach for lattice structures without skin considering orthotropic shell properties [60]. Due to the symmetric rib structure without skin, the stiffness matrix simplifies strongly and besides other geometric variables he could consider the rib angle as sizing variable.

In the early nineties, Chen developed an equivalent stiffness model for a grid with optional skin in the form of a Mindlin plate considering effects such as torsion, in-plane bending and shear of the ribs [13, 14]. Chen used a finite element model for calculation of the shell deformations under uniaxial or also combined loads. With the stress and moment resultants, the stresses and local buckling were proven in all elements. He concluded high accuracy for the panel displacements and reasonable accuracy for the strains and stresses.

At nearly the same time, Jaunky et al. developed an advanced smearing approach with which the skin-stiffener interaction is considered [3, 40]. This is carried out by a more exact consideration of the neutral axis at the stiffeners' position along the panel. They proved their approach with finite element models for axially, Orthogrid and tri-directional grid stiffened panels under uniaxial and combined load cases. A good correlation was summarised for global buckling in comparison to former approaches.

Vasiliev et al. described their closed-form smearing approach 1999 for the tri-directional lattice structure [90]. Global and local buckling as well as strength criteria are considered. Different grid designs (lattice or Anisogrid layout) are taken into account by different K-values (end fixing constants) for the stiffener local buckling criterion. Totaro uses the same smearing approach, verifying the stiffener buckling criterion by finite element models, and adding a stiffness criterion to the analytical sizing process [84].

In the early 2000s, Kidane et al developed a general smeared model for determination of the global buckling load of symmetrical and unsymmetrical stiffened grid structures optionally with a skin [42, 43]. The global buckling load is determined by a Rayleigh-Ritz method wherein the total potential energy of the cylinder shell is composed of the strain energy and the work by the external force.

### 3.3.2 Skin-Bay Buckling

The buckling of isotropic flat triangular plates was investigated by Tan et al [79] with the help of a finite-element model, resulting in given buckling value tables for specific triangular shapes, loads and boundary conditions. Jaunky et al. [39] developed a method for general triangular plates with anisotropic material properties, different boundary conditions and loadings. The method is based on a Rayleigh-Ritz approach and variation formulation.

In 2014, M. Weber presented a semi-analytical method, also based on a Ritz energy approach, to determine the local buckling value for rectangular, triangular, rhombic and hexagonal skin-bays [94]. In his method, he also implemented the consideration of anisotropic material properties and shell curvature. Particularly for the triangular skin-bays, Weber showed significant buckling value gain in comparison to rectangular skin-bays considering the same aspect ratio of unit cells. For high shell curvature, this increase is raised further. These impressive values support the expectation of higher weight-efficient Anisogrids in comparison to Orthogrid structures. On the other hand, it has to be taken into account that the same aspect ratio means the Anisogrid needs twice the stiffeners. On a global panel design, it is questionable as to whether the buckling value increase also results in corresponding panel weight benefits.

### 3.3.3 Optimisation and Potential of Grid Architectures

Reddy presented in 1985 a comparison of an Isogrid with Orthogrid structure with skin analysing two C130 fuselage load cases [65]. He calculated for both structures a 30% weight decrease in the metallic reference structure under consideration of global and local stability failure criteria.

Jaunky et al. optimised grid stiffened composite panels [41] as well as general stiffened composite cylinders [38]. In their investigation, they considered the local (stiffener and skin) and the global panel stability criteria. For optimisation, they used a genetic discrete algorithm being able to vary axial and transverse stiffener spacing, stiffener height and thickness of the skin laminate, and the stiffening configuration. As an example he sized an axial and grid stiffened cylinder for an axial load, achieving nearly the same weight (within 2%), and showed that the grid-stiffened cylinder can handle magnitudes higher additional loads (transverse compression and shear) than the axially stiffened structure. As a result, he concluded that the grid structure should be more damage tolerant.

In 1998, Meink et al [48] presented a weight comparison of a sandwich and advanced grid (AGS) shroud structure. The sandwich design is said to be the weight reference, because it is much lighter than a metallic concept, and the AGS concept is motivated most likely by the manufacturing costs than the further reduction of weight. Nonetheless, the AGS was sized with the same weight fulfilling the same sizing criteria than the sandwich structure, whereby the margins for all sizing criteria were quite different. The sandwich was seen to be stiffness driven whereby the AGS was material failure driven. The result was promising so that the authors proposed to scale up the manufacturing to 4-5 meter shrouds.

Vasiliev briefly showed a weight comparison of a lattice cylindrical structure with a frame-stringer stiffened shell and a sandwich structure, normalised to an unstiffened shell in [90]. All structures are sized with the same sizing criteria and resultant the lattice structure promises significant weight potential.

In 2011, Klinzmann presented a comparison of a semi-monocoque with a grid fuselage structure of the same design and material [45]. The comparison is based on a given semi-monocoque reference made from aluminium with load-bearing skin, hat-stringers and C-shape frames. In a fixed geometrical configuration, she designed a grid structure in which the stringers are skewed, keeping the same quantity of stiffeners as well as the same panel weight. As a consequence, the grid stiffeners are reduced in thickness and triangular skin-bays occur. With these two configurations, she performed different parameter studies, such as changing the skin thickness, varying the stiffener distances (or angle) and comparing the failure load of the panel. It could be shown that the grid structure only carries higher loads under shear-dominated load cases. This result seems to be plausible because for these loads, the helix stiffeners are carrying additionally to the skin loads. Nevertheless, it is one of the only comparisons in literature where the potential of an Anisogrid stiffened structure is shown much more differentiated, demonstrating that e.g. no weight potential can be generated under compression loads. The question arises as to whether this almost singular result is occurred due to the strong geometrical restrictions and, in consequence, that here two structures were compared with different margins of safety for the sizing criteria. The sizing did not include e.g. the stiffener shape or distance.

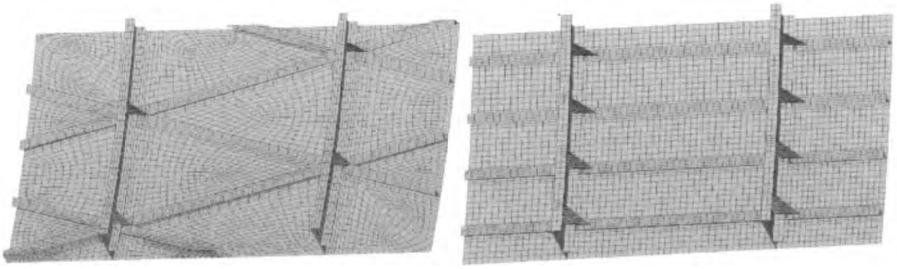

*Figure 10: Comparison of semi-monocoque and grid fuselage panel structure by Klinzmann [45]*

At this point, it should be mentioned that the procedure of Klinzmann in comparing the same quantity of stiffeners is clearly comprehensible, because she is comparing two differentially manufactured structures. Different quantities of stiffeners mean directly different manufacturing and, in particular, assembly efforts and costs, which would be difficult to compare when they are not the same. For integrally manufactured concepts, this restriction is seen to be not as strong, as only the manufacturing time would be different to some extent. As a result, this restriction can be left open.

## 3.4 Testing of Anisogrid Structures

A first wide panel test program was summarised by Rehfield in 1980 [67]. Flat composite Isogrid panels as wide columns were tested in compression and besides the scattering of results due to manufacturing reasons the correlation with used analysis theory was satisfying.

First tests on the damage tolerance of grid structures were performed and described by Reddy et al. 1983 [64]. Non-destructive buckling tests were performed on flat wide panel columns whereas the buckling resistance was measured and consequently, degraded in multiple test runs by destructive cutting of ribs. The comparison with finite element calculations was satisfying and a good structural damage tolerance was observed due to the occurring stress redistributions.

In 2000, Kim [44] analysed and tested a cylindrical Isogrid shell with skin. The cylinder reached the numerical predicted failure/buckling load quite well. The critical failure mode was the stiffener buckling which resulted in a global buckling of the cylindrical shell. After several skin-stiffener separations the overall structure failure occurred. The local buckling of the stiffeners and the further loading capacity of the structure Kim described as post-buckling behaviour and stated a good damage tolerance of the structure.

In 2002 Higgins et al [29] presented results of cylindrical axial-grid panel compression tests. A skin-bay buckling occurred and the relatively thick skin twisted the axial ribs whereby the final panel failure occurred as a result of rib-skin-separation. As the main focus area for further development, the improved joint failure prediction was determined amongst others. In 2005 and 2007, Biskner and Higgins [8, 9] showed their results on the reinforcement of a thin skin with lightweight foam to stabilise the skin-bay and the axial rib, and to prevent the most critical peel-off failure of skin and ribs.

Nicola et al tested two different manufacturing processes (wet-winding, prepreg winding) via compression test on element level [15] in 2009. Therefore they cut grid rib and knot specimens from the cylindrical structures. Due to the high fibre-volume-ratio of the prepreg, material built-up at the intersection area needed to be accepted. The results showed low stiffness and strength properties due to the misaligned fibres at the intersection. Tension properties have not been presented.

## 3.5 Semi-Monocoque Fuselage Design as State-of-the-Art Architecture

The fuselage, as central element of the aircraft, has to fulfil multiple, often contrarian requirements. There is basically the bearing of ground and flight loads (mechanical and thermal), capabilities for handling damages of different sizes, crash demands, lightning strike, thermal and noise insulation, and also reparability and inspection possibility during service. All these demands should be realised with the lowest possible structural weight for corresponding aircraft performance and fuel efficiency.

With increasing flight speeds, altitudes and cargo loads the change from wood to metal fuselages established in the first half of last century. Together with the change of material, the fuselage design also developed further. The framework truss designs were converted into shell constructions, whereby the longitudinal and transverse stiffeners were adopted and the skin replaced the diagonal beams or wires as shear element. Main reasons for the skin were the generation of a smooth aerodynamic outside surface and also the *stressed skin* which is increasing the structural efficiency. On the other hand the stressed stiff skin effected the change from statically determined to undetermined stiffened structures. As first step for dimensioning, the grid of longitudinal (stringers) and transverse stiffeners (frames) in addition with the skin were calculated as so-called shear field scheme, in German phrase *"Schubfeldschema"*. The stiffeners are sized to carry only normal loads and the skin the torsion/shear. However, with new failure modes of a now buckling skin e.g. under shear/torsion the quantity of stiffeners for stabilisation of the skin increased. As a result, the new demands required new sizing algorithms and methods and a lot of tests were performed to validate these new methods.

Today, the semi-monocoque design still consists of a load-bearing skin, but considered for the whole spectrum of loads, stringers, stiffening the skin in longitudinal fuselage direction, and frames, stabilising the fuselage in circumferential direction (see Figure 11). This shell design, in German phrase *"Schalenbauweise"*, established to all civil passenger aircraft from single to long range aircraft with capacity of >50 passengers. Only the cockpit section is in many cases a monocoque structure consisting of a relatively thick skin, which is stiffened only by frames. For smaller aircraft in the size of business aircraft, Monocoque and also Sandwich fuselage designs are in service today.

The frames fulfil multiple tasks in the fuselage. They provide the cross-sectional shape, are load application elements e.g. for the floor beam and hat track loads and work as zero-deflection lines to increase global buckling capabilities of the barrel. In addition to the standard frames, there are also reinforced frames e.g. at the door surround structures or the wing box integration.

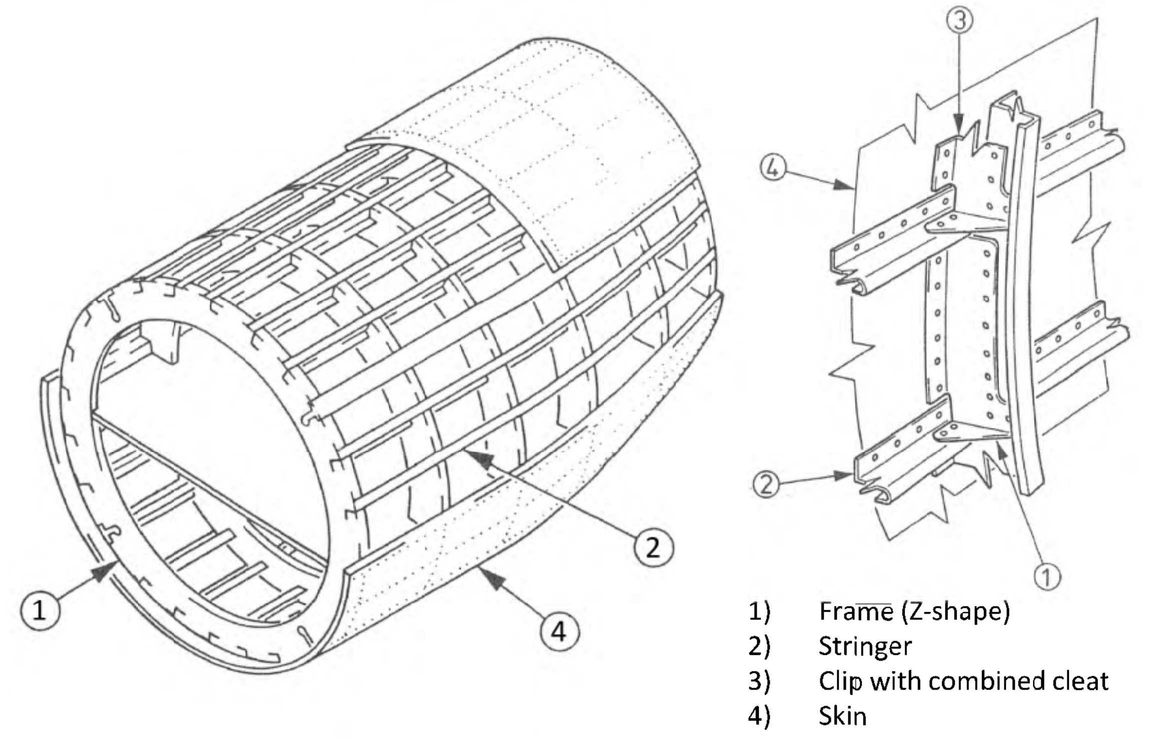

*Figure 11: Semi-monocoque structure design of today's large passenger aircraft, after [20]*

The frames are typical beam elements which are mainly sized by bending loads. They are open profiles with C or Z shape obtaining visual inspection and are joined to the skin by clips and cleats. Due to the uncut stringers which run on the skin, the frames need an offset from the skin/stringers which is generated by the clips. They generate a shear joining element to the skin and the cleats stabilise the frame against torsional-flexural buckling; both can also be combined in one element (see Figure 11). An alternative concept of using clips is that the frames have so-called mouse-holes to obtain clearance for the stringers.

The stringers carry in combination with the skin the bending loads of the fuselage. In addition, they divide the skin in multiple skin-bays to increase the panel buckling resistance between the frames. Therefore they need to prevent a deflection in the out-of-plane direction of the panel resulting in profile shapes with high moment of inertia.

The skin is a multiaxial loaded structural element in the fuselage. It is the essential structural element to carry the pressurisation and shear loads but is also loaded by the axially acting bending loads.

With the current material change from metallic to composites, the advantages of higher degrees of integration are strongly under investigation. Main motivation for an integral in comparison to the differential structural design is the reduction of stress concentrations at the joining elements (rivets) and the reduction of needed assembly efforts and costs. For new airframe architectures, the development chain is therefore tremendously long. In contrast to the structural design concept, where as many requirements as possible shall be considered, the concept analysis needs to be focused step-by-step on specific topics. Consequently, in this thesis the structural mechanical concept is developed and analysed under consideration of manufacturing demands.

# 4 Anisogrid-Prepreg-Design-Concept

*Thesis 1: An Anisogrid concept with variable helical angle, interface layers and laminate stacking of cut and uncut layers combines the advantages of grid structures and fulfils main laminate requirements for airframes.*

As the main developments on the grid structures have been made in the last decades for spacecraft structures, these designs can be considered as a basis. Deriving from these spacecraft designs, the challenge for an airframe structure concept is which design details can be transferred, and which ones need to be adapted or completely renewed. The main difference between a spacecraft and an airframe structure is the completely different durability demands. Simplified, it can be said that the spacecraft structure needs to fly only once, with, incidentally, a maximum of reliability, whilst the airframe structure has to sustain a life cycle of 20 to 30 years with thousands of load cycles.

To answer this question and to derive a suitable design concept, different structural levels are focused on in this chapter. In Section 4.1, the main aspects are explained which are evident for the integral concept. Subsequently, the design concept is developed in Section 4.2. In Section 4.3, the manufacturing concept is discussed in detail and in Section 4.4 specific design details are investigated.

## 4.1 Design Aspects for the Anisogrid Design Concept

Following, three main design aspects are examined: the manufacturing process, the intersection approach for the different oriented stiffeners and the interface of the rib structure with the skin.

### 4.1.1 Manufacturing Process

The prepreg Advanced Fibre Placement (AFP) process appears to fulfil the demands most beneficial of the presented processes in Section 3.2. Main advantage of the prepreg material are the highest quality assured properties due to the low tolerances in the prepreg production in terms of fibre-volume-ratio (FVR) scattering and fibre orientation deviation (under consideration of certified materials). As a result, prepreg processed parts are assuring very high material property tolerances of the cured part. The AFP process adds the advantages of a fully automated process which is quite established and proven now for aircraft production (Boeing 787 and Airbus 350 fabrication). As current AFP processes work mostly with unidirectional (slit-) tapes, also fabric or multiaxial tapes are in principle possible to process. Another and important difference of the AFP technique in comparison to e.g. the wet-filament winding process is seen in the flexibility to adapt locally the placed material. As a consequence, adaptable stiffener cross-sections and also more freedom for the placement path of the fibre are realisable since nearly no tension is arising in the tow during the AFP process. The tape is literally placed. At a winding process the needed and arising tension force in the tow limits the desired part geometry (e.g. needed convex curvature of fibre path) and bridging effects can occur. Bridging means that the tow is tensioned between the rib intersection points and a shell with more polygonal instead of a circle shape are fabricated. This effect becomes more critical the higher the ribs are.

Main disadvantage of an AFP process with prepreg material is that it is an expensive manufacturing process due to the prepreg raw material itself and the high amount of required large production facilities means the AFP robot or gantry facility plus large scale autoclave. The wet-winding process and also the dry-fibre placement process in combination with an infusion process have way lower costs, due to the much lower raw material costs of the rovings and the resin in comparison to the prepreg tows or slit tapes. On the other hand, the risk of the Liquid Composite Moulding processes (LCM) and, in consequence, the risk of scrap rate or needed rework is increasing drastically due to the process complexity, the high amount of processed materials and the size of a panel or even barrel section.

As a side note it shall be mentioned that the AFP material and process choice is, in general, also applicable to thermoplastic material. It is not the focus in this thesis but the pre-conditioned raw material and placement process itself can be adapted to these needed process conditions.

### 4.1.2 Grid Knots

The grid structures are significantly characterised by the design at the knots of the intersecting ribs. It is apparent to be the challenge between the variety of fibre volume content and the change of the rib cross-section dimensions.

A variety of the fibre volume content results when an *over-pressing* of layers in the knot is used. In this case, the plain rib between the knots features a relatively low FVR between 35% and 40%. At the rib knot the over-pressing causes the maximum possible fibre package between 70% and 75%. According to the plain rib fibre-volume-ratio relatively low stiffness properties are achieved for the overall rib-structure. This solution is typically used for the wet-filament-winding process (*lattice structures)*. The application of a low FVR together with over-pressing is also imaginable for prepreg material, but has not been utilised so far according to the state of knowledge.

For applications which require particular high stiffness properties, it is desirable to increase the FVR in the plain rib. As over-pressing in the knots is not suitable due to the high fibre package, the geometric variation of the rib cross-section can be used. In this case, two main ways are applicable: “*thickening*” the intersecting ribs at the knot into the height direction; or “*widening*” the knot into the rib width direction. Both kinds have the advantage that all fibres run through the knot and that the ribs have a high stiffness due to the high FVR. Disadvantages of the thickening method are seen that, depending on the rib height, high fibre waviness occur which reduces the strength properties. Additionally geometrical undefined rib surfaces occur with wide tolerances. For the widening, also, two ways are feasible: “*steering*” the tows by its half widths left and right beside the rib knot or “*spreading*” the tow at the point of the knot, which means spreading the tow in width direction. As a result, the height of the slit tape/tow is halved. Disadvantage of the steering are seen that in the steering areas before and after the knot fibre material is missing. In addition, the placement paths for the machine are quite complex and a tool with rib grooves seems to be impossible to use due to the necessary clearance for the placement head when it is turning along the fibre path. For the spreading of the tows, the main disadvantage is seen for the machine to realise the spreading of a tow on a small area in a continuous placement process. A weaving of the fibres would also occur even, that it might be not as much as it is expected for the steering method.

An alternative for using material with high fibre volume content but without thickening or widening the knot area is to simply cut the layers before the knot (*discontinuous* rib layers). This solution has the main disadvantage of expected strength reduction but, on the other hand, two main advantages which are a realisable high stiffness and an easy to automate, continuous slit tape placement process.

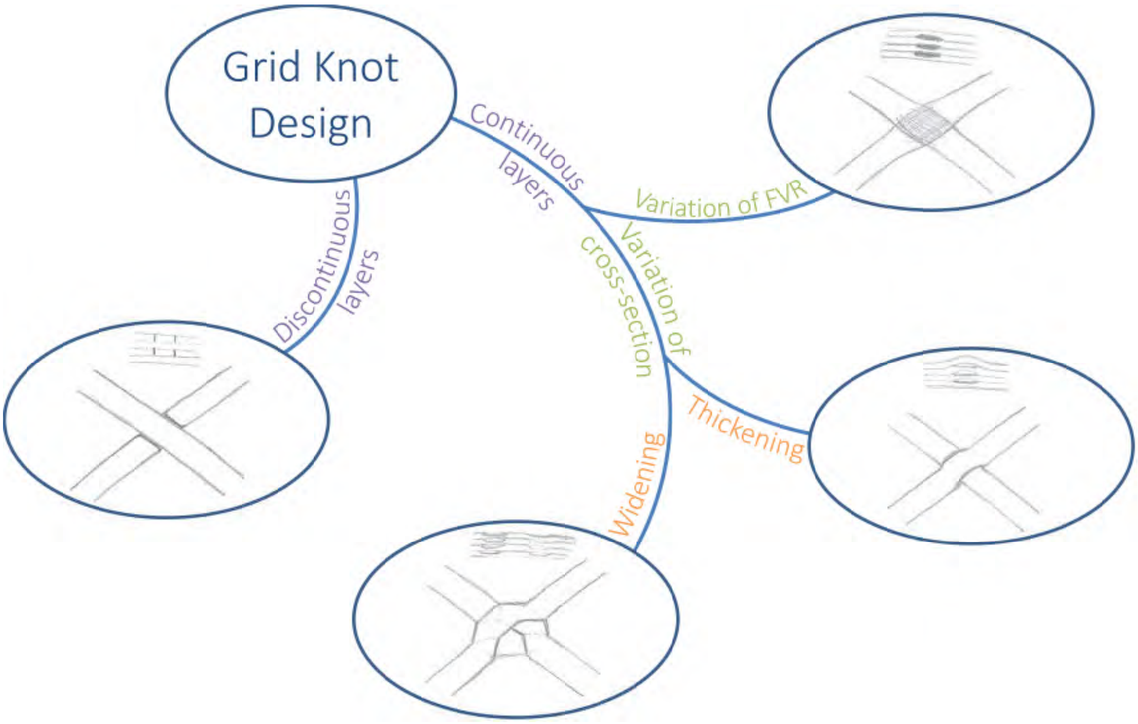

Figure 12: Variation of grid knot designs

In Figure 12 the described possibilities are shown. The use of cutting the layers before the knot is seen to be most suitable. Reasons are the quality assured prepreg process, high achievable stiffness properties, the constancy of the cross-section, and the placement process feasibility with relatively simple modifications.

### 4.1.3 Connection with Skin

For a long-lasting, highly loadable aircraft structure with required local buckling and damage tolerance capabilities, a proper interface between the rib structure and the load bearing skin is obviously essential. In contrast, classical grid structures combined with a skin provide only a very narrow joining area between the rib and the skin (see Figure 13). Such interface contains for example a low crack propagation resistance after impact damage.

As a result, different concepts are imaginable to increase the joining area (see Figure 13):

A. The rib layers are increased in widths in direction to the skin
B. The rib structure are “wrapped” with a hat laminate which is connects the skin with feet, working as shear connection between the rib and skin
C. Such “hat” layers are placed in several steps into the rib structure and run at the sides onto the skin

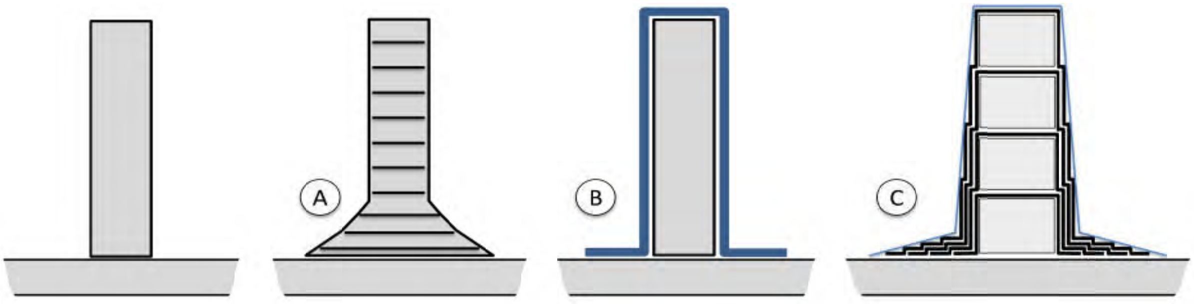

*Figure 13: Different variants for interface layers*

Variant A has the advantages that the rib layers, on the one hand, simply become wider, so that the same placement head and system can be used. The change of stiffness (stiffness jump) also decreases, so that peak stresses are reduced. On the other hand, the raw material needs to be wider or the number of tows, placed in parallel, needs to be increased. Additionally, a strengthening of rib properties in the third/thickness direction cannot be implemented with this method. A narrow and high rib is generated which is “open” at the sides.

Variant B and C improve the grid-skin connection in the same way. Both variants cover the rib completely and a large shear connection is generated between the rib sides and the skin. Variant B has the advantage that it is not as complex for the manufacturing process because only one laminate has to be place into the tool or maybe afterwards on top of the rib structure. Variant C has the advantage that with successive addition of interface layers in combination with constant rib layer widths automatically a draft angle is generated for the rib structure and also for the interface layer feet. This can be used advantageously for demoulding and during the placement process, because the groove is tapered in a certain extent providing more space for the head.

Additionally it may well be that the ribs with covering interface layers (variants B and C) does not have to be seen as open-edge structures such as blade stiffeners are typically considered. This can result in change of required damage tolerance design criteria which decreases the minimum weight. Open edges are risky for crack initiation and environmental conditions (e.g. moisture) and lowered allowable strains have to be considered.

## 4.2 Structure Mechanical Concept

The consideration of the laminate rules for aircraft structures (Section 3.5) and the different design aspects (Section 4.1) lead to the invention of an Anisogrid Prepreg Design Concept. This concept has been registered for a patent, which is currently under examination [50].

The Anisogrid Prepreg Design Concept consists of helical and circumferential ribs and a load-bearing skin (see Figure 14). The ribs are built with rib layers as main load-bearing elements in rib direction and interface layers for an improved connection of the rib structure with the load-bearing skin. The whole structure is intended to be placed fully automatically by fibre placement including the interface layers.

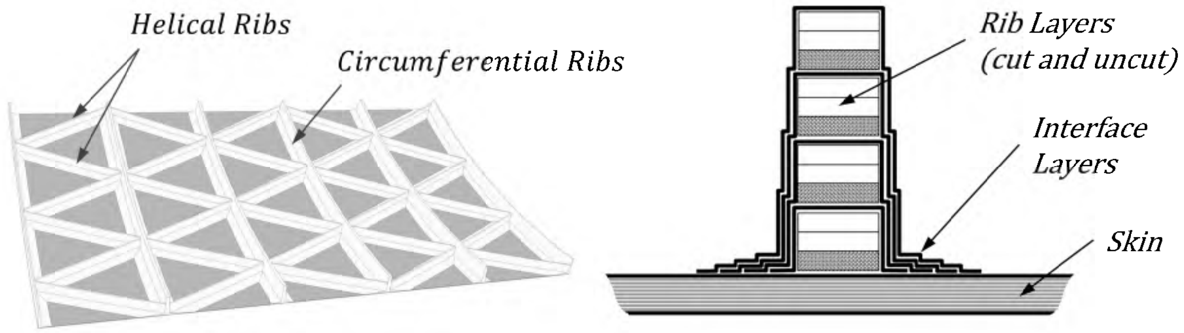

*Figure 14: Anisogrid Prepreg Design Concept [56]*

As described in Subsection 4.1.2, the desired high stiffness properties and the fully automated manufacturing process lead to the usage of cut layers in the intersection point of different rib directions. One layer runs through the knot, the other two are cut. This procedure alternates through the knot height for all layers (see Figure 15). Under consideration of e.g. three rib directions and an equal distribution of cut and uncut layers in all directions, the concept results in 33% of uncut layers for each rib direction.

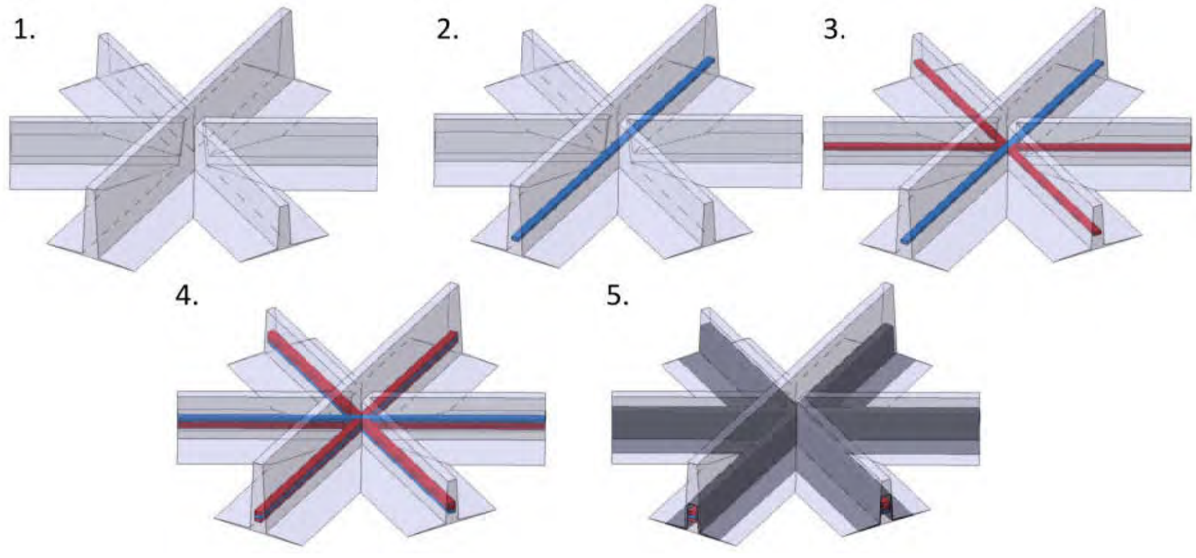

*Figure 15: Sequence of cut and uncut layers in Anisogrid prepreg concept [56]*

After a certain number of rib layers, an interface layer is stacked into the laminate (see Figure 15 No.5 and Figure 16). The interface layer fully covers the rib laminate and connects the rib with the skin by two resulting feet on the skin. Due to the successive addition and full covering, a draft angle results at the rib flanks. On the skin, the increasing length of the feet also generates a draft angle and additionally a smooth increase of the stiffness, which reduces peel stresses at the feet ends.

The thickness of the interface layer and the rib height until the next interface layer is added determine the resulting draft angle at the rib side. The interface layer thickness and the length of the feet layer steps determine the draft angle for the rib feet.

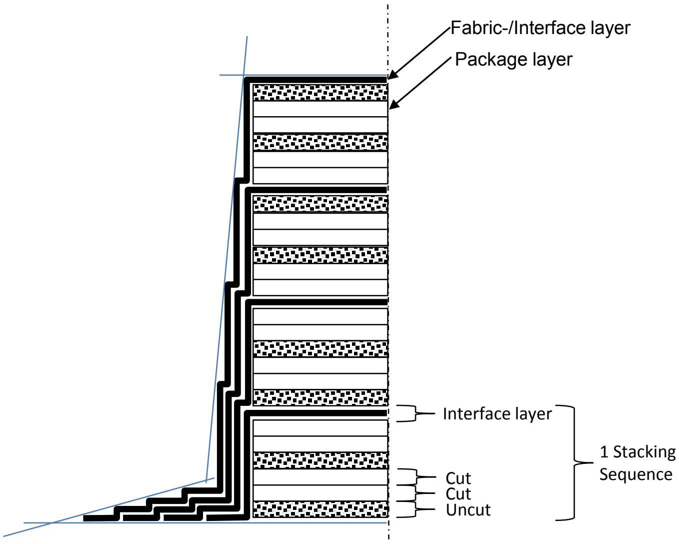

*Figure 16: Rib laminate in detail*

The interface layers do not only generate the connection of the ribs with the skin, but also help to fulfil the laminate rules in terms of adding layers with different orientation to the rib layers. Nevertheless, as laminate rules limit the maximum number of layers with the same orientation, additional layers are needed. This can be realised by the usage of so-called *package layers* for the rib structure laminate. It is intended that these package layers are prepared like typical slit-tapes but instead of containing only 0 degree layers, they also contain other orientations (see Figure 17). Another advantage of these package layers is the possibility to drastically increase the layup productivity, when multiple layers are placed in one step. The package layer thickness is investigated, in particular for the knot and rib specimens, under tension and compression in Chapter 4.

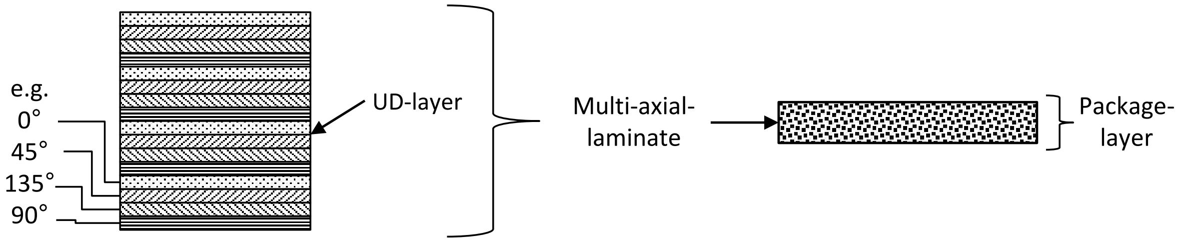

*Figure 17: Design of a so-called package layer built of multiple single plies*

The preparation of such package layers means an additional process step which the slit tape distributor needs to provide. At DLR laboratories, these layers are realised by the build-up of a laminate plate with a multi-oriented stacking and the subsequent cutting of strips as desired for the rib width. A similar process is imaginable on an industrial scale, as unidirectional slit tapes are also produced like this today. The limit of slenderness has to be seen in the range between 3 and 4 mm.

## 4.3 Manufacturing Process

### 4.3.1 AFP Process

An AFP process is intended to be used as explained in Subsection 4.1.1. The placement of the rib and the package layers respectively is seen to be state-of-the-art for current fibre placement machines. Typically, the machines place the tapes on flat or slightly curved (aircraft wing, fuselage) metal tools. The placement of the tapes into grooves has been carried out several times (compare Figure 18 left) but is not the typical application for aircraft manufacturers for the process. Depending on the height of the ribs, and in consequence the depth of the tool grooves, the required diameter of a placement roller needs to be quite large and the guidance of the slit tape becomes more critical.

Due to the angle of the helical ribs, the cutting edges of a tape also need to be adaptive to avoid material over-pressing or gaps. State-of-the-art cutting of slit tapes is carried out perpendicular to the slit tape direction. Nevertheless, it is seen to be relatively simple to implement an angle-adaptable knife in current placement heads. Different possibilities and dependencies regarding the cutting at the knot are explained in more detail in Section 4.4.

The placement of the interface layers is, in contrast, not state-of-the-art. The fabric interface layers need to be shaped continuously from plane into the profile cross-section, whereby the specific challenge is the desired slenderness of the profile. This means that a fully automated net-shape placement process is assumed to be used. A placement head with the ability to drape the interface layers directly into the grooves is under development (two patent applications in progress) [55] (see Figure 18, right).

In order to reduce the complexity of such a placement head, it is currently envisaged that the interface layers are provided as pre-conditioned roll material. This means that the single layers are already cut and rolled between two release foils. The two release foils are needed to keep the placement head parts clean from the resin. The head concept carries the material rolls, has a special draping unit, to avoid shearing the fibre material, an heating and compaction unit and two units to spool the release foils. This head is realised as a first prototype at the Technical University of Braunschweig in cooperation with DLR, and the placement process concept could be validated successfully.

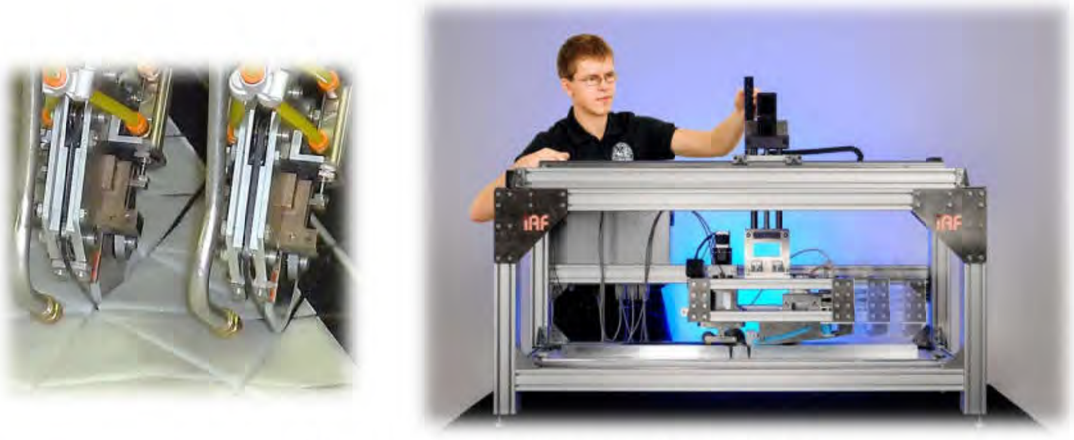

*Figure 18: left: placement head for grooves [37];*
*right: head developed for placement of interface layers [36]*

### 4.3.2 Tooling

As presented in Section 3.2, different manufacturing and tooling concepts has been developed for grid structures by different researchers so far. The tooling has to fulfil multiple requirements such as the geometrical accuracy of the desired structure, thermal and mechanical durability for high number of curing processes and simplicity for handling, process preparation and cleaning.

Therefore, it is seen to be most suitable to use a full metal tooling to ensure the high dimensional accuracy, reproducibility and tool life for reduced recurring costs. Drawback of a metal tool in comparison e.g. to a partly elastic tool is expected that the occurring undercuts of the positive curved grid structure leads to a multi core design. Due to the height and the radial orientation of the ribs, the tool cores need draft angles on all sides. As a consequence, a probably complex multi-core tool is needed including a handling mechanism.

As the manufacturing of high quality laminates depends strongly on the compaction and the avoidance of air pores, a tooling concept with expanding cores is proposed to use. In contrast to silicon rubber tools different thermal expansions coefficients of different metals are assumed to be exploited. Therefore the geometrical dimensions of the tooling is designed for the curing temperature and needs to be compensated (reduced) to the temperature, at which the material is placed into the mould.

The placement of the aerodynamic and load-bearing skin laminate can be carried out optionally wet on the wet grid structure in a co-curing process or in a co-bonded step e.g. wet on the cured grid structure.

## 4.4 Design Details

Following, specific concept details are discussed such as the draft angle, the cut complexity at the rib knot and the fulfilment of main laminate rules.

### 4.4.1 Draft Angle

As described in Section 4.2, the sequential usage of interface layers over the rib height is resulting in draft angles for the rib flanks and also the rib feet. The draft angle depends on the thickness of one interface layer as well as on the number of rib layers, compare Figure 19.

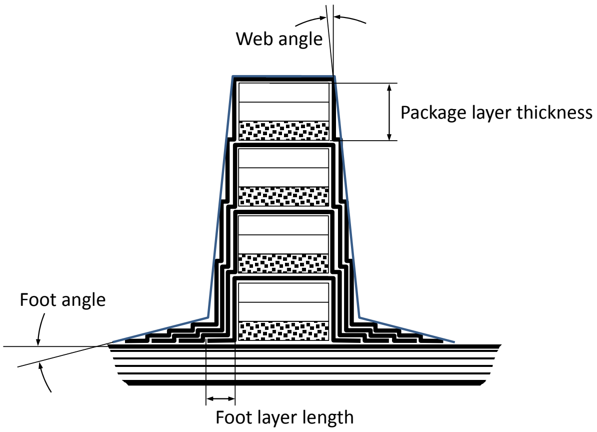

*Figure 19: Resulting draft angle in the rib due to interface layers*

The draft angle can be increased by the usage of thicker interface layers, reduction of the number of rib layers, or increase of the number of interface layers. In classical injection casting techniques, draft angles of approximately 1 to 2 degrees are recommended. With an interface layer thickness of 0.25 mm and 2° draft angle, for example, a distance of the interface layers stacked into the rib laminate of 7.1 mm results. This value seems to be quite applicable for the concept.

### 4.4.2 Cut Complexity (CC) of Package Layers

As the cutting of rib layers is intended for the Anisogrid concept, different complexities are imaginable, which are explained as follows:

The easiest and for example directly available complexity is the straight 90 degree cut – CC-1 (see Figure 20a). This is state-of-the-art at today's AFP-machines. For a grid with only two perpendicular oriented stiffener directions, like an Orthogrid, this is suitable.

The next higher complexity level is also a straight cut but with a desired angle – CC-2. This complexity is currently not state-of-the-art at AFP-machines but is seen as simple to implement in a placement head. With such a cutting, three rib directions can be placed without gaps only when one rib direction has a specific width in comparison to the other rib directions (see Figure 20b). Otherwise two small gaps occur for three rib directions (see Figure 20c). A beneficial aspect is that in both cases the cut angle remains constant along one rib direction. As a result, no waste needs to be removed and stored inside the placement head.

A further increase of complexity is reached with the usage of two straight cuts in desired angles – CC-3. This complexity for example is needed for three rib directions, to avoid any gaps (see Figure 20d). On a placement head this kind of complexity can be realised with two straight subsequent cuts. Crucial disadvantage is material waste occurring in the head.

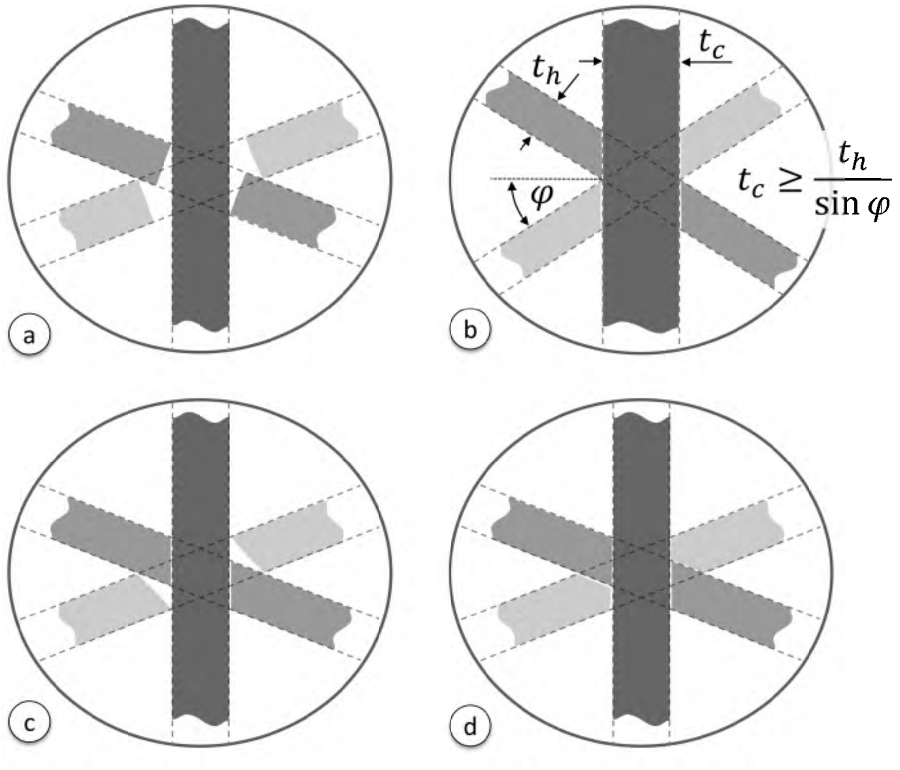

*Figure 20: Cut complexity of layers in the knot area*

Resultantly, the cutting complexity CC-2 seems to be the best compromise to reduce gaps on the one hand but to be implemented into a placement head without too much effort or with too many additional devices such as removing or storing of waste material.

### 4.4.3 Compliance with the laminate rules

In general, it is certainly questionable as to which laminate rules have to be fulfilled by this kind of structure. Most of these rules are developed or result from investigations of typical composite laminates. A typical laminate is a shell structure, whereby the in-plane dimensions are much larger than the thickness dimension. The grid structure does not even fulfil this aspect. The ribs are stacked by a high number of narrow plies generating a narrow but thick cross-section (high stiffener slenderness), generating required bending stiffness.

Meeting the laminate rules anyhow, different possibilities can be used and have been investigated. Following, main design guidelines are discussed for the concept [54]:

- The guideline of symmetric and balanced laminates can be fulfilled particularly due to the high number of layers in the rib structure; sufficient variants in terms of stacking order should be realisable.
- Minimum 10% of 0°, +45°, 90° and 135° shall be in the laminate: this rule can be fulfilled with the interface layers which are stacked into the rib laminate on the one hand. On the other hand the concept of using package layers which are pre-conditioned slit tapes, also allows implementing other fibre directions into the rib laminate. These layers are increasing the crack growth resistance inside the rib laminate. As mainly the uncut layers in the knot are seen to generate the strength properties, the layers with different orientations can be integrated best into the cut layers;
- Maximum 1 mm of layers on top of each other with the same fibre orientation: this requirement is indirectly limiting the thickness of the package layers, under consideration that all of the package layers shall have 0° orientation for maximum of strength in rib direction if they are uncut. As a result, the cut package layers should directly have a different oriented layer as a first and last ply.
- 45°/135° layer at the outside of the laminate: can be fulfilled with the interface layers, which will have as shear connection a high amount of 45°/135° layers anyway.

# 5 Determination of the Design Properties of Knots and Ribs

The advantages of cutting a part of rib layers at the stiffener intersection knots, like the constancy of the rib cross-section and fibre-volume-ratio, are faced with the drawback that the cut load-bearing fibres are interrupted. This may lead directly to the assumption:

*Thesis 2: The material properties of the knot specimen are significantly reduced by the cutting concept in terms of stiffness and strength.*

With the help of static tension and compression tests, the lack of material data shall be overcome for the proposed concept with cut layers in the knot area. The test goal is to analyse the expected property reduction of knots in comparison to the undisturbed, plain ribs. Therefore, the specimens are of element size to contain the knot area of the Anisogrid concept.

The rectangular ribs with their stacking in height are different to typical composite laminates. The layers are very narrow (thickness of the rib) but with a high laminate thickness (height of the rib). This kind of laminate is expected to be sensitive to edge effects, which reduces the material properties [49]. As a consequence, two additional specimen programmes are tested and compared to the rib and knot results.

## 5.1 Test Setup

The main question is whether uniaxial or multiaxial testing is most suitable in order to obtain the required properties. With uniaxial testing, the strength in only one rib direction is determined. A biaxial testing can e.g. be generated in such a way that two ribs are tested as an X-cross, whereby the loading is still uniaxial. In such a configuration, the in-plane strength properties of a lattice design could be tested and the properties in rib direction would be back-calculated. This procedure is seen to be adequate for wound structures because the knot as over-pressed area is of main interest. In the special case of the cut layers, the weakest point is not expected in the knot but in the cross-section directly before the intersection where the rib layers are cut. Resultantly, it is assumed that it is not a multiaxial loading in the knot but instead the pure uniaxial load in this weakest cross-section which causes the strength failure, and a uniaxial testing is seen to be preferable. Beneficially, this decision reduces the production effort of the knots and the evaluation of the test results as no back-calculation has to be carried out. Subsequently, the ribs and knots are tested uniaxially, pulling or compressing in one rib direction, whereas the other rib directions are not loaded.

As mentioned in the concept description, the thickness of the package layers is a design-driving aspect as the placement productivity can be increased significantly. Under consideration of the laminate rules, the testing programme is set to be investigated with the maximum package layer thickness of 1 mm. In Section 5.4, this aspect is focused on again with thinner package layers.

### 5.1.1 Standards and Geometry

For both tests, tension and compression, different types of specimen geometries are defined. The selection depends on the possibly required testing method, the specimen laminate (UD, multiaxial), and used fibres (glass, carbon, aramid). A specimen geometry is found to be applicable for tension and compression for testing multiaxial laminates, so that the specimen can be manufactured in the same tool (particularly relevant for the grid rib and knot specimens).

For tension, the standard DIN EN ISO 527-4 is considered, which is used for “Test conditions for isotropic and orthotropic fibre-reinforced plastics” [58]. The testing length of the tension specimen is 150 mm plus 50 mm load application elements on each side, resulting in 250 mm specimen length to manufacture. The thickness of the specimen is determined to 4 mm with respect to the standard. Only the width of the plate and grid specimen, which is the rib height, is reduced from required 25 mm to 18 mm because of tool limitations (see Figure 21, left).

For compression, the standard DIN EN ISO 14126 is considered. This standard is suitable for unidirectional as well as for multidirectional reinforced plastics, depending on the specimen geometry [59]. For a multidirectional laminate, as it is the case for the rib and knot specimens, the geometry type *B2* is recommended. The specimen thickness is similarly 4 mm and the overall specimen length need to be larger than 125 mm, which is why 250 mm is also used (see Figure 21, right). As mentioned for the tension specimen, the height of the compression grid and plate specimens is also reduced to 18 mm, due to tool limitations.

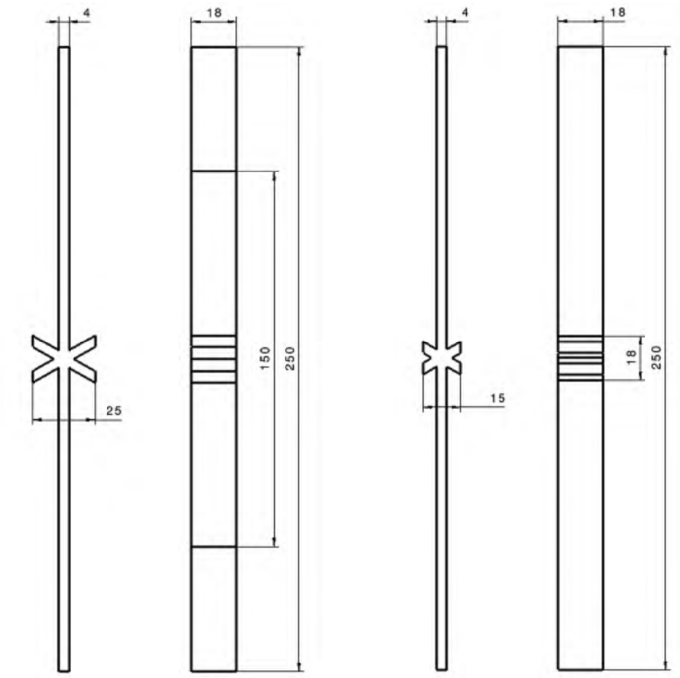

*Figure 21: Knot specimen dimension, left: tension, right: compression [56]*

### 5.1.2 Measurement Systems

For monitoring the compressive deformation and also a possibly bending of the specimen, two strain gauges are positioned on both of the wide rib sides. In case of bending, one of the strain gauges starts measuring drastically increasing tensile deformation.

Due to the large height of the rib it is possible to have additionally a look “into” the laminate and the strain distribution between the layers. For this purpose, an optical 3D digital image correlation (DIC) measurement system (see appendix D.1) is used to visualise and analyse the present stress concentrations between the cut and uncut layers in the knot area (see Figure 22). Therefore a contrast pattern is applied on the test area and photographed constantly during the test. The deformations are calculated by the change of the detected facets [78].

On the left side in Figure 22 the measurement installation is shown with the DIC camera focussing on the knot area of the specimen (Figure 22 centre picture). On the right side the DIC analysis picture is shown, whereas the fine contrast pattern can also be seen below the coloured analysis field.

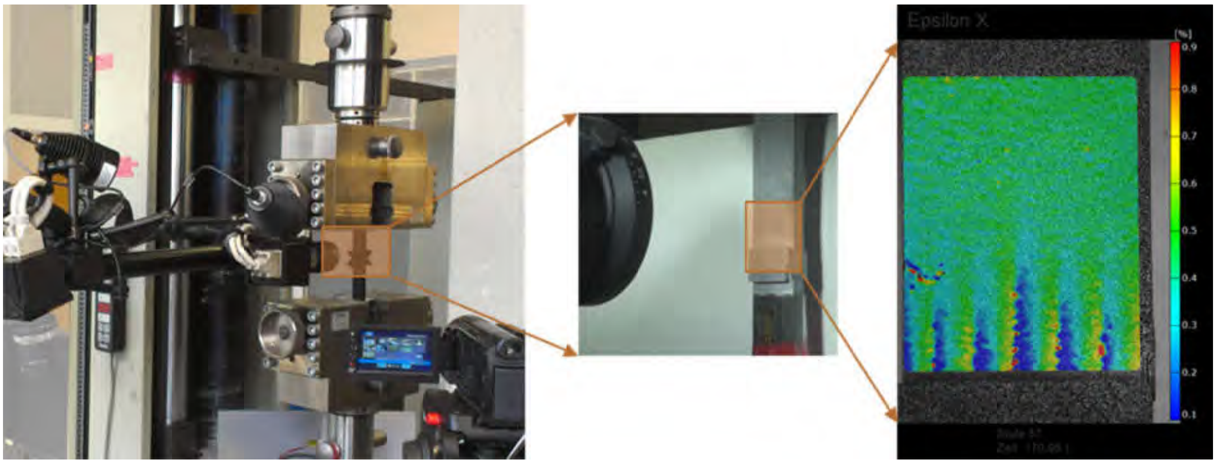

*Figure 22: Illustration of DIC measurement installation [56]*

### 5.1.3 Manufacturing and Material

For an efficient and batch-wise manufacturing, several knot and rib specimens shall be fabricated in one step. Due to the uniaxial testing, the specimens need to be straight/flat, which also reduces the tool complexity. The usage of expanding tool materials in the first attempts showed unsatisfying specimen results in terms of rib wall parallelism and constancy of cross-section dimensions. Hence, the tool was changed into a rigid aluminium tool, shown in Figure 23. The layers are placed into the grooves in a manual process. After placement of all layers into the tool grooves, additional tool pieces (distance blocks) are placed on top of the laminate plus a caul plate covering the entire tool. With the help of the caul plate and the distance pieces, the desired height is set up in the tool and the laminate is also compacted from the top.

Nine grid-knots and six grid-rib specimens are manufactured in one cycle in the tool (see Figure 23, left). The grid-knots are manufactured with three rib directions, realising the real staking of the concept in the knot area. After fabrication, the two unloaded directions are cut to a certain length to fit into the testing rig.

As discussed in the design concept in Subsection 4.4.2, the complexity of ply cutting in the knot area can vary depending on the realisable placement head. In order to investigate the influence of the ply cutting complexity in the knot area, two kinds of grid-knots are manufactured and tested. The layers with the lowest cut-complexity (CC-1) are cut in a 90-degree angle. This results in gaps in the knot area (compare with Figure 23, centre, above). Such gaps do not occur at the highest cut-complexity (CC-3), which is illustrated in Figure 23, centre, below.

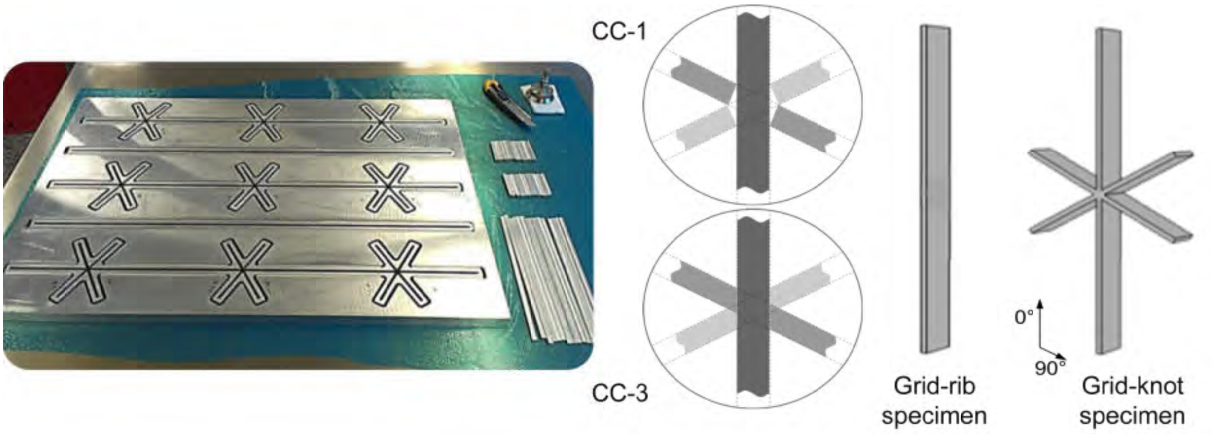

*Figure 23: Tool for manufacturing undisturbed "grid"-ribs and grid-knots [56]*

The grid specimen quality in terms of pores and fibre-volume content is appropriate, although the manufacturing is carried out manually and the tool design cannot produce proper compaction from all sides. As a consequence, slightly reduced stiffness and strength properties are expected due to the laminate quality and present edge effects.

In order to investigate the influence of the laminate quality on the strength and stiffness properties, the following reference test programme is added. First, a monolithic thick plate is manufactured in a standardised prepreg process. The better compaction of the prepreg ensures an increased laminate quality in terms of pores and constant fibre-volume content. The thick plate has the same thickness as the height of the manufactured grid-ribs and grid-knots. The stacking of the thick plate equals the stacking in the grid-rib specimen. In order to realise disturbed-plate specimens, which are similar to the grid-knots, the same number of layers are cut in the centre of the plate (see Figure 24 right). The cut layers are placed face-to-face (see Figure 24, right illustration). After curing, the undisturbed-plate (rib) and disturbed-plate (knot simulation) specimens are cut lengthwise from the plate with a width of 4 mm.

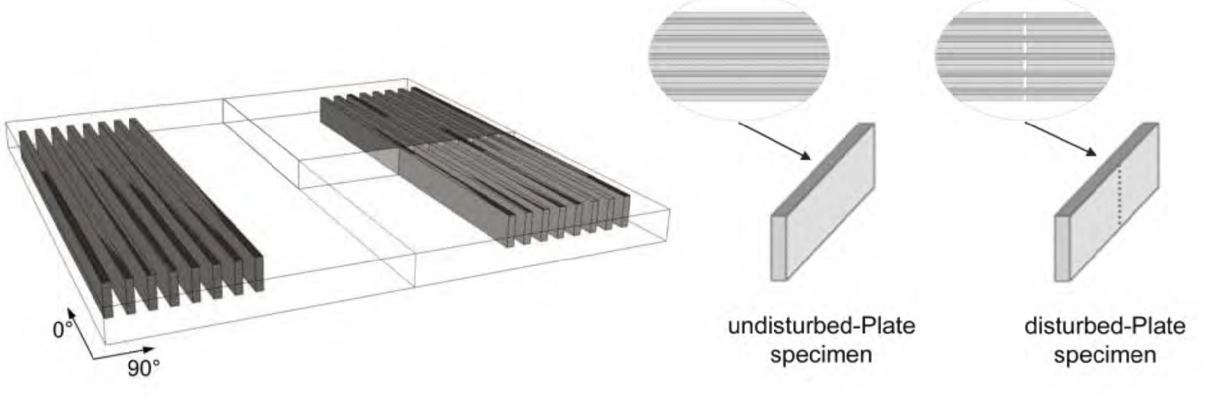

*Figure 24: Manufactured thick "plate" and illustrated undisturbed (left) [56]*

Within the second reference test programme, standard laminate specimens are chosen for manufacture (see Figure 25). This test programme is seen to be suitable in order to analyse the influence of the expected edge effects on the strength and stiffness properties. The laminate-rib specimens have the same ratio of fibre orientations as the grid-ribs and the undisturbed-plate specimens. The laminate-knot specimens have the same ratio of fibre orientations as the grid-knots at the weakest point. This point is the rib cross-section just before the knot, where the plies are cut. At this point, there are only the plies which run through the knot and the matrix of the cut plies. For the laminate-knot specimen, these cut plies are simulated with 90°-fibre orientation.

*Figure 25: Manufactured thin plate for "laminate" rib and knot specimen [56]*

As material, a standard epoxy resin prepreg is taken, reinforced by widely used HT-carbon fibres (Hexcel HexPly® 8552/AS4). In order to ensure comparability among the grid and reference test programmes and to reduce the manufacturing complexity of necessary laminate stackings, a basic laminate with 66% 0-degree fibre orientation and 33% 90-degree fibre orientation (66/0/33) is chosen for the undisturbed ribs. Consequently, the grid-ribs, the undisturbed-plate and the laminate-rib specimens have this stacking sequence.

In the strict sense, a laminate at the knot occur with 33% 0°, 33% +60° and 33% of -60° fibre orientations, resultant from the different rib directions. The grid-knot specimens contain this laminate in the knot area. However, as only 33% of the layers run uncut through the knot and the weakest point is seen directly before the knot, this cross-section is set into focus for the disturbed-plate and laminate-knot specimens. The disturbed-plate specimens have, in general, the 66% 0° and 33% 90° stacking whereby 33% of the 0° layers are cut in the centre of the plate to simulate this weakest cross-section of the grid-knots.

The laminate-knot specimens have, in general, a laminate stacking of 33% 0° and 66% of 90° fibre orientation in order to obtain a stiffness reference at the weakest cross-section position of cut plies. As a consequence, the laminate-knot specimens can be cut simply transverse from the laminate plate (see Figure 25). A summary of all laminate stackings is given in Table 1. An additional illustration of the grid-knot and disturbed-plate specimen stackings are attached in A.1.

*Table 1: Summary of laminate stackings in all specimens*

| | Grid | Grid CC-1 | Grid CC-3 | thick Plate | Laminate (thin plate) |
|---|---|---|---|---|---|
| Rib / undisturbed | 66% 0°,<br>33% 90° | - | - | 66% 0°,<br>33% 90° | 66% 0°,<br>33% 90° |
| Knot / disturbed specimens | - | 33% 0°,<br>66% ±60° resp. cut plies | 33% 0°,<br>66% ±60° resp. cut plies | 33% 0°,<br>66% 90° or cut 0° plies | 33% 0°,<br>66% 90° |

### 5.1.4 Analytical Load Calculation and Test Analysis

*Maximum Load calculation*

With the classical laminate theory (CLT), the stiffness matrix of the laminate can be calculated and a layerwise failure analysis performed. The global laminate properties are determined with the material properties of the single ply (data sheet information [27]) and the corresponding laminate stacking. Under a given external force, the global laminate strains are calculated and transformed into the strains of each single ply considering the ply angle and thickness. The resulting local strains respectively stresses in each ply are used to determine the fibre and matrix failure according to the Hashin 2D failure criteria [25]. There are a lot of failure criteria available for composites today. In general, it can be stated that most important for ply-based laminate analysis the usage of a physically-based or also called failure-type criterion is recommend, separating fibre and matrix failure (e.g. Hashin 2D, Puck, Cuntze Criterion) [71]. Out of these criteria, the Hashin 2D is selected since only unidirectional material properties are needed. Due to the pure uniaxial load in combination with only 0° and 90° layer orientations in the specimens, the results obtained with different criteria are almost identical. Differences occur mainly for layers with orientations between 0° and 90°, as the failure envelopes are differing for the resulting multiaxial stress states.

*Calculation of maximum strength from test results*

The maximum strength $\sigma_{Bten}$ or $\sigma_{Bcom}$ is calculated with the fracture test force divided by the cross-section area of the specimen:

$$\sigma_{Bten} = \frac{P_B}{A} \qquad (1)$$

*Calculation of modulus of elasticity from test results*

The modulus of elasticity $E$ is determined by calculating the slope of the stress-strain curve. This tangent modulus is the slope in one or between two points of the curve (a secant modulus is calculated between zero and one point of the curve). As a standard, the modulus of elasticity is calculated between 0.05% and 0.25% elongation of the specimen for tension and compression:

$$E = \frac{\sigma_{0.25\%} - \sigma_{0.05\%}}{\varepsilon_{0.25\%} - \varepsilon_{0.05\%}} \qquad (2)$$

*Determination of 1st standard deviation (SD)*

The standard deviation of test results shows the range, in which the results deviate from the average:

$$s = \sqrt{\frac{1}{n}\sum_{i=1}^{n}(x_i - \bar{x})^2} \qquad (3)$$

Even that the quantity of specimens for each kind of specimen and both loadings is quite low (between 4 and 6 values each) and statistics are not reasonably applicable, the standard deviation is used to give an impression of the scattering of the results.

## 5.2 Test Results

In the following, the tensile and compression tests are presented, containing the results of over 70 specimens of element size. The full list of geometry measurements of all specimens is attached for tension in appendix A.2.1 and for compression in A.3.1. The determination of the exact dimensions per specimen is essential for further stress and modulus calculation, due to the used cross-section area.

### 5.2.1 Tension

The diagrams in Figure 26 show the stress-strain curves for the grid rib and knot (CC-3) specimens. The test results for the plate and laminate specimens are attached in A.2.2.

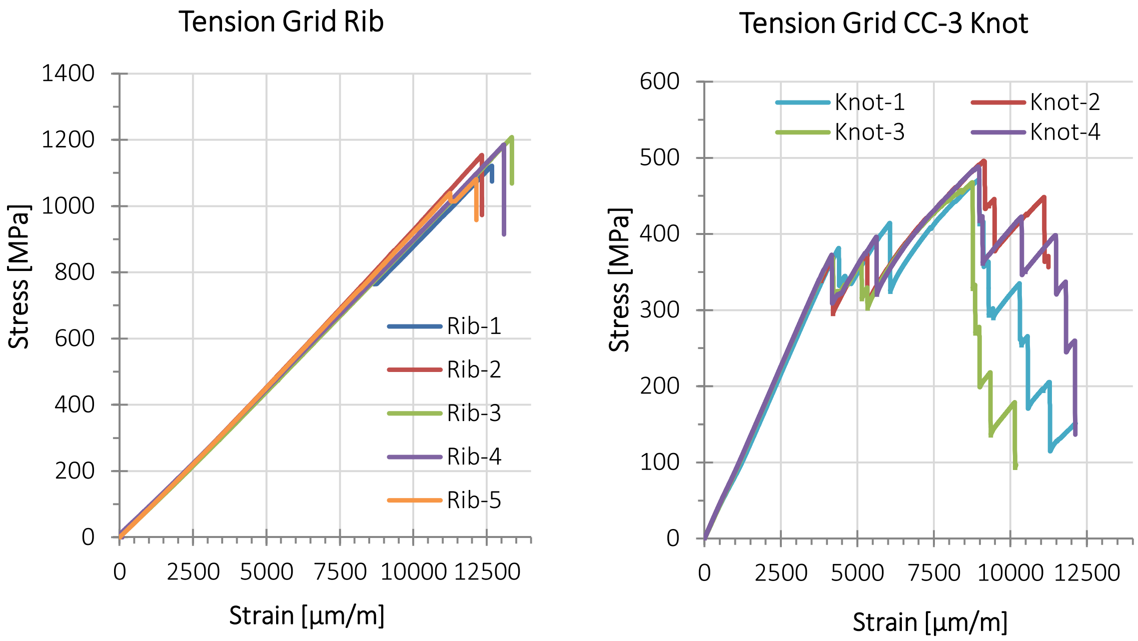

*Figure 26: left: Tensile stress-strain-curves of grid-rib specimens;*
*right: Tensile stress-strain-curves of grid-CC3-knot specimens*

The grid-rib specimens have a typical brittle failure mode and the stress-strain-curves show a linear behaviour. Only the curve progression of Rib-1 is interrupted by a slight strength drop which indicates a major interlaminar fracture. In contrast to the rib specimens, the grid-knots with the 1 mm-thick package layers have a distinctive successive failure behaviour. There are two major failure peaks observable before the maximum failure load occurs. Especially the first maximum failure stresses have, over all knot specimens, the same order of magnitude, which is unexpected. After analysis of the video data and comparison with the CC-1 and disturbed-plate specimens, it is assumed that these two peaks are the stresses occurring when the cut layers are separating from the layers of the other rib directions, first at one side of the knot and then at the other side. With the disturbed-plate specimen, it can be seen that all cut layers are separating at the same time and as a result, the second peak is not observable or it is lower than the first one (in A.2.3, two detailed stress-displacement curves are shown, including pictures of the specimen at different load levels).

The stiffness of all specimens is quite similar in the linear elastic range, compare e.g. until 2500 microstrains. The achieved average values for the modulus, failure stress and strains are listed for all specimens in Table 2.

*Table 2: Summary of test results for tension*

| | Modulus | | Stress | | Strain | |
|---|---|---|---|---|---|---|
| | [GPa] | 1st SD | [MPa] | 1st SD | [µm/m] | 1st SD |
| TEN-Lam-Rib | 89.6 | 1.61 | 1275.6 | 51.4 | 14048 | 751.5 |
| TEN-Plt-Rib | 87.4 | 1.99 | 1251.1 | 73.3 | 14318 | 692.2 |
| TEN-Grid-Rib | 84.7 | 2.42 | 1145.8 | 42.3 | 13536 | 691.1 |
| TEN-Lam-Knt | 50.3 | 0.48 | 700.3 | 23.1 | 13925 | 413.3 |
| TEN-Plt-Knt | 87.0 | 0.86 | 385.9 | 29.5 | 4435 | 324.6 |
| TEN-CC3-Knt | 83.2 | 0.80 | 481.0 | 11.6 | 5782 | 104.0 |
| TEN-CC1-Knt | 83.9 | 3.02 | 472.4 | 17.7 | 5642 | 315.7 |

The bar diagrams in Figure 27 compare the values for the tensile module. As a result, of the CLT analysis, a tensile modulus of 98 GPa is calculated for the rib stacking (66/0/33). The test results of all rib specimens are lower and within a range of 92% and 87% to the analytical reference. The grid-rib specimens have the lowest tensile modulus, as is expected.

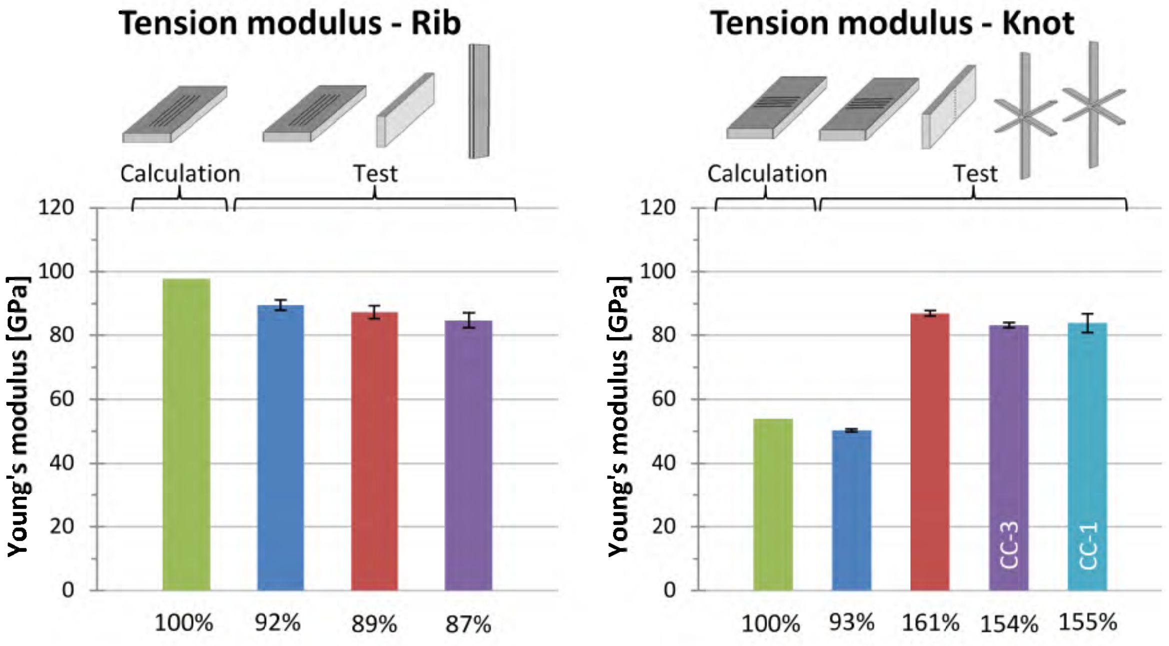

*Figure 27: Analysis (green) and test results for tensile modulus;*
*left: Laminate-rib (blue), undisturbed-plate (red), grid-rib specimen (violet);*
*right: laminate-knot (blue), disturbed-plate (red), grid-knot CC-3 (violet), grid-knot CC-1(turquoise)*

For the knot laminate stacking (33/0/66), a tensile modulus of 54 GPa is calculated (see Figure 27, right). The results for the knot specimens are, in contrast to the ribs, quite different. The laminate-knot specimens achieve an around 7% lower modulus than calculated, which is nearly the same reduction as achieved for the laminate-rib specimens in comparison to the analytics. On the one hand, it is questionable as to why such a reduction occurs for the laminate-rib and laminate-knot specimens; on the other hand, the fact that both laminates have the same reduction inspires confidence.

At first glance, the results for the disturbed-plate and the grid-knot specimens are surprisingly high, because they are 61%, 54% and 55% higher than the calculated value (see Figure 27, right). It can, however, be seen that the values of the knot specimens just about attain the modulus of the undisturbed-plate and grid-rib specimens, whereas the plate specimens again have a slightly higher modulus.

Overall, the stiffness results lead to the conclusion that the small knot area with cut layers and locally different fibre orientations is not significantly influencing the stiffness of the knot specimens in tension. Thus, for sizing, the stiffness of the grid-rib should be suitable for use in the entire rib structure, even though the local knot laminate stacking is different.

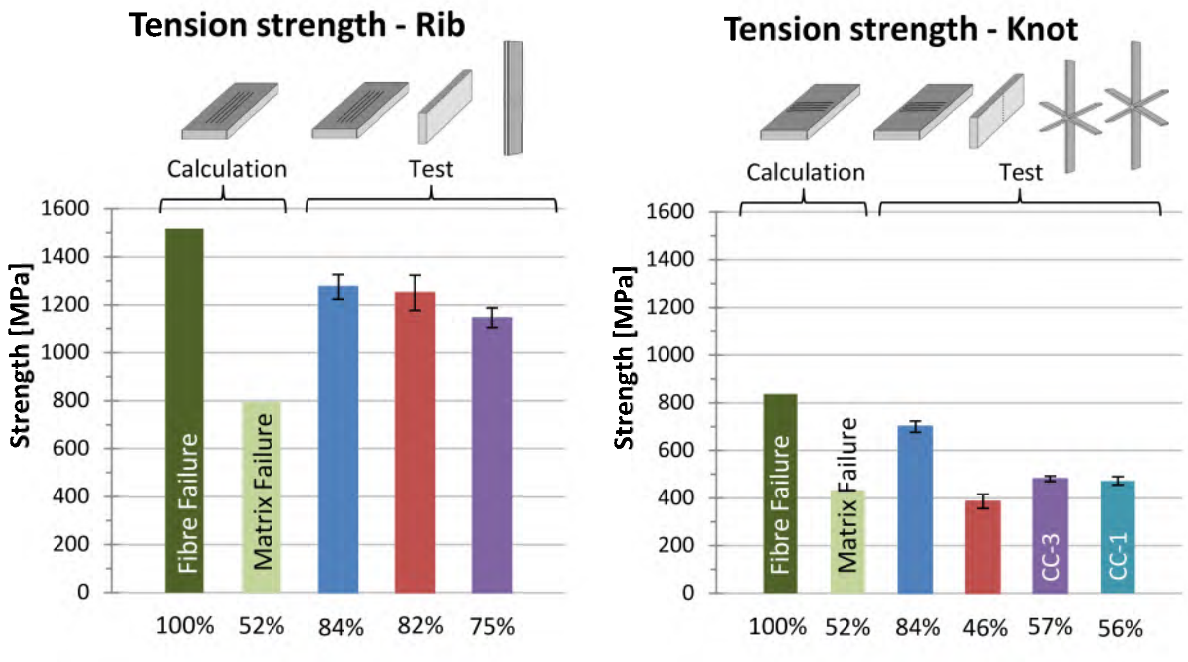

*Figure 28: Analysis (green) and test results for tension strength;*
*left: laminate-rib (blue), undisturbed-plate (red), grid-rib specimen (violet);*
*right: laminate-knot (blue), disturbed-plate (red), grid-knot CC-3 (violet), grid-knot CC-1(turquoise)*

The diagrams in Figure 28 compare the maximum-attained tensile strengths for all specimens. In the CLT analysis, the fibre failure is expected in the rib laminate at 1500 MPa. The test results for all rib specimens are remarkably lower: in a range of 84% and 75% of the analytical reference. The grid-rib specimens again have the lowest maximum tensile stress of approx. 1150 MPa.

The fibre failure of the knot specimen is determined according to the analytical solution at 830 MPa (see Figure 28, right diagram). The laminate-knot specimens reach the same reduction of the analytical maximum strength as the laminate-rib specimens with 84%. This is also a surprisingly high reduction. On the other hand, it is again interesting that both laminate test results are reduced by the same amount. Considering the 7% lower achieved stiffness with the same failure strain, 1350 MPa for the rib and 750 MPa for knot laminate would be calculated. However, instead of 15000, only 14000 microstrains are achieved. Background for the lowered failure strain can be the unconsidered clamping forces and locked transversal contraction in the load application areas. The reduced stiffness properties can most likely be found in a lower fibre-volume-ration in the specimen. FVR-measurement, however, showed 60.7% in the laminate as desired, which is why there is currently no adequate explanation.

A massive reduction of maximum tensile strength is seen for the disturbed-plate specimens and the grid-knot specimens. Especially the disturbed-plate specimens attain a low tensile strength of approx. 400 MPa. The grid-knot specimens achieved a slightly higher but still low tensile strength of approx. 480 MPa. The grid-knots with the higher cut complexity CC-3 attain negligibly higher strength and the scattering is also slightly lower/better. Nonetheless, for tension a higher cut complexity does not seem to justify the significantly higher manufacturing efforts.

Overall, a strong reduction of tensile strength is observed for the knot specimens. Consequently, this strong reduction of the material strength has to be considered in sizing processes. Comparing to the calculated rib strength, this reduction correlates to the number of uncut layers in the knot (CC-3 - 32%, CC-1 – 31%).

### 5.2.2 Compression

The stress-displacement curves for the grid-rib and grid-knot specimens are shown in Figure 29. The stress-strain curves for the plate and laminate specimens are given in the appendix A.3.2.

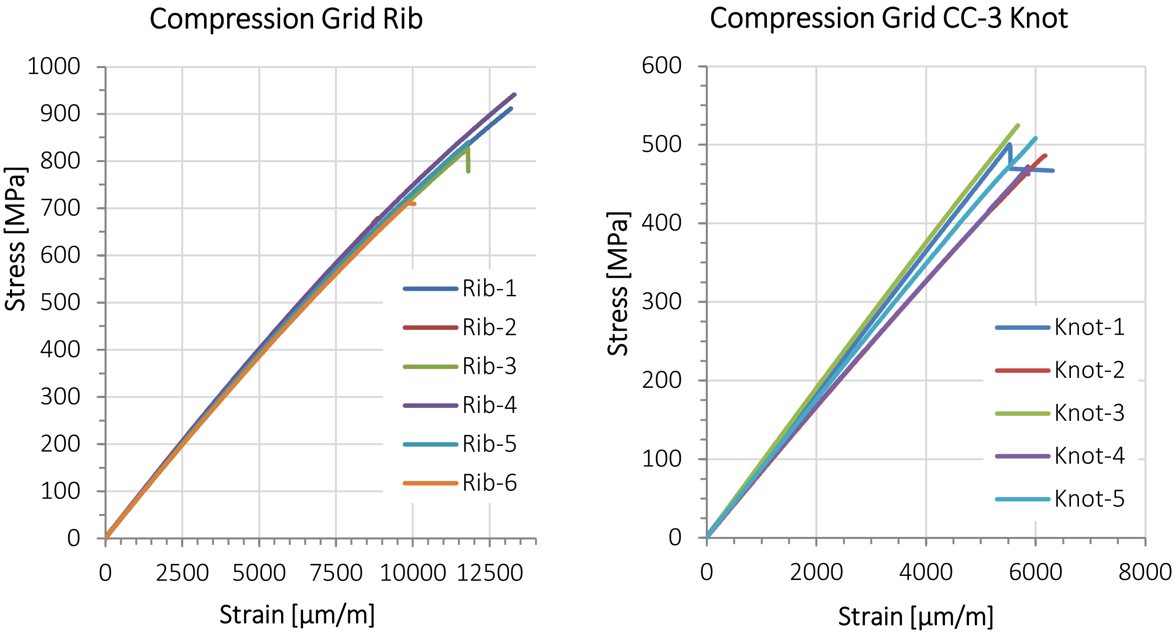

*Figure 29: left: Compression stress-strain-curves of grid-rib specimens; right: Compression stress-strain-curves of grid-CC3-knot specimens*

The grid-rib specimens as well as the grid-knot specimens have a brittle failure mode in compression (see Figure 29). A distinctive successive failure, which occurs for the knot specimens under tension, is not visible. All failure curves of the ribs show a quite similar stiffness in the elastic range, only the maximum compression stresses differ between the specimens. In contrast, the stress-strain curves of the grid-knot specimens vary quite strongly for elongations over 2000 microstrains. The average compression values of the moduli, failure stresses and strains are listed for all specimens in Table 3.

*Table 3: Summary of compression test results*

| | Modulus [GPa] | 1st SD | Stress [MPa] | 1st SD | Strain [µm/m] | 1st SD |
|---|---|---|---|---|---|---|
| COM-Lam-Rib | 82.4 | 1.37 | 998.1 | 55.6 | 13998 | 1176 |
| COM-Plt-Rib | 81.6 | 0.63 | 936.6 | 47.0 | 13798 | 1199 |
| COM-Grid-Rib | 79.6 | 1.47 | 832.7 | 78.2 | 11753 | 1805 |
| COM-Lam-Knt | 45.9 | 0.41 | 654.5 | 10.8 | 14244 | 211 |
| COM-Plt-Knt | 80.6 | 0.49 | 705.6 | 6.6 | 10484 | 757 |
| COM-CC3-Knt | 88.9 | 4.54 | 503.0 | 19.2 | 5933 | 199 |
| COM-CC1-Knt | 80.7 | 3.03 | 431.9 | 14.3 | 5984 | 1036 |

A compression modulus of 89 GPa is calculated for the rib stacking (66/0/33) and 50 GPa for the knot laminate stacking (33/0/66) (see Figure 30). Similar to tension, the test results for all rib specimens are slightly lower and within a range of 92% and 89% to the analytical reference (see Figure 30, left). The laminate-knot specimens also attain a lowered modulus of 93% like the laminate-rib specimens. The results for the disturbed-plate and the grid-knot CC-1 specimens have almost the same modulus like the undisturbed-plate and grid-rib specimens. Only the grid-knot CC-3 specimens obtain a higher compression modulus in comparison to all other specimens. After checking all test details, this high value is seen to be faulty (as the stiffness is a calculated value via the measured strain; wrong k-values of the strain gauges might be the reason).

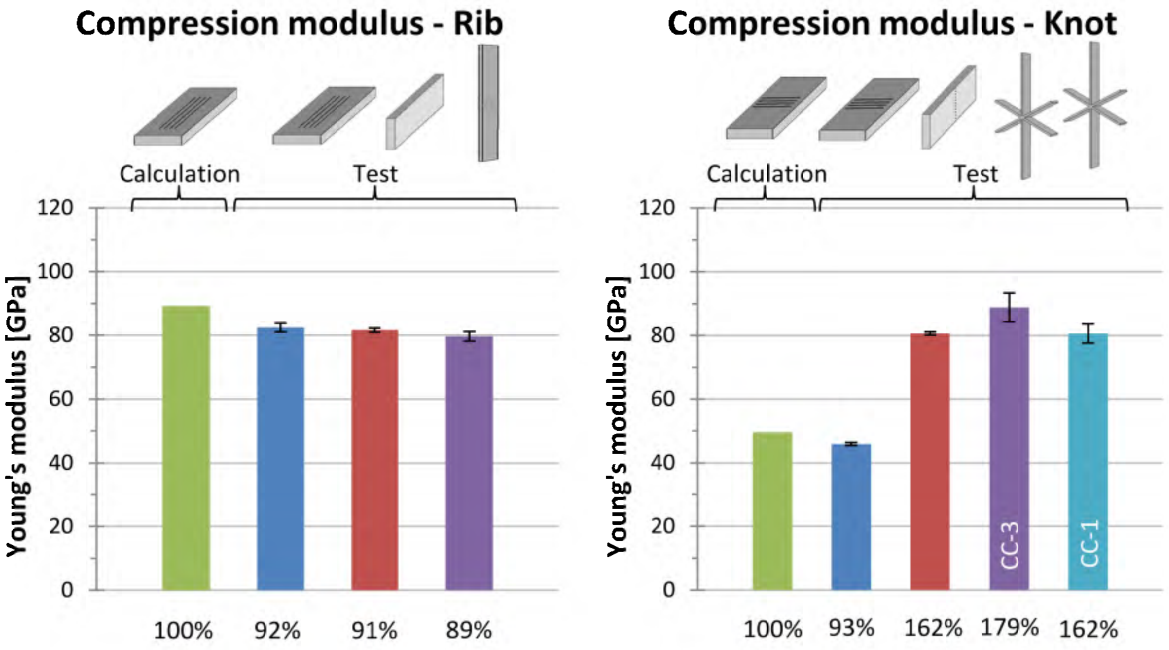

*Figure 30: Analysis (green) and test results for compression modulus;*
*left: laminate-rib (blue), undisturbed-plate (red), Grid-rib specimen (violet);*
*right: laminate-knot (blue), disturbed-plate (red), grid-knot CC-3 (violet), grid-knot CC-1(turquoise)*

Despite the CC-3 grid-knot result, it can be concluded that the small knot area with varying laminate stacking is not influencing the stiffness of the knot specimens in compression, similar to the observations at the tension tests. Resultantly, for sizing, the compression stiffness value of a grid-rib should also be suitable for use of the entire rib structure.

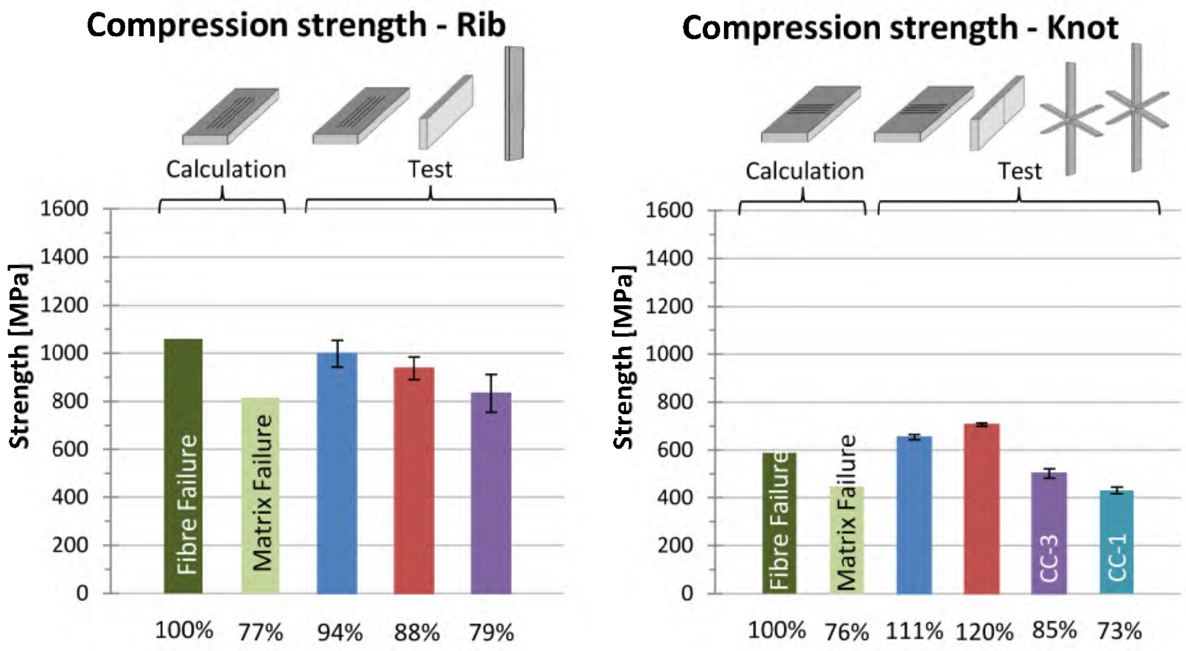

*Figure 31: Analysis (green) and test results for compression strength;*
*left: laminate-rib (blue), undisturbed-plate (red), grid-rib specimen (violet);*
*right: laminate-knot (blue), disturbed-plate (red), grid-knot CC-3 (violet), grid-knot CC-1(turquoise).*

The bar diagrams in Figure 31 show the results for the maximum compression stresses. The fibre failure is expected in the rib laminate at 1050 MPa according to the CLT solution. The test results for all rib specimens are lower and within a range of 94% and 79% of the analytical solution. This reduction is lower in comparison to the tension specimens. For the knot laminate stacking, the fibre failure is calculated at 590 MPa (33/0/66). In the tests, the laminate-knot specimens attain a slightly higher maximum strength. An even higher maximum strength is achieved for the disturbed-plate specimens. This might be questionable in the first moment. Considering, however, that the plate has a higher number of 0° layers in the cross-section before and after the knot area than the laminate-knot specimen, it can be assumed that even the cut layers transfer compressive load to some extent as long as the laminate is in thickness direction intact.

A high reduction of maximum compression strength is again observed for the grid-knot specimens. Compared to the calculated rib strength, a reduction to approx. 40% is attained for the CC-1 (47% for CC-3). In comparison to tension, where a reduction to 32% is determined, the decrease is lower for compression. The compressive load transfer between cut layers, observed significantly for the plate-specimen, also seems to work for the grid knots. The maximum strengths are lower, but a clear difference is observable between the CC-3 and CC-1 results. This strengthens the approach that cut layers without gaps should be preferred for compression and the additional effort seems to be reasonable.

Resultantly, a high reduction of maximum strength has also to be noted for compression, although the reduction is not as high as for tension. Nevertheless, it needs to be considered for sizing processes.

## 5.3 Visualisation of Stress Concentrations with Optical Measurements

In a special series, the tension and compression grid-knot tests are additionally monitored with the DIC system, described in Subsection 5.1.2. Due to the narrow width but great thickness it can be nicely looked from the rib side “into” the rib laminate at the intersection. Therefore, the unloaded rib directions are shortened strongly to reduce the shadowed area. The coloured areas in Figure 32 and Figure 33 are the zones directly above the knot area. The pictures show different load states and the strain $\varepsilon_x$ is visualised, which is the tension or compression direction respectively.

The DIC optical measurements of a tension specimen are shown in Figure 32. The picture numbers reflect the load step. After picture number 60, the global failure occurred. Picture number 1 shows the unloaded specimen. It can be seen that even at state 50 the load distribution is quite homogeneous. Strain concentrations fade away within 3 mm. (compare with Figure 32). These strain concentrations, however, rise rapidly when the first failure occurs.

The optical measurements of a compression specimen are shown in Figure 33. A similar deformation behaviour can be seen as for tension. First, the strain concentrations are limited to the area directly before the knot. With load increase, however, the strain concentrations propagate rapidly.

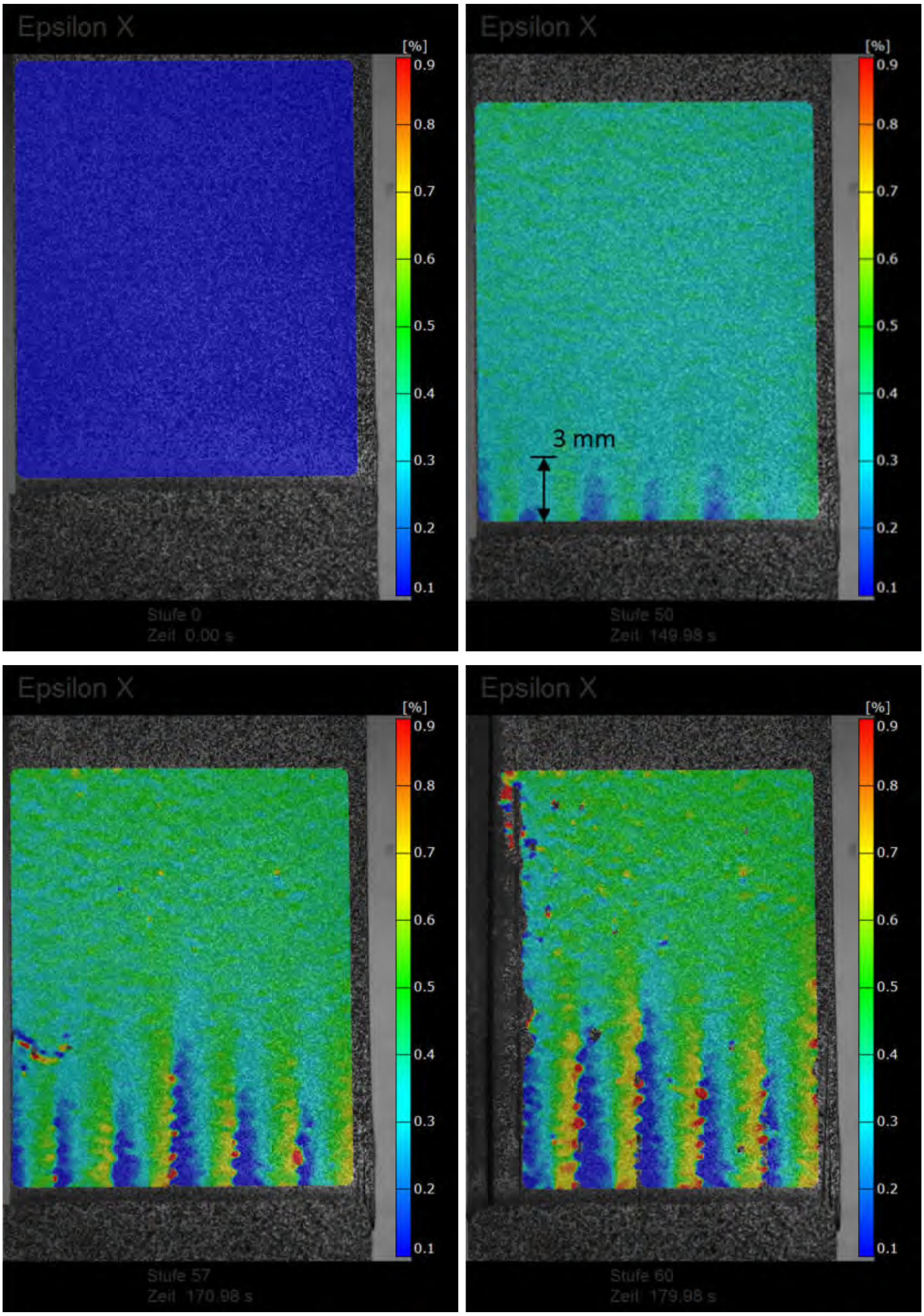

*Figure 32: Optical measurement pictures of grid-knot strains under tension load [56];*
*left, above: picture 1/60; right, above: picture50/60;*
*left, below: picture 57/60; right, below: picture 60/60*

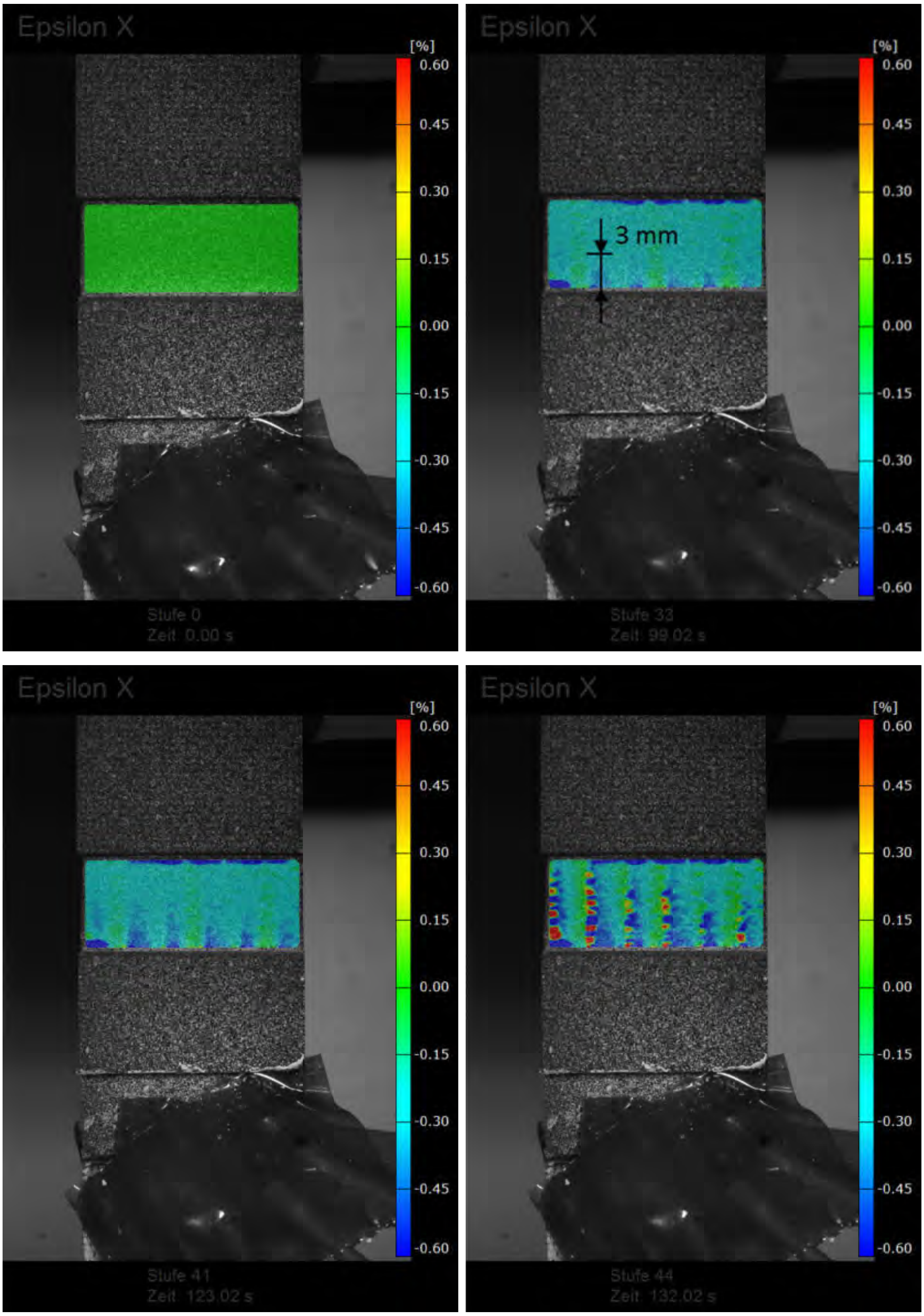

*Figure 33: Optical measurement pictures of grid knot under compression load [56];*
*left, above: picture 1/44; right, above: picture33/44*
*left, below: picture 41/44; right, below: picture 44/44*

## 5.4 Tension Tests of Specimens with Thin Package Layers

Motivated by the investigation of maximum productivity for the placement process, the determination of rib and knot properties is carried out with 1 mm-thick package layers. As these layers have only 0° orientation according to the limit of plies with the same orientation, such a package layer can be seen as one 1 mm-thick single ply. As a result, a 1 mm uncut ply is alternating constantly with two 1 mm cut plies through the whole laminate. Such stacking is quite "rough" and laminates made from relatively thick single plies are seen to have less strength as laminates made from thin single plies [72]. As a consequence, it should be beneficial for the strength to decrease the resulting thickness of cut and uncut plies, although the fibre placement speed is thereby decreased accordingly. A brief investigation on this aspect is carried out in this chapter.

In addition to the above-mentioned general maximum strength improvement of thin ply laminates, it is observed for the tensile tests that the grid-knot specimens as well as the disturbed-plate specimens do not fail due to fibre fracture. Instead, the package layers are pulled out of the cross-section. This means that a shear or delamination failure occurred for the investigated thick package layers.

With the help of fracture mechanical energy-based analysis, this observation can be confirmed. For the analysis, an existing crack is considered in the specimen and the tensile load can be calculated at which the delamination is growing through the entire specimen lengthwise along the interface between the cut and uncut layers. The delamination failure as *in-plane shear failure* is categorised as *Mode II* (an overview and more detailed information in terms of the different Modes and analysis are attached in A.4).

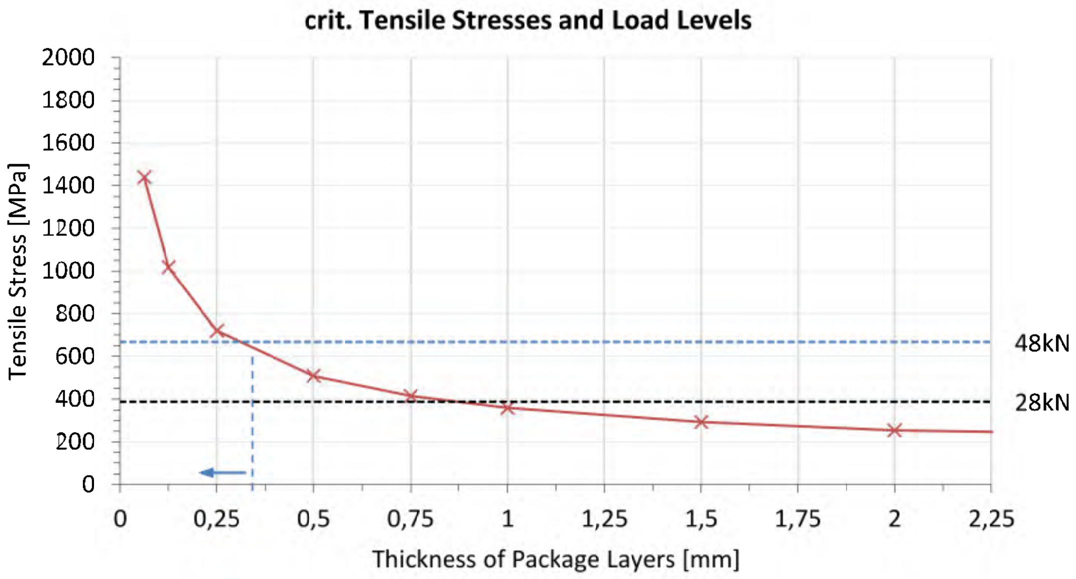

*Figure 34: Critical tensile stress for plate-knot specimen dimension*

The diagram in Figure 34 shows the critical tensile stress, causing delamination growth, versus the package layer thickness for the dimensions of the tested plate-knot specimens. The background is that with increasing package layer thickness, it is carrying a higher amount of the overall tensile load of the specimen. Resultantly, the limit, when the critical stress for crack growth is reached, is decreasing (red curve in the diagram). The obtained average maximum test force of the plate-knot specimens of 28 kN is plotted in addition. It can be seen that the test force cross the critical stress curve at approximately 0.9 mm, which matches quite well with the 1.0 mm-thick layers used in the tests. In contrast, the fibre tensile strength of the uncut layers would be reached for the investigated cross-section dimensions at 48 kN tensile force. With the help of the diagram, a maximum thickness of package layers of approx. 0.3 mm can be determined.

In order to validate this result, a small testing programme of disturbed-plate specimens is produced, as the plate specimen are also the cheapest to manufacture and prepare. A package layer thickness of 0.25 mm is chosen as the next smaller thickness step, thereby also providing some reserve.

For this small test series, 6 disturbed-plate specimens are produced as described in Subsection 5.1.3 with the same laminate stacking (66/0/33), whereby 33% of 0° layers are uncut and the rest are placed face-to-face in the centre of the plate (see Figure 24).

In Figure 35, the stress-strain-curves for these specimens are plotted, including an example curve of the grid-knot and plate-knot specimens with 1 mm-thick package layers.

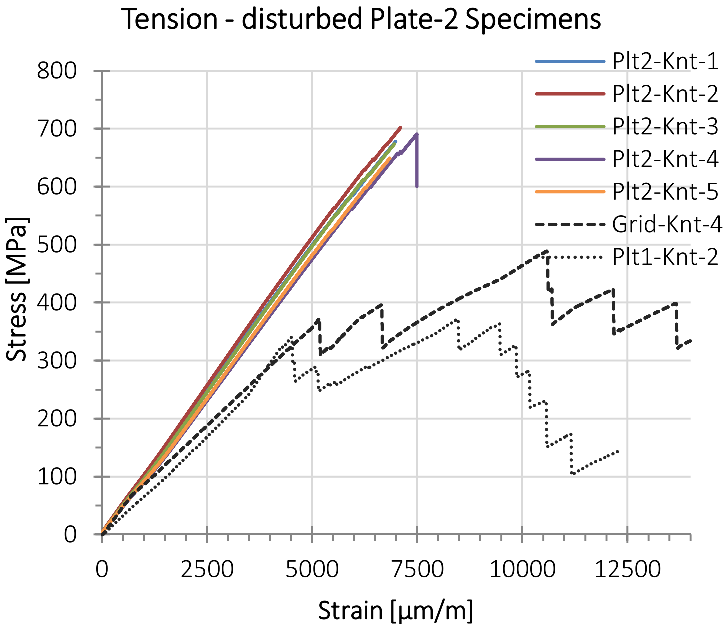

*Figure 35: Tension results for disturbed plate knot specimen with 0.25mm package layers*

It can be seen that the specimen with thin package layers also show a brittle failure behaviour like that of the ribs or the compression tests. The average maximum tensile strength of 380 MPa of the plate1-knot specimens increases to an average of 670 MPa.

Comparing these results as strain values over the whole test programme, it can be stated that the maximum tensile strain of the uncut 0°-layers of approx. 14000 microstrains is reached for all specimen except for the grid-knot specimen and the plate-knot specimens with thick package layers (see Figure 36). The aspect that the fibre failure strain is reachable with an adapted package layer thickness leads to the assumption that the maximum tensile stress corresponds with the number of uncut layers or, as the width of the ribs is so narrow, directly to the number of uncut 0°-layers.

Reflecting on the results of the thin package layers, it might be questionable as to whether the grid-knot and plate-knot results with thick package layers are meaningful. In terms of maximum stress allowable, the results of the grid-knot and plate-knot are obviously not giving the right answer, but the results show that the package layer thickness has to be proven through e.g. fracture mechanic analysis. This criterion was not seen as so critical before the tests. On a panel or barrel structure, the observed shear failure in the test specimen is expected to result in delamination failures within the load-bearing rib cross-section.

Besides the reduction of package layer thickness, other actions can also be taken into account, such as the usage of prepreg material with higher $G_{IIc}$ property, a decrease of the stiffness of the original rib cross-section, or inversely an increase of the stiffness of the uncut package layers.

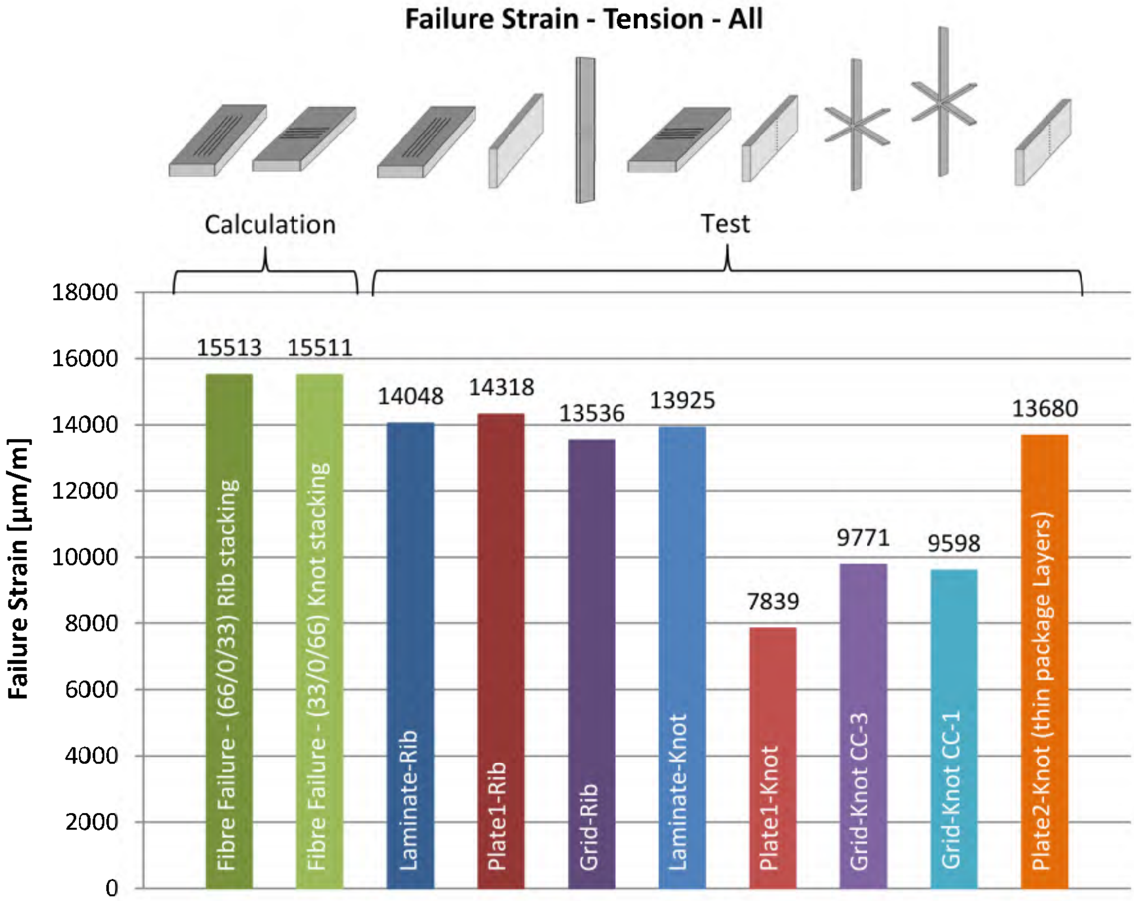

*Figure 36: Maximum tensile strains in uncut 0°-layers of all specimens*

## 5.5 Discussion and Summary of the Test Results

The static tests show, in general, similar results for tension and compression. The determined stiffness parameters for the grid-knot specimen attain a similar value to the grid-rib specimen. For sizing, a reduction of stiffness does not have to be considered. This result was initially not assumed but seems to be plausible due to the fact that the knot area is quite small compared to the overall specimen size. As long as there are no failures, such as matrix cracks at the cut layers in the knot specimen, the load distribution is relatively homogenous in the cross-section. In contrast, as soon as the matrix interface starts cracking at the cut layers, strong load redistribution and concentrations arise at the uncut layers. Then only the uncut layers are carrying the load but with a much smaller cross-section; consequently, the stresses in these layers rise drastically. As a result, the knots (1 mm package layers) fail at a similar magnitude to the matrix failure calculated for a typical laminate.

Considering the package layer thickness, it can be concluded that it is possible to calculate with the maximum fibre strength of the uncut 0°-layers in the knot. Besides the maximum fibre failure (FF), which reflects the maximum strength, the inter-fibre failure (IFF) criterion also needs to be investigated under consideration of the angle of the cut layers. As conservative approach, a 90° angle is seen as the most suitable to be used.

The expected reduction of properties between all three kinds of specimens (laminate, plate and grid) can be noticed quite clearly. Especially all rib specimens show a step-by-step reduction for the modules and the strengths. The initial assumptions seem to be valid that edge effects reduce the properties for the first time (laminate to plate specimens), and the lower quality of the grid specimens does this in addition (plate to grid specimens).

The investigation of different cut-complexities shows that under compression, the maximum strength correlates with higher complexity of the layer cutting. For the tensile strength and also for the stiffness (compressive and tensile), no significant difference is observed. However, it needs to be considered that the tests present only static results, and this effect is seen to be even more relevant for dynamic loadings because gaps and resulting pores are typically starting points for cracks. Resultantly, the proposed cut-complexity CC-2 is assumed to be a good compromise as regards avoiding gaps and limiting the placement head expenditure.

# 6 Investigation of Anisogrid Architecture on Panel Level

The positive results regarding weight efficiency found in literature in Section 3.1 for grid structures in aerospace together with the high buckling values of triangular skin-bays, motivated the following hypothesis:

*Thesis 3: The triangular stiffened Anisogrid concept has an inherent weight benefit in comparison to the Orthogrid concept.*

In order to analyse this hypothesis for airframes, the semi-monocoque structure, as the state-of-the-art stiffening structure for aircraft, seems to be the right approach at first glance. However, the comparison of the integral Anisogrid stiffening architecture with the frame-stringer-skin design would be quite difficult, because numerous constraints other than the pure panel-sizing ones focused on here lead to the final design of an aircraft. All these constraints, such as cabin integration, crash or secondary system demands, lead to a multi-parameter optimisation problem, whereby most of the constraints are difficult to get. In addition, the focus of this work is to answer the question as to whether there is a weight potential only due to the skewing of the stiffeners. Consequently, it is preferable to avoid all other influencing factors, which means keeping the material, the design and manufacturing concept the same for this investigation. In this case, an Orthogrid structure seems to be the best variant for comparison with the Anisogrid design, as only the rectangular grid of stiffeners differs from the Anisogrid design.

For the comparison of the weight of an Anisogrid versus an Orthogrid structure, both are sized under consideration of the same strength and stability sizing criteria in all elements. This investigation is assumed to be suitable for carrying out on a panel level with constant line loads as uniaxial compression or shear or as combined load case of compression with shear. The panel level has the advantage that it is big enough for all sizing criteria to be crucial for sizing but it can still be calculated with constant line loads for an investigation of specific effects. Moreover, a fuselage barrel is a set of different panels and a load case such as bending can be approximated in panel sections with constant line loads at the different positions of the barrel (top, bottom or side panels).

The analysis of the most weight efficient structure is carried out in two stages. In Section 6.2 and 6.3, the two architectures are analysed separately to show important dependencies between the minimum weight and single variables. In Section 6.4, the comparison of the Anisogrid and Orthogrid is shown for the different load cases and load levels.

## 6.1 Analysis Methodology

For the examination of the two architectures on panel level, the load cases, panel geometry, design variables, material, sizing criteria and the evaluation/comparison criterion are explained in this chapter.

### 6.1.1 Load Cases

The panel loads in an aircraft fuselage vary strongly according to the position and the airplane manoeuvre. In general, the loads can be divided into symmetric and asymmetric load cases. Symmetric loads stress the fuselage symmetrically to its vertical centre plane (X-Z-plane).

Such loads are e.g. ground load cases such as towing or braking and flight load cases such as vertical gusts. Asymmetric load cases occur at ground or in flight through cross winds or also due to asymmetric fuselage masses such as cargo doors (which are only integrated on one side of the fuselage).

The high amount of different load cases is simplified for the architecture comparison by line loads, such as compression or shear, or the combination of both. The structures are sized for a compressive load range between 50 N/mm and 1000 N/mm. Such load variation represents a wide range for load states along different fuselage positions. 50 N/mm – 100 N/mm are light loaded panels in the front of the fuselage behind the cockpit section. High loads of over 500 N/mm are found in the centre of the fuselage in the section before and after the centre wing box, as the wing works as main support of the fuselage beam during flight. At aircraft with lengthened fuselages, such as the A321, or other aircraft configurations (e.g. rear mounted wing configurations) the panel loads can further increase to the higher bending moments which why the load range is extended to 1000 N/mm. Shear loads are typically lower and reaches their maximum in the rear fuselage section directly behind the wing. To obtain a better overview of the relation, the same load range between 50 N/mm and 1000 N/mm is examined.

### 6.1.2 Design Variables

For the comparison flat and curved panels are analysed. The stiffener design is the same for the Anisogrid as well as for the Orthogrid panel and monolithic skin laminates and monolithic stiffeners are considered.

#### *Anisogrid Design*

The Anisogrid panel consists of vertical and diagonal stiffeners and a skin. With respect to the focused curved structures, the vertical stiffeners are called circumferential ribs and the diagonal stiffeners helical ribs. Figure 37 shows an Anisogrid panel with all design variables, which are: the global panel dimensions, the height, width and distance of the circumferential and helical ribs, the thickness of the skin, and, if applicable, the radius (R=2000mm).

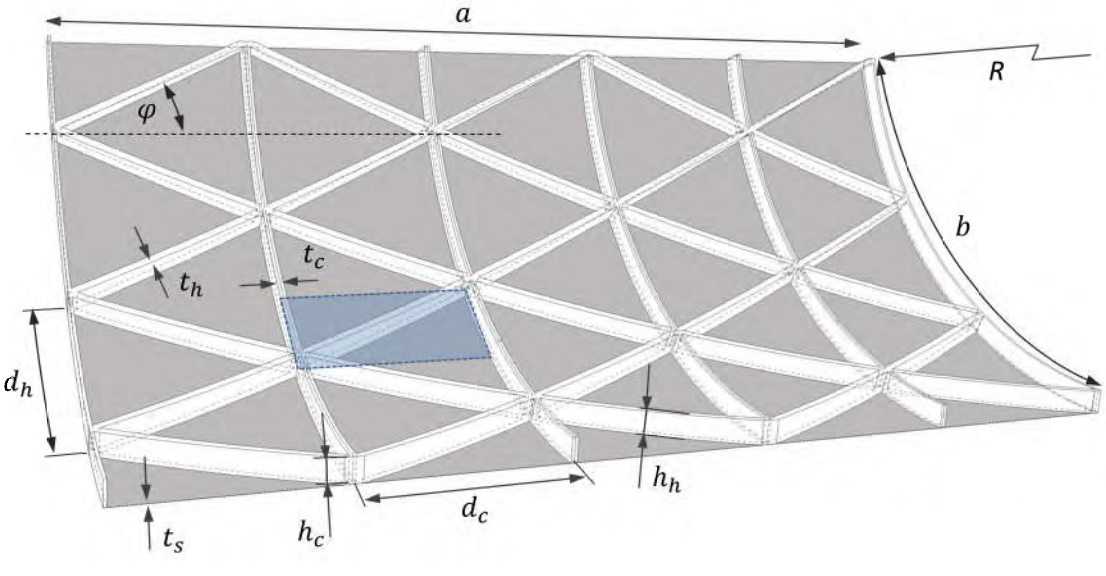

*Figure 37: Anisogrid panel with blue marked unit cell*

The distance of the helical and circumferential ribs are directly related to the angle of the helical ribs, because of the constant and regular pattern of the stiffened structure. Despite the fact that all the rib directions intersect at one point, a stiffened structure with triangular skin-bays derives. Figure 38 shows the Anisogrid unit cell out of which an Anisogrid panels is built of (considering also mirroring). Both helical rib directions have the same angle, so that an equal-sided triangular skin-bay results.

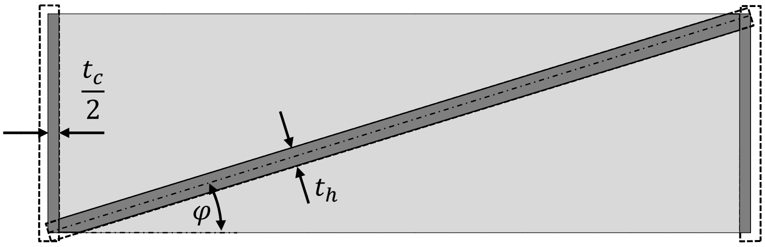

Figure 38: Anisogrid unit cell

In order to achieve full variability of the unit cell in terms of geometrical dimensions, only one of the two variables needs to be adaptable (circumferential or helical/axial stiffener distance). Due to the great influence of the circumferential stiffener distance to other airframe structures, it is seen most suitable to fix the circumferential distance.

### *Orthogrid Design*

The Orthogrid panels consist of vertical and horizontal stiffeners and a load bearing skin. The vertical stiffeners are also called circumferential ribs and the horizontal stiffeners axial ribs. Figure 39 shows an Orthogrid stiffened panel. The geometrical parameters are, in principle, the same like for the Anisogrid design only that the angle is now the diagonal angle of the skin-bay. Figure 40 shows the unit cell of the Orthogrid design.

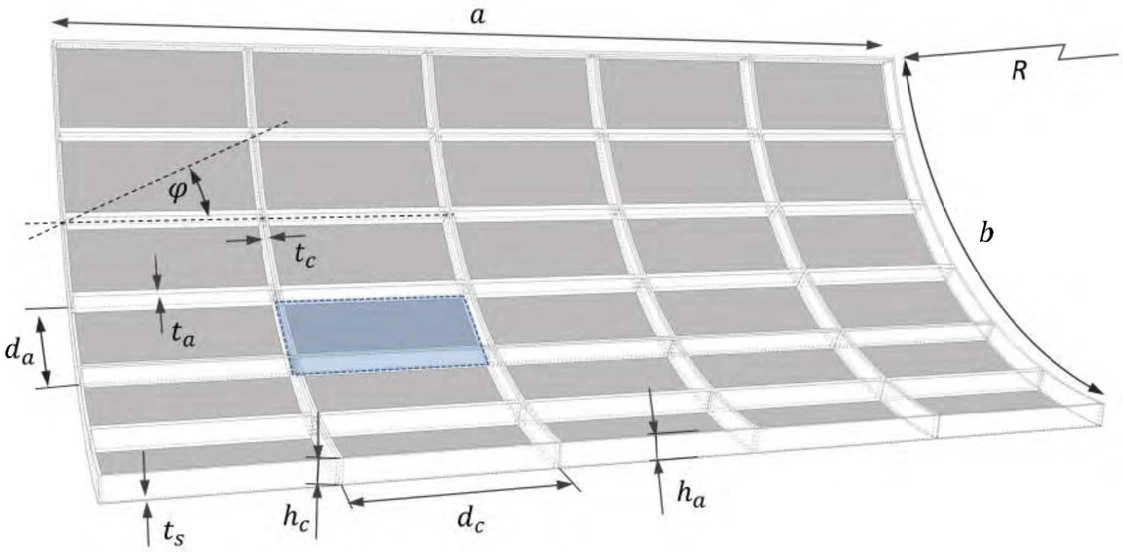

Figure 39: Orthogrid panel with blue marked unit cell

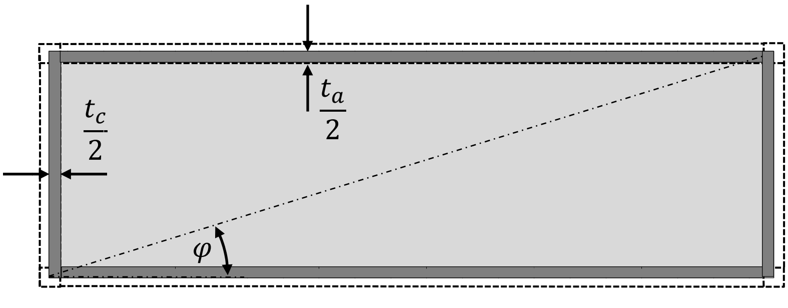

Figure 40: Orthogrid unit cell

### 6.1.3 Material

In this investigation, orthotropic composite properties are used for the grid structure and, in principle, also for the skin, whereby only quasi-isotropic laminates are considered for the skin. To simplify the analytical dimensioning process, smeared stiffness values are the basis for sizing. Resultantly, only the thickness (of the ribs and skin) needs to be sized, instead of working with discrete laminate stackings, in which the quantity and the order must be taken into account. Due to the fundamental comparison of the architectures, this procedure is assumed to be valid at this design stage.

#### *Grid Structure*

In this investigation, an HT-fibre (*High Tenacity*) with Epoxy matrix is considered as basic material. This type is the most used high performance carbon fibre material due to its combination of stiffness and strength properties and fabrication costs. The Hexcel 8552/AS4 [27] material is such a kind of CFRP-prepreg, which has also been used for testing the grid properties in Chapter 5.

With the results found in the knot and rib tests, the stiffness of the plain rib and the strength of the knots are determined for the maximum axially reinforced laminate:

*Table 4: Material data for ribs made from prepreg with HT-fibre*

| | Modulus $E_x$ [GPa] | Modulus $E_y$ [GPa] | Modulus $E_{xy}$ [GPa] | Density $\rho$ [g/cm³] |
|---|---|---|---|---|
| 70/10/10/10 – calc. CLT Average (25°C) | 100 | 10 | 5.3 | 1.55 |

The transverse laminate stiffness is neglected and set to the unidirectional value.

#### *Skin*

For the skin laminate, the same prepreg system is chosen as for the grid structure. The skin laminate is focused on quasi-isotropic layups to reduce the number of variables, on the one hand, but also because laminates with or with almost quasi-isotropic properties are typical for fuselage skins. Reasons are that there are numerous demands to the skin such as multi-axial loads, damage tolerance and fatigue demands, or bolted reparability.

*Table 5: Material data for the skin made from prepreg with HT-fibre*

| | Modulus $E_x$ [GPa] | Modulus $E_y$ [GPa] | Modulus $E_{xy}$ [GPa] | Density $\rho$ [g/cm³] |
|---|---|---|---|---|
| 25/25/25/25 – calc. CLT Average (25°C) | 52.5 | 52.5 | 20.0 | 1.55 |

### 6.1.4 Constraints - Sizing Criteria

An analytical sizing tool is used for the panel dimensioning where the following criteria are implemented. In Subsection 6.1.6, the sizing tool/the algorithm is described in detail.

#### *Global Stability*

The failure due to loss of global stability is characterised by simultaneously buckling of the skin and stiffener. With the usage of a continuum model for the skin and the smeared stiffeners, the calculation of global stability is carried out for an unstiffened plate and with a Rayleigh-Ritz energy-based method. The usage of the continuum model is valid as long as the calculated buckling half-length is significant higher than the distance of the stiffeners. As rule of thumb the buckling half-length shall be longer than at least two or three times of the stiffener distance in each direction. Resultantly, a functional constraint is determined that the helical as well as axial stiffener distance is not allowed to exceed 250 mm. In particular for the shear load cases, it has to be expected that this constraint is reached during sizing. However, on the other hand, the results will not be valid inside the smearing approach.

It shall be noted at this point that this model is not capable to generate results with very stiff single ribs dividing the panel in several single panels, such as e.g. frames are used for. Even when stiffeners are obtained by the sizing algorithm with high stiffness, the global panel stability is calculated for the whole panel, neither considering these local stiffening's nor automatically separating the panel into smaller ones.

In terms of panel size, it needs to be large enough so that the smearing approach is valid. This is the case when the panel is buckling in global mode over several stiffeners. On the other hand, the analytical computation time is increasing (due to the Ritz method for the buckling criteria) and the panel size should not be too large (it seems to be negligible but due to the large design space also the analytical computation time sums up to remarkable magnitude). Accordingly, a panel size of 2000 x 2000 mm is chosen for this study.

#### *Local Stability of the Ribs*

Local buckling of stiffeners is understood as deformation or buckling of the rib web/blade sideways, whereby the connection of the stiffener to the skin is still intact and in line. The stiffener web is considered as orthotropic plate stripe which is simply supported at three edges and one long free edge. For the determination of the buckling factor, an orthotropic simply-supported plate at all edges is calculated and multiplied by a ratio factor. In B.1.2 the basic analytical formulation is attached.

#### *Local Stability of the Skin*

As local stability failure of the skin, buckling inside one skin-bay is defined. The stiffeners generate the boundary conditions for the skin-bay. As basic approach, all edges of the skin-bay are considered as simply-supported. Therefore, the stiffeners need to have sufficient bending stiffness. The additional support due to the torsional stiffness is in this case not taken into account. For the Orthogrid structure, the rectangular skin-bay is considered as orthotropic plate. In the case of biaxial compression loading, an exact closed-form analytical solution is available. For shear loads, a regression solution is used approximating more calculation intensive solutions.

For the Anisogrid structure with triangular skin-bays, a criterion is available which bases on the NACA TN-3781. This fundamental criterion is harmonised with the help of results derived in a wide finite element study. During this investigation, the published semi-analytical approach by M. Weber [94] was compared to the implemented method. Therefore, the Weber results are approximated by regressions functions and implemented into the analytical tool. The comparison of the two methods with FEM results show, that the Weber method is more accurate than the underlying analytical tool method for unstiffened single skin-bays. On stiffened panels, the available criterion in the analytical tool proved to give better correlation with FEM-results and is finally chosen for the following panel study. Results of the method comparison are attached in B.1.3.

#### *Material Strength*

For analysis of the static in-plane strength, it is established to use a maximum strain criterion in the pre-sizing process [5]. A layer-wise and failure-type strength analysis is not taken at this stage to reduce the number of sizing variables. An additional reason is that the margins shall be investigated and the separation of compression and shear is of special interest due to the specific load-case analysis instead of the separate investigation of fibre and inter fibre failure.

The allowable strains are quite low and include reductions for material B-values, climate conditions and damage tolerance demands. With respect to the performed tests, following allowable strains are considered for the grid and skin:

*Table 6: Allowable strains*

| | Anisogrid | Orthogrid | Skin |
|---|---|---|---|
| Tension | ≤ 4000 µm/m | ≤ 4000 µm/m | ≤ 4000 µm/m |
| Compression | ≤ 3000 µm/m | ≤ 3000 µm/m | ≤ 3000 µm/m |
| Shear | ≤ 5000 µm/m | ≤ 5000 µm/m | ≤ 5000 µm/m |

#### *Overview of Sizing Criteria*

For the sizing process, the margins of all sizing criteria are determined depending on the present aircraft load levels. In the Certification Specification for passenger airplanes, two load levels are defined [12]:

Limit Load (LL) – Maximum loads to be expected in airplane service

Ultimate Load (UL) – Limit Loads multiplied by a factor of safety

Any part of the airplane structure must be able to withstand its expected limit load without permanent deformation. The limit loads are determined from the flight and also ground loads of an aircraft.

At least 1.5 of the limit load is used as the safety factor for all design criteria, whereby the specific load level for the calculation may deviate. For example, the load level differs between several fuselage positions at which local buckling can be allowed. Due to the linear analysis of the panel structures in this investigation, a no-buckling policy is pursued.

### 6.1.5 Objective Function – Evaluation Criterion

The design goal of the investigation is the minimisation of the *weight-per-square-meter* which is also used as evaluation criterion for the comparison of the Aniso- and Orthogrid structure. This criterion normalises the structure weight to equal in-plane-dimensions and means that the element weights of the unit cell are divided by the area of the unit cell. This approach allows the comparison of different sizes of unit cells, which is seen to be evident for comparison with as few as possible geometric restrictions.

Such a procedure can be questionable for differentially manufactured structures due to the direct consequences of the unit cell size on the quantity of stiffeners, which directly affect the assembly time and costs. For integrally manufactured structures, neglecting this restriction is assumed. There is undoubtedly a similar effect, but because no extra assembly steps are needed, the amount of material to be placed seems to be more important.

There are other criteria for a design evaluation, such as the load divided by the stiffener distance or divided by the cross-section area, which are called e.g. *"structural values"* or in German phrase "Strukturkennwerte" by Wiedemann [96]. These approaches are, however, differing slightly. As the weight-per-square-meter criterion is comparing the minimum weight for structures sized under the same load, the load-per-area criteria are comparing the maximum load under the same mostly given structural weight. In this investigation, the load-based method is chosen, because it is seen to be closer to a realistic sizing process for an application.

### 6.1.6 Sizing Algorithm

The procedure of the sizing algorithm is shown in Figure 41. In the beginning, it has to be defined the structural configuration, the material and the sizing criteria. The structural configuration is characterised by choosing the geometry, determining the loads or different load cases and defining the boundary conditions. For the material model, two main approaches can be considered, which are the use of smeared properties or the definition of discrete laminate stackings. It is also possible to combine these methods, which means to define discrete laminate stackings but calculating with derived smeared properties. As sizing criteria, it can be chosen out of global and local stability criteria, stress/strain criteria and stiffness/deformation or geometric requirements.

In the second step, the parameters are defined which remain constant (constants) and which are sized (variables). By determining the interval and the step size for all variables, the design space is set. In this investigation, only geometric parameters are set as variables.

In the following analysis process, the algorithm is sorting all possible parameter sets by their weight or to be precise by their area weight in [kg/m²]. Subsequent, the margin of safety (MoS) of all sizing criteria are calculated step by step for the designs beginning with the lightest. As soon as all MoS of a design set are higher than Zero, the lightest design is found. Depending on the amount of sizing variables, several iteration loops are used to cover a large design space and finding the global weight minimum. Subsequently, the result is improved by refining the interval and step size for the variables. In the appendix B.2, the sizing process for the Anisogrid panel under compression is given exemplary.

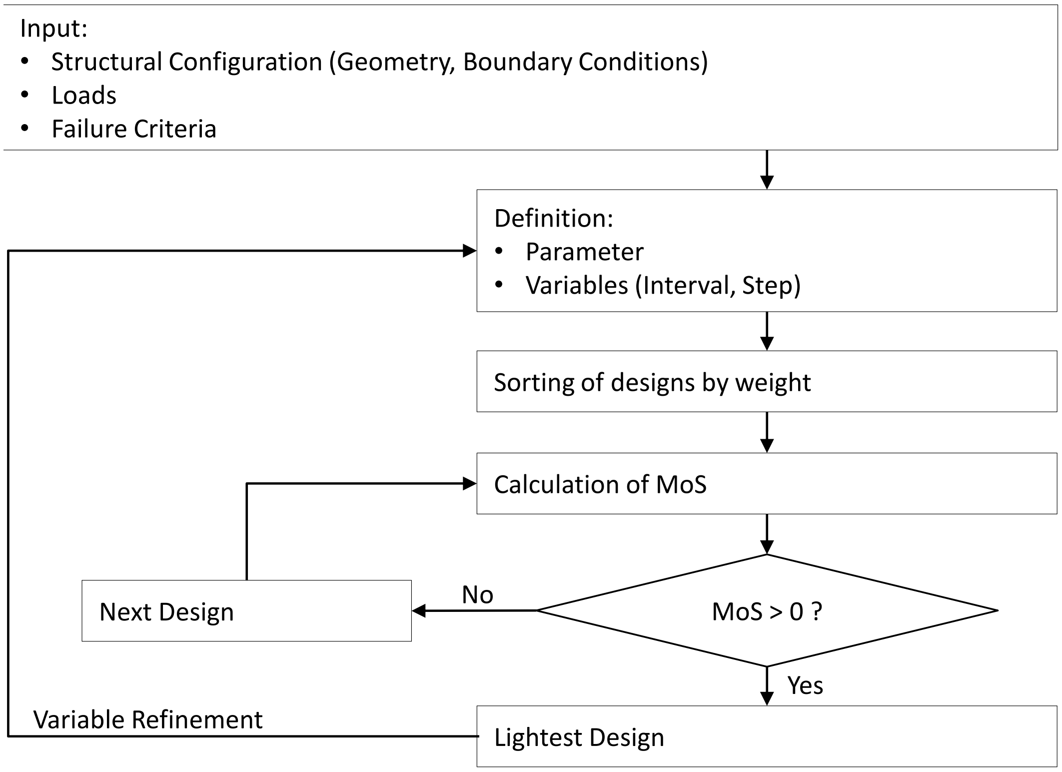

*Figure 41: Sizing Algorithm implemented in the sizing tool HyperSizer®*

## 6.2 Sizing Results for the Anisogrid-Panel

In this section, the results of the panel sizing are presented for the Anisogrid architecture. The minimum weight curve is plotted over the load. Each point of the minimum weight curve represents the result of the iterative sizing algorithm, described in the previous subsection. Each of the 20 points comprises a design space between 1 and 2 million calculated designs, with three to four iterations executed.

### 6.2.1 Flat Panel Results

#### *Uniaxial Compression*

The resulting minimum panel weight curve is characterised by a constantly increasing but degressive progression, which means that with higher loading, a lower amount of additional material is needed to fulfil all sizing criteria (see Figure 42, top). Regarding the margins of safety, it can be seen that, for compression, it is a pure stability problem. The global as well as the local stability criteria are sized nearly to zero and dimension the panel (see Figure 42, below).

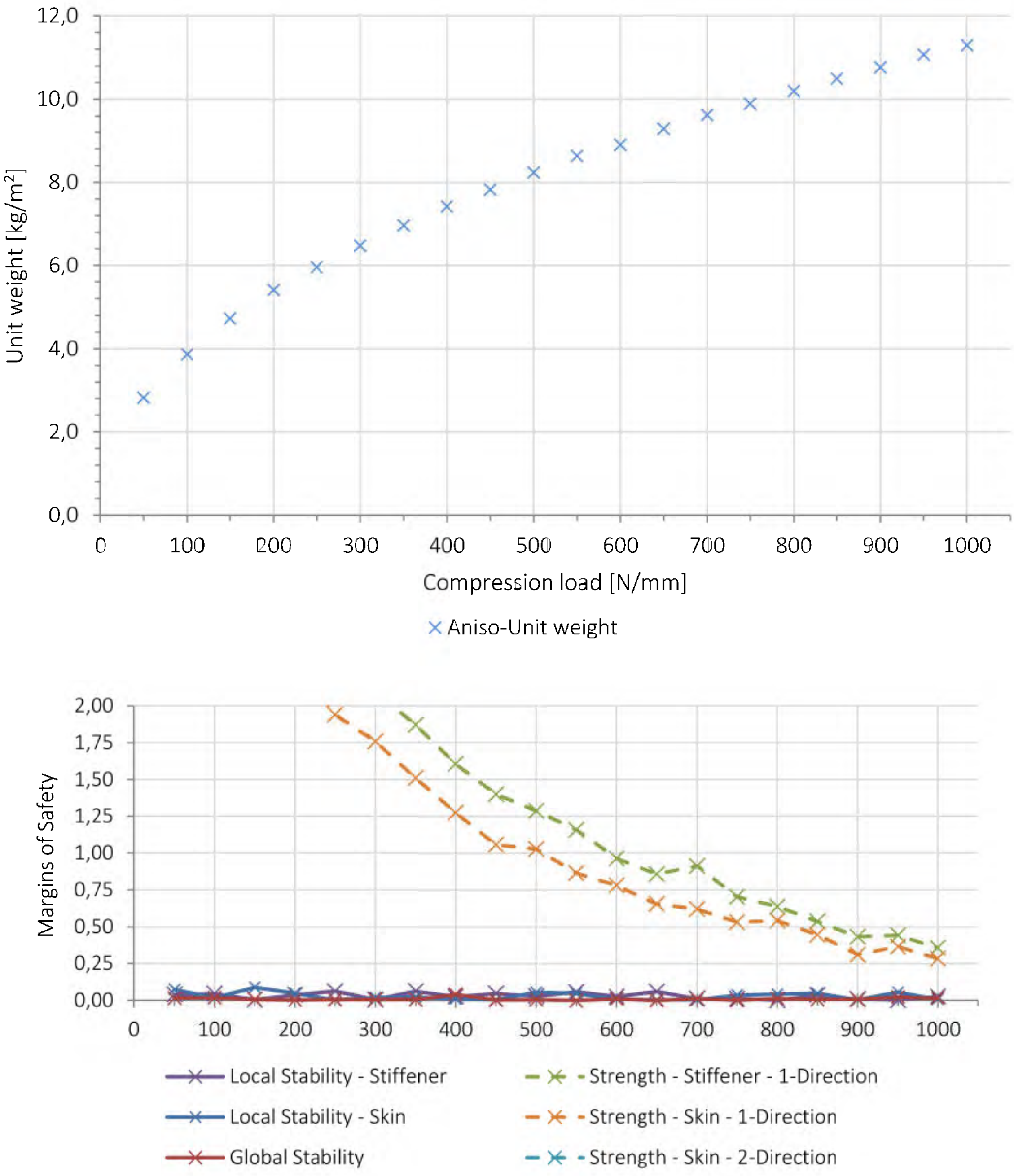

*Figure 42: Anisogrid flat panel sizing results; above: minimum weight; below: margins of safety*

The strength criteria become critical only for higher loads. This behaviour depends on the distance of the circumferential stiffeners. The lower the chosen distance of the circumferential stiffeners, the earlier the strength criteria become critical. Nevertheless, the main characteristic of a stability driven problem for uniaxial compression stays the same on a shell structure relevant for an airframe. Relevant means in this case that the circumferential stiffener distance will be at least 250 mm, as used here. It should be recalled that the classical frame distance is 533 mm.

As mentioned before, each point of the minimum weight curve stands for a discrete design set of the panel variables, which are shown in Figure 43 in detail. All the design variables increase with rising compressive load, whereby the magnitude differs greatly. The degressive increase of the panel unit weight is also observable for the skin thickness, the distance of helical stiffeners or the width of the helical ribs. The width and height of the circumferential ribs increase more linearly.

It shall be mentioned again that these results are found within the selected iteration step and size. The design sets for each load are undoubtedly local minima and there are other valid design sets with nearly the same weight (other local minima). However, more important than a specific design set is, for this investigation, to get close to the global minimum which shall be ensured by several iteration steps explained in Subsection 6.1.6 and shown in the appendix B.2.

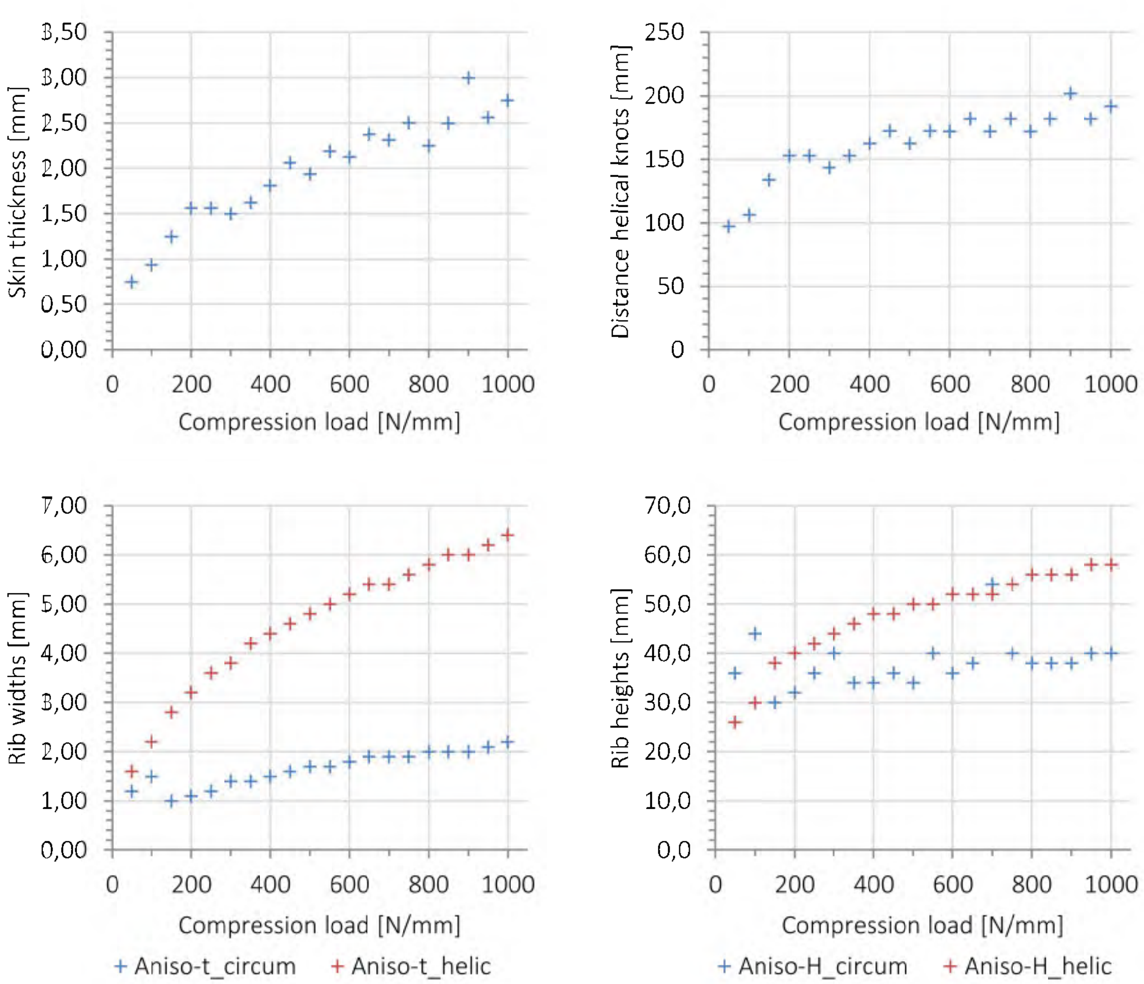

*Figure 43: Variable results for compression – Anisogrid flat panel*

In order to illustrate how the minimum weight curve is “shaped” depending on specific variables, in Figure 44 and Figure 45 the minimum weight is shown for several constant skin thicknesses and angles of helical ribs. These curves show how these parameters are limiting/generating the overall minimum weight curve. For a specific load range, the parameter will lead to the minimum weight of the panel. For example, a skin thickness of 1.0 mm leads to a design with the minimum weight in a compressive load range between 100 and 200 N/mm. A skin thickness of 1.6 mm results in a panel weight within 3% of the minimum weight over a wide load range between 150 and 650 N/mm. A skin thickness of 3.0 mm is, in contrast, not causal to the minimum weight for the investigated compressive load range and leads, for example, at very low compressive loads to more than twice the panel weight.

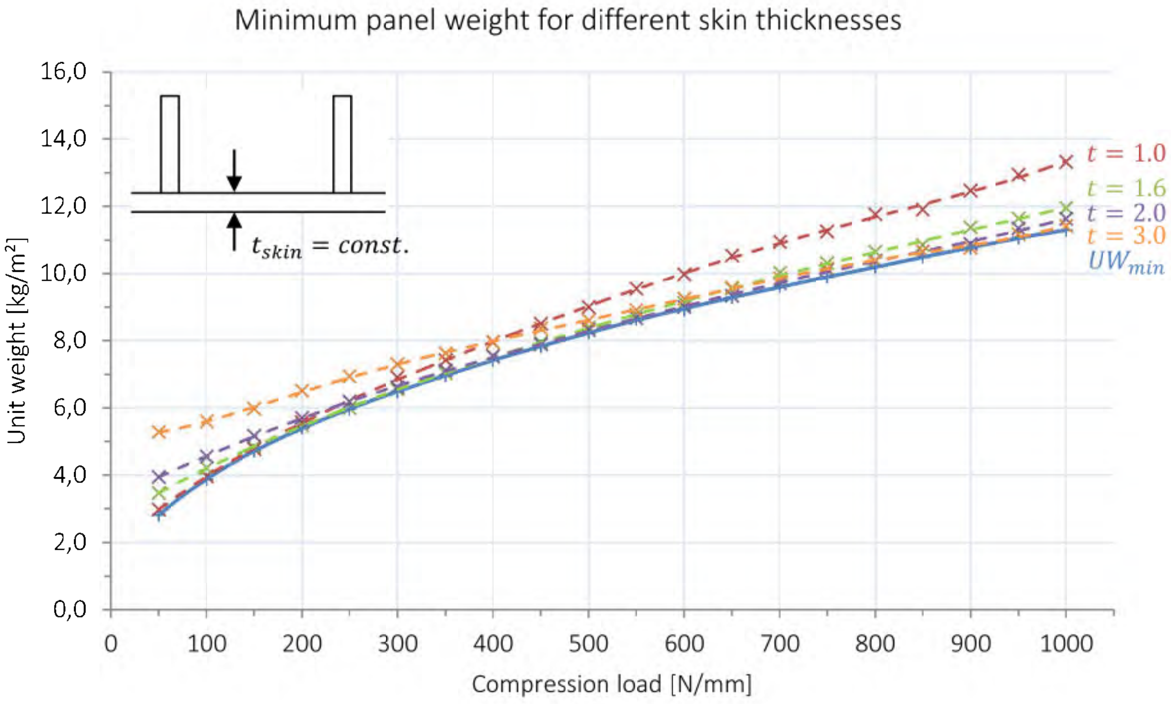

*Figure 44: Minimum Anisogrid panel weight under variation of skin thickness*

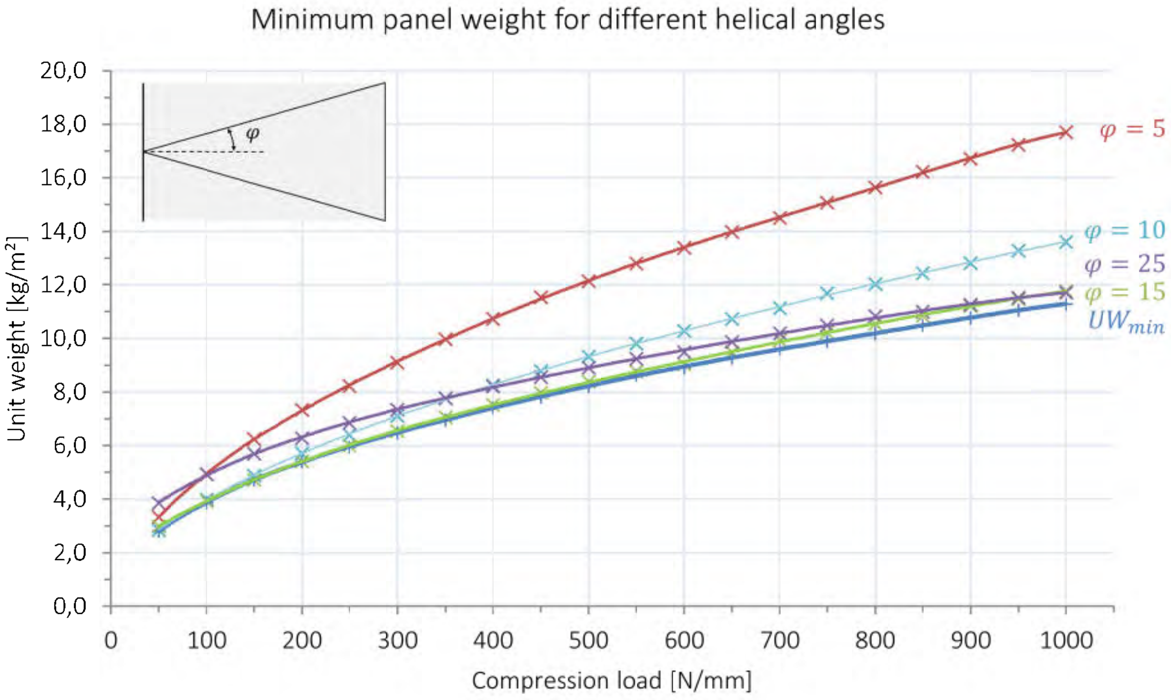

*Figure 45: Minimum Anisogrid panel weight under variation of helical angle*

The investigation of minimum weight for different helix angles shows that φ=15° is causal nearly over the whole compressive load range to the minimum panel weight (<5% deviation). The lowest weight results at an angle of φ=10° for low loads between 50 and 150 N/mm.

### *Pure Shear*

The resulting minimum weight curve for shear can be divided into three zones. The first zone, characterised by very low loads between 50 N/mm and 150 N/mm, has the degressive character like for compression, followed by two linear zones with different progression, whereas the third linear zone between 550 N/mm and 1000 N/mm has a higher slope and is nearly a line through the origin (virtually lengthened to the left) (see Figure 46, top). Such a line reflects that the structure is purely strength driven, because no load means no weight and with increasing load the structure weight increases with the same amount.

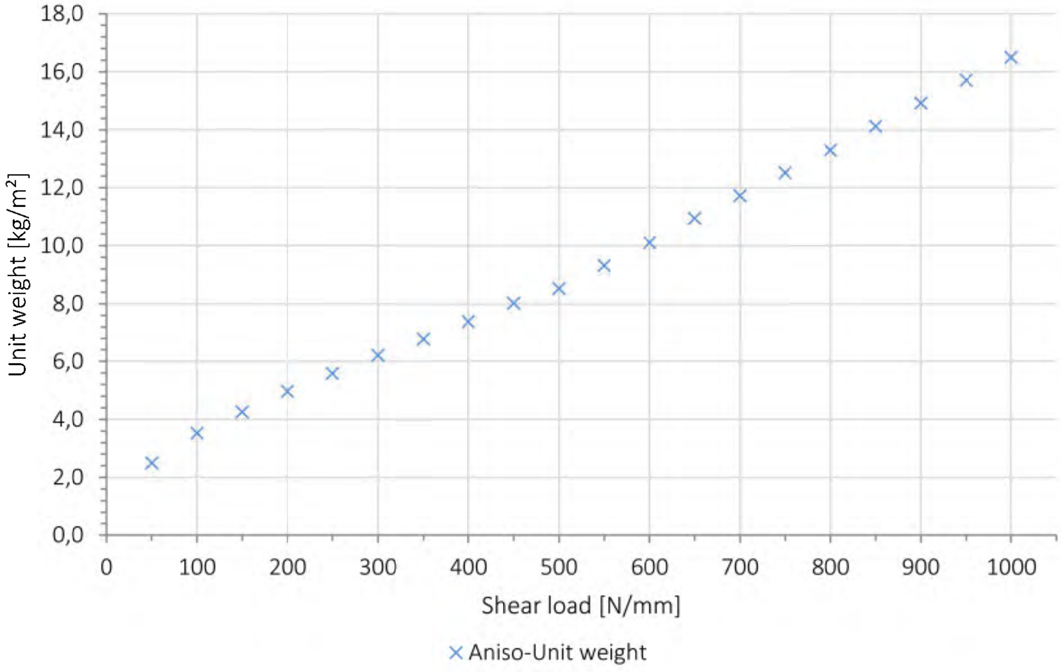

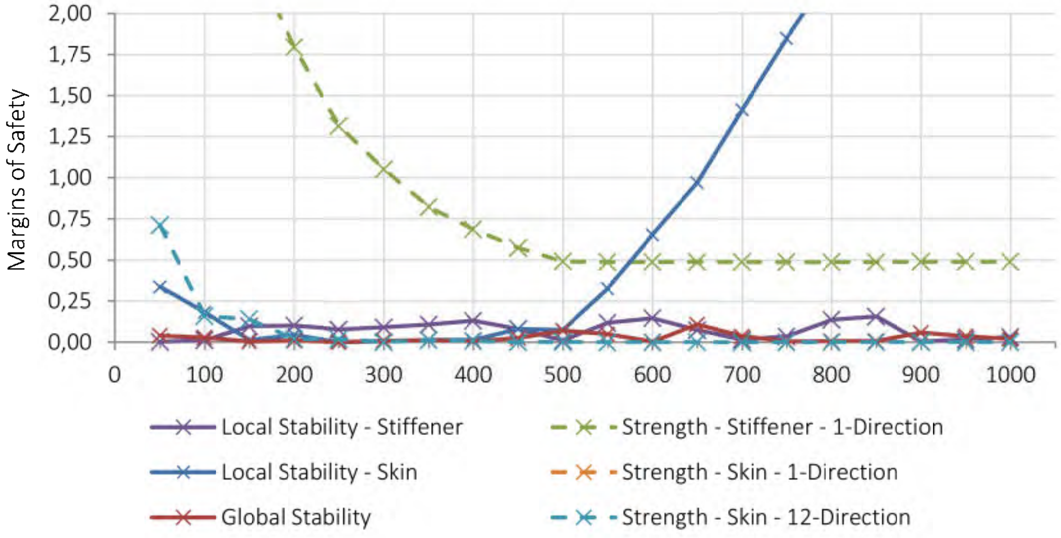

*Figure 46: Anisogrid flat panel shear results; above: minimum weight; below: margins of safety*

Examining the margin of safety diagram these three zones matches particularly with the strength criteria. From 150 N/mm on, the skin strength criterion dimensions additionally the previous pure stability driven design and the first linear zone starts. The second linear zone begins when the maximum stiffener distance is reached which can be seen directly with the increasing skin stability MoS. In comparison to compression, the strength criteria are much more critical, reaching the geometrical limits so that the local skin-bay criterion cannot be minimised anymore.

In Figure 47, the results for all variables are presented. The mentioned three zones are clearly visible e.g. in the 'Distance of Helical Knots' diagram. In contrast to compression, the distance of the helical stiffeners increases much faster and also reaches the limit, which was not expected. In the rib height diagram, a sharp drop in the rib height of the circumferential stiffener can be observed for the third region. It is assumed that with the skin thickness, which now increases stronger than in the first two zones and in combination with the constant stiffener amount, less stiffness needs to be provided by the helical ribs and their height drops.

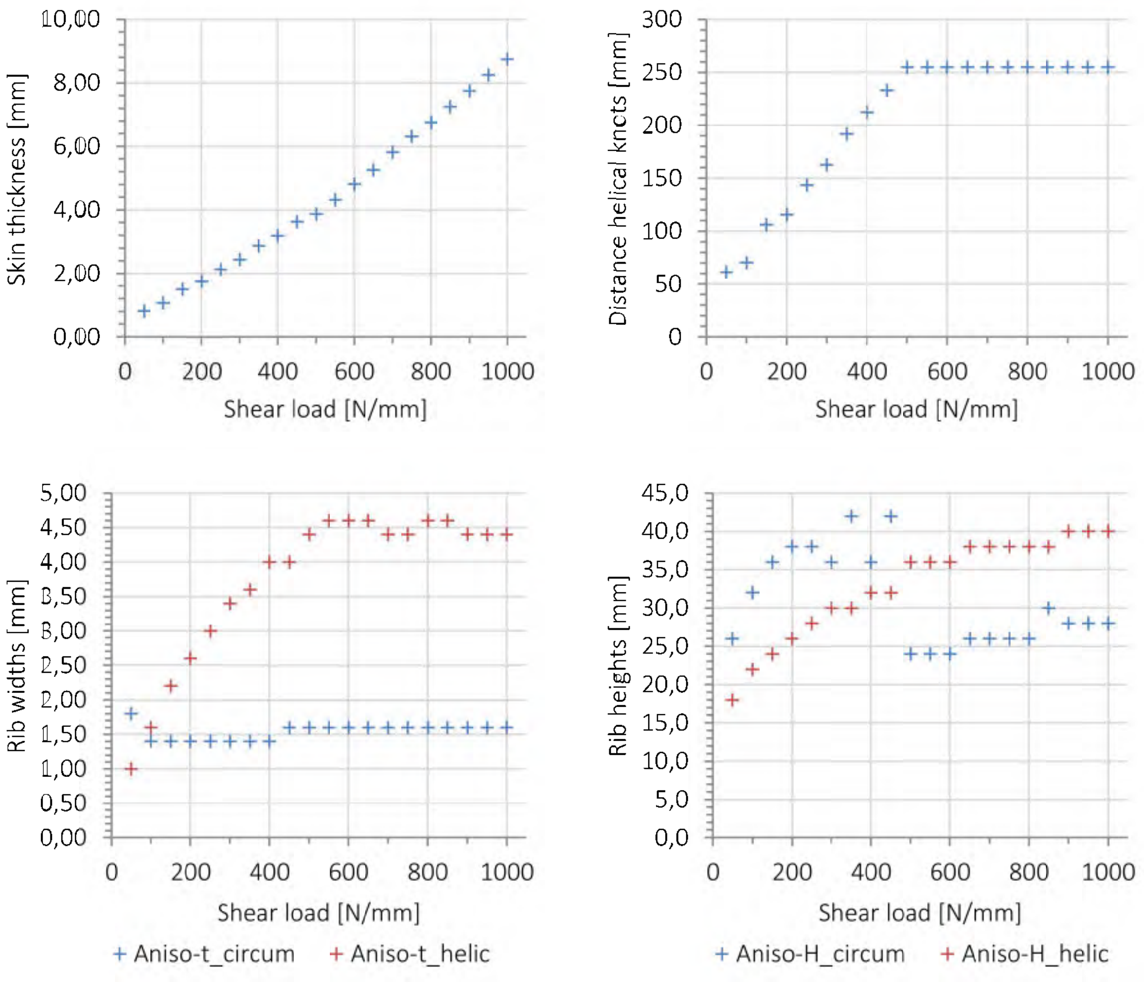

*Figure 47: Variable results for shear – Anisogrid flat panel*

### *Combination of Compression and Shear*

Due to the high number of calculations not a complete compression-shear-interaction curve is analysed. Instead, three combined load ratios are investigated. First, the same amount of compression and shear load ('compression 1:1 shear'), and additionally two cases where one of the loads has half the quantity of the other ('compression 1:0.5 shear' and 'compression 0.5:1 shear').

In Figure 48 the ‘compression 1:1 shear’ minimum weight curve is plotted. Overall, the characteristic looks similar to the pure shear load, whereby the first degressive curve progression is more distinctive at lower to middle load levels. From 600 N/mm on, the linear zone starts which correlates with the change in sizing to a pure strength driven problem.

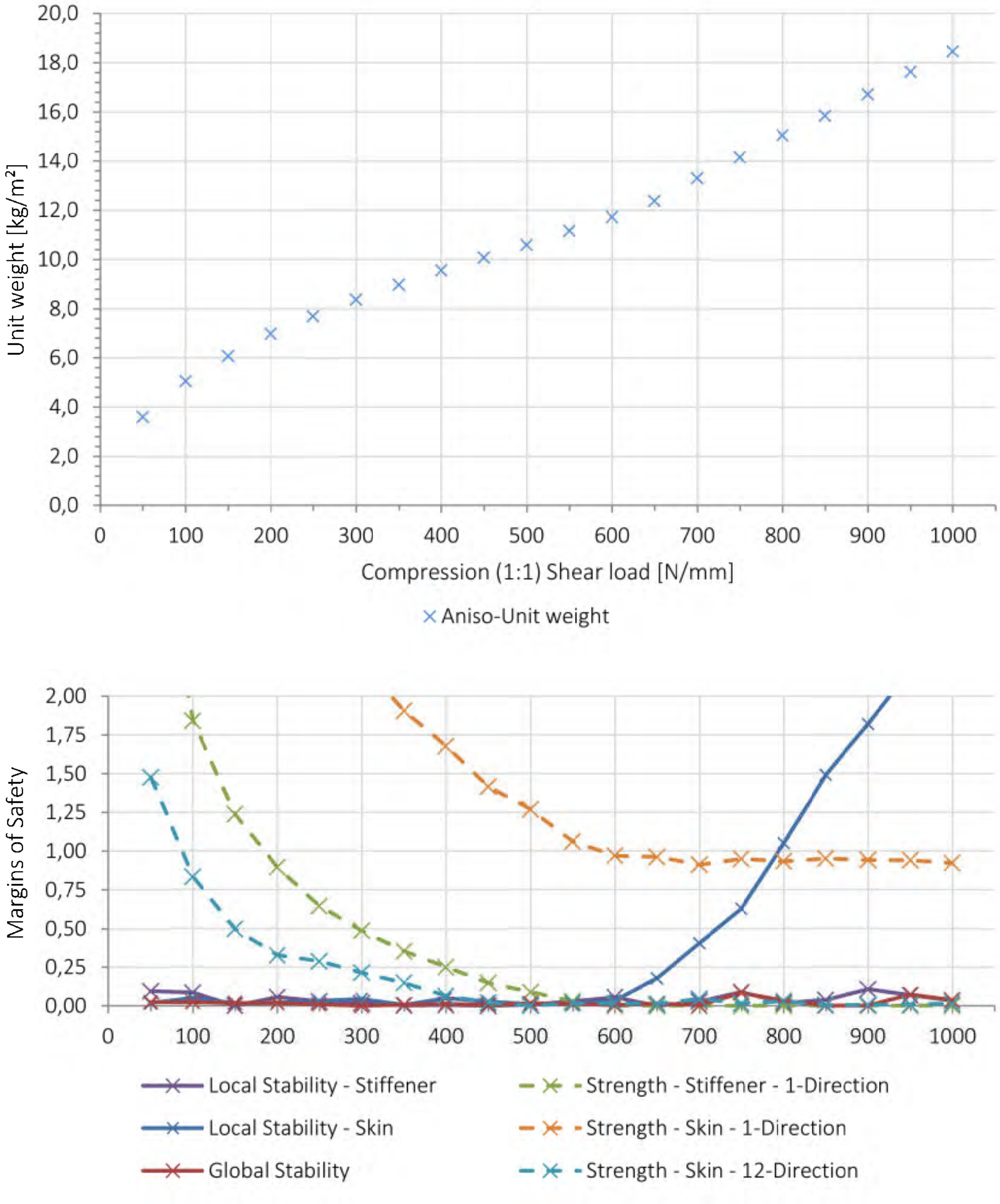

*Figure 48: Anisogrid flat panel compression 1:1 shear load combination*

The progression of the MoS look very similar to the results for shear whereby all curves seem to be shifted to the right which means that the strength criteria become critical at higher loads. Due to the additional compression, it is concluded that the additional material results in a certain higher reserve for strength to fulfil the global and local stability criteria.

The sizing results for the other two compression-shear combinations are given in the appendix B.3.1 including the MoS and the results for all variables.

### 6.2.2 Curved Panel Results

#### *Uniaxial Compression*

The minimum weight curve is characterised by two zones. First, a quite degressive part of the curve; the higher compressive load is applied the lower amount of additional material is needed. In the second zone, the minimum weight curve changes into a linear progression, which means with increasing compressive load the weight increases accordingly.

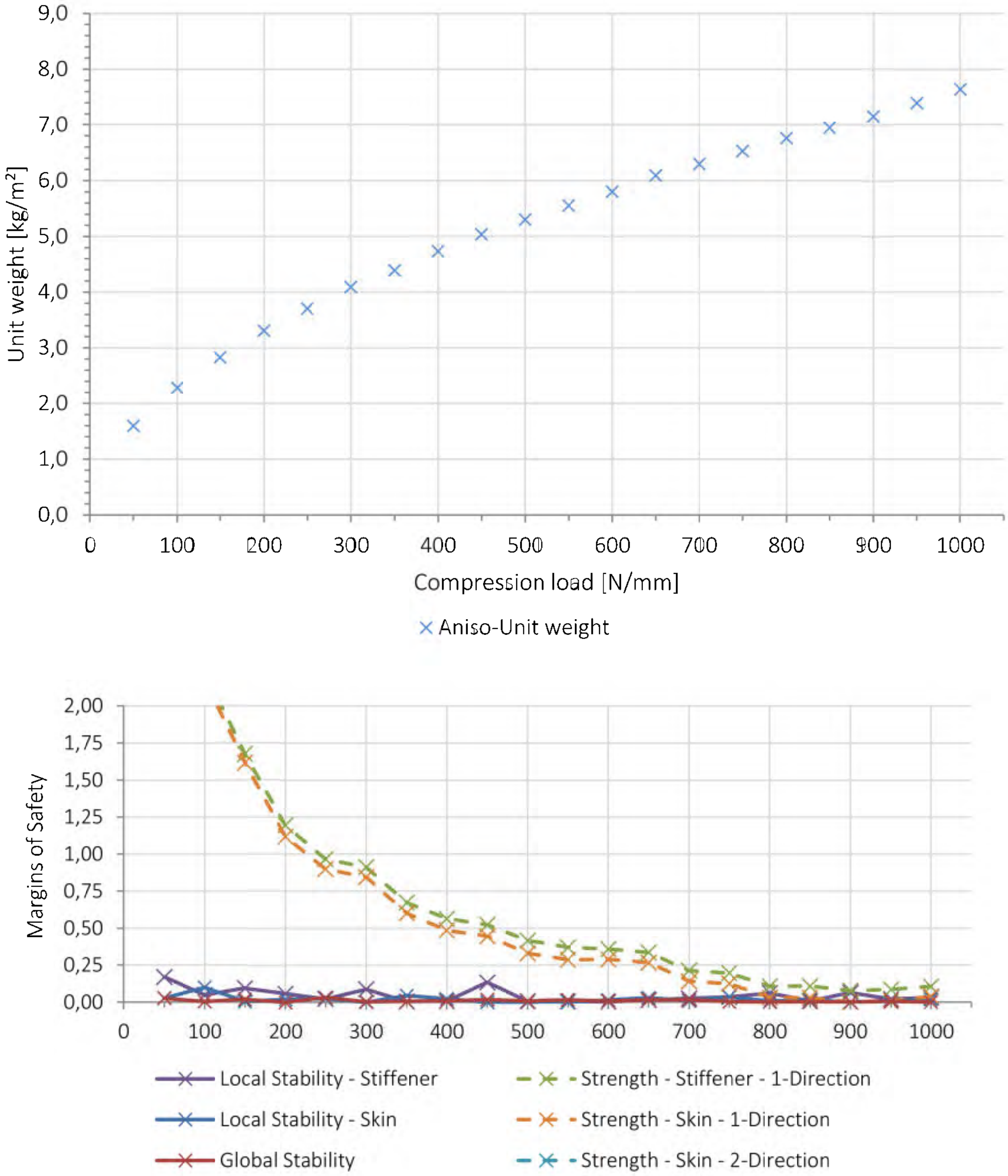

*Figure 49: Anisogrid curved panel sizing results; above: minimum weight; below: margins of safety*

The MoS-diagram in Figure 49 shows that the panel is a purely stability driven design over most of the load range. The global and both local stability criteria are optimised almost to zero. The stiffener and skin strength criteria dimension the panel additionally at high compressive loads from 700 N/mm. This also coincides with the two zones when the degressive curve changes into a linear curve. This characterises a strength critical construction and higher loading can only be obtained by more material in terms of larger cross-sections.

The diagrams in Figure 50 show the change of all design variables as a function of the compressive load. It can be seen that all design variables increase according to the increasing load in a specific extent. For the skin thickness and the distance of the helical knots (which is also the angle of the knots), again, these two zones can be observed. In the first zone, both variables increase with increasing compressive load. In the second zone, these two variables remain nearly constant. This zone corresponds with the compressive load when the strength criteria additionally size the design. Due to the higher allowable stress of the ribs, it is more efficient to simply increase their cross-section instead of increasing the skin thickness.

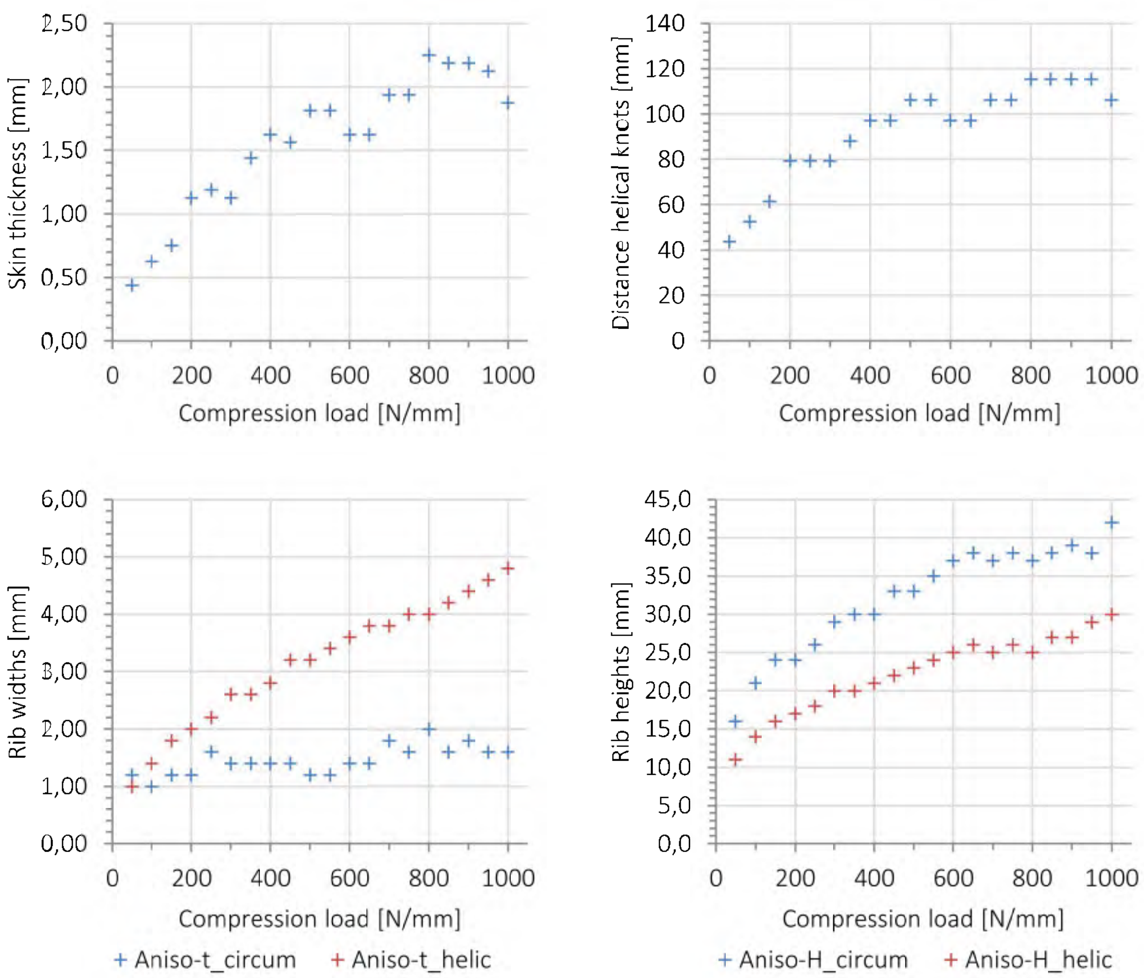

*Figure 50: Variable results for compression – Anisogrid curved panel*

### *Pure Shear*

The minimum weight curve of the curved Anisogrid panel has, in general, a similar progression as the flat panel. Due to the limitation of maximum stiffener distance a first linear zone changes into a second linear zone with higher slope (see Figure 51). Similar to the flat panel, the second linear part of the curve is also a line through the origin, showing that it is a strength-driven sizing for this range of load.

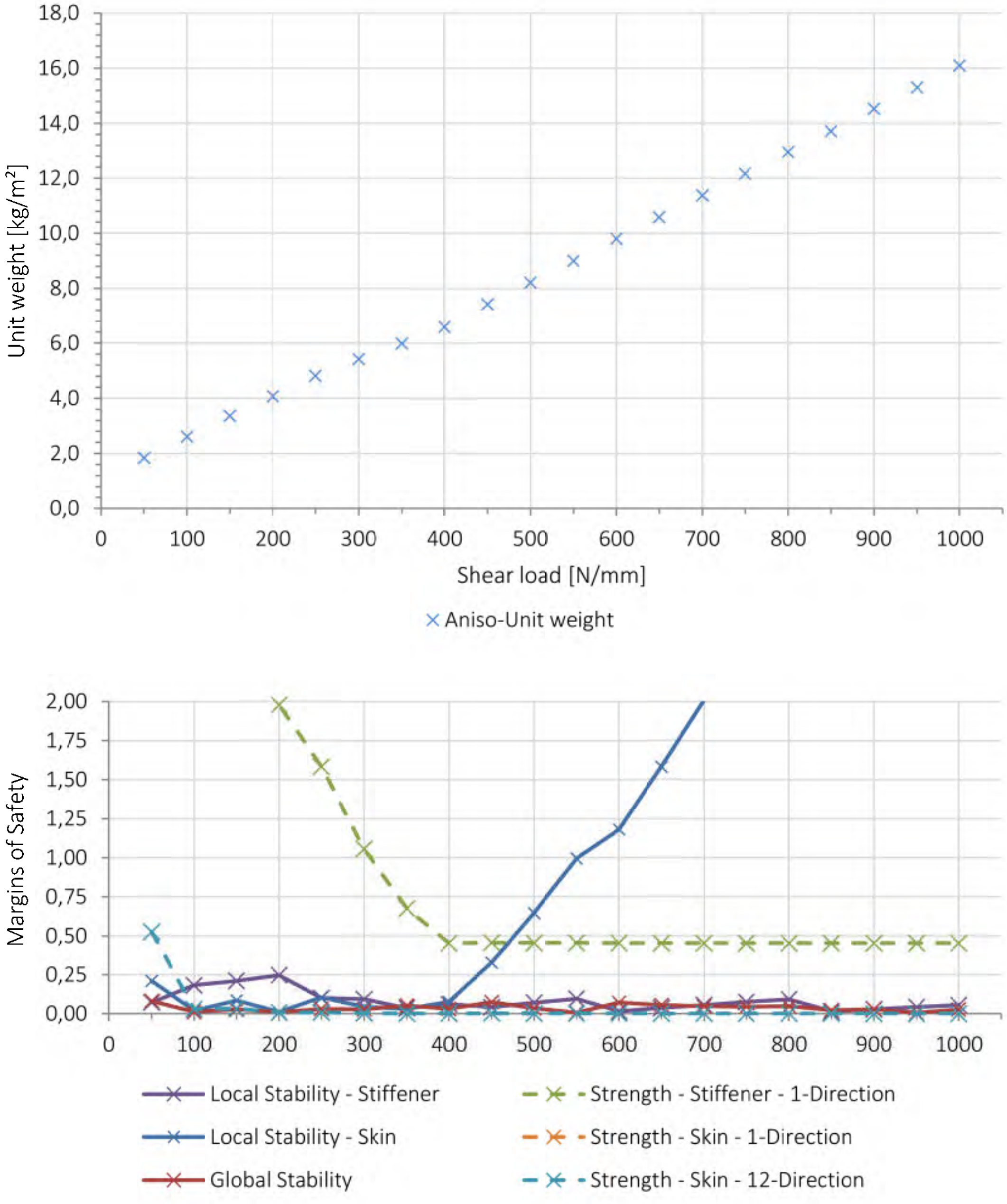

*Figure 51: Anisogrid curved panel sizing results; above: minimum weight; below: margins of safety*

The detailed variable results are shown in Figure 52. The skin thickness increases almost linearly over the load range. The distance of the helix stiffeners also rise rapidly until the limit is reached. The maximum is achieved at a lower load compared to the flat panel, as the curved panel has higher global buckling resistance due to its curvature.

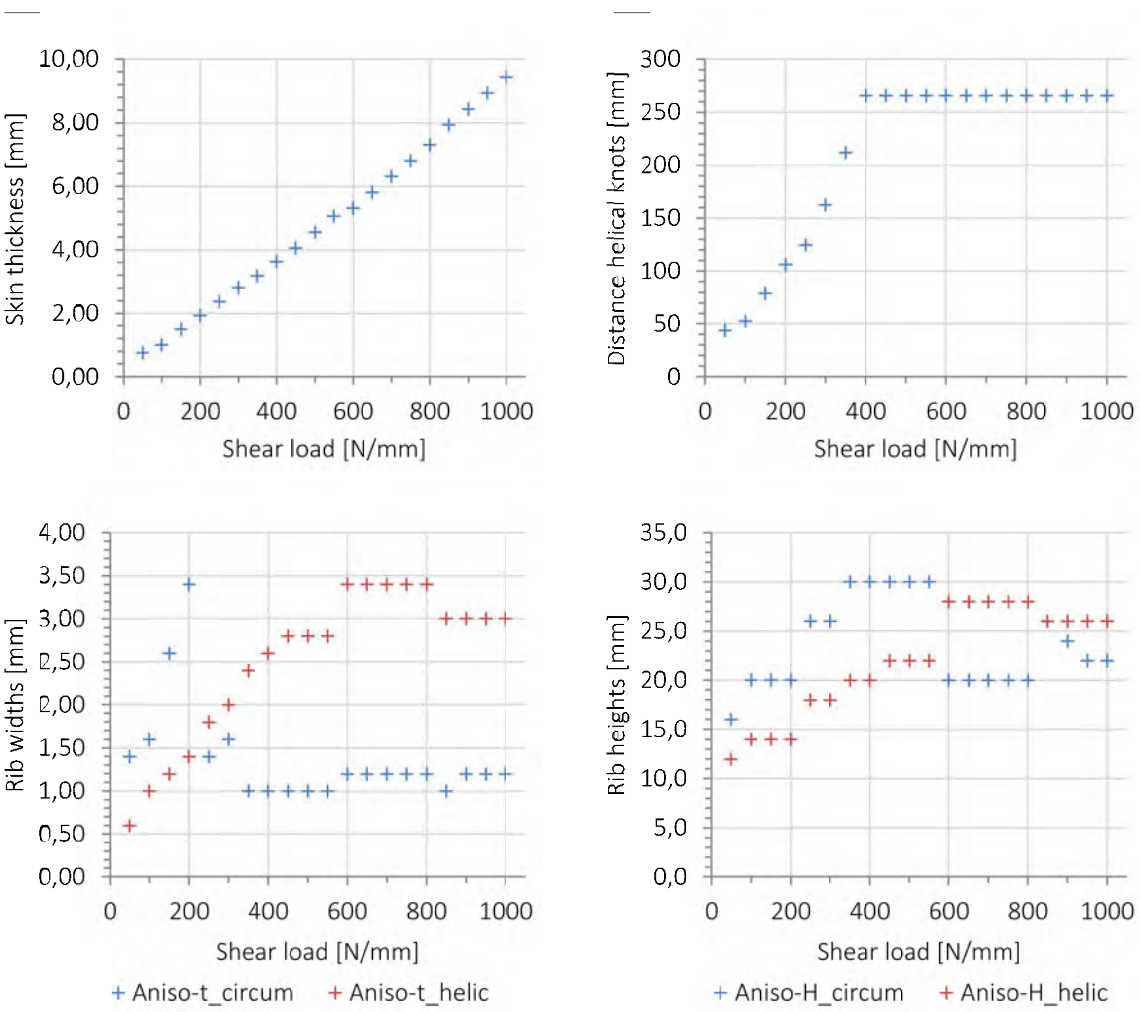

*Figure 52: Variable results for shear – Anisogrid curved panel*

### *Combination of Compression and Shear*

The diagrams in Figure 53 show the minimum weight curve of the combined 'compression (1:1) shear' together with the MoS-diagram. The curve is characterised by a degressive increasing first part of the curve, followed by a linear zone like seen at the flat panel. The change between these two zones can be observed at 450 N/mm.

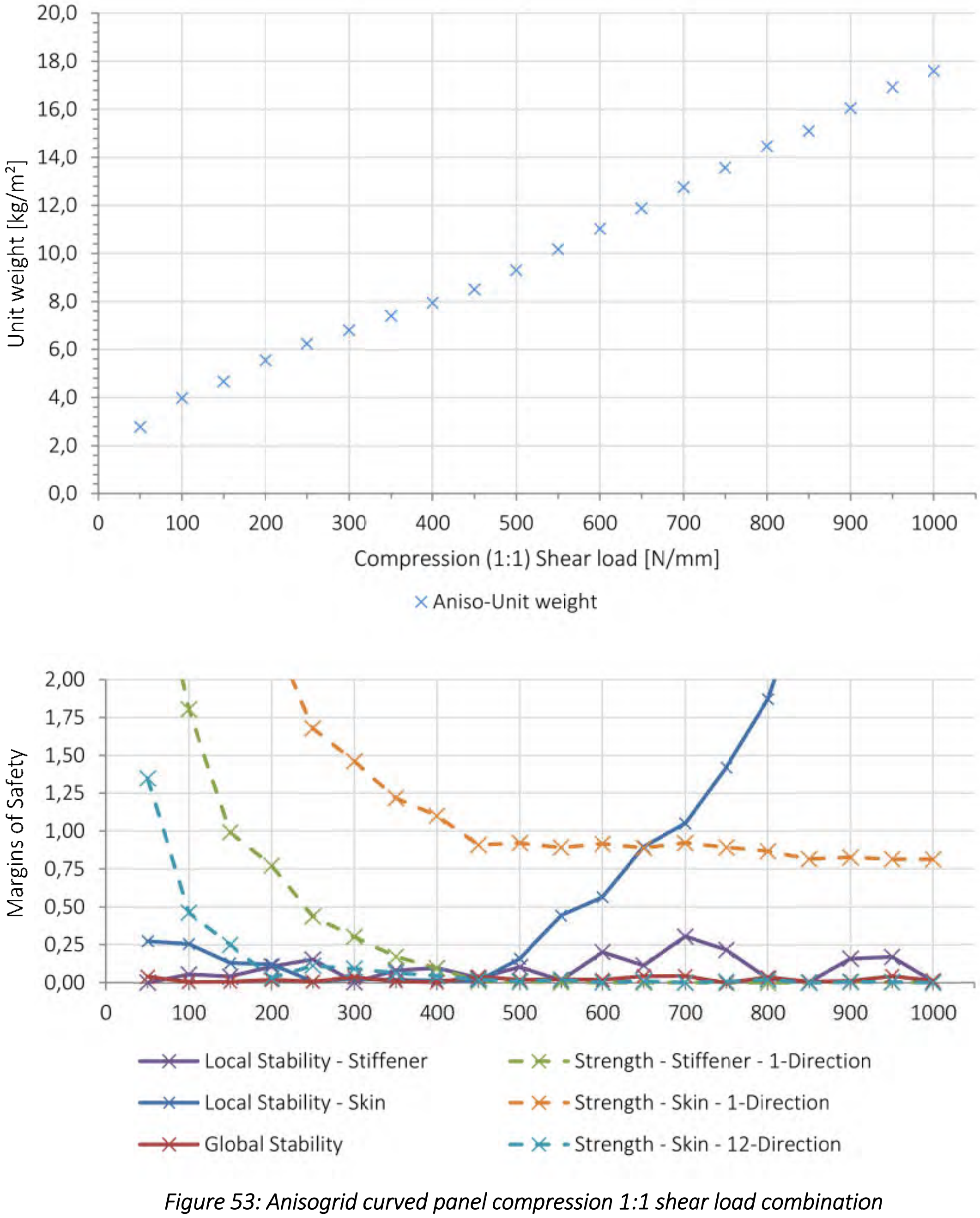

*Figure 53: Anisogrid curved panel compression 1:1 shear load combination*

The progressions of the MoS curves are similar to the flat panel. The change between the two zones matches at 450 N/mm with the point when the skin stability criterion is not design-driving anymore. Although the same refinement step-sizes and intervals are used at the last iteration the design seems not to be as optimised as the flat panel structure (curves are not very smooth).

The weight curves for the two cases with lower compression or shear load are again attached in B.3.2.

## 6.3 Sizing Results of the Orthogrid-Panel

According to the results of the Anisogrid panel, in the following, the sizing results are presented for the Orthogrid panel. The chapter is also divided in showing separately the flat und curved panel results.

### 6.3.1 Flat Panel Results

#### *Uniaxial Compression*

The compression results are quite similar to the Anisogrid panel results. The minimum weight curve has an increasing degressive character over the whole load range (see Figure 54).

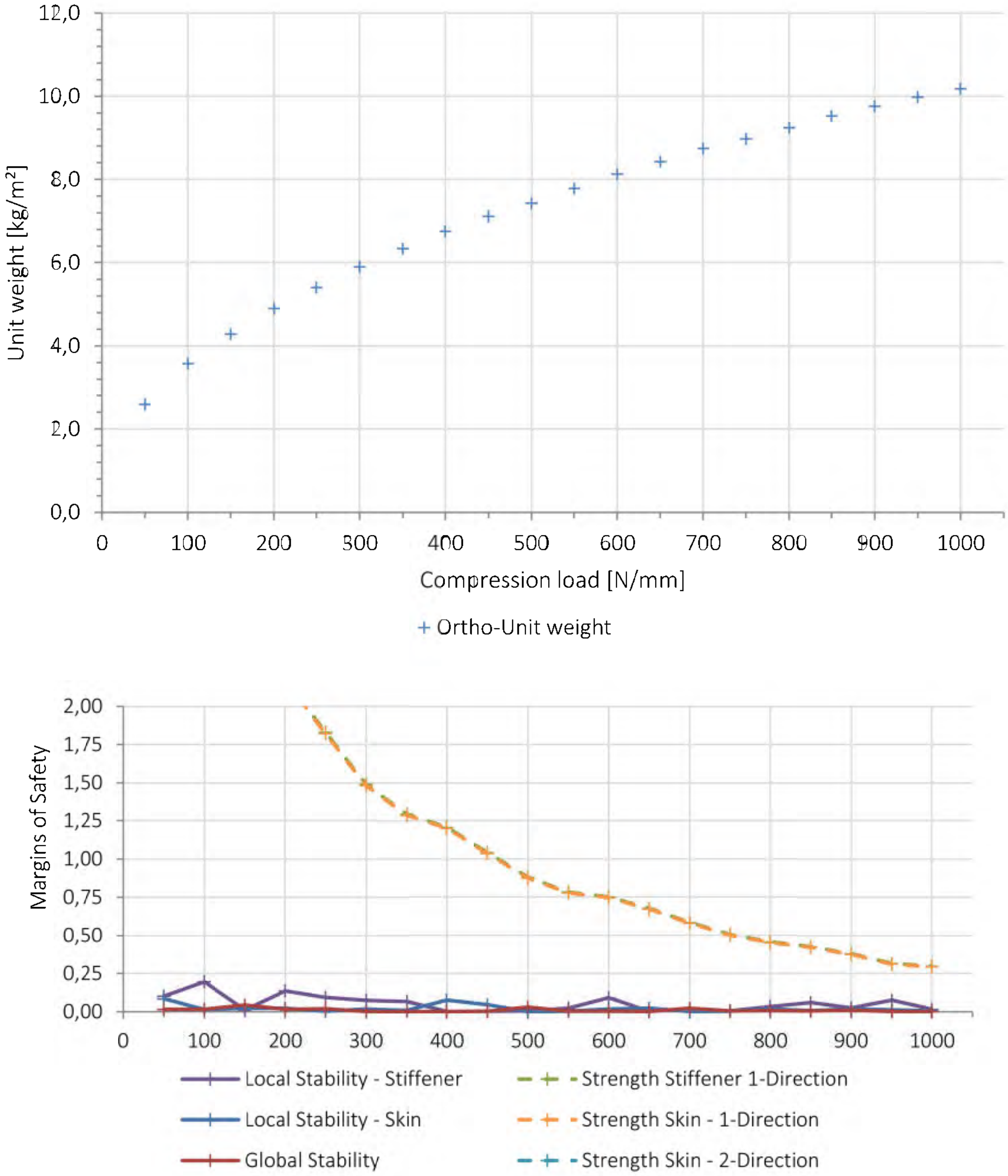

*Figure 54: Orthogrid flat panel sizing results; above: minimum weight; below: margins of safety*

The margin of safety curves also show that the uniaxial compression is a stability problem and the strength criteria do not size the panel. A difference can be seen for the stiffener and skin strength MoS, which curves are lying on top of each other. In contrast, the strength curves of the Anisogrid panels have always a certain distance to each other. Reason is that the axial stiffener and the skin are oriented in the same direction at the Orthogrid. Resultantly, from calculating a smeared element and transferring the global strain to both elements, both have the same margins, as also the material failure strains are the same. Figure 55 show the results of all variables.

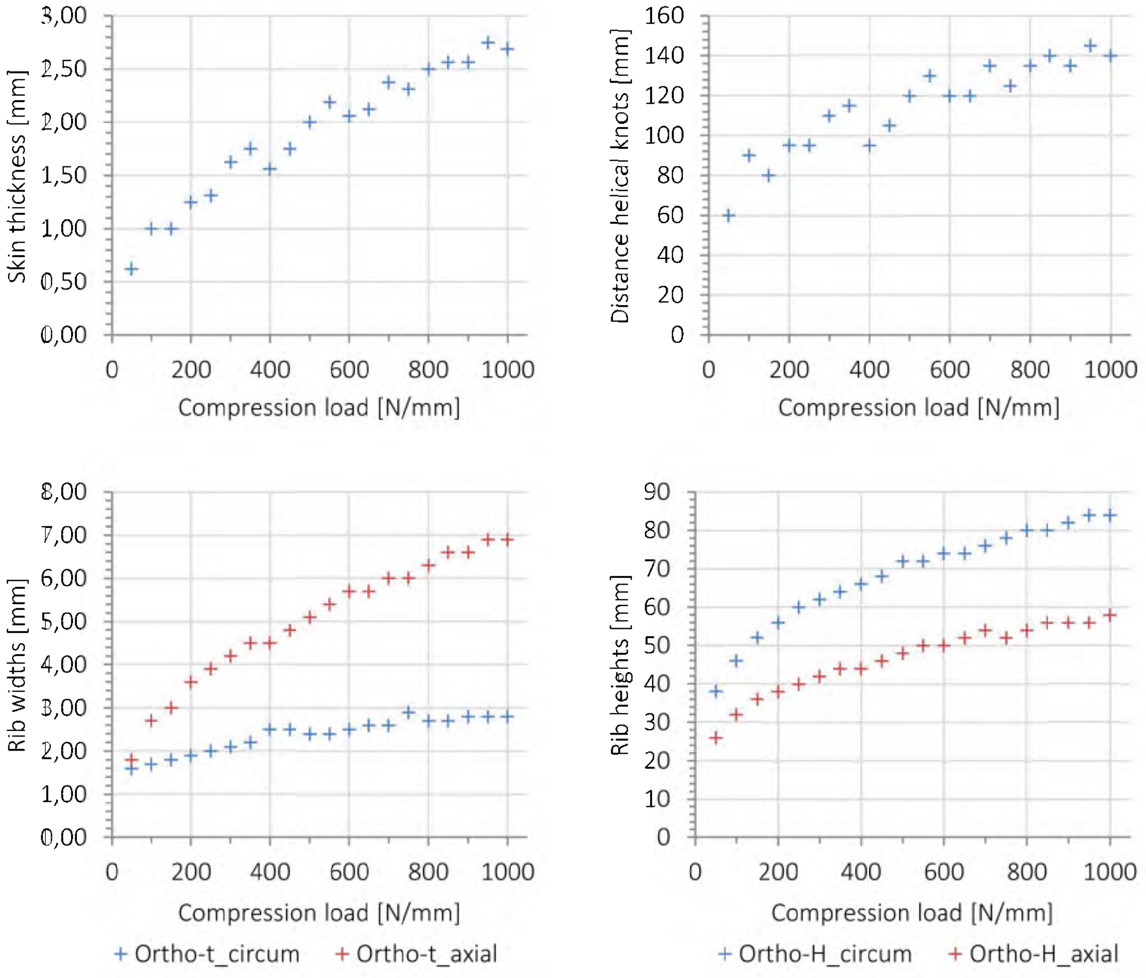

*Figure 55: Variable results for compression – Orthogrid flat panel*

According to the Anisogrid panel, Figure 56 and Figure 57 present the dependencies of the minimum weight curve when the skin thickness and the distance of the axial stiffeners are fixed to constant values. It can clearly be seen how a skin thickness of 1.0 mm is leading to the minimum panel weight (within 3% deviation) between 100 and 200 N/mm, 1.6 mm between 200 and 600 N/mm and 2.0 mm between 300 and 900 N/mm. Resultantly, the load range for keeping the skin thickness constant is quite wide, whereby this has to be seen under the condition that the other variables can change almost arbitrarily.

The axial stiffener distance is shown in Figure 57 indirectly as angle comparably to the Anisogrid panel. Similar to the Anisogrid panel, a stiffener distance equal to an angle of $\varphi$=15° is leading over a wide load range between 300 and 1000 N/mm to the minimum panel weight (within 3% deviation).

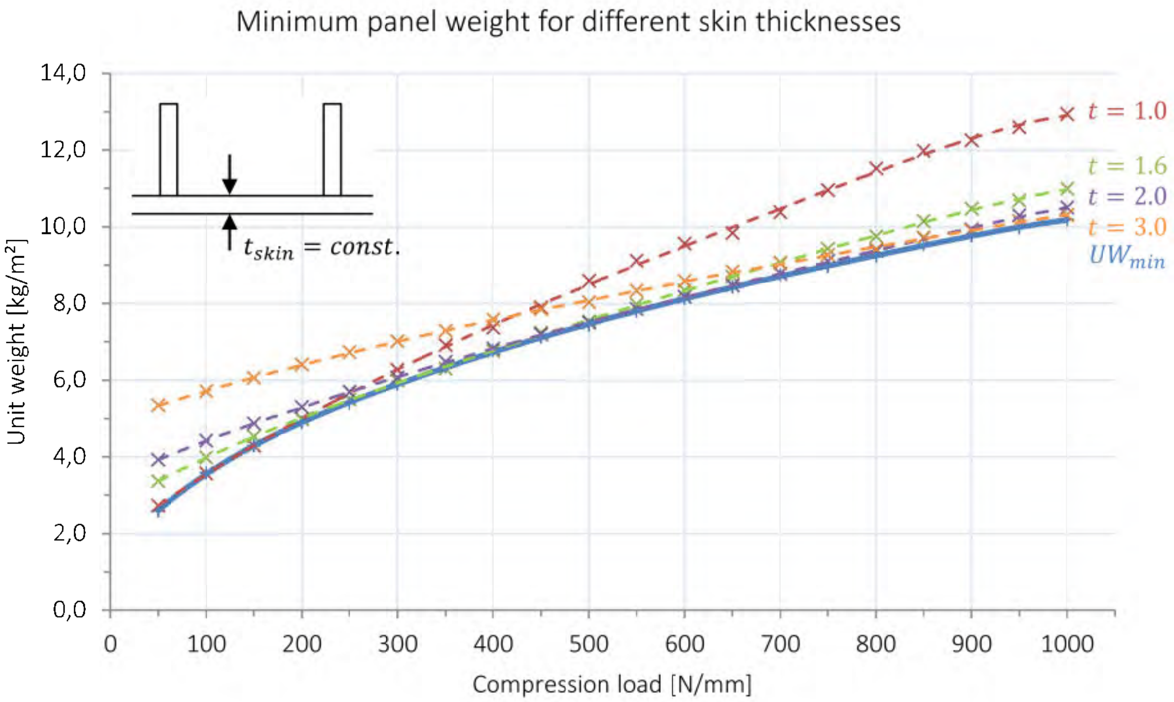

*Figure 56: Minimum Orthogrid panel weight under variation of skin thickness*

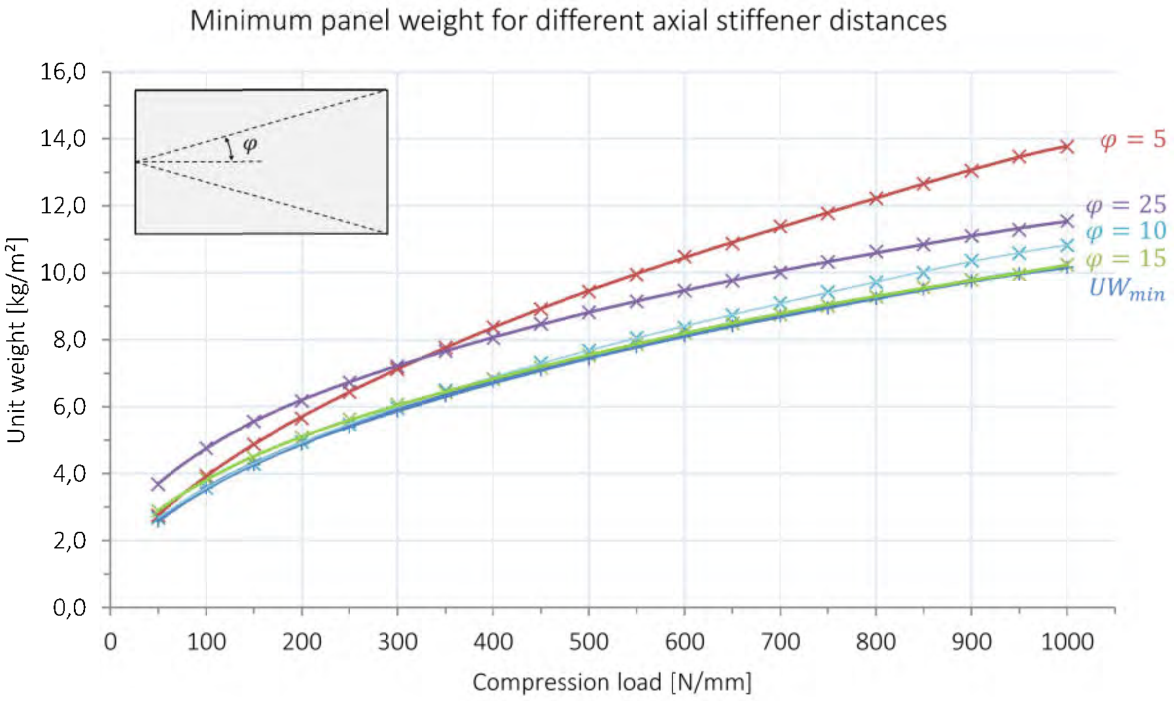

*Figure 57: Minimum Orthogrid panel weight under variation of helical angle*

### Pure Shear

In Figure 58, the minimum weight curve for the flat Orthogrid panel is shown under pure shear. The curve progression is linear except at a very low load level. The sizing of the Orthogrid panel for pure shear appears to be quite 'artificial' because the stiffeners are not directly loaded by the shear load. They only contribute to the global stability of the plate. Resultantly, it can be seen that there are no MoS curves for local stiffener stability or stiffener strength. As the stiffeners are not strength-driven at all they result, in addition, with high slenderness (see Figure 59).

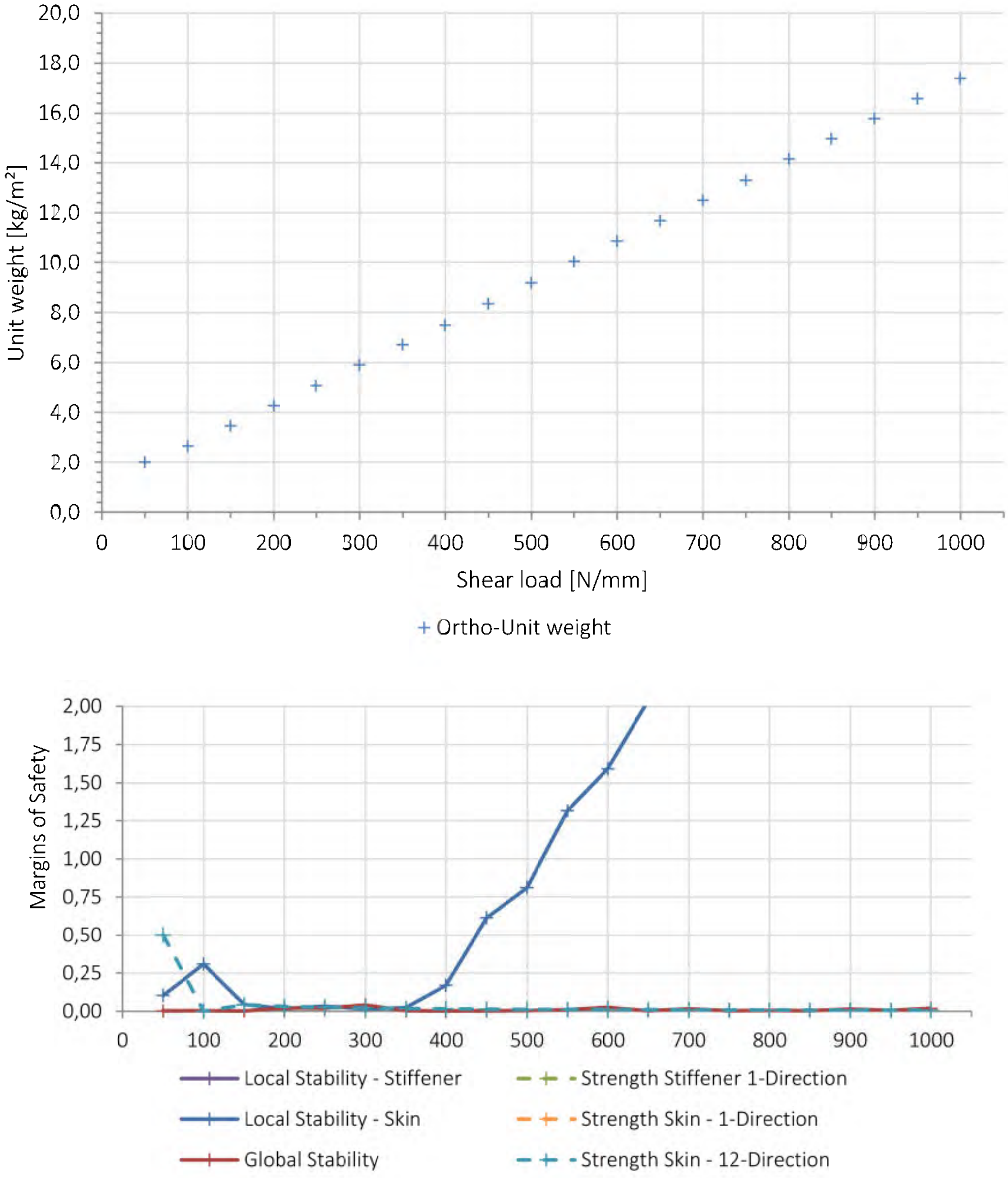

*Figure 58: Orthogrid flat panel shear results; above: minimum weight; below: margins of safety*

Nevertheless, this result is seen to be meaningful in a basic manner and in context with the additionally calculated combined load cases. However, if the pure shear result would give a fundamentally different solution than the combined load cases, this result would be doubtful.

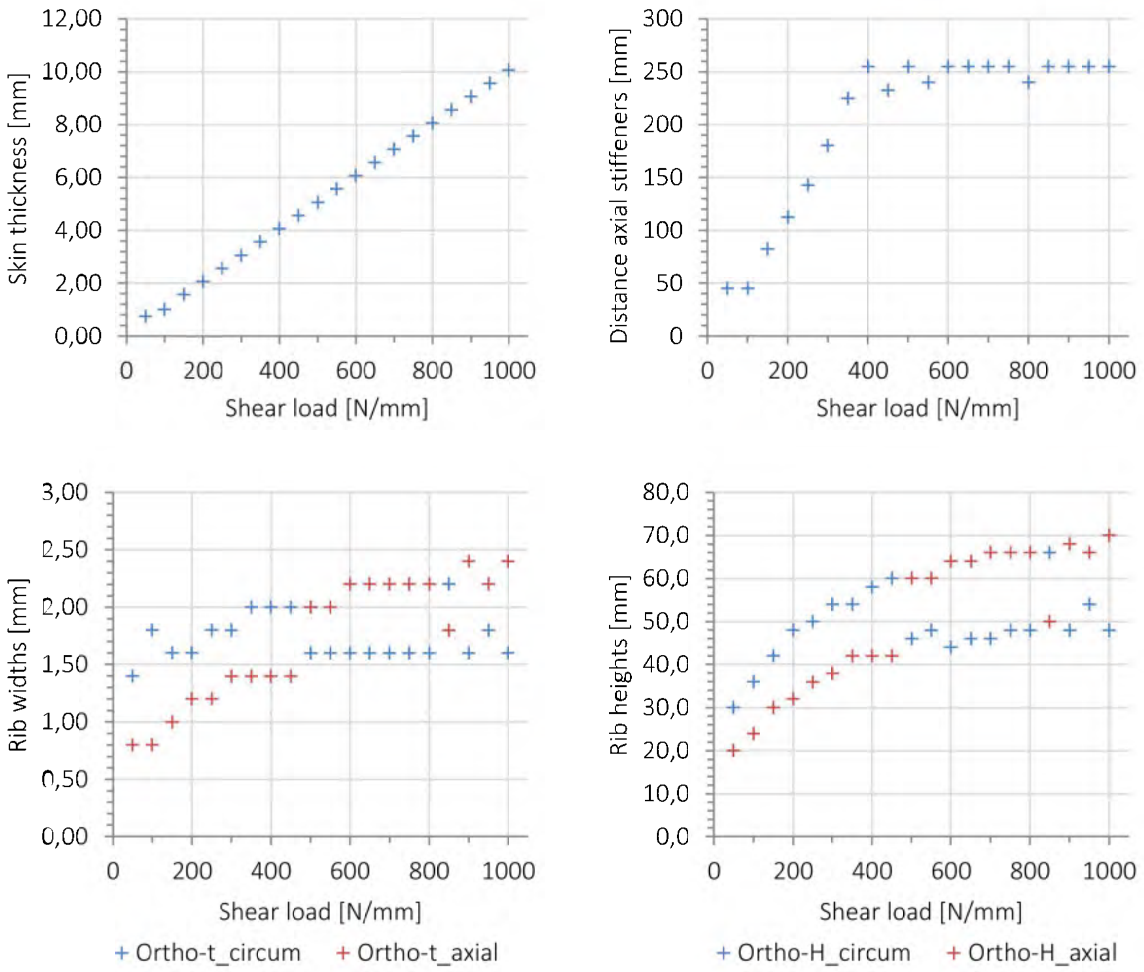

*Figure 59: Variable results for shear – Orthogrid flat panel*

An interesting effect can be observed in the diagrams of the rib widths and heights. In general, two curves are visible in both diagrams, whereby the circumferential and axial variables are shaping alternately these two curves. This results due to the effect that the maximum stiffener distance is fixed to 250 mm which is also the distance of the circumferential stiffeners. For the quadratic unit cell in combination that the stiffeners are not sized to strength or local stability, it makes for the sizing algorithm no difference as to whether the shear load is applied from 'one or the other' side.

### *Combined Compression and Shear*

The combined load case with the same amount of compression and shear is plotted in Figure 60. The unit weight curves for the other two cases are given in the appendix B.3.3.

The curve progression is quite similar to the pure shear result of an Orthogrid panel and differs due to its nearly constant linear progression to the characteristic of an Anisogrid panel under combined load.

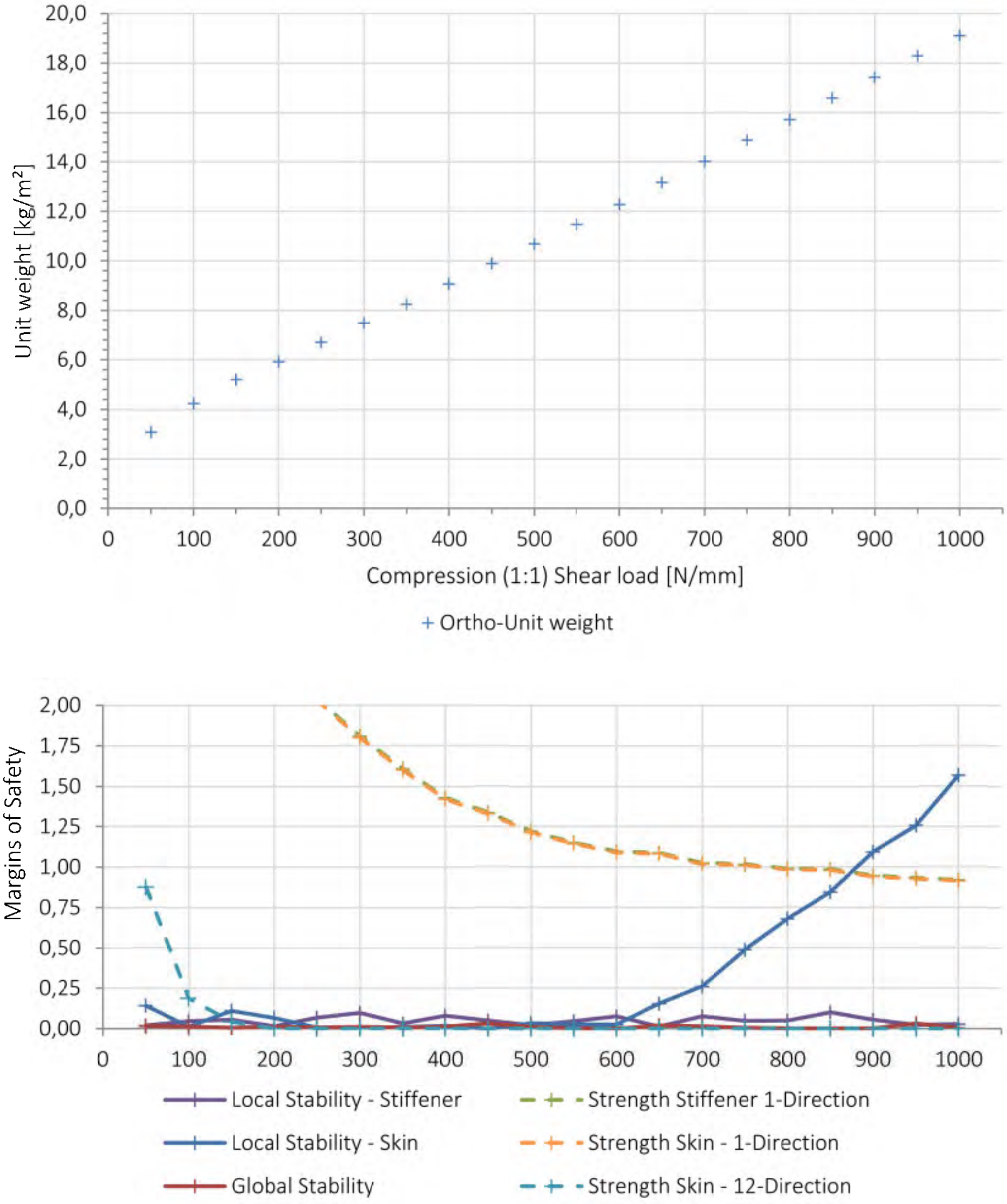

*Figure 60: Orthogrid flat panel compression 1:1 shear load combination*

In contrast to the pure shear load case the compressive strength criteria of the stiffener and the skin can clearly be seen as relevant but not design-driving, which are still the panel and local skin-bay stability and shear strength of the skin. From the point when the maximum stiffener distance is reached, the skin stability criterion can no longer be minimised.

### 6.3.2 Curved Panel Results

#### *Uniaxial Compression*

The minimum weight of the curved Orthogrid panel under compression shows similar to the curved Anisogrid panel two areas of curve progression. In the first region between 50 and 700 N/mm, the curve increases degressively and changes into a nearly linear progression at higher loads. This again matches with the strength criteria which start to dimension the panel structure from 700 N/mm.

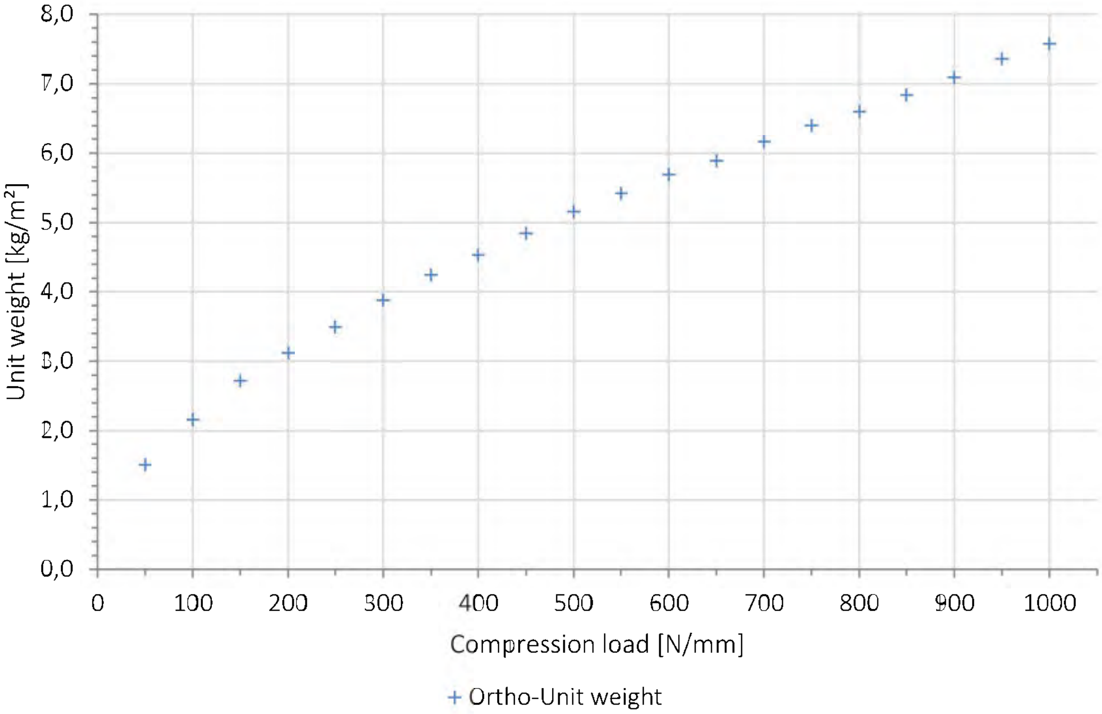

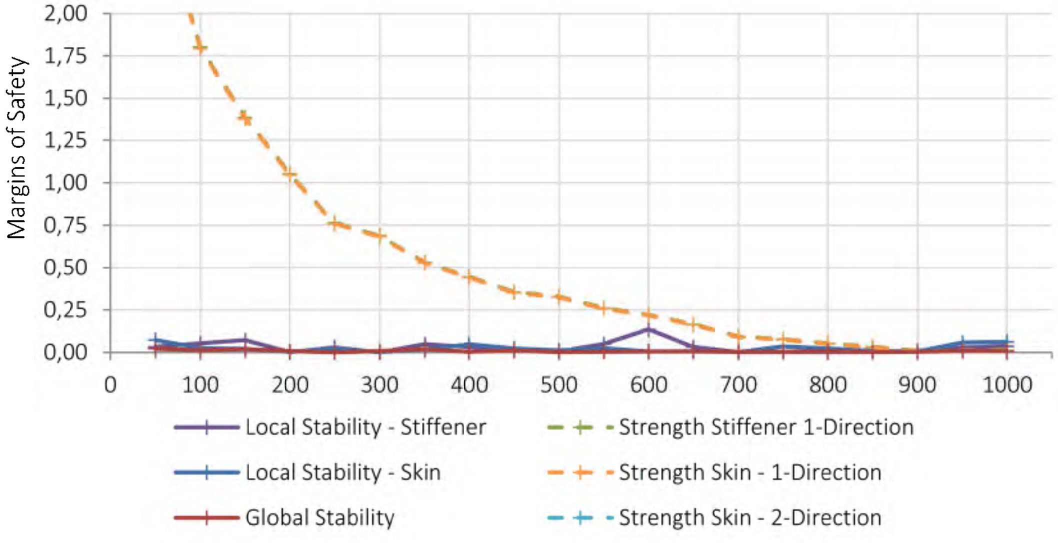

*Figure 61: Orthogrid curved panel sizing results; above: minimum weight; below: margins of safety*

The diagrams in Figure 62 show the results of all variables. The two zones can be observed when the stability-driven structure turns into a strength-driven structure. The skin thickness and the distance of axial ribs stay constant as it is more effective to increase the cross-section of the stiffeners in contrast to thicken-up the skin because in parallel the stability capabilities of the panel are also increased. With a constant skin thickness, the distance of the axial stiffeners stay constant, too, because of the local skin-bay buckling criteria.

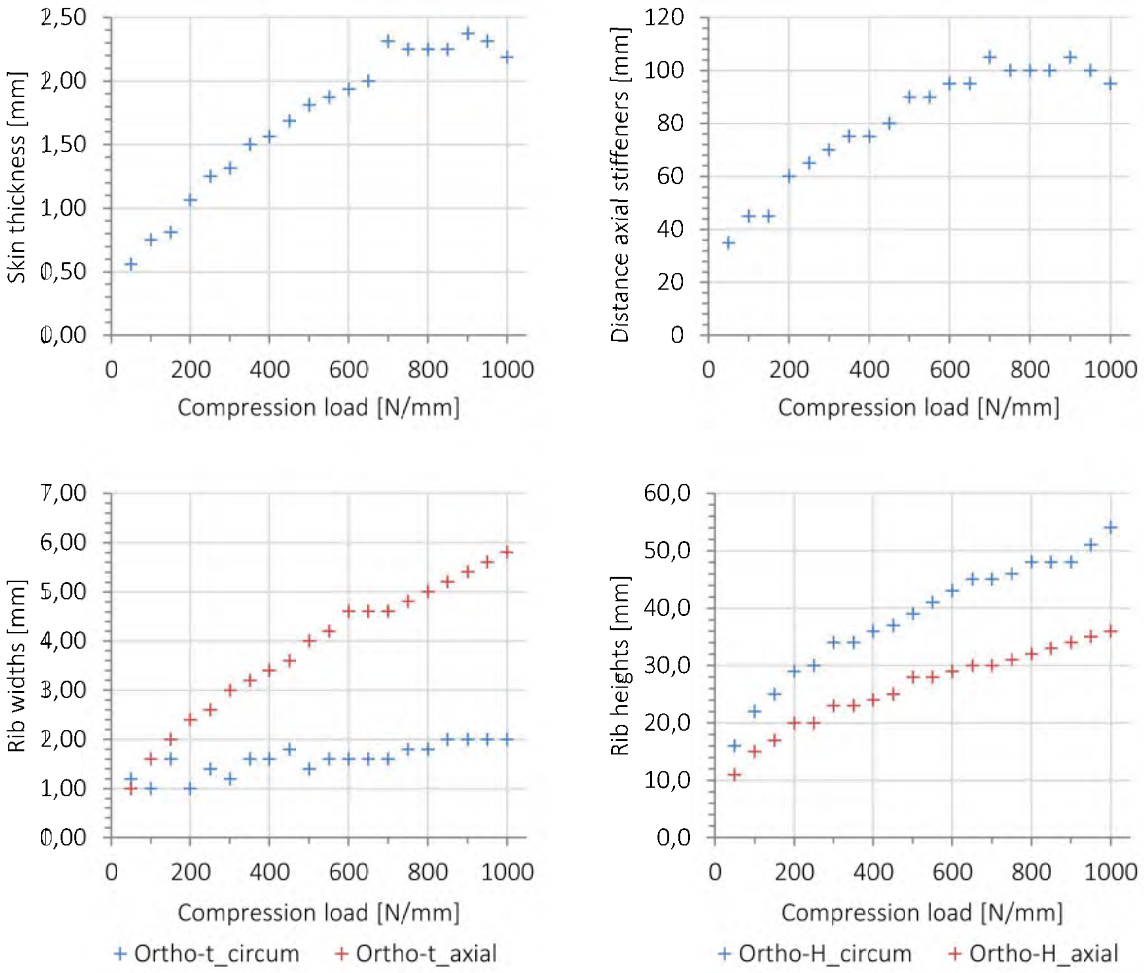

*Figure 62: Variable results for compression – Orthogrid curved panel*

### *Pure Shear*

The minimum weight curve for the curved Orthogrid panel under pure shear is shown in Figure 63. The curve progresses linearly and quite similar to the flat Orthogrid panel under pure shear, which could be expected.

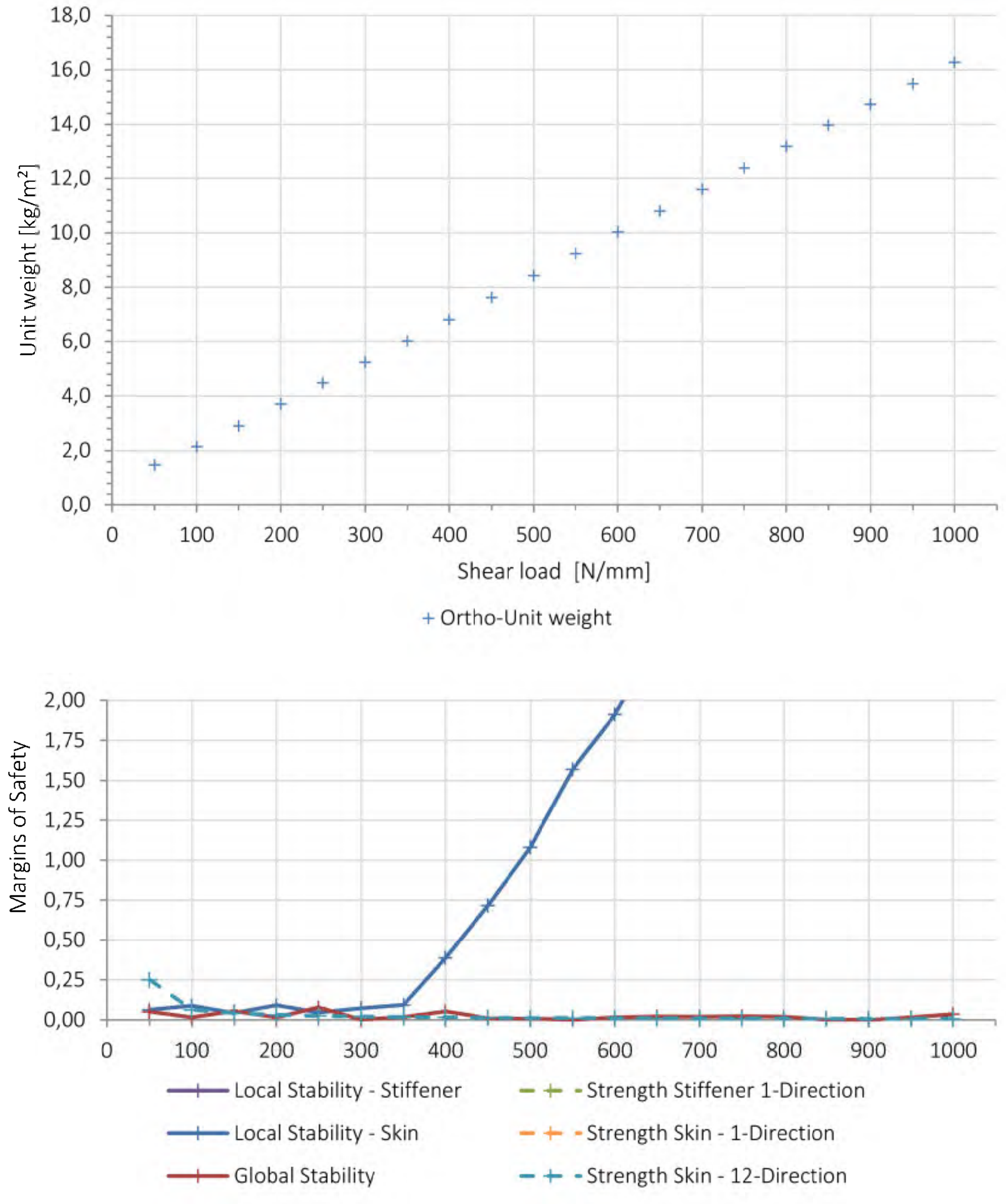

*Figure 63: Orthogrid curved panel sizing results; above: minimum weight; below: margins of safety*

The MoS-curves, presented in Figure 63, have the same character as the flat Orthogrid panel. The stiffeners are not strength-dimensioned at all, as they are not directly loaded. The only difference, which can be observed between the Anisogrid and Orthogrid, is that for the Anisogrid curved panel the strength MoS seems to be shifted to the left. This cannot be observed between the curved and flat Orthogrid panel.

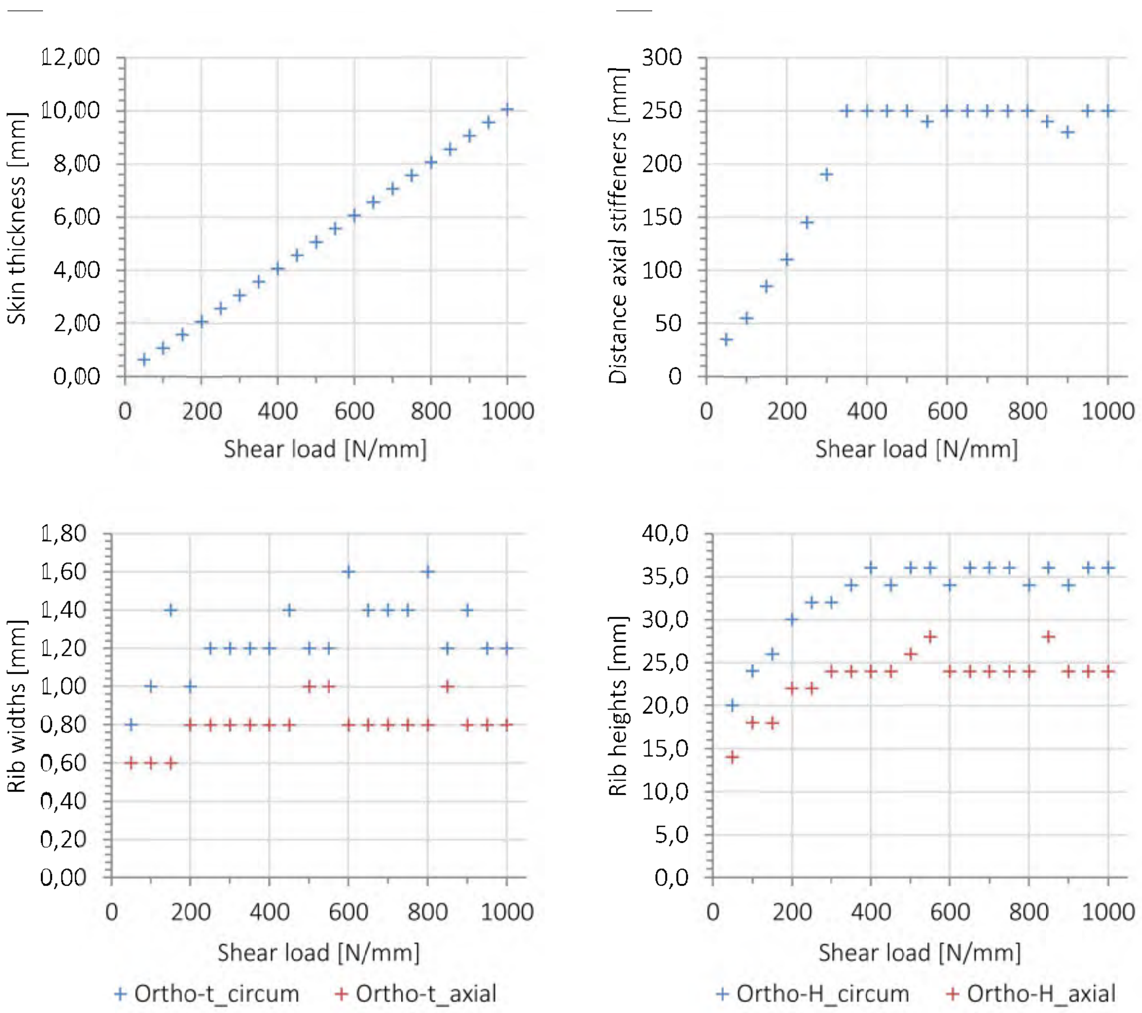

*Figure 64: Variable results for shear – Orthogrid curved panel*

The panel results of the sizing variables are plotted in the diagrams of Figure 64. A mixture of the rib widths and heights do not occur as it is observed for the flat Orthogrid panel under pure shear. The single curvature of the plate prevents this effect due to the stabilising of the panel only in one direction.

### *Combined Compression and Shear*

The results for the combined compression and shear are plotted in Figure 65. Similar to the previous sections, the other two compression-shear combination results are attached in B.3.4.

The minimum weight curve has similarly to the flat Orthogrid panel the characteristic of the shear loading, which means it is nearly linear. Most critical are the local stiffener and skin stability, the global panel stability and the skin shear strength. The compressive strength of the stiffener and skin are also of relevance but not critical. Clearly, the load can be seen at which the local skin stability criterion is no longer design-driving, which coincides with reaching the maximum stiffener distance.

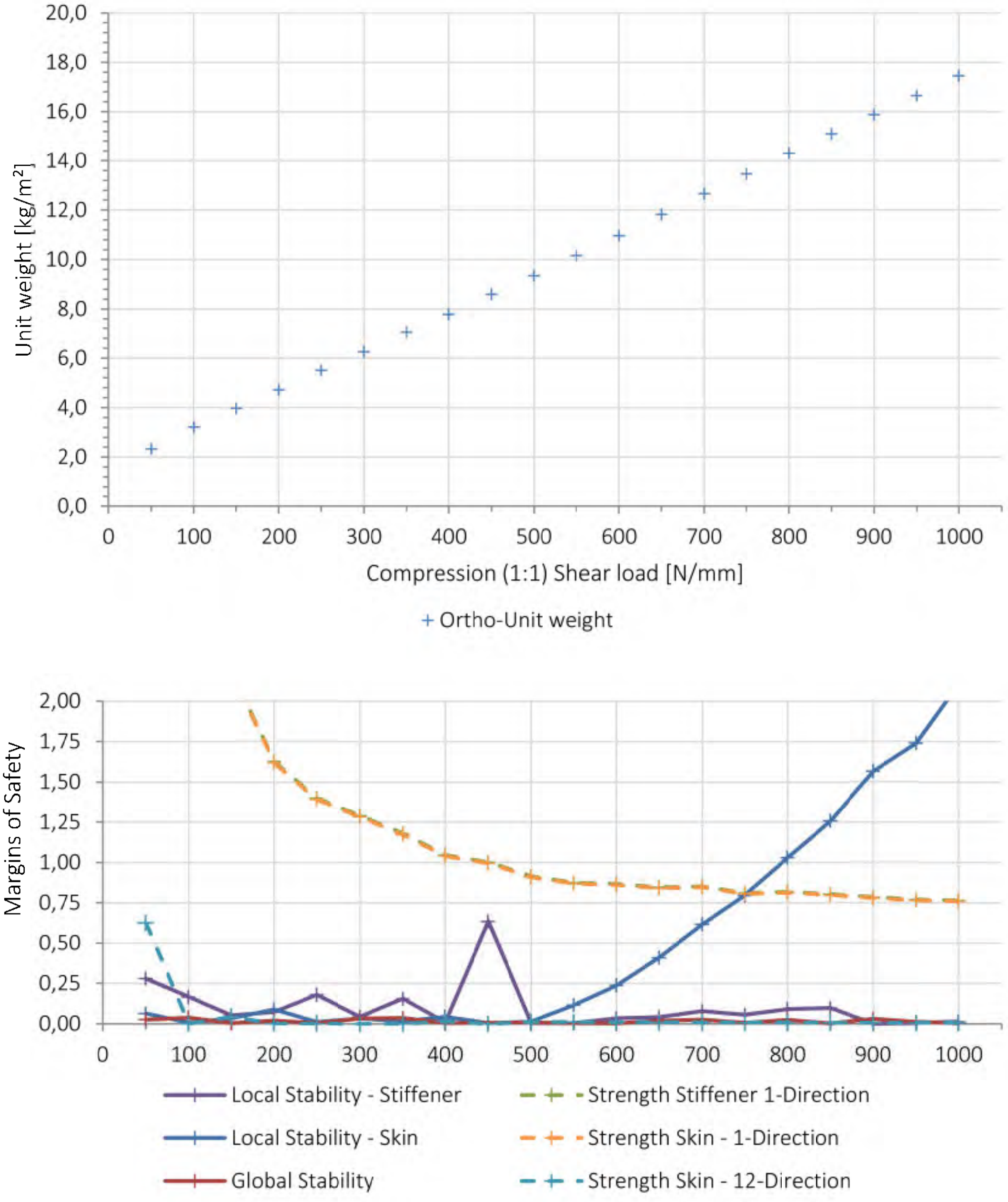

*Figure 65: Orthogrid curved panel compression 1:1 shear load combination*

## 6.4 Comparison of Aniso- and Orthogrid

After the detailed presentation of the panel results for the Anisogrid and Orthogrid panels, the minimum weight curves are compared in this chapter. The results are discussed separately, again divided into the flat and curved panels.

### 6.4.1 Flat Panel Results

#### *Uniaxial Compression*

The diagram in Figure 66 shows the sizing results of the flat panels under compression including the percentage curve of the unit weight difference. The Anisogrid flat panel under compression is, on average, 10% heavier than the Orthogrid panel, considering a no-buckling policy in all elements. This weight penalty is almost constant over the whole investigated load range.

This result is in contrast to the original expectation supported e.g. by the investigation of the local skin-bay buckling coefficient by Weber [94]. On the other hand, it can be seen that the comparison of a fixed aspect ratio of the triangular and rectangular skin-bay, for which also a different number of stiffeners is compared, cannot be transferred directly to a stiffened structure. Consequently, the result of this study strengthens the findings of Klinzmann [45].

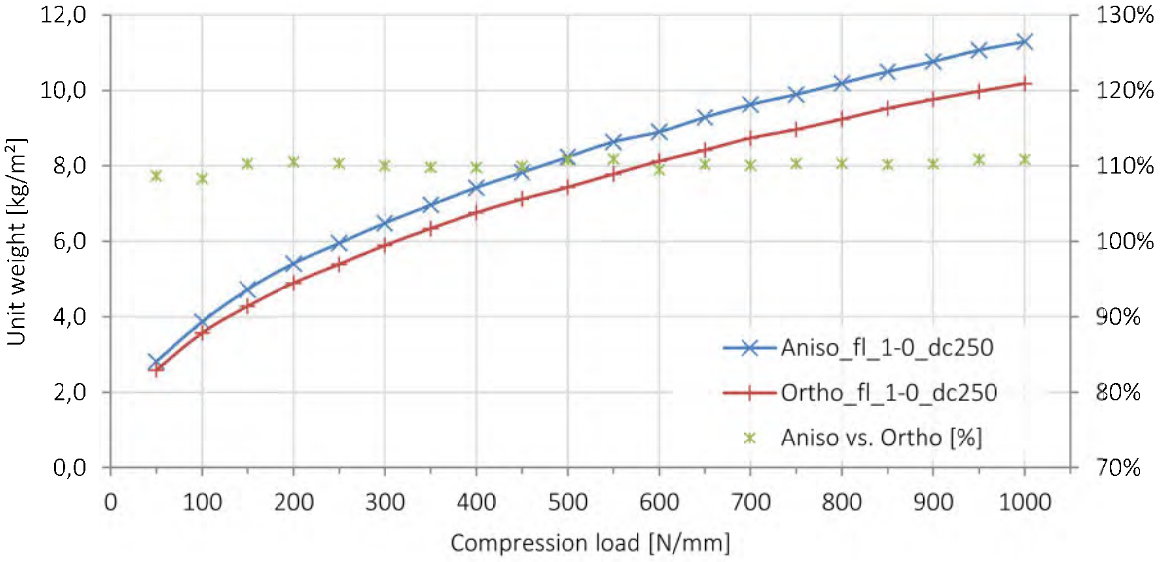

*Figure 66: Comparison of Anisogrid and Orthogrid on flat panel for uniaxial compression*

Comparing the stiffener distances in Subsections 6.2.1 and 6.3.1, it can be seen that on the Anisogrid panel, the helical knots are approximately 1.5 times wider than on the Orthogrid panel. Taking into account that on one Anisogrid unit cell, double the quantity of stiffeners is placed than on the Orthogrid unit cell, the distance of the stiffeners with respect to their quantity is one third smaller than on the Orthogrid panel. As a result, the panels compared in this study, which represent the panels with the lowest panel weight, consist of approximately 1.5 times more stiffeners than the Orthogrid panels. In Figure 67, the sizing results for both 1000 N/mm panels are shown on the same scale. The different quantity of stiffeners can be easily counted along one circumferential rib (horizontally oriented in the figure).

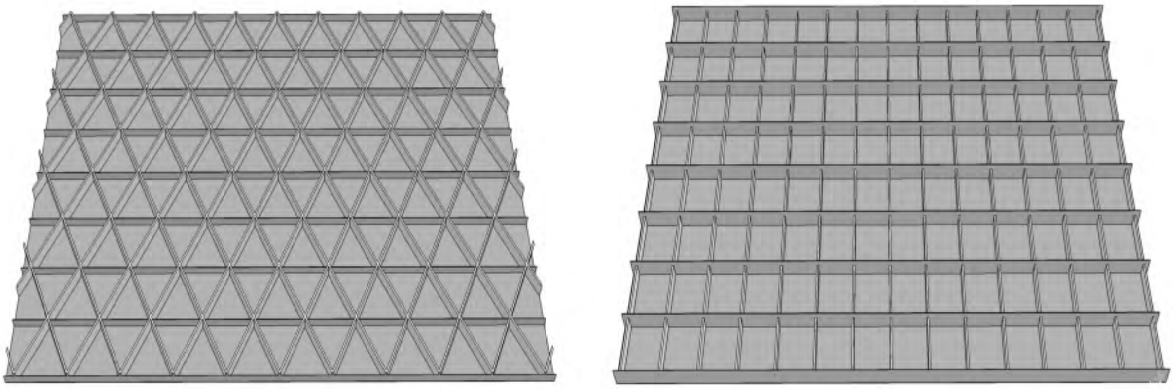

*Figure 67: Illustration of 1000 N/mm compression panels*

### *Pure Shear*

In contrast to the result of the compression load case, the pure shear load result is quite different. There are three zones observable. First the Anisogrid panel has a great weight penalty of approx. 25% at the very low loads. The second zone is a continuous transition between the 25% weight disadvantage to approx. 5% weight benefit in opposite to the Orthogrid panel. This weight advantage is quite constant for the middle and higher loads.

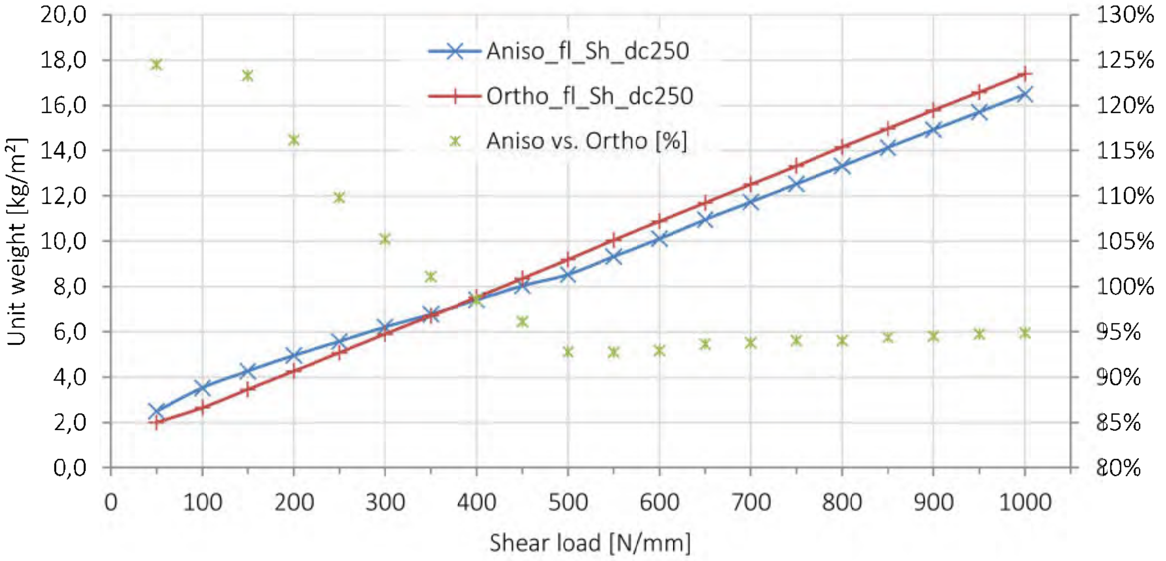

*Figure 68: Comparison of Anisogrid and Orthogrid on flat panel for pure shear*

Comparing this result with the sizing results in Subsections 6.2.1 and 6.3.1 it can be seen that the three zones observed in the sizing match with the zones observed in Figure 68. In the first zone, both panels are stability driven (50 N/mm – 100 N/mm). In this stability driven zone, the Orthogrid benefits significantly, as the stiffeners, which are also present (for global stability), do not need to be sized in terms of local stability as they are not directly loaded. This speciality is not the case for the helical stiffeners. The transition zone where the weight difference constantly decreases, the skin strength criterion is sizing both panels in addition to the stability criteria. Since the helical stiffeners are also handling a specific amount of shear load, they are unloading the skin and the Anisogrid becomes more efficient. In the third zone, where the panels are mainly strength-driven, the Anisogrid achieves constantly the 5% weight benefit by the mentioned stressed helical stiffeners.

### *Combined Compression and Shear*

Following all three results of the analysed compression and shear combinations are presented. In Figure 69, the result of the combination of compression and shear in a ratio of 1 to 0.5 is plotted. This ratio means that at a compression load of e.g. 500 N/mm the panel is additionally loaded with 250 N/mm shear. In Figure 70, the compression shear ratio of 1 to 1 is shown, presenting the case that the same amount of compressive and shear load is acting. This case is described in detail in the Subsections 6.2.1 and 6.3.1. The third analysed case is plotted in Figure 71 where a higher shear force is loading the panel. The ratio of compression is 0.5 to 1 of the shear load. In the diagrams, only the maximum load range is given in numbers on the axis of abscissae.

For the compression-shear ratio of 1:0.5 in general, a weight difference with the characteristic of the compression panel can be observed. There is a nearly constant weight penalty for the Anisogrid panel whereby the amount is even higher with +15% over a wide load range between 50 N/mm and 600 N/mm. For higher loads, this weight penalty decreases to the +10% like seen for the uniaxial compression load case. This result is quite surprising, as it was expected that the helical ribs also carry a certain amount of the shear forces and the Anisogrid becomes lighter. In contrast, exactly this effect leads to the result that the helical stiffeners need to handle more load than the axial stiffeners of an Orthogrid structure and due to the stability driven design, the helical stiffeners need to have higher thickness to prevent local stiffener buckling. From the load level, where the strength criteria become critical, which happens at the high loads, the Orthogrid structure also need additional material for the strength and both designs achieve the same weight difference as for compression only.

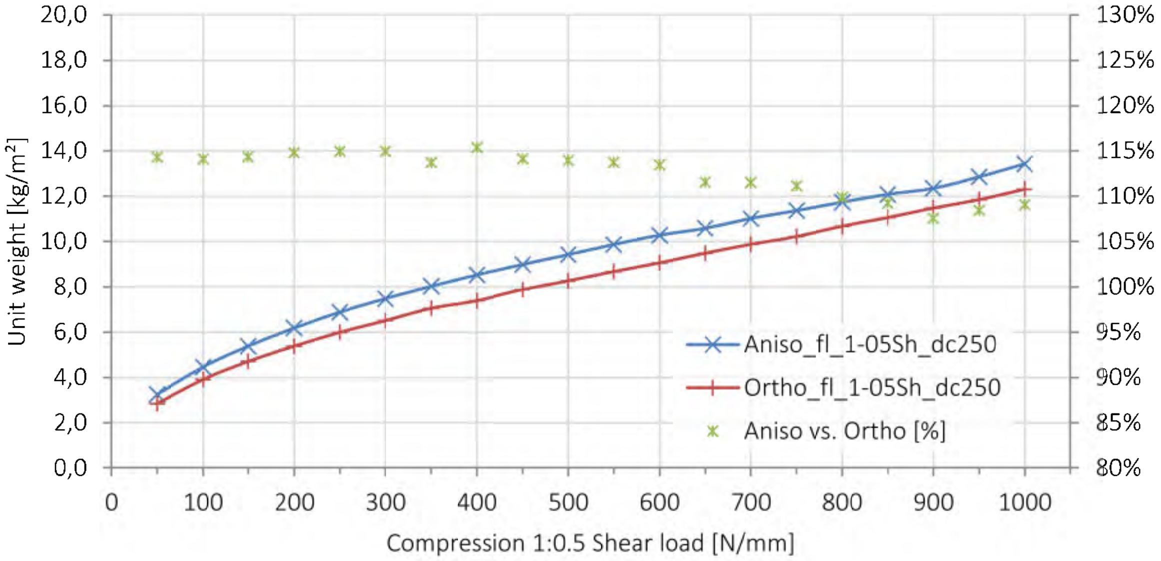

*Figure 69: Comparison of Anisogrid and Orthogrid on flat panel for combination of compression 1:0.5 shear load*

The weight difference result shown in Figure 70 for the combined load case, where the same amount of compression and shear load is applied to the panel, has the same character like seen for pure shear. At very low loads the Anisogrid panel has a weight penalty of up to 20%, followed by a transition zone with decreasing weight difference until the third zone where the Anisogrid panel achieves a weight benefit of constant 5% in opposite to the Orthogrid panel.

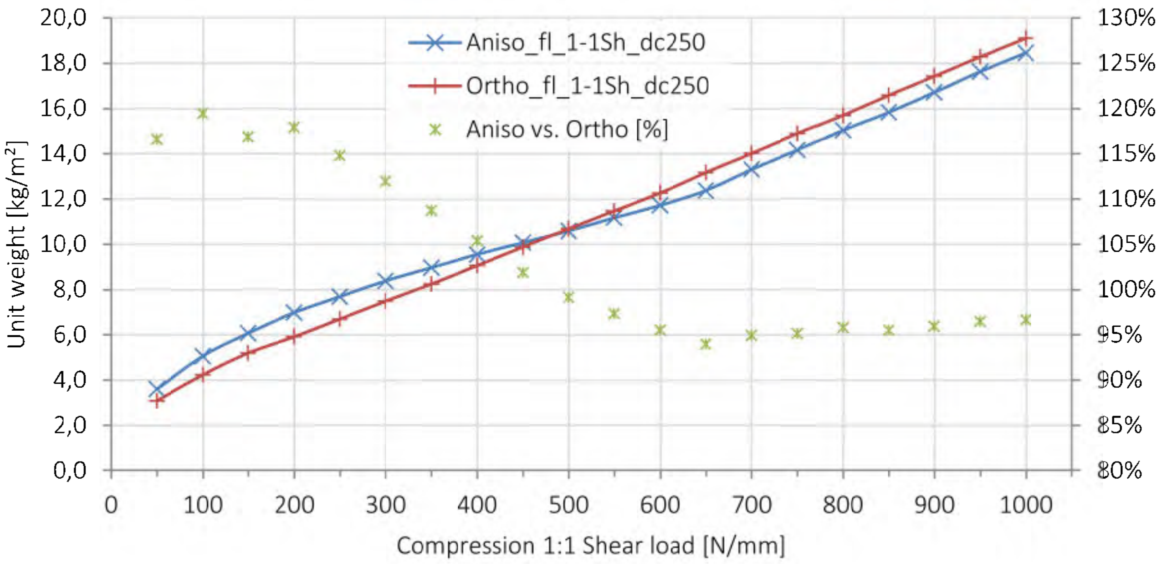

*Figure 70: Comparison of Anisogrid and Orthogrid on flat panel for combination of compression 1:1 shear load*

Comparing the panel results in the Subsections 6.2.1 and 6.3.1 the three zones matches again with the zones identified in the MoS-curves. In the stability driven design, the Anisogrid is less efficient due to the additional stiffener loading and in the strength driven zone the Anisogrid panel achieves a weight benefit.

The same behaviour can be seen for the third combined load case, plotted in Figure 71. In this load case, higher amount of shear load with additional compression load is applied. The weight penalty of the Anisogrid panel is approximately 25% for the very low loads but can achieve almost constant 10% of weight benefit for high load levels, in this case from 600 N/mm and higher.

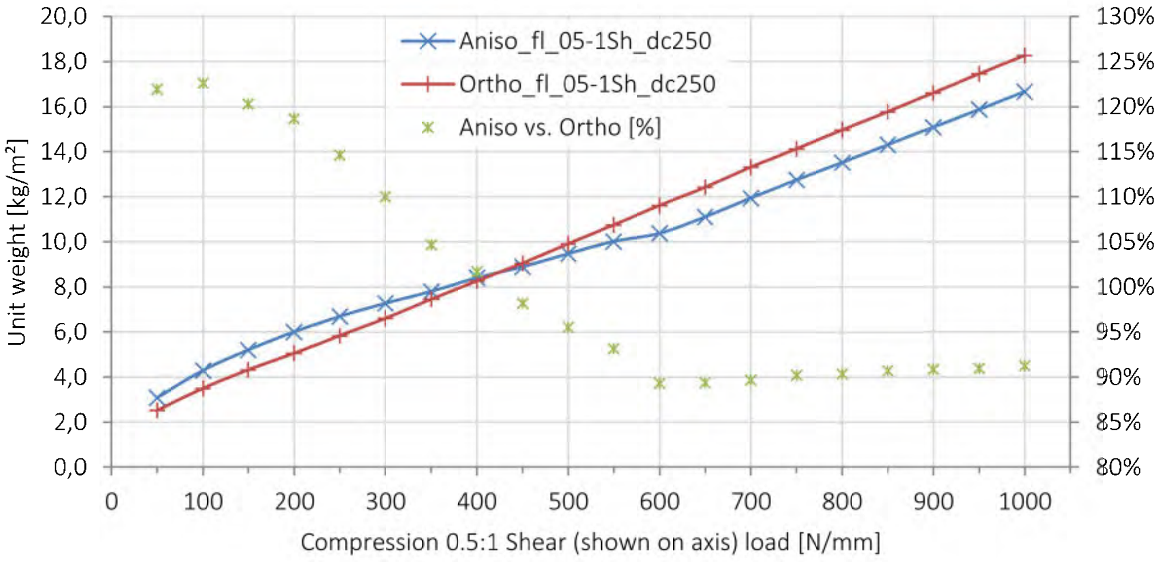

*Figure 71: Comparison of Anisogrid and Orthogrid on flat panel for combination of compression 0.5:1 shear load*

### 6.4.2 Curved Panel Results

#### *Uniaxial Compression*

The diagram in Figure 72 shows the comparison of the Aniso- and Orthogrid panel under uniaxial compression. Similar to the flat panel result, the Anisogrid panel is heavier under compression fulfilling a no-buckling policy for all elements. The difference is, however, lower and decreases constantly from 107% at low to 100% at high load levels.

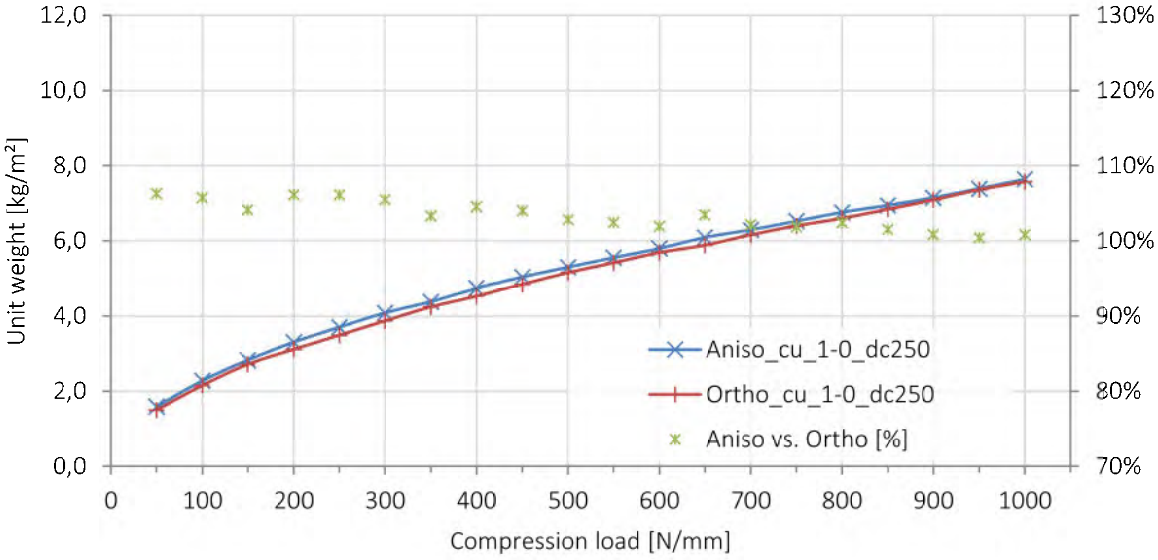

*Figure 72: Comparison of Anisogrid and Orthogrid on curved panel for uniaxial compression*

Due to the curvature, the global panel stabilisation seems to superimpose the other sizing criteria in the way that, as a result, both architectures achieve nearly the same minimum weight, particularly at higher loads. It can also be noted that the absolute weights of the curved panels are significantly lower than the flat panels.

#### *Pure Shear*

The characteristic of the weight difference curve for the curved panels under pure shear is similar to the flat panel result (see Figure 73). The curve consists of a transition zone where the maximum weight penalty of +25% for the Anisogrid panel constantly decreases to the zone where a nearly constant weight benefit of -2% to -3% is achieved for the Anisogrid panel. This is less than for the flat panel (approx. -5%).

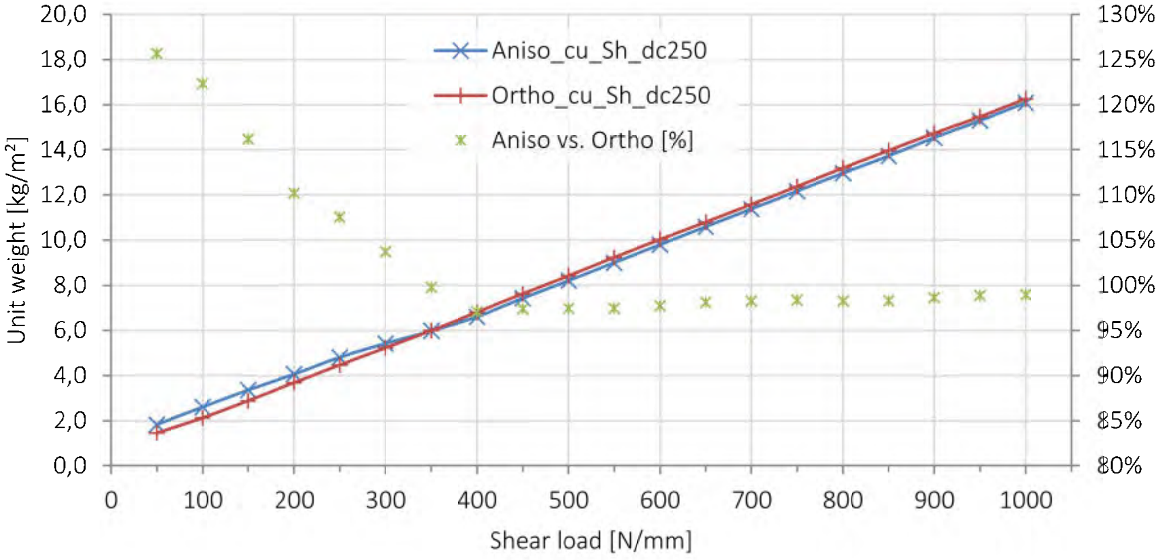

*Figure 73: Comparison of Anisogrid and Orthogrid on curved panel for pure shear*

In comparison to compression, where the weight difference between the flat and curved panel changes positively for the Anisogrid, this is not the case for shear. On the other hand, it is noted that on the curved panel both architectures are reaching simply the same minimum weight (considering higher loads).

### *Combined Compression and Shear*

Similar to the results for the flat panel, also for the curved panel three combined load cases are analysed and presented following.

In Figure 74 the combination of compression and shear is plotted whereby the compression load is shown on the axis of abscissae and half of the amount is additionally applied with shear. Similar to the result on the flat panels it can be said that in general a weight difference occurs like seen at compression and the Anisogrid has a +15% weight penalty in opposite to the Orthogrid structure.

The progression over the load range is slightly different. Achieving the minimum of +10% on the flat panel at the highest analysed load, on the curved panel this is only the case at a load level of 600 N/mm. The difference again increases afterwards for higher loads.

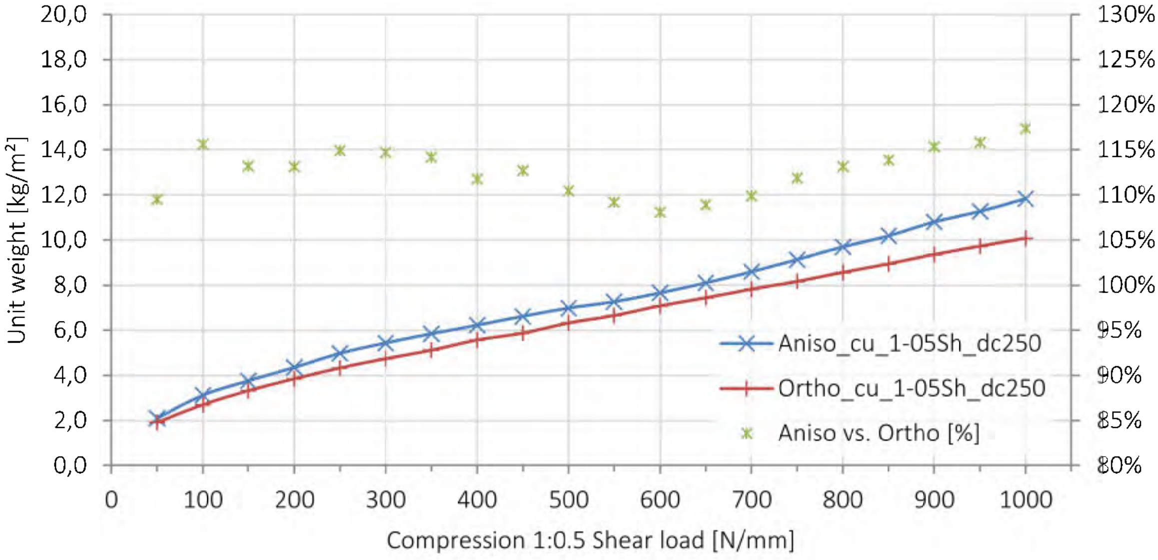

*Figure 74: Comparison of Anisogrid and Orthogrid on curved panel for combination of compression 1:0.5 shear load*

The results for the equally compressive and shear loaded panels are presented in Figure 75. For this load case, the shear characteristic can be seen again. At low loads the Anisogrid panel is with +20% less efficient. This weight penalty decreases to around zero when both structures are mainly strength driven (considering the MoS curves in Subsections 6.2.2 and 6.3.2).

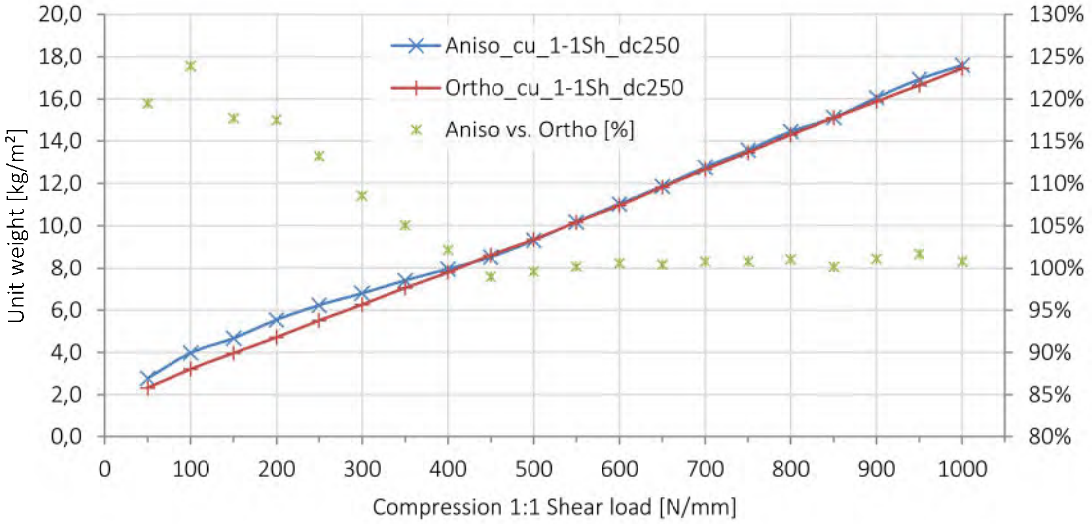

*Figure 75: Comparison of Anisogrid and Orthogrid on curved panel for combination of compression 1:1 shear load*

The diagram in Figure 76 shows the result of the shear load dominated curved panels. For this load case, the panel is applied with shear load, plotted on the axis of abscissae. Additionally, compression is applied with half of this amount. The characteristic shear curve progression can also be noted for this load combination. The difference is that the curve is shifted downwards. First, the Anisogrid has a weight disadvantage of approx. 18% decreasing to a weight benefit of almost constant 5% for load levels of 500 N/mm and above.

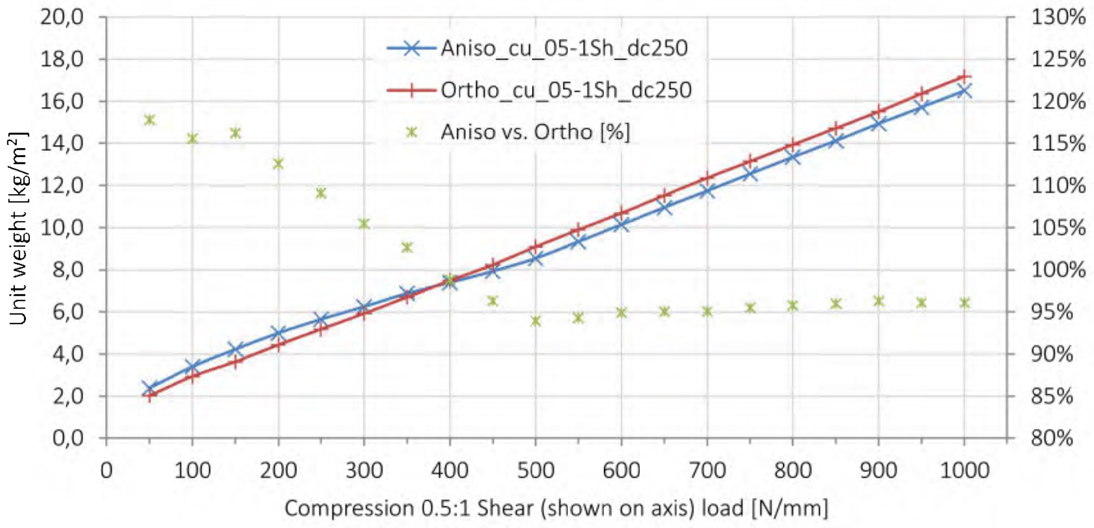

*Figure 76: Comparison of Anisogrid and Orthogrid on curved panel for combination of compression 0.5:1 shear load*

## 6.5 Discussion

The two diagrams of Figure 77 plot the obtained maximum and minimum values of the weight difference curves to get a brief overview about the flat and curved panel results. It can be noted that the achieved values are comparable between the flat and curved panels. The maximum values, which occurred constantly at the low load levels, rise with additional shear load achieving the maximum at pure shear with almost the same magnitude. The minimum values are also quite similar in terms of their progression but have different values. For the flat and the curved panels, it can be stated that the Anisogrid is less weight efficient at high compression load ratio, whereby the compression-dominated combination with additional shear is the worst case. The highest weight benefit for the Anisogrid structure is obtained in the shear-dominated combination with additional compression while only at middle and high load levels.

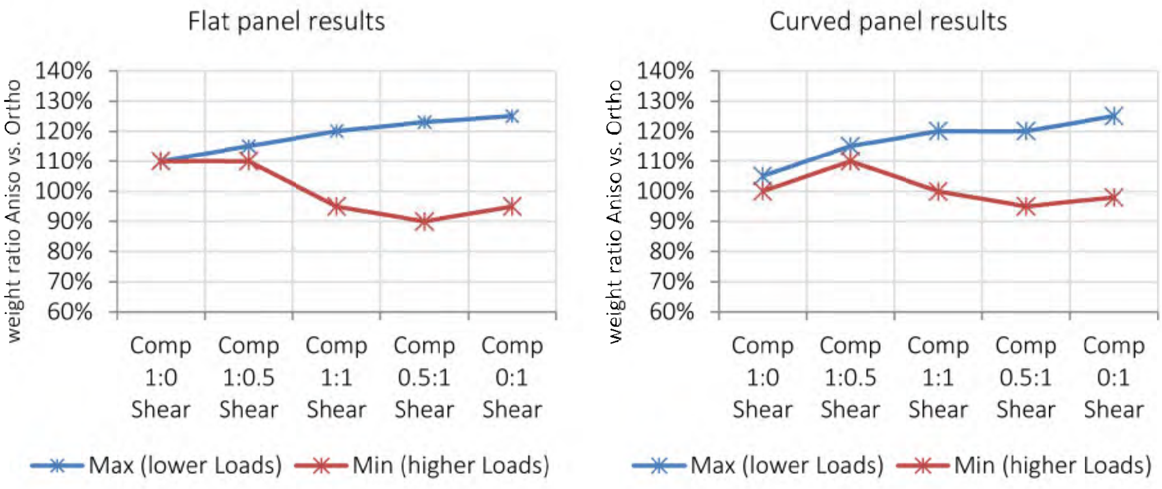

*Figure 77: Overview of Max and Min values occurred in the weight difference curves*

## 6.6 Summary of the Aniso- and Orthogrid Sizing Results

Summarising the sizing results, the compression load case is noted to be purely stability driven, which is especially the case for the flat panel over the whole load range. For the curved panel, the strength is additionally critical at higher loads.

As a result, a 10% weight increase is calculated for an Anisogrid structure under uniaxial compression on the flat panel. For the curved panel (R=2000mm), the weight penalty is lower between 6% for low loads and almost the same weight for high compressive loads.

The pure shear load case is, in contrast, a strongly strength-driven load case. Particularly for the Orthogrid structure, the stiffeners are only required for global stiffness, whereby this stiffness is also generated for middle and high loads by the skin. Resultantly, the algorithm is trying to eliminate the stiffeners and the results are running into the defined maximum stiffener distance. For the Orthogrid panel, this behaviour was expected, but the Anisogrid panel also showed the same response which leads to the conclusion that the helical stiffeners are not as efficient for shear as they seemed to be.

Regarding the combination of compression and shear loading, differentiation is necessary due to the fact, that as long as the panel is stability driven, the Anisogrid architecture has an even higher weight disadvantage of up to 25% in comparison to an Orthogrid structure, whereby this only occurs at very low loads. With rising load levels and resulting critical strength criteria, the Anisogrid architecture generates a weight benefit of between 5% and 10% on a flat panel and up to 5% on a curved panel (R=2000mm).

# 7 Validation of Anisogrid-Concept with Panel Compression Test

*Thesis 4: Anisogrid structures with interface layers are able to generate a reliable connection of the grid and skin, even during a deep buckling state.*

In literature, different tests on panel and on barrel level show the separation of the rib structure and the skin as the main global failure mechanism [19, 22, 24, 28]. As a result, the use of interface layers is seen to be essential for the connection of the rib structure with the skin, especially in a post-buckling state, and the thesis 4 is formulated. Peeling stresses rise drastically when the skin starts to deform locally between the stiffeners. After a first failure of the interface, the crack subsequently grows and the skin separates largely from the rib structure. After loss of integrity, the structure fails globally. To overcome this failure mode, the Anisogrid structural concept contains interface layers which connect the skin and the ribs as shear loaded element. The large connection areas on the rib sides and the skin surface should ensure a necessary shear area. The panel test is intended to validate the functionality of the interface layers.

*Thesis 5: Anisogrid structures with triangular skin-bays show a post-buckling behaviour without mode-switches which is different to stiffened panels with rectangular skin-bays.*

In numerical investigations on panel level, a different post-buckling behaviour is observed for triangular stiffened panels in comparison to rectangular stiffened skin structures [93]. A post-buckling state in this case means the compressive load range at which the skin between the stiffeners begins to buckle until the (first) maximum of compressive load is reached. During this load range, the load-bearing capacity of the panel increases further, even though the skin is buckling locally in the skin-bays. Under dependence of, amongst other aspects, the stiffness distribution between the stiffeners and the skin, such post-buckling state can be quite long until the global panel failure occurs. During such a post-buckling state of a classical rectangular skin-bay, different local buckling patterns can occur. Quasi-isotropic skin laminates with an aspect ratio (skin-bay length divided by skin-bay width) higher than 1 typically start with small local buckles, which move and combine into bigger local buckles. This behaviour is called mode-switch in the buckling state. In literature, mode-switches are described as dynamic processes which are difficult to simulate and therefore critical for sizing [11, 21]. The occurrence of mode-switches depends on various factors such as aspect ratio of the skin-bay, stiffness matrix of the skin laminate, boundary conditions by surrounding stiffeners, and also the global panel behaviour. In triangular stiffened Anisogrid panel designs, such a mode-switches are not seen in numerous numerical simulations carried out at DLR [93], which led to thesis 5. A local skin-bay buckling pattern occurs under a compressive load and stays constant until the global stability failure of the panel. To validate this observed behaviour, a panel test is designed, performed and analysed.

The derived failure stresses in Chapter 4 are used for the panel sizing. However, it has to be recognised that global bending deformations will be caused by the eccentricity on the one-side-stiffened panel. As a result, the maximum stresses at the compression and tension side of the bended structure are analysed for sizing with the static test results.

In summary, three main goals are defined for the panel test:

- Validation of functionality of interface layers
- Validation of missing mode switch during the post-buckling state
- Comparison of failure strength on panel level with strength out of element tests

In general, it should be noted that although a wide experience basis is available for panel compression testing of classically stringer stiffened panels [16, 23, 70, 97, 98], little experience is available with Anisogrid stiffened structures. A pure diagonal stiffened panel was tested in an European research project [47] but with different dimensions and without interface layers. As a consequence, the testing procedure, load levels and, especially, the failure behaviour of such panels are analysed during this test.

To investigate the test goals, it seems most suitable to size a kind of “generic” panel adapted to the desired buckling behaviour and the joining between the skin and rib interface, instead of sizing a specific fuselage load level. Therefore, a very early skin-bay buckling load shall be designed with respect to the maximum panel failure load due to global buckling or strength. The possible switch of buckles can be proven as well as the ability of the interface layers to keep the skin attached, even at high deformation levels of the buckling skin.

In order to conduct a valid panel test, a load state possibly free of boundary effects shall be designed to ensure the test objectives. Therefore, several skin-bays in compression direction and also in transverse direction are envisaged, as well as several grid ribs running from one end of the panel to the other.

## 7.1 Sizing of Anisogrid Test Panel

In order to transfer the test objectives into sizing criteria, the following objectives are defined:

- Skin-bay buckling very early below stiffener strength and global panel buckling
- Stiffener strength failure defines the limit load (strain sizing limits from knot tests)
- Skin strength failure at limit load or higher (data sheet values)
- Global panel buckling after limit load (particularly for flat panels critical)
- Stiffener buckling after limit load

### 7.1.1 Analytical Pre-Sizing

The analytical pre-sizing is also carried out with the method used in Chapter 5, whereby the sizing process does not include the interface layers. As a consequence, the pre-sizing can only be seen as first stage and the verification and refinement by FEA is required additionally.

In difference to the panel analysis in Chapter 5, limitations need to be considered due to the laboratory manufacturing process and the test facility:

- Panel width maximum 1000 mm (test facility)
- Panel length limited to 1200 mm including potting length on both ends (test facility)
- Due to handling reasons and the number of individual tool parts a minimum distance of helical knots of 150 mm seems to be suitable
- A flat panel with equal height for all ribs - to keep the costs for the tooling and manufacturing in certain limits has been defined.
- Available slit tape width: ¼” resp. 6.35 mm ➔ rib width is fixed

- The skin laminate shall be quasi-isotropic 25/50/25 (0°/±45°/90°) ➔ strong limited quantity of possible stackings considering a single ply thickness of 0.13 mm
- Different configurations of load cells are used in the test facility. Due to reduction of measurement mistakes, it is recommended to keep the desired load analysis between 0 kN and 500 kN (load cell configuration No.1) or between 500 kN and 1000 kN (load cell configuration No.2) ➔ measurements out of these ranges result in higher measurement mistakes or damage of the load cells

Under consideration of all requirements and limitations, the design space for the panel is quite restricted. The rib height, rib angle, and in some extend the skin thickness are left as main design variables. The result for the panel dimensions are listed in Table 6.

*Table 7: Dimensions of Anisogrid test panel*

| Parameter | | Value | Unit |
|---|---|---|---|
| Rib width (net, w/o interface layers) | t_h | 6.35 | mm |
| Rib height (net) | H | 18.0 | mm |
| Interface thickness (max) | t_I | 1.2 | mm |
| Interface feet length | L_I | 10.0 | mm |
| Skin thickness | t_s | 1.04 | mm |
| Distance of circumferential Ribs | d_c | 300 | mm |
| Angle of Helical Ribs | ϕ_h | 15 | degree |
| Panel Length | a | 1020 | mm |
| Panel width | b | 770 | mm |

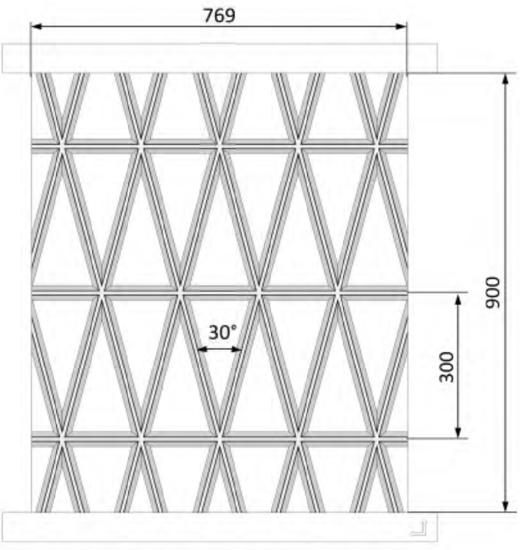

## 7.1.2 Numerical Test Verification

As already mentioned, the numerical analysis is carried out in addition to the analytical sizing. The reason for this is that the influence of the interface layers can be analysed in the required detail. The numerical analysis is set up as shell-element model for the skin and grid structure and a geometrical non-linear analysis is carried out. Step-by-step the axial compression load is applied to the numerical model, whereby the panel deformation is calculated and the basis for the next load-step. Motivation for the non-linear analysis is to investigate more accurate the panel deformations and stiffness change in the post-buckling state. Additionally, the manufacturing induced imperfection in terms of a global panel deformation can be included into the analysis. The numerical model and analysis are not part of this thesis and are discussed in detail by Wagner and Niemann in [57]. However, the result is also plotted in the Section 7.4.

## 7.2 Manufacturing of Anisogrid Test-Panel

The manufacturing of the Anisogrid Prepreg Design Concept is intended to be highly-automated by the Automated Fibre Placement process (AFP). As this process is not state-of-the-art, because of the high required accuracy for the placement of the cut layers and even more the placement of the interface layers, the manufacturing of the test panel is carried out manually.

The tool is designed similar to the descriptions in Subsection 4.1.1, which means that a metallic base tool is used with thermally expanding tool parts generating the grooves and the compaction of the prepreg material from the sides. Instead of highly elastic materials, aluminium cores are positioned on the plate made from steel. The different geometric thermal expansions are simulated and adapted to the final dimensions at the resin's curing temperature.

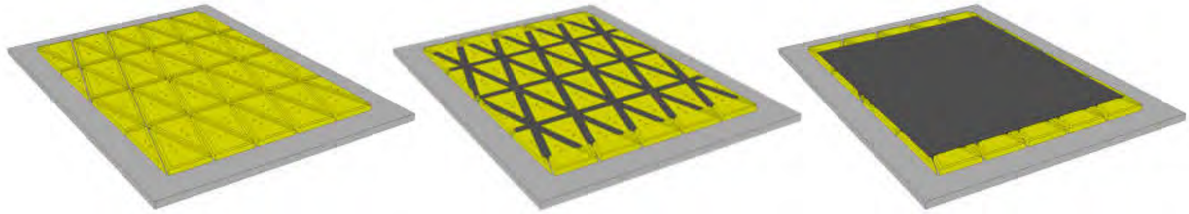

*Figure 78: left: multi-core manufacturing tool; centre: placed grid structure; right: skin on top of grid structure*

In Figure 78, the procedure of the manufacturing process is shown. On the negative multi-core tool (see Figure 79) the grid structure is placed via prepared slit tape stripes and interface layers followed by the application of the wet skin laminate for a co-curing process.

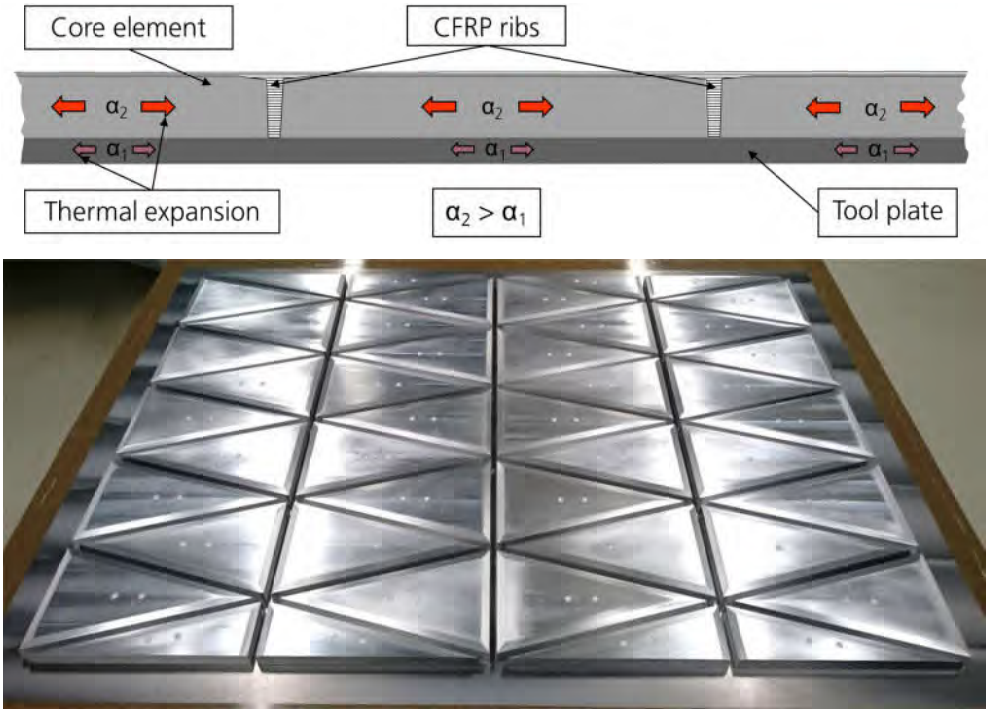

*Figure 79: Above: Tool concept of expanding tool cores, below: manufactured aluminium tool*

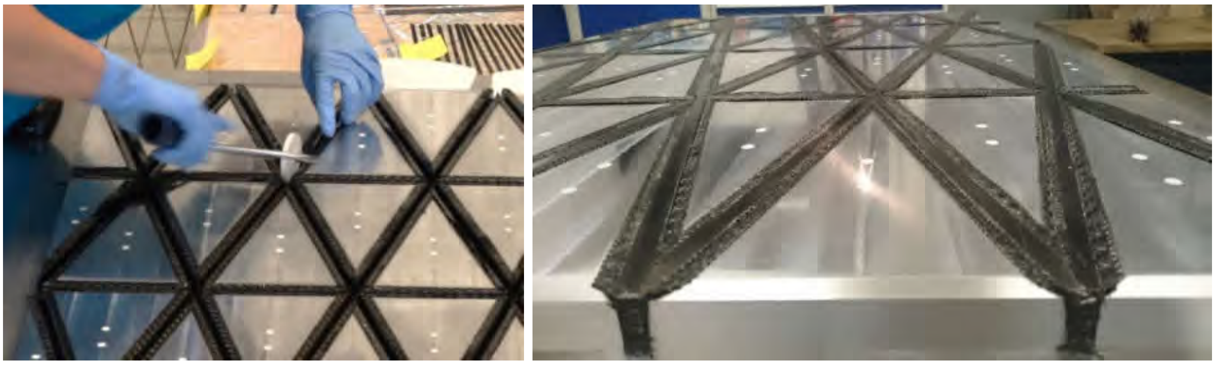

*Figure 80: left: manual roller compaction tool; right: smooth rib structure after last compaction step*

Similar to an automated process, roller tools are used by hand for placement of the rib layers into the grooves (see Figure 80). After intermediate compaction steps the skin can be placed directly on top of the rib structure laminate and co-cured in one step.

The photos in Figure 81 show the manufactured test panel after demoulding. The quality of the panel fully met the expectations in terms of geometrical accuracy and laminate quality. The entire rib structure including the co-cured skin is fully consolidated with matrix. No dry or bleed areas are observed. In particular, the visible first interface layer aligns as desired and no fibre wrinkles or other disturbances are observable.

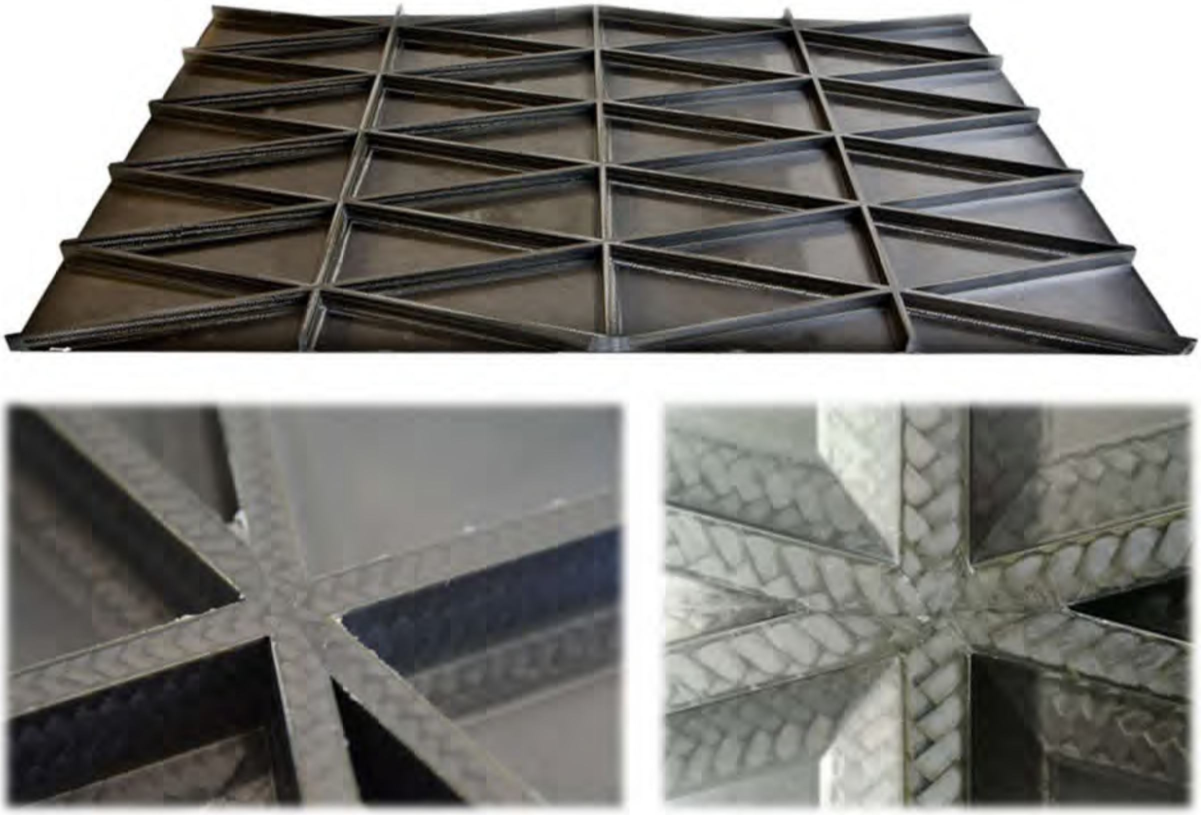

*Figure 81: Demoulded Anisogrid test panel with co-cured skin*

### Geometry Check

The comparison of the CAD-model with an optical 3D surface scan show that a global manufacturing-induced deformation of the panel occurred. Reason is seen in the eccentric panel design of the stiffeners on only one side of the skin. After co-curing, the skin shrinks on the whole area and the local stiffeners are limiting the shrinkage on only one side. Resultantly, the deformation is constantly like the panel is bent over a large spherical (a radius of 33000 meters can be fit into the skin curvature) whereby the stiffeners run on the outside. For the finally trimmed and tested panel, which is shown with dotted boundary lines in Figure 82, a maximum deflection of 3.5 mm is measurable in the centre of the panel.

The dimensions of the helical ribs (height and width) and the skin thickness match well with the CAD-model. Only the width of the circumferential ribs (horizontal ribs in Figure 82) is constantly 0.5 mm wider than in the CAD model. Reason is the non-considered compensation of the thermal expansion of the steel basis plate. As undesired this deviation is, the load direction is perpendicular to these ribs and the effect to the test is seen as negligible, whereby the numerical model is adapted accordingly.

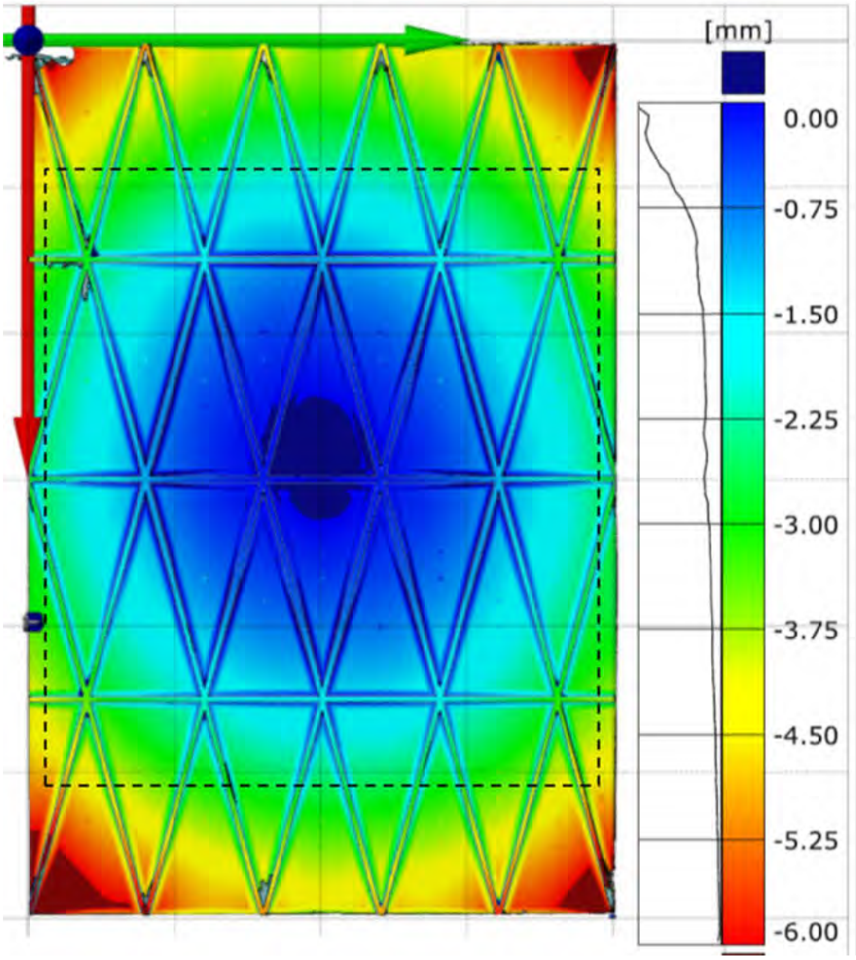

*Figure 82: Optical dimension measurement of manufacturing induced global panel deformation*

## 7.3 Static Uniaxial Compression Test

### 7.3.1 Test Facility and Setup

For application of the desired compressive load into the test panel, the top and bottom edges are potted to create stiff and defined boundary conditions. These potted edges are milled at the top and bottom faces to generate parallel surfaces in the tolerances of the CNC machine. After this milling an additional step is performed at which the panel is potted in two stages into the load application rigs of the test machine. This extensive procedure has proved to generate a constant load application into a test panel.

A flat test panel without additional lateral edge support tends to buckle globally like a panel stripe lowering or even without previous skin-bay buckling. Therefore the test rig is extended with two guiding profiles at the panel sides to avoid the out-of-plane deformation (see Figure 83, right). It is of special interest for these guiding profiles that they might start to work as axial stiffeners due to their high stiffness. As a consequence, the supports are mounted with transition fit to the panel edge. They prevent the out-of-plane deformation (uz=0) and as they are also formed like clamps the rotation around the side edges (urx=0). This approach has been proven on previous compression tests on the mentioned diagonal stiffened panel.

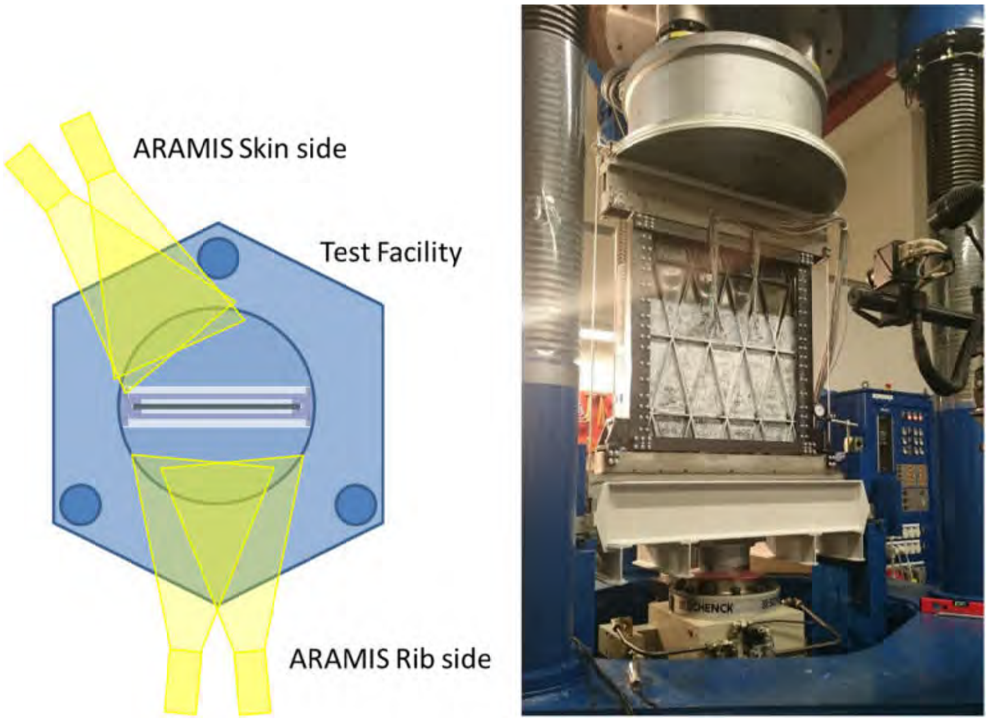

*Figure 83: Anisogrid test panel in test facility*

Thirty-nine strain gauges are used on the rib and skin side. In the upper half of the panel four helical and one circumferential rib are measured on the rib and skin side with unidirectional strain gauges. Five skin-bays are measured with strain gauge rosettes (0°, 90°, 45°) on the rib and X-Y strain gauges on the skin side.

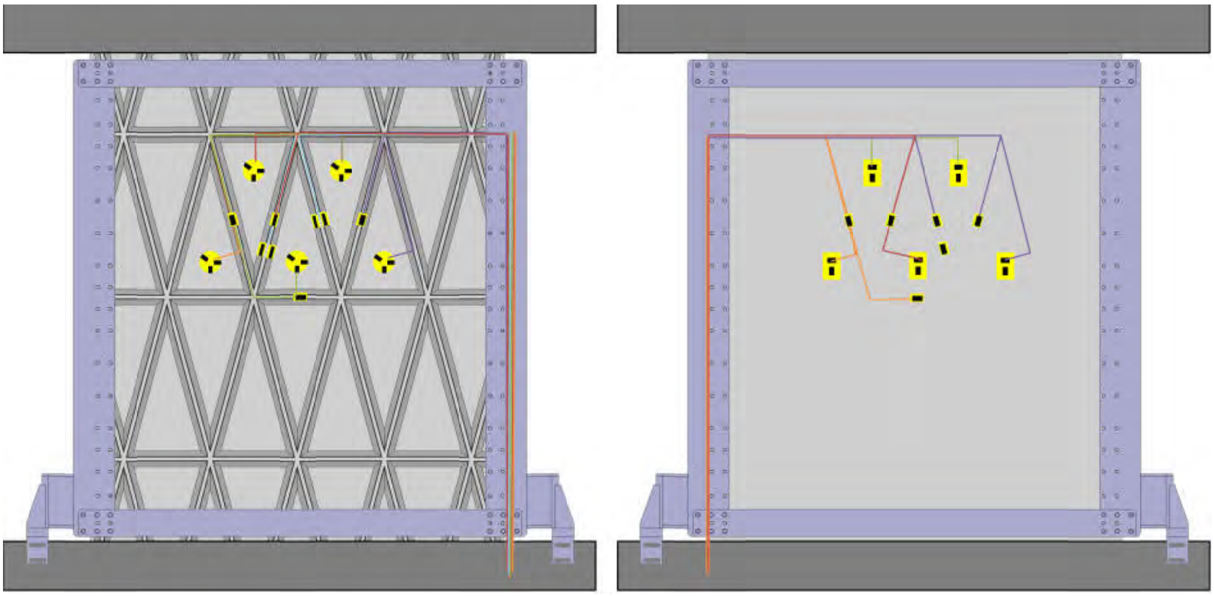

*Figure 84: Positions of strain gauges*

In addition to the strain gauges two optical DIC measurement systems (see appendix D.2) are used for both panel sides. The rib side is measured with a very fine contrast pattern and a high resolution as it is tried to analyse the ribs and skin-bays in detail. The skin side of the panel is measured in full dimension with a course contrast pattern because the pixel number is limited and has to be adapted to the maximum picture dimension.

### 7.3.2 Test Procedure

For the investigation of the post-bucking behaviour and the interface layers, the procedure is split into three main phases. Within the first phase a low level loading is applied to check the functionality of the entire testing rig and the panel stiffness. This step can be seen as standard procedure for panel tests. In the second phase, a specific compression test series is conducted. In several steps, the panel is loaded to a specific load level and fully unloaded again. The background is to proceed cautiously to achieve the load level at which the first skin-bay buckling occurs. After every load step the out-of-plane deformations are checked with DIC measurements.

Knowing the skin-bay buckling load, the elastic post-buckling range is investigated similarly. In several load steps, the compressive load is increased achieving a higher post-bucking state. The last, third phase appears when the panel is loaded until the global failure of the structure occurs. Particularly, when a structure is tested in a new configuration the second and third test phases are difficult to predict exactly before the test. Resultantly, the testing team monitors continuously the load-displacement progression and listens to occurring crack noises. The team decides during a load-step of the second test phase as to whether they unload the panel again or the final test is performed because a clear crack noise was audible.

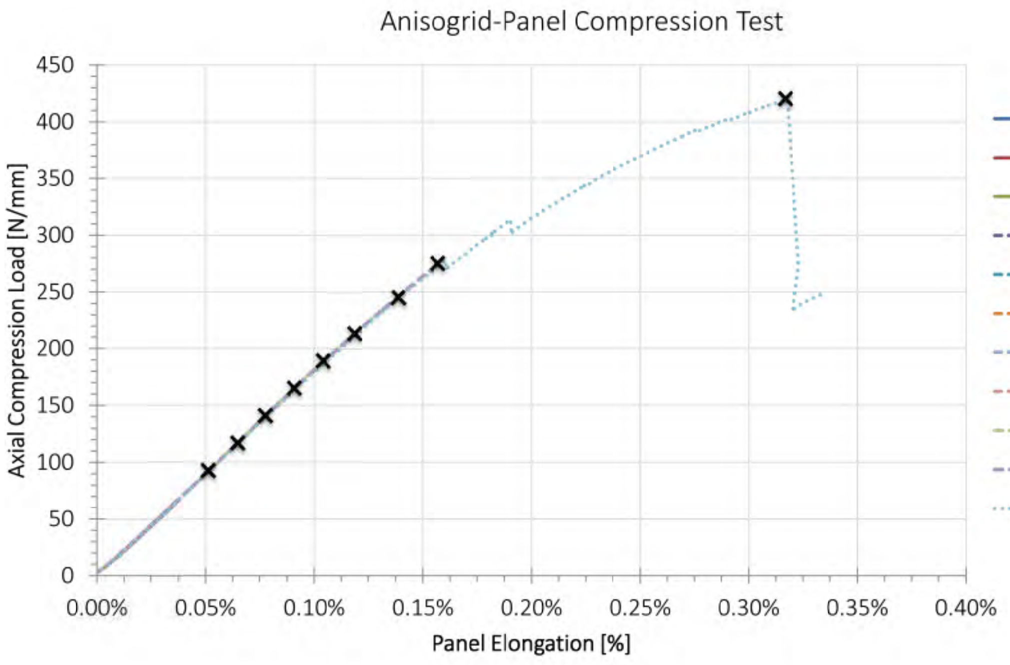

*Figure 85: Load-elongation-curve with test procedure steps*

The diagram in Figure 85 represents the mentioned load steps by X-marks in the load-displacement curve of the test panel (the load-elongation curve is attached in C.1). The stiffness test is repeated three times with the lowest load level of 50 kN (65 N/mm). Subsequently, the compression load is increased in 20 kN steps (26 N/mm) until a load level of 150 kN (195 N/mm) is reached. Afterwards 30 kN steps are conducted. At the eleventh load step the first failure occurred at approximately 218 kN (283 N/mm) together with a clear audible crack noise and drop in the load-displacement curve, and the compression load is increased until the global panel failure of 322 kN (419 N/mm).

## 7.4 Test Results

The first ten compression load steps represent the elastic load range of the panel. All load-displacement curves lie on top of each other and no change in the panel stiffness is observable (see Figure 85). Local skin-bay buckling is monitored at approx. 120 N/mm (see Figure 86), which is higher than the analytical (95 N/mm) but matches well with the numerical model. The difference of the analytical solution can be found in the non-considered interface layers, which are stiffening the skin-bay.

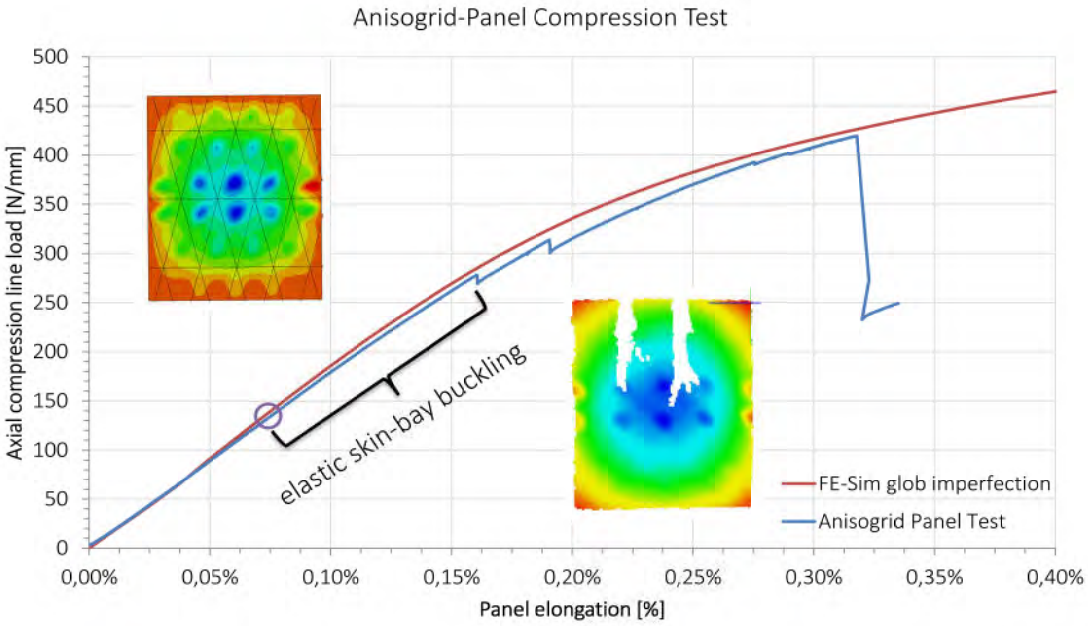

*Figure 86: Load-elongation-curve; elastic skin-bay buckling state; simulation picture above left; DIC measurement picture in the centre*

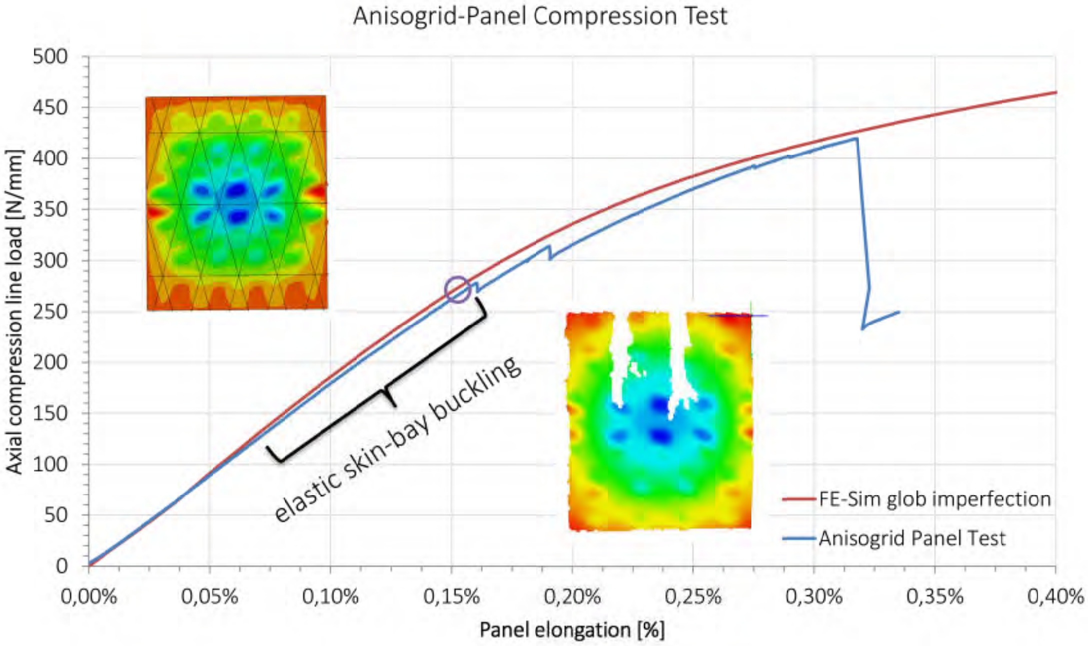

*Figure 87: Load-elongation-curve; elastic skin-bay buckling state; simulation picture above left; DIC measurement picture in the centre*

The buckling pattern is stable for more than twice of the local skin-bay buckling load (see Figure 87). This behaviour can be observed in all tests from No. 6 to No. 11 showing that this post buckling state is elastic and could be reached in several steps without change of the panel behaviour or stiffness (in C.3 DIC pictures at different load-steps are shown).

The first failure occurred in test No. 11 at approx. 280 N/mm when the skin peeled off the grid structure at the centre left edge of the panel. The second failure appeared at approx. 318 N/mm when the skin also separated from the grid on the right centre edge of the panel (compare the two load drops in Figure 87 after elastic skin-bay buckling). In contrast to other tests from literature, further load could be applied. These two failures remained locally and the skin-rib-separation does not grow further, which is deduced especially through the ultrasonic inspection results after the test.

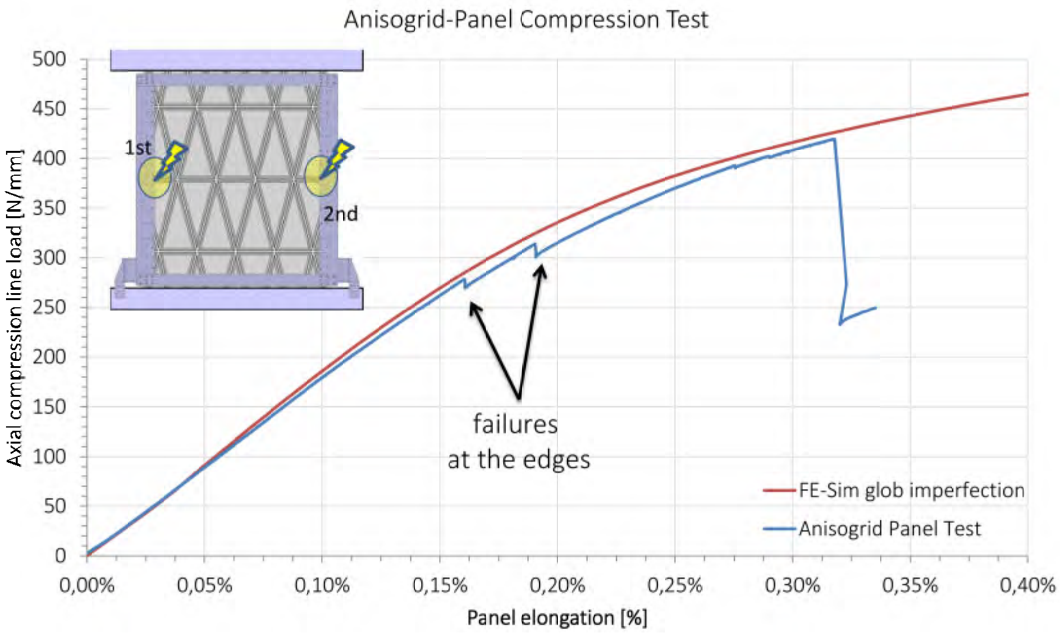

*Figure 88: Load-displacement-curve; $1^{st}$ and $2^{nd}$ local skin separation*

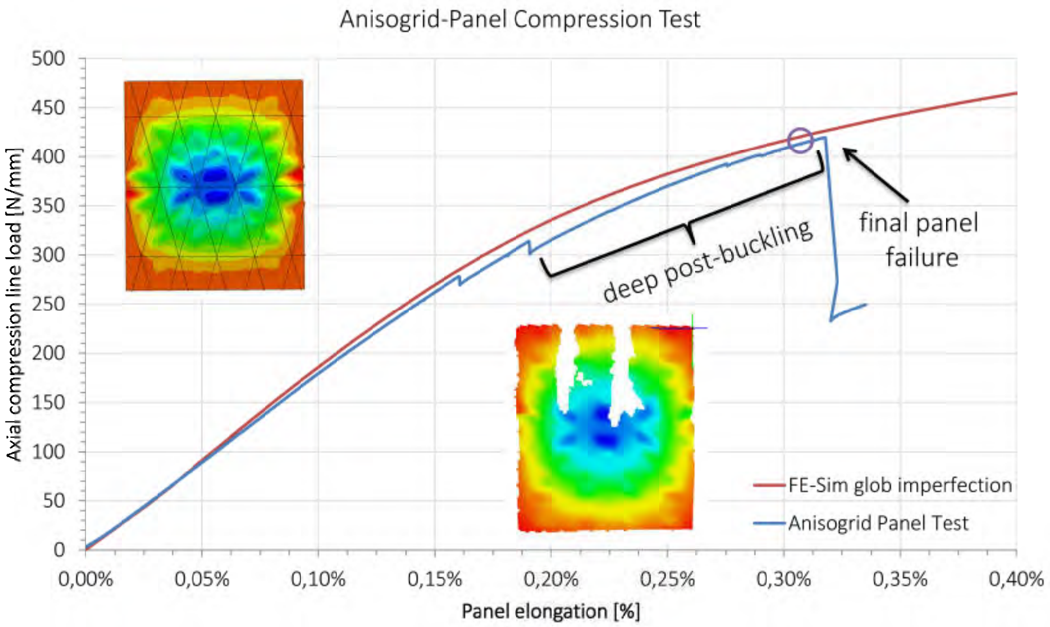

*Figure 89: Load-Displacement-curve: deep post-buckling state and final failure; simulation picture above left; DIC measurement picture centre picture*

After these two cracks/delamination at the panel sides, a stable deep post-buckling behaviour follow until the collapse at a load level of about 418 N/mm (see Figure 89). The local buckles increase drastically, and due to the additional high global deformation the skin-bay buckles start to deform in the direction of the panel centre. Impressively, the numerical model shows a concordant deformation; compare the FE and DIC pictures in Figure 89.

At final failure, the panel breaks in the middle, starting from the right side (looking towards the rib side) and proceeding to approximately three-quarters of the panel width, until the machine stopped compressing. Figure 90 shows the test panel after final failure at the displacement position when the machine stopped the test (panel is not unloaded). After final failure, a wrinkling deformation can be seen on the skin side in the centre of the panel. Smaller bulges can be observed at the central horizontal rib (right picture). The buckles in the skin-bays are also clearly visible, e.g. in the upper left corner. With the help of the DIC pictures, cracks can be identified at three of the four rib knots of the horizontal rib (see Figure 91). The corresponding massive drop in the load-displacement-curve confirms the global panel failure (this drop is also monitored by the machine for stopping a test).

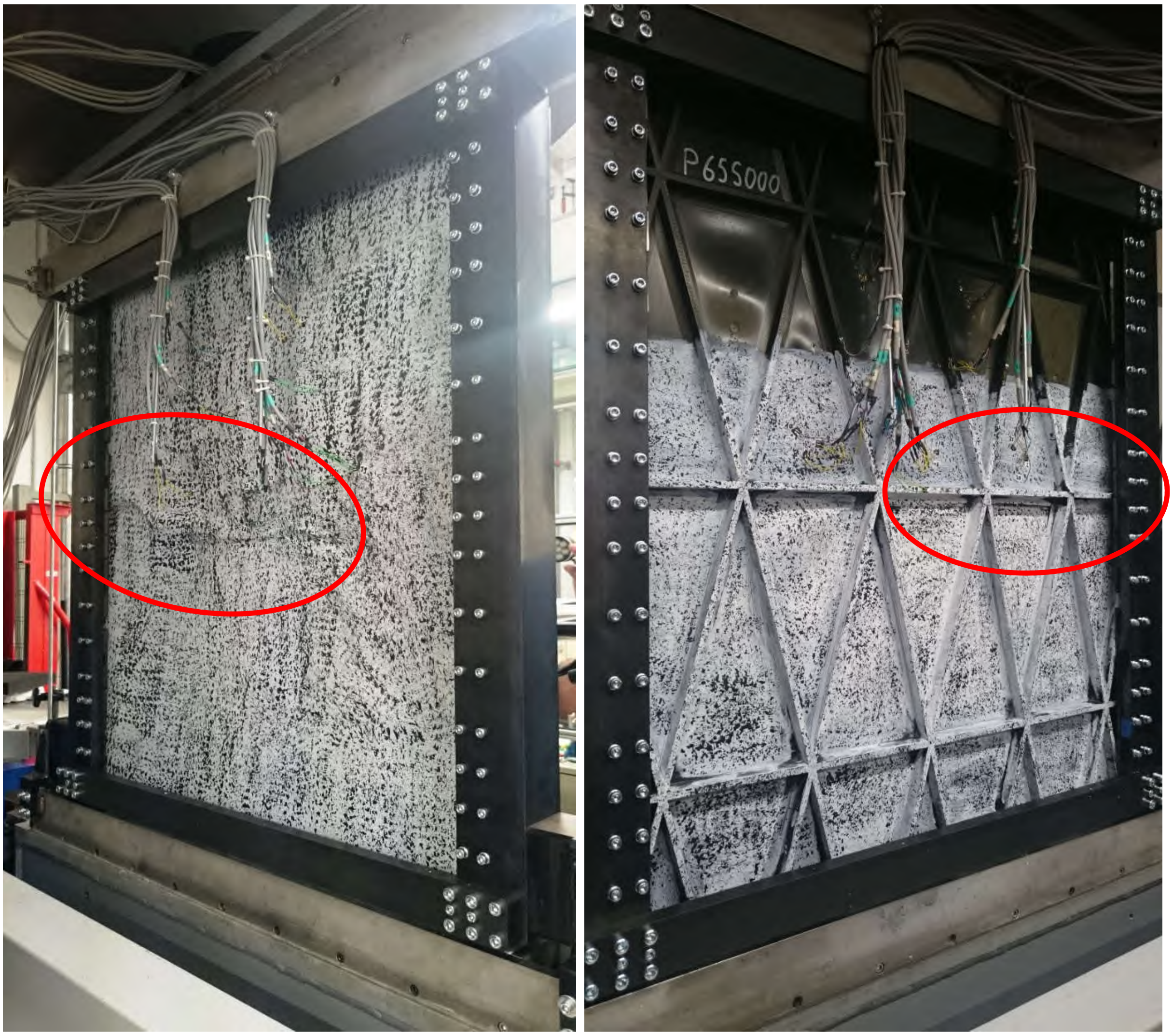

*Figure 90: Test panel after final failure*

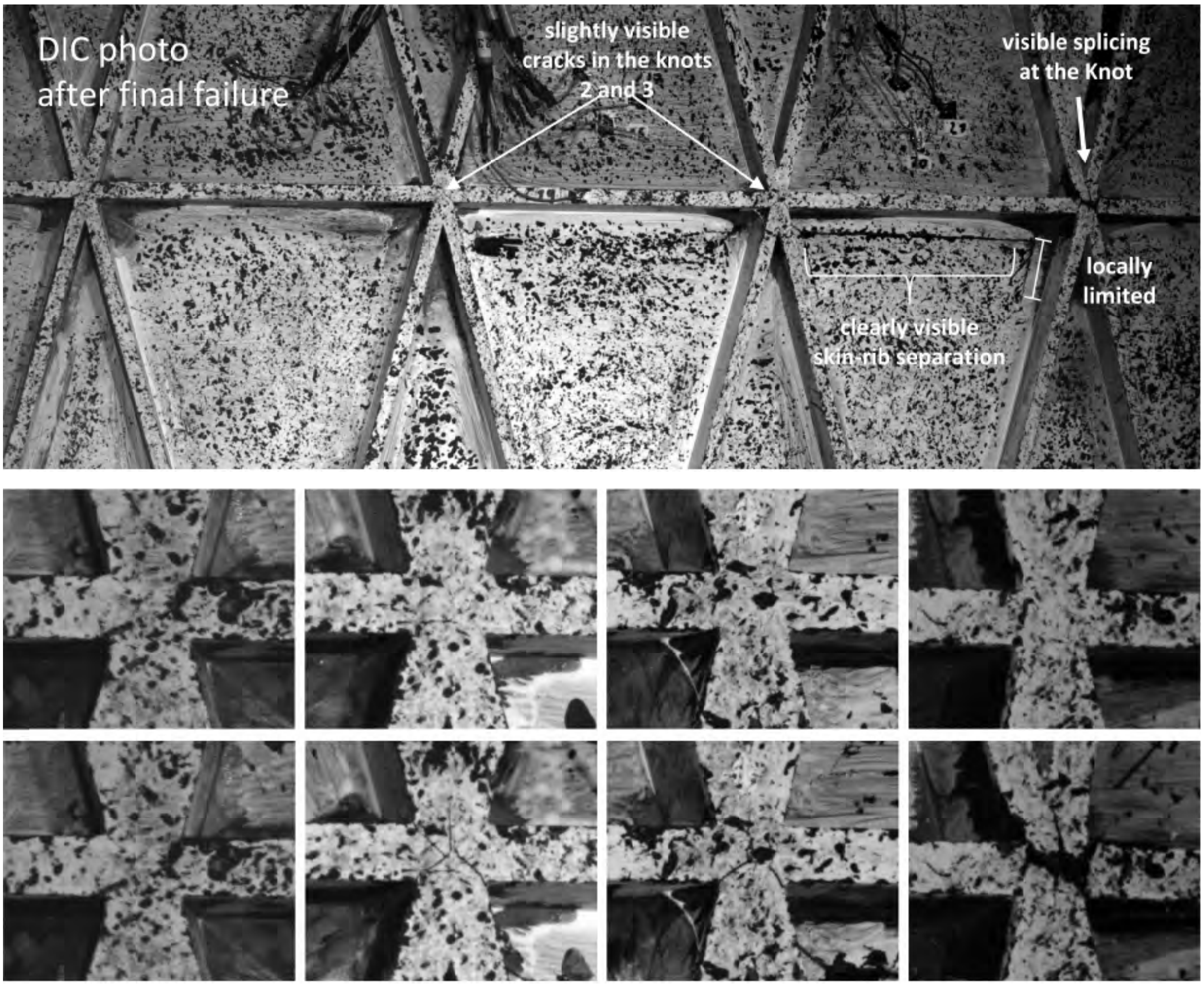

*Figure 91: Above: Centre rib of the panel after final failure;
Picture series below: knot enlargements right before (centre) and after (below) global failure;
knot No. 1 to 4 from left to right looking towards the rib side*

The simultaneous DIC analysis of the skin-bays and ribs has not proved to be possible. The skin-bays could be very well examined with this DIC measurement setup, while the visible surfaces of the ribs have shown to be too narrow. An even smaller panel section needs to be focused on to evaluate the deformations of the ribs.

### 7.4.1 Strain Gauge Measurements

With the strain gauges on the skin-bays, the buckling can be observed well. During elastic compression of the panel, the strain gauges on the rib (IML) and skin (OML) side measure equal compressive strains. As soon as the skin starts to buckle one strain gauge measures rapidly increasing tension and the other further increasing compression strain, compare Figure 91 which shows the strain gauge results in the skin-bays 3, 4 and 5. As can be expected, the maximum strains are obtained in skin-bay No.4 in the centre of the panel, whether the strain gauge in skin-bay 5 measured the same magnitude in tension. As maximum 5000 microstrains in compression and nearly 3000 microstrains in tension are monitored. Clearly different drops are visible in the curve progressions. With these drops and in combination with video and DIC data, the two local failures can be localized. The first failure is only visible as curve drop in the strain gauge measurements of skin-bay 3 and the second only in the strain gauge curves of skin-bay 5.

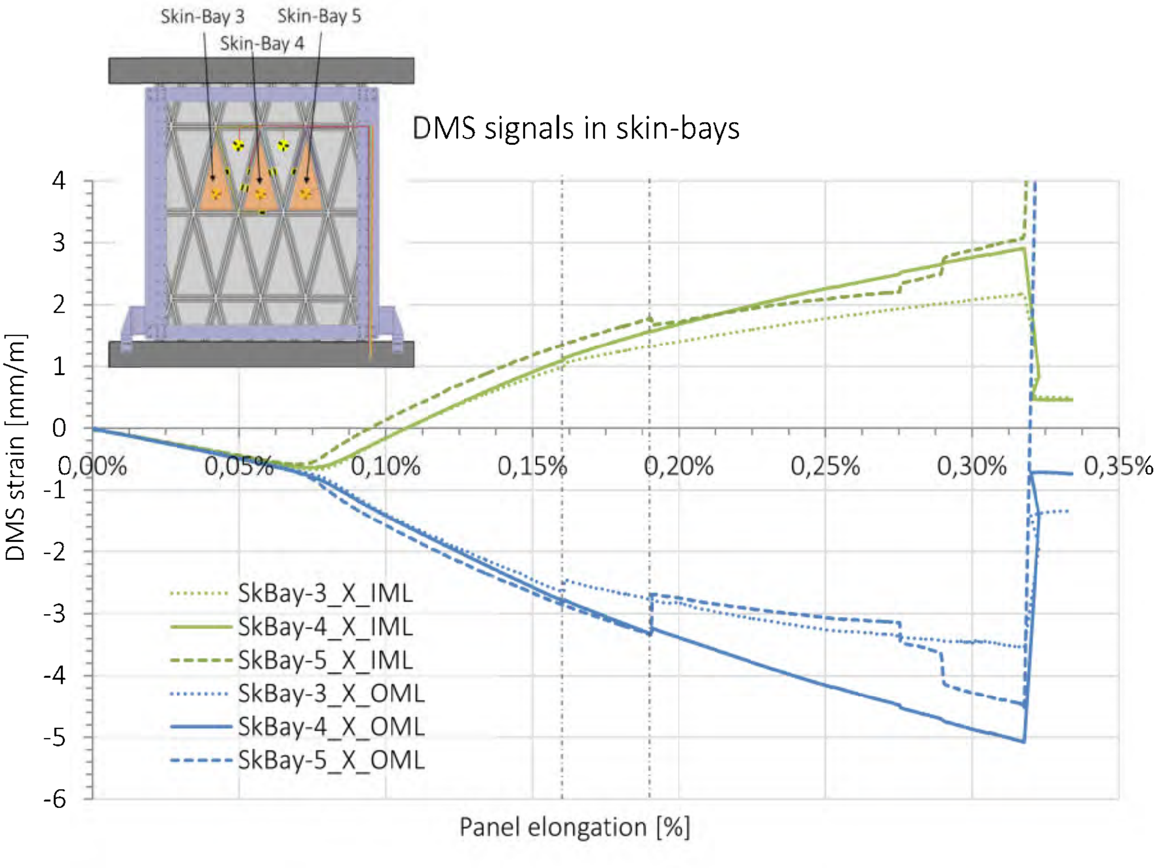

*Figure 92: Diagram of strain gauge measurements on skin-bay 4*

The strain gauges on the ribs show clearly the global bending deformation of the panel during the test (see Figure 92). On the skin side (OML) increasing compressive strains are measured whereas on the rib side (IML) lower compressive strains are monitored directly from the beginning, which are getting superimposed by tension approximately at 0.15% panel elongation. In the diagram, two curves are shown for the rib side at position two (dashed red and green line). At this position, it is intended to detect rib buckling during the test. Therefore two strain gauges are bonded at the sides of a rib at the maximum distance to the skin (rib height). In Figure 92 it can be seen that no buckling is observable in the rib due to the parallel curves of the strain gauges *Rib-2_Pos-2_IML left* and *right*. As maximum nearly 1500 microstrains in tension and 4000 microstrain in compression are monitored. In the centre of the panel even higher strains occurred due to maximum bending deformation.

With the measurements from the strain gauges at the rib positions and with respect to the results of the knot element tests it can be concluded that the maximum compression strength has been reached in the knots. The compression failure of the knots resulted in the loss of structural integrity of the panel. Subsequently, the skin separated from the rib structure in the area of the failed knots due to the abrupt rising of panel deformation when it crushes. In C.2, a brief calculation of the resulting stresses in the ribs is given.

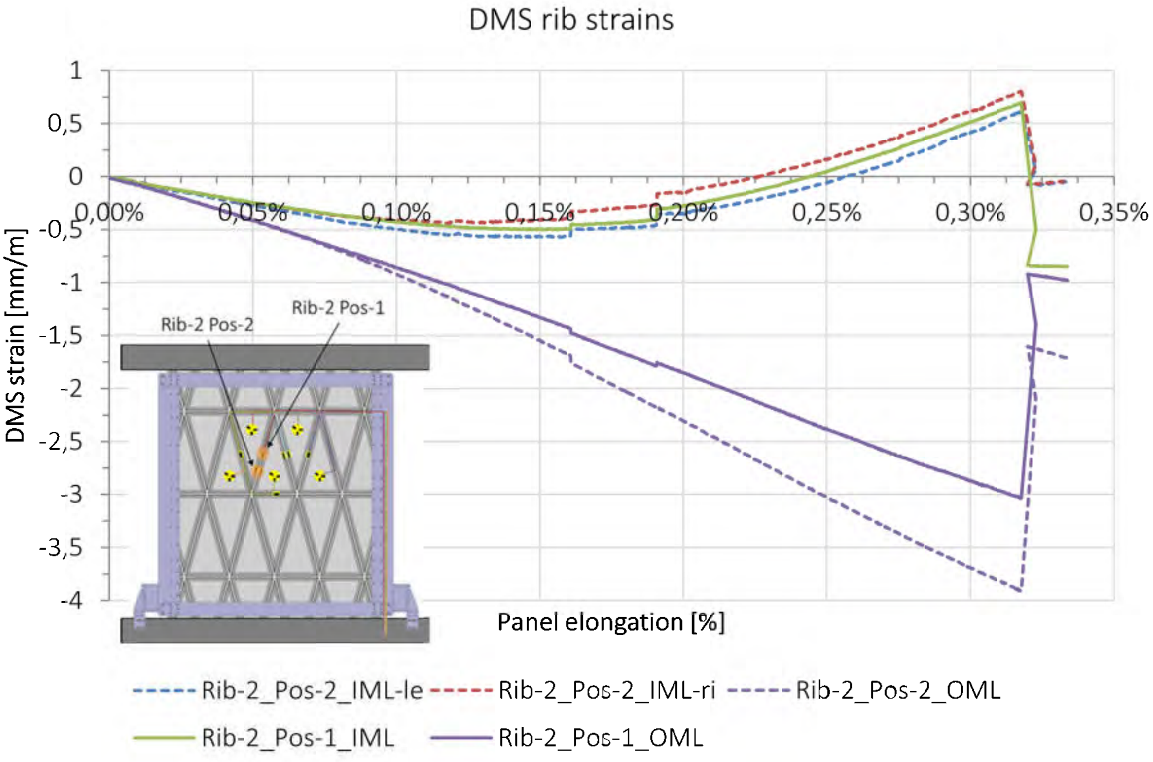

*Figure 93: Diagram of strain gauge measurements of a stiffener*

### 7.4.2 Skin Buckling Deformations

In Figure 93, the DIC data of the final compression test is analysed in terms of the skin deformations in Z-direction, the out-of-plane direction, over the panel length. A curve is a section of the skin-sided surface (illustrated with the blue dashed line). The different curves show several panel deformation states (0.8 mm to 2.8 mm) which corresponds to different load levels during the test. With increasing compressive load/panel deformation, the out-of-plane deformation increases. The skin buckles can be seen clearly as peaks in the curves (particularly at panel deformation higher 1.6 mm).

Just before final failure (2.8 mm curve), the skin buckles reaches a deformation of up to three times the skin thickness, which is a very high value. Additionally, it can be seen that the skin buckles (peaks in the curves) do not change their position. All these peaks remain at the same panel length position. Accordingly, no buckling pattern change is visible and strengthening the observations in the numerical calculations.

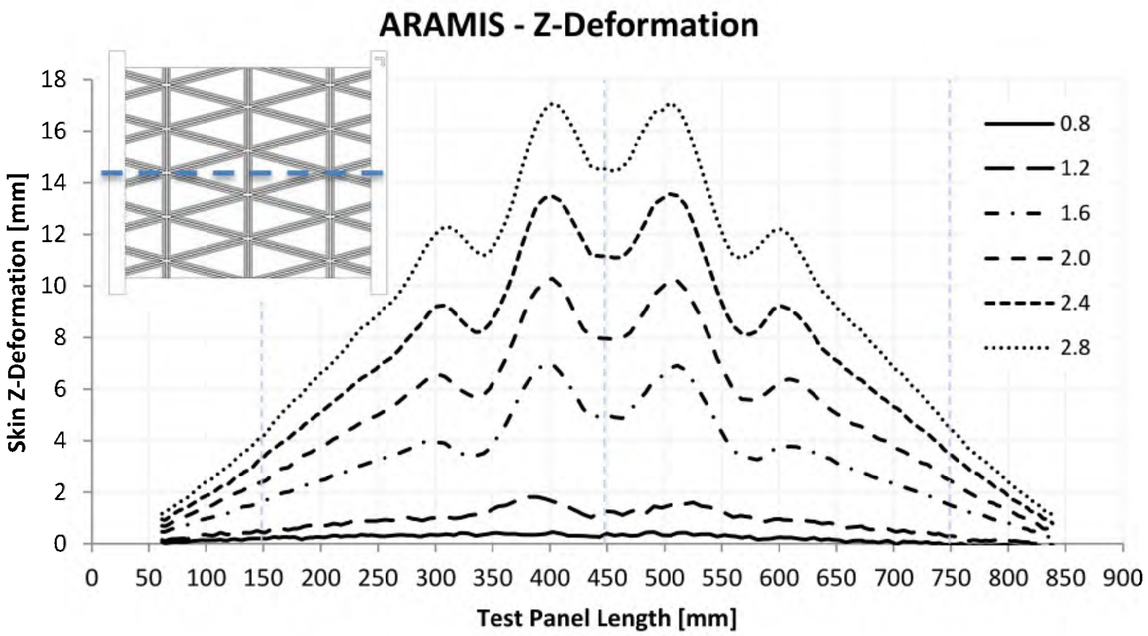

*Figure 94: Out-of-plane skin deformation at different load levels during test*

### 7.4.3 Inspection Results

The ultrasonic inspection of the panel showed that separations of the rib structure from the skin occurred only in the region of the centre circumferential rib (see Figure 94 purple colour in the centre picture and black colour in the right picture). The local failure on the left side can also be seen (see Figure 94 centre picture, small purple rectangle in the centre left of the panel), which occurred probably at the first local failure in the panel, mentioned before. In the left ultrasonic picture before the test, a purple rectangular area is also visible. This is a sticker on the skin for orientation and does not show damage.

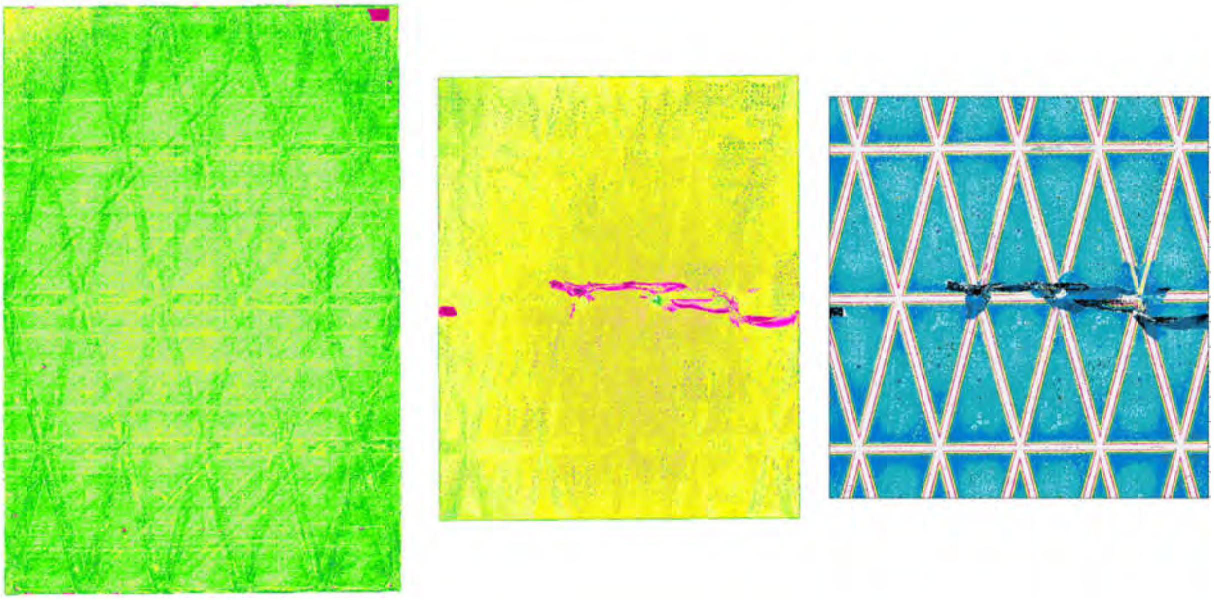

*Figure 95: Ultrasonic inspection; left: before test; centre: skin side after test; right: rib side after test (picture turned for comparison)*

## 7.5 Discussion and Conclusion of Test Results

For the validation of two main aspects of the Anisogrid structure concept, a static uniaxial compression test of a flat panel is designed and conducted until global failure. Additionally, the rib and knot properties derived in the element tests could be compared on a panel level.

The functionality of the interface layers is proven as one of the two main test goals. A grid-skin-separation occurred, which should be prevented by the interface layers, but shows significant differences to other tests in literature. Two skin-rib-separations appeared in the centre of the left and right panel edges at which high deformation amplitudes raised, due to the cutting of the helix ribs directly before the "next" knots. As a result, the load of almost one skin-bay needed to be carried by only one helical rib (compare the panel picture next to Table 6). Such failure is not expected in a barrel structure, as no open edges exist in such a kind. However, these unexpected failures clearly demonstrate that the skin-rib-separation emerged only locally, did not run through the whole skin-grid interface, and the panel could be significantly loaded further. No other local separations are observed on the panel besides the damages which occurred at global failure of the panel, located in the centre of the panel along the horizontal (circumferential) stiffener. Even these separations, however, are locally restricted damages, indicating that the peak stresses of the cracks are distributed efficiently in the wide interface, stopping the crack growth early. Also, the huge skin deformation in the deep buckling range does not generate peel stresses high enough to separate the skin and rib. Under consideration of other published tests of grid structures with load-bearing skin, it can be clearly concluded that interface layers are needed for such loaded structures.

Provoking a deep local buckling state in the skin-bays was the second main goal, in order to monitor whether changes of the buckling pattern or even mode-switches are occurring. On the tested Anisogrid panel, none of these effects were observed. Instead, a "stable" pattern of local buckles appeared in the skin-bays with constantly increasing amplitudes of up to three times the skin thickness. This behaviour validates or at least strengthens the numerical results which are achieved on flat and also curved Anisogrid stiffened shells. Perspectively, the observed difference in the buckling behaviour of triangular skin-bays may not be longer in terms of maximum deformation but it is seen that the higher reliability of numeric prediction might be a significant enabler for exploiting the possible buckling capabilities.

The final failure of the panel is concluded to have occurred due to the failure of the knots. The measured maximum strains on the compression side of the bended panel reached the static strength obtained in the element tests. As a consequence, the test results of the element test are seen to be valid.

The observed bending of the panel is significant, whereby it can be concluded that only the maximum knot strength was exceeded earlier than desired. The test goals could be fully investigated. The side supports for preventing additional out-of-plane deformation are seen to be appropriate for use.

# 8 Perspective for Anisogrid Design Concept

One of the key features of the integral stiffened structure is the automated manufacturing process which is capable to produce intersecting stiffeners and a proper interface of the rib structure with the load-bearing skin. This production approach can lead to significantly decreased production costs and lead-time because no assembly is required for the grid-stiffened shell structure itself. In order to realise such a one-shot manufacturing, multiple robots can be equipped with such placement head and fabricating a barrel or big shell structure in parallel (see Figure 96).

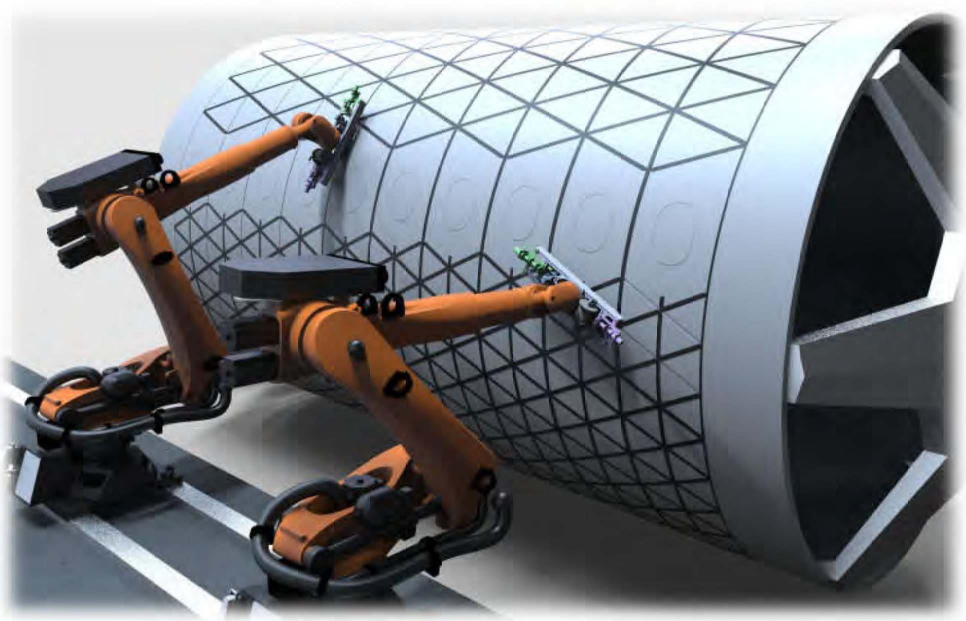

*Figure 96: Barrel manufacturing with multiple robot system*

Considering the results presented in the Chapters 4 to 7, several advantages and drawbacks can be summarised for the developed Anisogrid concept.

Advantages:

- Achievable high stiffness properties of prepreg material
- Full integral manufacturing concept
- High design freedom of integral stiffened skin structure
- Possibility of fulfilment of main laminate rules
- Improved interface concept between rib structure and skin
- Interface layers cover the otherwise open rib laminate, which should be beneficial for damage tolerance and protect against environmental conditions
- Additional load path to the skin for Anisogrid concept with almost no weight penalty for curved panel, especially for strength-driven load cases
- “Stable” and better predictable buckling behaviour of triangular skin-bays

One main drawback is facing the concept:

- Cut layers at intersections of rib stiffeners → low static strength properties

This main drawback of the current concept is seen to be crucial, probably preventing the usage of the concept for fuselage structures. As a consequence, another approach is started, wherein the developed Anisogrid concept with interface layers is combined with a grid manufacturing process developed by a Dutch company. The developers overcome the cutting of the layers in the intersection area through a special spreading of the tows. The stiffener knots are not thickened in rib height direction and the fibres are steered only slightly in rib width direction. As a result, the layers are not cut at the knots and also retain high strength properties. Important for this concept is the specially adapted tool geometry at the stiffener intersections [62].

With such an approach and concept adaptation, a significant perspective of the design is opening up. Being able to manufacture in a one-shot process intersecting stiffeners with different orientations, keeping the stiffness and strength properties, and a strong connection with a (load-bearing) skin, structures with changing stiffening architecture can be realised up to bionic-looking topology-free concepts as shown in the visionary concept picture from AIRBUS in Figure 97.

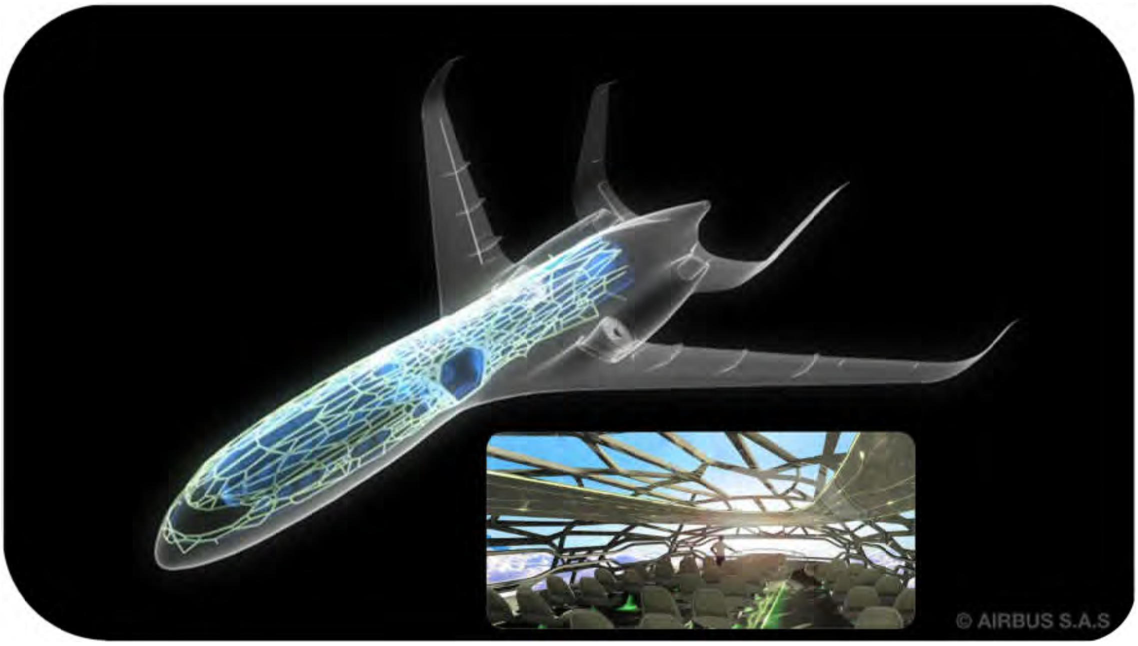

*Figure 97: Perspective of highly integral manufactured grid structures, figure after [1]*

The main question in addition to the validation of the combined manufacturing concept is the further development of an efficient tooling concept. Basic concepts are being developed and validated on a laboratory scale and need to be taken to the full-scale panel or even barrel level.

# 9 Summary and Conclusion

In this thesis, a structural Anisogrid fuselage design concept for civil aircraft is presented. The developed design concept consists of a load-bearing skin, stiffened by a grid of circumferential and helical ribs including special interface layers for the connection of the rib structure with the skin. Particularly, this design fulfils main laminate guidelines and focuses on a fully automated manufacturing process with pre-conditioned material, in this case CFRP-prepreg. For utilisation of high stiffness properties, a prepreg with 60% fibre volume content is processed. In order to achieve the highest-possible efficiency in the fibre placement process, the maximum allowable ply thickness of 1 mm slit tapes (*"package layers"*) forms the basis of the investigation. As a compromise between high fibre-volume-ratio and efficiency of placement process, the cutting of rib layers in the intersection region is chosen. For the automated placement of the interface layers, a new placement head is developed.

In order to overcome the lack of available material properties of the Anisogrid structural design concept, element specimens are manufactured and tested. Static tension and compression tests are performed, wherein rib and knot specimens are investigated separately. For a better evaluation of the results, a wide reference test programme is also manufactured and tested. Firstly, undisturbed and disturbed-rib specimens are investigated, cut from a thick plate. Secondly, typical laminate specimens are produced with the same rib and knot fibre orientation ratio.

The tests show that the stiffness of a grid-rib (plain rib between knots) can be used for sizing of the whole rib structure including knot areas. A resulting different stacking in the knot area showed no remarkable influence on the stiffness for tension as well as for compression. As a consequence, the advantage of achievable high stiffness can be fully used for the Anisogrid prepreg concept. This can be exploited especially for stiffened structures, where stability is a more critical design driver than strength.

In terms of strength, the Anisogrid prepreg concept with investigated 1 mm-thick and cut layers has to operate with much lower maximum allowable stresses for the knot area. For such thick package layers, the inter-fibre failure of the cut plies in the knot area cause ply-separation from side to side and delaminations need to be expected. As a consequence, the reduction of layer thickness is strongly recommended. In a smaller test series with 0.25 mm-thick package layers the maximum fibre failure of the uncut 0°-layers are attained. Considering this aspect, the resulting knot strength should be applied for the whole grid structure for sizing purposes.

The comparison of the Orthogrid and Anisogrid architecture is performed through the sizing of panel structures under the same constraints and manufacturing process, differing only in the orthogonal or helical stiffened architecture. Therefore, an analytical sizing algorithm is used which minimises the same failure criteria for both. The sizing criteria are global panel buckling, local stiffener and skin-bay buckling and the strength in all stiffeners and the skin. The sizing is performed for flat and curved panels loaded with uniaxial compression, pure shear and the combination of both. The results are compared via the minimised weight per area.

An inherent weight benefit for the Anisogrid stiffening architecture with load-bearing skin cannot be observed for the performed static analysis. Under uniaxial compression, a weight increase is calculated for an Anisogrid structure of 10% on the flat panel and between 6% for low loads and almost the same weight for high compressive loads on the curved panel (R=2000mm). A compression-dominated loading in combination with shear leads to a slightly higher weight penalty (max. 15%) on the flat and curved panel. For load-cases with the same amount of compression and shear, shear-dominated or pure shear loads, the Anisogrid obtains a weight benefit between 5% and 10% on the flat panel, and up to 5% on the curved panel, especially at higher loads.

A panel test with the developed design concept has been conducted to validate the observed different buckling behaviour on the one hand and the functionality of the proposed interface layers on the other.

A different buckling behaviour can be observed under compression for Anisogrids in comparison to classical rectangular stiffened structure designs. After local stability loss in a skin-bay, so-called mode-switches can occur in rectangular skin-bays, when the local buckle pattern is changing. These are highly dynamic processes and are often the point of occurrence of different kinds of failures. In triangular skin-bays, these kinds of mode-switches are not seen in this manner. A stable buckling pattern and behaviour could be validated according to the FE calculations the first time with the test panel, which has a thin skin and, in consequence, a long skin-bay buckling state. As this test is at the moment only a single result, further tests should be performed, also with combined compression and shear loads. Nevertheless, the result is inspiring and the perspective of a reliable prediction of the buckling behaviour increases the confidence for the sizing process and can help to exploit structural weight potential.

In addition to the buckling behaviour, the panel test validates the functionality of the interface layers. The skin buckled deeply locally without separating from the grid structure. Even two occurring cracks on the left and right central side of the panel did not grow, in contrast to the behaviour typically observed in other grid tests with skin. This design feature is seen to be essential for a valid airframe Anisogrid concept. The optimisation of the quantity of interface layers and the feet widths should be analysed in following investigations.

It can be concluded that the proposed Anisogrid concept features high stiffness properties and a fully automated manufacturing process for a stiffened shell structure. The Anisogrid architecture is, in compression, slightly less weight efficient; on the other hand, it can be maintained that with this weight increase, a second load path for shear loads can be integrated into the structure. For damage tolerance reasons, this could prove to be remarkably interesting. The convincing predictability of the “stable” buckling behaviour also supports this architecture.

Perspectively, the intended manufacturing process is of significant interest, due to the possibility of manufacturing a multi-oriented stiffened shell structure in a real one-shot process. The fabrication of topology optimised architectures seems to be realisable. Euphoric, on the one hand, diverse further aspects still have to be investigated. Despite the combination of a knot concept without cut layers, the damage tolerance and fatigue of such a grid structure is of evidential interest. Due to the long in-service life of an aircraft, the first concepts which are developed regarding reparability need to be detailed and validated. Furthermore, the joining of such a design on panel or barrel level is another important aspect.

# 10 References

1. AIRBUS S.A.S. The Future by Airbus: Concept plane cabin (available at www.thefuturebyairbus.com).
2. AIRBUS S.A.S. Global Market Forecast: Mapping Demand 2016-2035 (available at http://www.airbus.com/company/market/global-market-forecast-2016-2035/).
3. Ambur, D.R; Jaunky, N; and Knight, N.F. Buckling analysis and design optimization for grid-stiffened composite structures. *International SAMPE Symposium and Exhibition (Proceedings), 44* (1999).
4. AMRO Fabricating. Machined and formed Aluminum Isogrid Structure: Picture shown on the homepage under Capabilities/Forming. (5 May 2017) (available at http://amrofab.com/).
5. Baker, A. (ed.) (2004). *Composite materials for aircraft structures,* 2nd edn. Reston Va.: American Institute of Aeronautics and Astronautics.
6. Barynin, V.A; Bunakov, V.A; Razin, A.F; and Vasiliev, V.V. Aerospace Composite Lattice Structures. *12th International Conference on Composite Materials*, 1999.
7. Bill McKinley (1995). The Yates Geodetic Plane. *Oregon Aviation Museum Newsletter,* Dec. 1995, 1–6 (available at https://oregonaviation.files.wordpress.com/2012/01/1995-12-reduced.pdf). (4 December 2015).
8. Biskner, A.C. and Higgins, J.E. Design and evaluation of a reinforced advanced-grid stiffened composite structure. *Collection of Technical Papers - AIAA/ASME/ASCE/AHS/ASC Structures, Structural Dynamics and Materials Conference, 7* (2005), pgs. 4324–4332.
9. Biskner, A.C. and Higgins, J.E. Testing and analysis of large curved grid-stiffened composite panels. *16th International Conferences on Composite Materials*, 2007.
10. Brink, W.M. van den and Vankan, W.J. Design for manufacturing of fuselage panels with curved grid stiffening.
11. Bushnell, D; Rankin, C.C; and Riks, E. Optimization of stiffened panels in which mode jumping is accounted for. *Collection of Technical Papers - AIAA/ASME/ASCE/AHS/ASC Structures, Structural Dynamics and Materials Conference, 3* (1997), pgs. 2123–2162.
12. Certification Specifications for Large Aeroplanes: CS-25. EASA (available at https://www.easa.europa.eu/system/files/dfu/CS-25_Amdt%203_19.09.07_Consolidated%20version.pdf).
13. Chen, H.J. and Tsai, S.W. Analysis and optimum design of composite grid structures. *Journal of Composite Materials, 30,* 4 (1996), pgs. 503–534.
14. Chen, H.-J. *Analysis of optimum design of composite grid structures*. Dissertation, 1995.
15. De Nicola, F; Totaro, G; Lenzi, F; and Ferrigno, A. Mechanical properties of composite anisogrid shell structures. *59th International Astronautical Congress*, 2008, pp. 5481–5492.
16. Degenhardt, R; Kling, A; Klein, H; Hillger, W; Goetting, H.C; Zimmermann, R; Rohwer, K; and Gleiter, A. Experiments on buckling and postbuckling of thin-walled CFRP structures using advanced measurement systems. *International Journal of Structural Stability and Dynamics, 7,* 2 (2007), pgs. 337–358.
17. Del Olmo, E; Grande, E; Samartin, C.R; Bezdenejnykh, M; Torres, J; Blanco, N; Frövel, M; and Cañas, J. Lattice structures for aerospace applications. *European Space Agency, (Special Publication) ESA SP*, 2012.

18. Deutsche Lufthansa AG. Nachhaltigkeitsbericht Balance: Ausgabe 2012. Lufthansa Group (available at https://www.lufthansagroup.com/de/themen).
19. Díaz, V; Del Olmo, E; and Frövel, M. Design & development of advanced composite isogrid structural solutions for primary structures of future reusable launch vehicle. *European Conference on Spacecraft Structures Materials and Mechanical Testing*, 2009.
20. Engmann, K. (ed.) (2006). *Technologie des Flugzeuges,* 3rd edn. Würzburg: Vogel.
21. Falzon, B.G. and Steven, G.P. Buckling mode transition in hat-stiffened composite panels loaded in uniaxial compression. *Composite Structures, 37,* 2 (1997), pgs. 253–267.
22. Frövel, M; Del Olmo, E; Torres, J; Carrion, G; Pintado, J.M; and Blanco, N. Health monitoring of a weight efficient lattice spacecraft structural element with FBGS sensors. *6th European Workshop on Structural Health Monitoring*, 2nd edn., 2012, pp. 1084–1090.
23. Gädke, M; Geier, B; -Chr. Goetting, H; Klein, H; Rohwer, K; and Zimmermann, R. Damage influence on the buckling load of CFRP stringer-stiffened panels. *Composite Structures, 36,* 3 (1996), pgs. 249–275.
24. Gagauz, F; Kryvenda, S; Shevtsova, M; Smovziuk, L; and Taranenko, I. Manufacturingand testing ofcompositewafer components with dual-purpose integrated semi-loopjoints. *16th European Conference on Composite Materials*: European Conference on Composite Materials, ECCM, 2014.
25. Hashin, Z. Failure Criteria for Unidirectional Fiber Composites. *Journal of Applied Mechanics, Transactions ASME, 47,* 2 (1980), pgs. 329.
26. Hayashi, T. Buckling Strength of Cylindrical Geodesic Structures. In 1981, pp. 428–435.
27. Hexcel Corporation. HexPly 8552 Product Datasheet. (13 October 2016) (available at http://www.hexcel.com/Resources/DataSheets/Prepreg-Data-Sheets/8552_eu.pdf).
28. Higgins, J.E; Wegner, P.M; Viisoreanu, A; and Sanford, G. Design and testing of the Minotaur advanced grid-stiffened fairing. *Composite Structures, 66,* 1 (2004), pgs. 339–349.
29. Higgins, J.E; Wegner, P.M; West, B.P. van; and Viisoreanu, A. Post-buckling test response and analysis of fiber composite grid-stiffened structures. *Collection of Technical Papers - AIAA/ASME/ASCE/AHS/ASC Structures, Structural Dynamics and Materials Conference, 2* (2002), pgs. 1032–1042.
30. Hosomura, T; Kawashima, T; and Mori, D. New CFRP Structural Elements. In 1981, pp. 447–452.
31. Huybrechts, S.M. *Analysis and behavior of grid structures*. Dissertation. Michigan: UMI, 1995.
32. Huybrechts, S.M. and Meink, T.E. Advanced grid stiffened structures for the next generation of launch vehicles. *IEEE Aerospace Applications Conference Proceedings, 1* (1997), pgs. 263–269.
33. Huybrechts, S.M; Meink, T.E; Wegner, P.M; and Ganley, J.M. Manufacturing theory for advanced grid stiffened structures. *Composites Part A: Applied Science and Manufacturing, 33,* 2 (2002), pgs. 155–161.
34. Huybrechts, S.M. and Tsai, S.W. Analysis and behavior of grid structures. *Composites Science and Technology, 56,* 9 (1996), pgs. 1001–1015.
35. IATA. The IATA Technology Roadmap Report: 2013. International Air Transport Association (available at https://www.iata.org/whatwedo/environment/Documents/technology-roadmap-2013.pdf).
36. Institut für Adaptronik und Funktionsintegration @ TU Braunschweig: Karl-Doetsch-Nachwuchspreis für Torben Glindemann. (11 March 2018) (available at https://www.tu-braunschweig.de/iaf).

37. Isogrid Composite Canada Inc. Company Homepage. ICCI (available at http://www.isogridinc.com/).

38. Jaunky, N; Knight, N; and Ambur, D. Optimal design of general stiffened composite circular cylinders for global buckling with strength constraints. *Composite Structures, 41,* 3 (1998), pgs. 243–252.

39. Jaunky, N; Knight, N.F; and Ambur, D.R. Buckling analysis of general triangular anisotropic plates using polynomials. *AIAA Journal, 33,* 12 (1995), pgs. 2414–2417.

40. Jaunky, N; Knight, N.F; and Ambur, D.R. Formulation of an improved smeared stiffener theory for buckling analysis of grid-stiffened composite panels. *Composites Part B: Engineering, 27,* 5 (1996), pgs. 519–526.

41. Jaunky, N; Knight, N.F; and Ambur, D.R. Optimal design of grid-stiffened composite panels using global and local buckling analyses. *37th AIAA/ASME/ASCE/AHS/ASC Structure, Structural Dynamics and Materials Conference* (1996), pgs. 2315–2325.

42. Kidane, S. *Buckling analysis of grid stiffened composite structures*. Master Thesis. Baton Rouge, La., 2002.

43. Kidane, S; Li, G; Helms, J; Pang, S.S; and Wodesenbet, E. Buckling load analysis of grid stiffened composite cylinders. *Composites Part B: Engineering, 34,* 1 (2003), pgs. 1–9.

44. Kim, T.D. Postbuckled behavior of composite isogrid stiffened shell structure. *Advanced Composite Materials, 9,* 3 (2000), pgs. 253–263.

45. Klinzmann, A. *Optimierung von nicht konventionellen Strukturen als Flugzeugrumpfversteifung*. Dissertation. Braunschweig, Germany: Cuvillier, 2011.

46. Knighton, D.J. *Delta launch vehicle isogrid structure NASTRAN analysis*, 1972.

47. MAAXIMUS: European Research Project funded in FP7 framework programme (available at http://www.maaximus.eu/).

48. Meink, T.E. Composite grid vs. composite sandwich: A comparison based on payload shroud requirements. *IEEE Aerospace Applications Conference Proceedings, 1* (1998), pgs. 215–220.

49. *Military Handbook - MIL-HDBK-17-3F: Composite Materials Handbook, Volume 3 - Polymer Matrix Composites Materials Usage, Design, and Analysis*. [Place of publication not identified]: U.S. Dept. of Defense.

50. Müller, M; Niemann, S; Jörn, P; Ströhlein, T; Hühne, C; and Kleineberg, M. A method and a device for the manufacture of a lightweight structure, and also a lightweight structure, EP2674290A1.

51. Mummert, H.C. Metal framed structure for aeroplanes. US19290364347*, B64C1/08,* US1818423 (A), 1929.

52. Murray, I.R. *Bouncing-bomb man: The science of Sir Barnes Wallis*. Sparkford: Haynes, 2009.

53. NASA. *Isogrid design handbook*. Huntington Beach, CA: The Company, 1973.

54. NASA. A Summary and Review of Composite Laminate Design Guidelines. National Aeronautics and Space Administration, Hampton, Virginia. (14 January 2017) (available at http://abdmatrix.com/site/openrepository/files/Composite%20Laminate%20Guidelines.pdf).

55. Niemann, S; Sinapius, M; Transier, G; and Pöppelmann, M. Faserlegekopf zum Legen von Faserhalbzeugprofilen, Faserlegeanlage sowie Verfahren hierzu, EP3210766.A1, 2017.

56. Niemann, S; Wagner, H.R; Beerhorst, M; and Hühne, C. Testing and analysis of Anisogrid Prepreg element specimens under uniaxial tension and compression. *Composite Structures, 160* (2017), pgs. 594–603.

57. Niemann, S; Wagner, R; and Hühne, C. Testing and Analyis of Post-Buckling Behaviour of Anisogrid Prepreg Panel Under Compression. *5th Aircraft Structural Design Conference*, 2016.
58. Normenausschuss Kunststoffe (FNK) im DIN Deutsches Institut für Normung e.V. DIN EN ISO 527-4: Bestimmung der Zugeigenschaften für isotrop und anisotrop faserverstärkte Kunststoffverbundwerkstoffe. Berlin: Beuth Verlag GmbH, 1997.
59. Normenausschuss Kunststoffe (FNK) im DIN Deutsches Institut für Normung e.V. DIN EN ISO 14126; Bestimmung der Druckeigenschaften in der Laminatebene. Berlin: Beuth Verlag GmbH, 2000.
60. Onoda, J. Optimal Design of Lattice Cylinders. *Transactions of the Japan Society for Aeronautical and Space Sciences, 29,* 83 (1986), pgs. 46–62.
61. Onoda, J. and Mori, D. The Development of Structure and Mechanisms for Mu-3SII. *Journal of Space Technology and Sciences, Vol.2 No.1* (1986-1987), pgs. 38–46.
62. Pavlov, L; Kloeze, I; Smeets, B.J; and Simonian, S.M. Development of Mass and Cost Efficient Grid-Stiffened and Lattice Structures for Space Applications. *14th ECSSMET*, 2016.
63. Powell, K. (1961). Geodetic Aircraft Structure, 10 August 1961, 17–24 (available at http://www.homebuiltairplanes.com/forums/attachments/classics/13531d1312626313-thalman-t4-1961_08_10.pdf). (10 September 2015).
64. Reddy, A.D; Rehfield, L.W; Haag, R.S; and Widman, C.G. Compressive buckling behavior of graphite/epoxy isogrid wide columns with progressive damage. *ASTM Special Technical Publication* (1983), pgs. 187–199.
65. Reddy, A.D; Valisetty, R.R; and Rehfield, L.W. Continuous Filament Wound Composite Concepts for Aircraft Fuselage Structures. *Journal of Aircraft, 22,* 3 (1985), pgs. 249–255.
66. Rehfield, L.W. and Deo, R.B. *Buckling of Continuous Filament Advanced Composite Isogrid Wide Columns in Axial Compression*. Ft. Belvoir: Defense Technical Information Center, 1978.
67. Rehfield, L.W; Deo, R.B; and Renieri, G.D. Continuous Filament Advanced Composite Isogrid: A Promising Structural Concept. In E.M. Lenoe; D.W. Oplinger; and J.J. Burke (eds.), *Fibrous Composites in Structural Design*. Boston, MA: Springer US, 1980, pp. 215–239.
68. Rehfield, L.W. and Reddy, A.D. Damage Tolerance of Continouous Filament Composite Isogrid Structures: A Preliminary Assessment. In 1981, pp. 471–477.
69. Rehfield, L.W; Reddy, A.D; Yehezkely, O; and Armanios, E. Buckling of Continuous Filament Composite Isogrid Panels: Theory and Experiment. In 1982, pp. 545–555.
70. Rohwer, K. Post-Buckling Behavior of Fiber Reinforced Plates and Curved Panels. *Zeitschrift fur Flugwissenschaften und Weltraumforschung, 10,* 4 (1986), pgs. 228–235.
71. Schürmann, H. *Konstruieren Mit Faser-Kunststoff-Verbunden,* 2nd edn. Berlin: Springer-Verlag Berlin and Heidelberg GmbH & Co. KG, 2008.
72. SIHN, S; KIM, R; KAWABE, K; and TSAI, S. Experimental studies of thin-ply laminated composites. *Composites Science and Technology, 67,* 6 (2007), pgs. 996–1008.
73. Slysh, P. Conical structure. US19740495029*, B64G99/00;E04C2/32;E04C2/38,* US3940891 (A), 1974.
74. Slysh, P. High strength composite structure. US19740513661*, B64C1/08;E04C2/38;B32B3/12,* US4012549 (A), 1974.
75. Slysh, P. Isogrid shell gun mount. US19760733662*, F41A23/00;B64D7/06,* US4040333 (A), 1976.

76. Stroud, W.J; Greene, W.H; and Anderson, M.S. Buckling Loads of Stiffened Panels Subjected to Combined Longitudinal Compression and Shear: Results Obtained with PASCO, EAL, and STAGS Computer Programs. *NASA Technical Paper* (1984).

77. Šuchov, V.G. and Graefe, R. (eds.) (1990). *Vladimir G. Šuchov, 1853 - 1939: Die Kunst der sparsamen Konstruktion*. Stuttgart: Dt. Verl.-Anst.

78. Sutton, M.A; Schreier, H.W; and Orteu, J.-J. *Image correlation for shape, motion and deformation measurements: Basic concepts, theory and applications*. New York: Springer, 2009.

79. Tan, H; Bettess, P; and Bettess, J. Elastic buckling of isotropic triangular flat plates by finite elements. *Applied Mathematical Modelling, 7,* 5 (1983), pgs. 311–316.

80. Totaro, G. *Multilevel optimization of anisogrid lattice structures for aerospace applications*. Dissertation. Delft, Netherlands, 2011.

81. Totaro, G. Local buckling modelling of isogrid and anisogrid lattice cylindrical shells with triangular cells. *Composite Structures, 94,* 2 (2012), pgs. 446–452.

82. Totaro, G. Local buckling modelling of isogrid and anisogrid lattice cylindrical shells with hexagonal cells. *Composite Structures, 95,* 0 (2013), pgs. 403–410.

83. Totaro, G; De Nicola, F; Grilli, A; Ferrigno, A; and Caramuta, P. Micromechanics of composite anisogrid structures. *16th European Conference on Composite Materials*: European Conference on Composite Materials, ECCM, 2014.

84. Totaro, G. and Gürdal, Z. Optimal design of composite lattice shell structures for aerospace applications. *Aerospace Science and Technology, 13,* 4–5 (2009), pgs. 157–164.

85. Totaro, G. and Nicola, F. de. Recent advance on design and manufacturing of composite anisogrid structures for space launchers. *Acta Astronautica, 81,* 2 (2012), pgs. 570–577.

86. Totaro, G. and Vasiliev, V.V. Isogrid and Anisogrid design concepts for axially compressed cylindrical structures. *International SAMPE Technical Conference* (2004), pgs. 915–928.

87. Vasiliev, V.V; Barynin, V.A; and Razin, A.F. Anisogrid lattice structures – survey of development and application. *Third International Conference on Composite Science and Technology, 54,* 2–3 (2001), pgs. 361–370.

88. Vasiliev, V.V; Barynin, V.A; and Razin, A.F. Anisogrid composite lattice structures – Development and aerospace applications. *Composite Structures, 94,* 3 (2012), pgs. 1117–1127.

89. Vasiliev, V.V; Barynin, V.A; Razin, A.F; Petrokovskiy, S.A; and Khalimanovich, V.I. Anisogrid Composite Lattice Structures - Development and Space Applications. *European Conference on Spacecraft Structures Materials and Mechanical Testing*, 2009.

90. Vasiliev, V.V. and Gürdal, Z. *Optimal design Theory and applications to materials and structures*. Lancaster, Pa: Technomic Pub. Co., 1999.

91. Vasiliev, V.V. and Razin, A.F. Anisogrid composite lattice structures for spacecraft and aircraft applications. *Fifteenth International Conference on Composite Materials ICCM-15 Fifteenth International Conference on Composite Materials, 76,* 1–2 (2006), pgs. 182–189.

92. Vasiliev, V.V. and Razin, A.F. Development of geodesic composite aircraft structures. *28th Congress of the International Council of the Aeronautical Sciences*, 2012, pp. 2184–2190.

93. Wagner, H.R; Niemann, S; and Hühne, C. Structural Robustness Analysis of Anisogrid Lattice Structures. *20th International Conference on Composite Materials*, 2015.

94. Weber, M.J. and Middendorf, P. Semi-analytical skin buckling of curved orthotropic grid-stiffened shells. *Composite Structures* (2014), pgs. 616–624.

95. Wegner, P.M; Ganley, J.M; Huybrechts, S.M; and Meink, T.E. Advanced grid stiffened composite payload shroud for the OSP launch vehicle. *IEEE Aerospace Conference Proceedings, 4* (2000), pgs. 359–365.

96. Wiedemann, J. *Leichtbau: Elemente und Konstruktion,* 3rd edn. Berlin, Heidelberg, New York: Springer, 2007.

97. Wilckens, D; Degenhardt, R; Rohwer, K; Zimmermann, R; Kepke, M; Hildebrandt, B; and Zipfel, A. Cyclic buckling tests of pre-damaged CFRP stringer-stiffened panels. *International Journal of Structural Stability and Dynamics, 10,* 4 (2010), pgs. 827–851.

98. Zimmermann, R; Klein, H; and Kling, A. Buckling and postbuckling of stringer stiffened fibre composite curved panels - Tests and computations. *Composite Structures, 73,* 2 (2006), pgs. 150–161.

## *Patents*

*in terms of grid architecture:*

Kolesnikov, Boris; Huehne, Christian; Wolff, Johannes; Fink, Axel; Nickel, Joerg; Niemann, Steffen et al. (2012b): Aircraft has front longitudinal section to receive cockpit area, rear longitudinal section to receive rear body section and central longitudinal section to receive intermediate region of body between cockpit area and rear body section. Applied for by DEUTSCH ZENTR LUFT & RAUMFAHRT [DE] on 2/8/2012. App. no. DE20121002352 20120208. Patent no. DE102012002352 (A1). B64C1/00. Priority no. DE20121002352 20120208.

Kolesnikov, B.; Niemann, S.; Mierheim, O.; Lohse-Busch, H.; Hühne, C. (2012): Rumpfstrukturbauteil für Fahrzeuge, insbesondere für Luft- und/oder Raumfahrzeuge. Applied for by German Aerospace Center on 10/10/2012. Patent no. DE102012019905B3.

Müller, M.; Niemann, S.: A method and a device for the manufacture of a lightweight structure, and also a lightweight structure. App. no. 13172082.3. Patent no. EP2674290A1.

Niemann, S; Sinapius, M; Transier, G; and Pöppelmann, M. Faserlegekopf zum Legen von Faserhalbzeugprofilen, Faserlegeanlage sowie Verfahren hierzu, EP3210766.A1, 2017.

Niemann, S.; Glindemann, T.; Scholle, P.; Sinapius, M.; Hühne, C. : Bauteil zur verscherungsarmen Faserlagenumformung in einem Ablegekopf, App. no. 102017118876.2. *in progress*

## *Publications*

Niemann, S.; Kolesnikov, B.; Lohse-Busch, H.; Hühne, C.; Querin, O. M.; Toropov, V. V.; Liu, D. (2013): The use of topology optimisation in the conceptual design of next generation lattice composite aircraft fuselage structures. In *Aeronautical Journal* 117 (1197), pp. 1139–1154.

Niemann, S.; Wagner, R.; Beerhorst, M.; Hühne, C. (2017): Testing and analysis of Anisogrid Prepreg element specimens under uniaxial tension and compression. In *Composite Structures* 160, pp. 594–603. DOI: 10.1016/j.compstruct.2016.10.100.

## *Conference Proceeding-Papers*

Niemann, S.; Wagner, R.; Hühne, C. (2014): Design and Analytical Analysis of an Anisogrid Prepreg Structure Concept. In : European Conference on Composite Materials. ECCM. Sevilla, Spain, 22-26 Jun. European Society of Composite Materials. 16th ed.

Niemann, S.; Beerhorst, M.; Wagner, R.; Hühne, C. (2015): Testing and Analysis of Anisogrid Prepreg Element Specimen under Uniaxial Tension and Compression. In : International Conference on Composite Materials. ICCM. Copenhagen, Denmark, 19-24 Jul. 20th: International Committee on Composite Materials.

Niemann, S.; Wagner, R.; Hühne, C. (2016a): TESTING AND ANALYIS OF POST-BUCKLING BEHAVIOUR OF ANISOGRID PREPREG PANEL UNDER COMPRESSION. In : 5th Aircraft Structural Design Conference. ASDC. Manchester, Great Britain, 4.10.-6.10. Royal Aeronautics Society.

Hühne, C.; Niemann, S.; Shanygin, A.; Kondakov, I.; Wagner, R.; Dubovikov, E. (2016): ANISOGRID DESIGN FOR FUSELAGE PRIMARY STRUCTURES – RESULTS OF EU/RU PROJECTS ALASCA AND POLARBEAR. In : 5th Aircraft Structural Design Conference. ASDC. Manchester, Great Britain, 4.10.-6.10. Royal Aeronautics Society.

## 11 List of Figure

# 12 List of tables

# A Appendix – Element Tests

## A.1 Overview Laminate Stackings of Knot Specimens

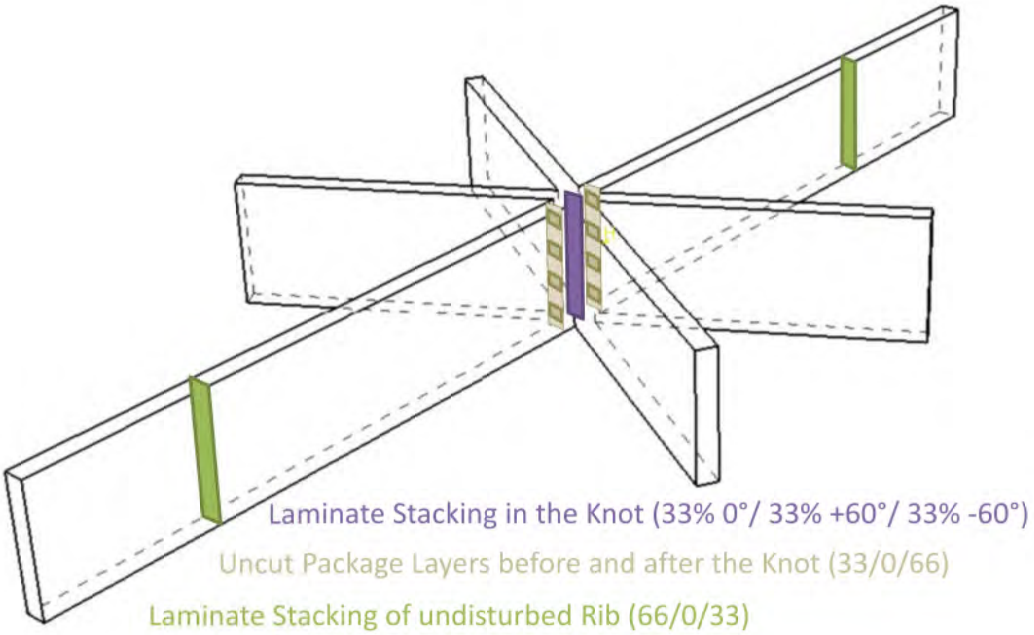

*App.Fig. 1: Laminate Stackings in the Grid-Knot Specimens*

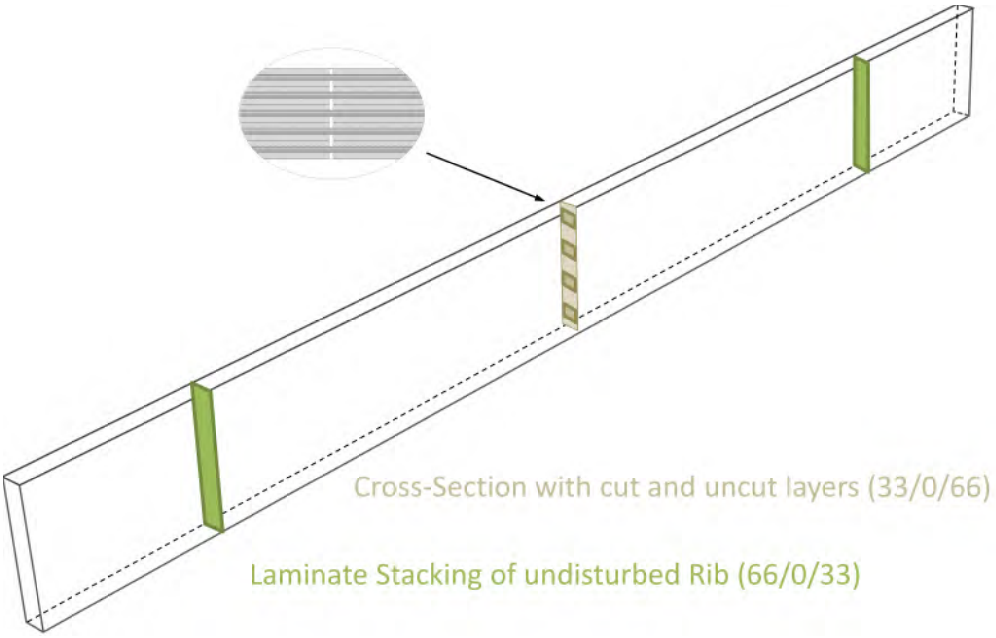

*App.Fig. 2: Laminate Stackings in the Plate-Knot Specimens*

## A.2 Result Details Tension

### A.2.1 Tension - Table with dimensions of all specimens

| | width [mm] | height [mm] |
|---|---|---|
| TEN-Lam-Rib-1 | 3.80 | 25.10 |
| TEN-Lam-Rib-2 | 3.84 | 25.10 |
| TEN-Lam-Rib-3 | 3.82 | 25.10 |
| TEN-Lam-Rib-4 | 3.71 | 25.10 |
| TEN-Lam-Rib-5 | 3.84 | 25.10 |
| TEN-Plt-Rib-1 | 4.07 | 18.40 |
| TEN-Plt-Rib-2 | 4.06 | 18.40 |
| TEN-Plt-Rib-3 | 3.99 | 18.30 |
| TEN-Plt-Rib-4 | 4.06 | 18.40 |
| TEN-Plt-Rib-5 | 4.08 | 18.30 |
| TEN-Plt-Rib-6 | 4.10 | 18.30 |
| TEN-Grid-Rib-1 | 4.92 | 17.60 |
| TEN-Grid-Rib-2 | 4.89 | 17.80 |
| TEN-Grid-Rib-3 | 4.89 | 18.00 |
| TEN-Grid-Rib-4 | 4.88 | 17.90 |
| TEN-Grid-Rib-5 | 4.86 | 18.00 |

| | width [mm] | height [mm] |
|---|---|---|
| TEN-Lam-Knot-1 | 3.83 | 25.00 |
| TEN-Lam-Knot-2 | 3.84 | 25.10 |
| TEN-Lam-Knot-3 | 3.83 | 25.10 |
| TEN-Lam-Knot-4 | 3.83 | 25.10 |
| TEN-Lam-Knot-5 | 3.84 | 25.10 |
| TEN-Plt-Knot-1 | 4.05 | 18.10 |
| TEN-Plt-Knot-2 | 4.05 | 18.40 |
| TEN-Plt-Knot-3 | 4.06 | 18.40 |
| TEN-Plt-Knot-4 | 4.05 | 18.40 |
| TEN-Plt-Knot-5 | 4.03 | 18.40 |
| TEN-CC-3-Knot-1 | 4.80 | 17.90 |
| TEN-CC-3-Knot-2 | 4.91 | 17.60 |
| TEN-CC-3-Knot-3 | 4.91 | 17.60 |
| TEN-CC-3-Knot-4 | 4.82 | 18.10 |
| TEN-CC-1-Knot-1 | 4.91 | 17.60 |
| TEN-CC-1-Knot-2 | 4.80 | 17.90 |
| TEN-CC-1-Knot-3 | 4.91 | 17.60 |
| TEN-CC-1-Knot-4 | 4.80 | 17.90 |

### A.2.2 Tension - Stress-strain curves of all specimens

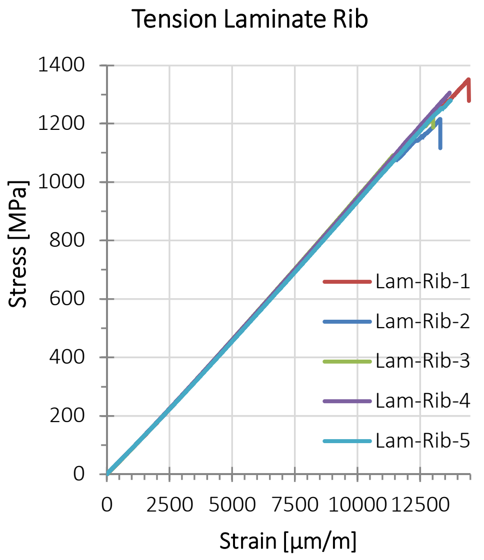

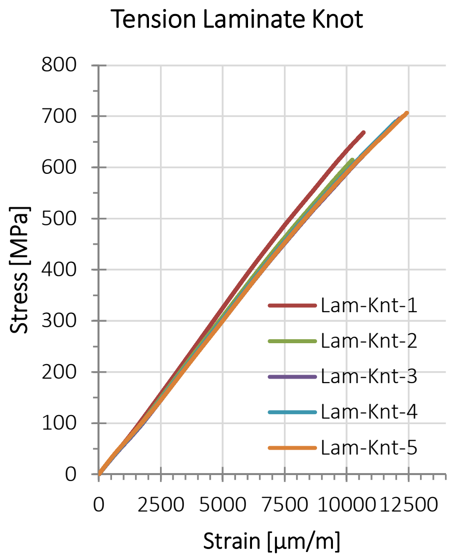

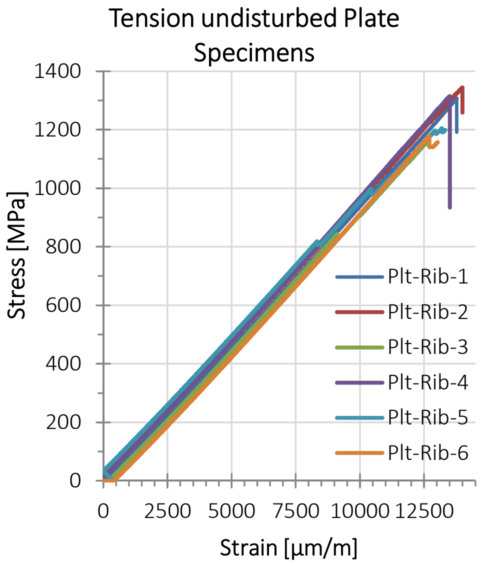

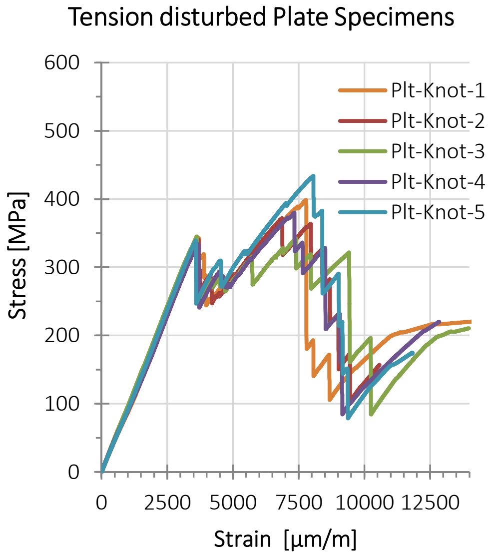

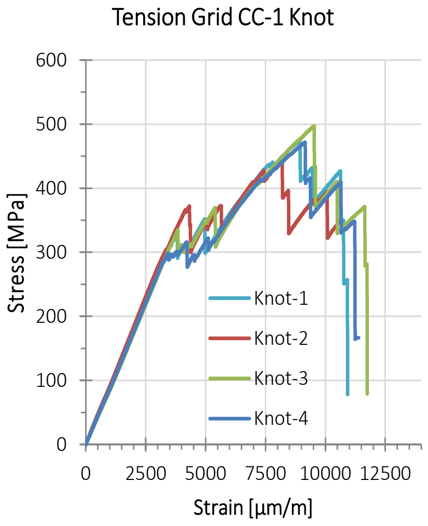

### A.2.3 Stress-Displacement-Curve of a Grid and Plate Knot under Tension

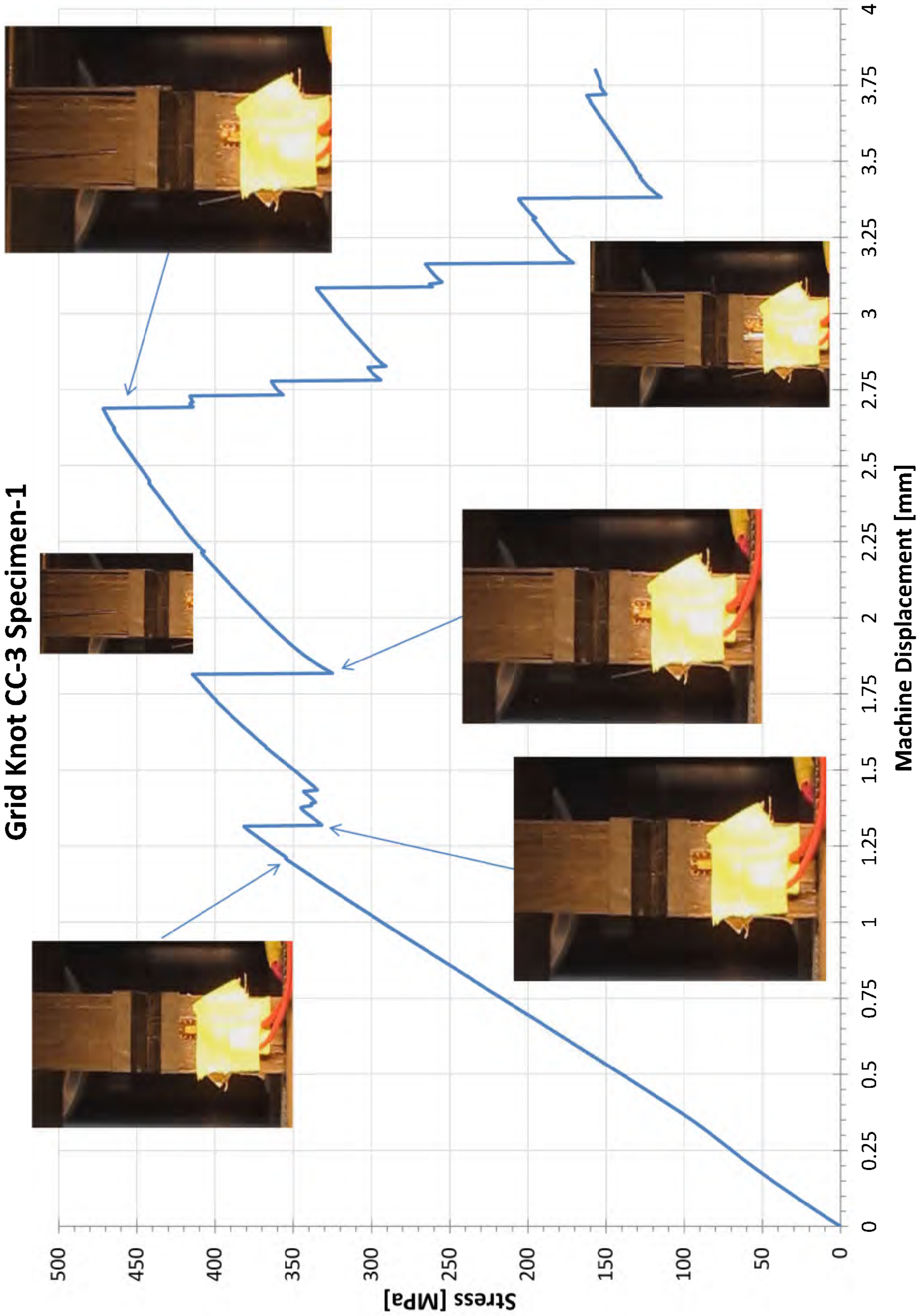

*App.Fig. 3: Stress-Displacement-Curve of a Grid-Knot CC-3 Specimen*

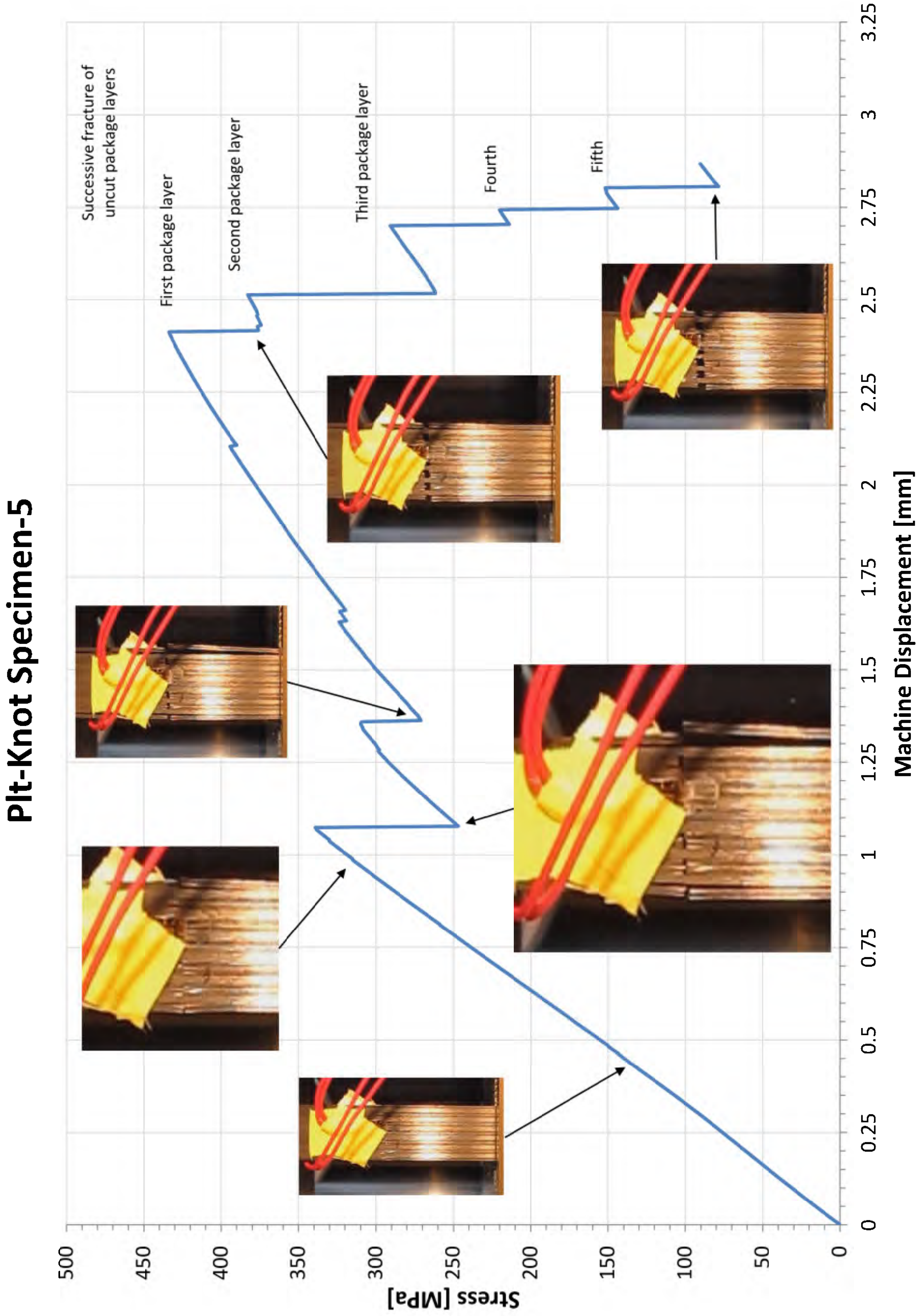

App.Fig. 4: Stress-Displacement-Curve of a disturbed Plate-Knot Specimen

## A.3 Result Details Compression

### A.3.1 Compression – Table with dimensions of all specimens

| | width [mm] | height [mm] |
|---|---|---|
| COM-Lam-Rib-1 | 3.80 | 25.10 |
| COM-Lam-Rib-2 | 3.76 | 25.10 |
| COM-Lam-Rib-3 | 3.85 | 25.10 |
| COM-Lam-Rib-4 | 3.85 | 25.10 |
| COM-Lam-Rib-5 | 3.85 | 25.10 |
| COM-Lam-Rib-6 | 3.85 | 25.10 |
| COM-Plt-Rib-1 | 3.86 | 18.30 |
| COM-Plt-Rib-2 | 4.04 | 18.40 |
| COM-Plt-Rib-3 | 4.06 | 18.40 |
| COM-Plt-Rib-4 | 4.02 | 18.40 |
| COM-Plt-Rib-5 | 4.07 | 18.40 |
| COM-Plt-Rib-6 | 4.03 | 18.40 |
| COM-Grid-Rib-1 | 4.93 | 17.80 |
| COM-Grid-Rib-2 | 4.90 | 17.80 |
| COM-Grid-Rib-3 | 4.95 | 17.80 |
| COM-Grid-Rib-4 | 4.83 | 18.00 |
| COM-Grid-Rib-5 | 4.83 | 18.00 |
| COM-Grid-Rib-6 | 4.92 | 18.00 |

| | width [mm] | height [mm] |
|---|---|---|
| COM-Lam-Knot-1 | 3.75 | 25.10 |
| COM-Lam-Knot-2 | 3.85 | 25.10 |
| COM-Lam-Knot-3 | 3.85 | 25.10 |
| COM-Lam-Knot-4 | 3.87 | 25.10 |
| COM-Lam-Knot-5 | 3.85 | 25.10 |
| COM-Lam-Knot-6 | 3.86 | 25.10 |
| COM-Plt-Knot-1 | 3.96 | 18.40 |
| COM-Plt-Knot-2 | 4.05 | 18.40 |
| COM-Plt-Knot-3 | 4.07 | 18.40 |
| COM-Plt-Knot-4 | 4.07 | 18.40 |
| COM-Plt-Knot-5 | 4.06 | 18.40 |
| COM-CC-3-Knot-1 | 4.66 | 18.10 |
| COM-CC-3-Knot-2 | 4.67 | 18.10 |
| COM-CC-3-Knot-3 | 4.60 | 18.10 |
| COM-CC-3-Knot-4 | 4.65 | 18.00 |
| COM-CC-3-Knot-5 | 4.67 | 18.00 |
| COM-CC-1-Knot-1 | 4.45 | 18.20 |
| COM-CC-1-Knot-2 | 4.43 | 18.10 |
| COM-CC-1-Knot-3 | 4.42 | 18.00 |
| COM-CC-1-Knot-4 | 4.50 | 17.90 |
| COM-CC-1-Knot-5 | 4.48 | 18.10 |

### A.3.2 Compression - Stress-strain curves of all specimens

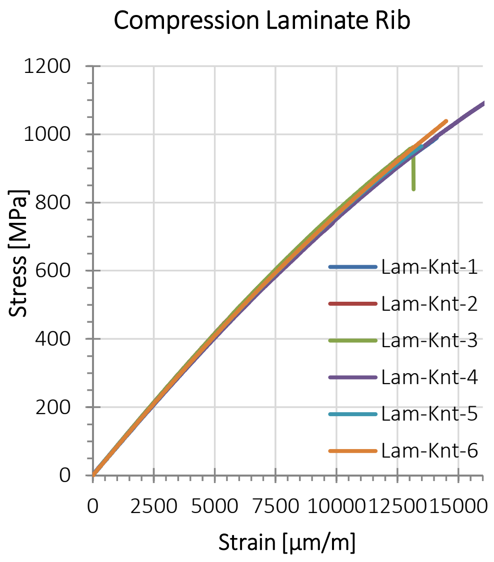

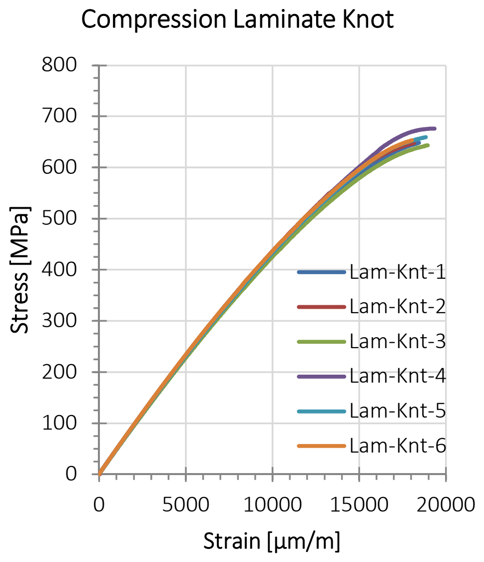

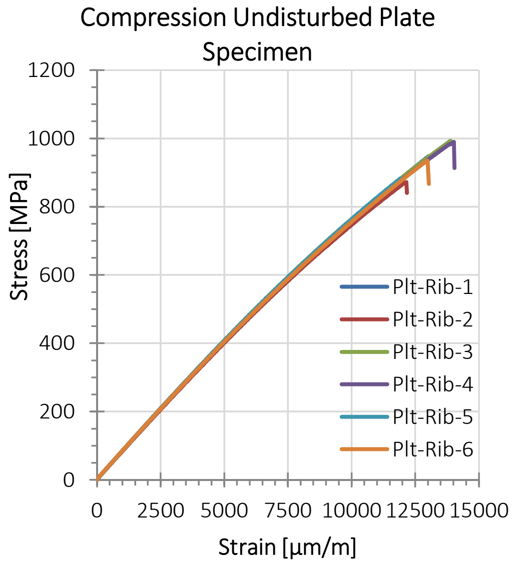

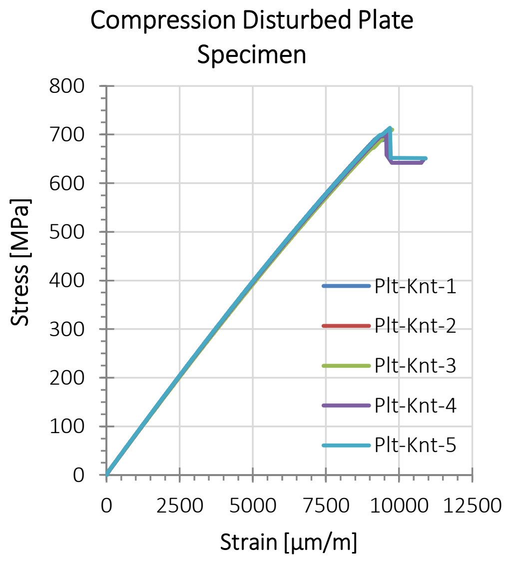

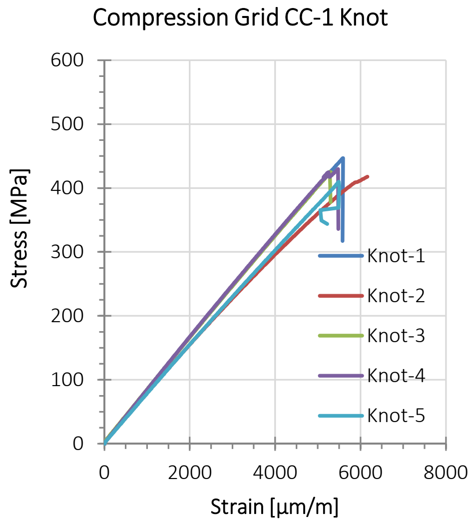

## A.4 Tensile Delamination Growth - Fracture Analysis

The low interlaminar strength of composites causes one of the main failure modes in composites which are delaminations. In fracture mechanics, three main separation modes are differentiated:

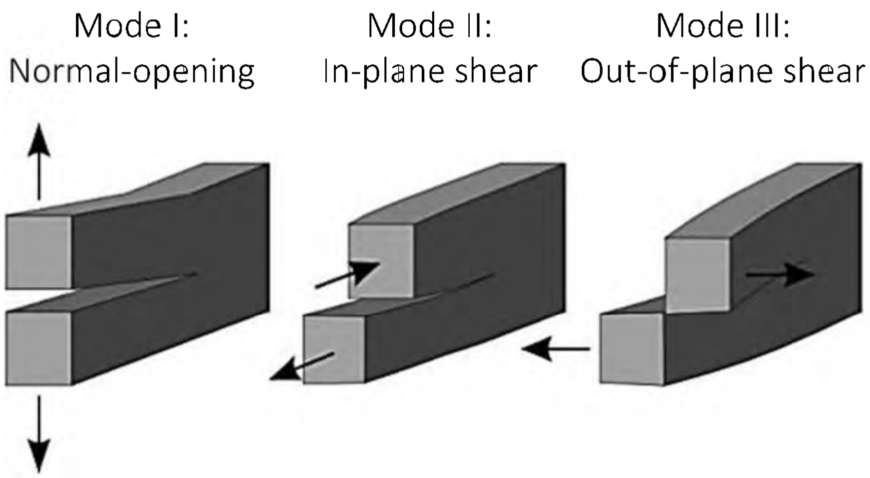

For the observed rib failure, the in-plane shear failure occurred. According to analytical investigations of A. Fink[1] for calculation of delamination stresses in CFRP-metal hybrid laminates, following model is used:

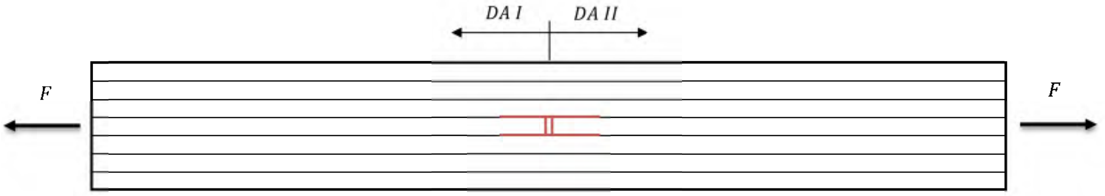

A matrix crack between two cut layers can be considered as two delamination areas (DA) where cracks/delaminations are initiated at both interfaces to the uncut layers (*j = 2*). Analysing one delamination area, the following model is deriving:

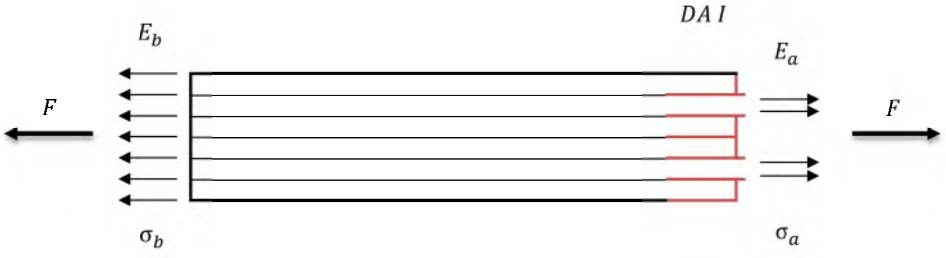

With this model and under consideration of fracture Mode II, the critical tensile load is calculated, at which the delamination grows through the interfaces of the uncut layers. As worst case, it is assumed that all cut layers are separated and cracks/delaminations are present.

---

[1] Fink, A.. 2010. Lokale Metall-Hybridisierung zur Effizienzsteigerung von Hochlastfügestellen in Faserverbundstrukturen. Dissertation. Technical University of Braunschweig

The critical tensile stress for delamination growth can be calculated with following equation for the plain stress state:

$$\sigma_{ten\,del} = -\frac{\lambda_2}{2\lambda_1} + \sqrt{\left(\frac{\lambda_2}{2\lambda_1}\right)^2 + \frac{jG_{IIc} - \lambda_3}{\lambda_1}}$$

with

$$\lambda_1 = h_b\left(\frac{h_b}{h_a E_a} - \frac{1}{E_b}\right) - \frac{1}{2}\sum_{i=1}^{n_a}\left(\frac{h_b}{h_a E_a}\right)^2 E_i h_i + \frac{1}{2}\sum_{i=1}^{n_b}\frac{E_i h_i}{{E_b}^2}$$

$$\lambda_2 = h_b \Delta T(\alpha_a - \alpha_b)$$

$$\lambda_3 = -\frac{1}{2}\sum_{i=1}^{n_a}\frac{h_i}{E_i}\sigma_{t,i,a}^2 - \frac{1}{2}\sum_{i=1}^{n_b}\frac{h_i}{E_i}\sigma_{t,i,b}^2$$

| | | |
|---|---|---|
| $G_{IIc}$ | Energy release rate; material value by Karnati[2] | $G_{IIc} = 1.146\frac{J}{m}$ ; (8552/AS4) |
| $h_b$ | Height of plain rib | $h_b = 18\,mm$ |
| $h_a$ | Sum of uncut/0° layer heights | $h_a = 6\,mm$ |
| $j$ | Amount of delaminations | e.g. for 1mm-thick package layers<br>$j = 12$ |
| $E_b$ | Youngs modulus of plain rib | $E_b = 70\,GPa$ |
| $E_a$ | Youngs modulus of 0° layers | $E_a = 141\,GPa$ |
| $\Delta T$ | Temperature difference for consideration of residual stresses | $\Delta T = 0\,K$<br>(more relevant for hybrid materials) |
| $\sigma_{t,i,a}, \sigma_{t,i,b}$ | Residual stresses in the layers | $\sigma_{t,i,a}, \sigma_{t,i,b} = 0$ |
| $\alpha_a$ , $\alpha_b$ | Thermal expansion coefficients | |

---

[2] Karnati, S.R. 2014. A Mixed-Mode (I-II) Fracture Criterion for AS4/8552 Carbon/Epoxy Composite Laminate. Master Thesis. Greensboro, North Carolina.

# B Appendix – Panel Analysis

## B.1 Sizing Criteria

Following information are given to the implemented design criteria in the analytical tool according to the manual.

### B.1.1 Global Panel Stability

For the global panel stability analysis an energy-based method is used computed with the help of Rayleigh-Ritz variation method. With this criterion/approach, following configurations can be analysed: flat plate, cylindrical shells or full cylinders; combinations of simply-supported, clamped and free boundary conditions; fully anisotropic material properties.

The methodology is based on the constancy of energy and can be written as stationary potential energy theorem:

$$V + U + Q - T = constant$$

V = strain energy

U = potential energy of membrane loads

Q = potential energy of lateral loads

T = kinetic energy

For a static deflection problem, the kinetic energy becomes zero and for the stability problem the lateral loads are also neglected:

$$V + \lambda U = constant$$

where λ is the buckling eigenvalue.

With the Rayleigh-Ritz method the displacement function of the panel is approximated by a linear combination of trial functions. The unknown displacements u, v, w are represented by a double Fourier series (width and length in panel direction):

$$u = \sum_{m=m_i}^{m_f} \sum_{n=n_i}^{n_f} a_{1mn} X_{1m}(x) Y_{1m}(y) \sin(\omega\tau)$$

$$v = \sum_{m=m_i}^{m_f} \sum_{n=n_i}^{n_f} a_{2mn} X_{2m}(x) Y_{2m}(y) \sin(\omega\tau)$$

$$w = \sum_{m=m_i}^{m_f} \sum_{n=n_i}^{n_f} a_{3mn} X_{3m}(x) Y_{3m}(y) \sin(\omega\tau)$$

with

$$m_i = i_x;\ m_f = i_x + n_x - 1$$

$$n_i = i_y;\ n_f = i_y + n_y - 1$$

### B.1.2 Local Stiffener Stability

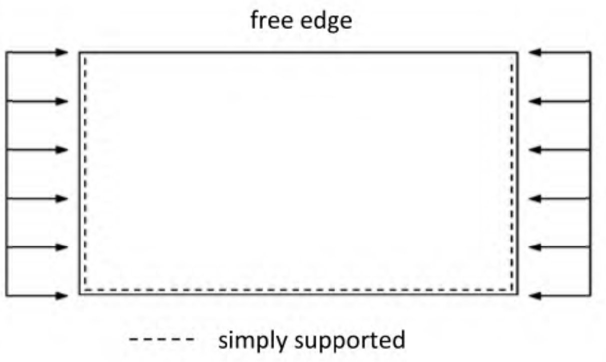

The local stability of a blade stiffener is calculated as a three-sided simply-supported plate with one long free edge. To simplify an exact but calculation costly solution for a general laminate due to the one free plate edge, the buckling load is calculated for the orthotropic simply-supported plate on all 4 edges, by:

$$N_{xcrit} = \frac{-\pi^2 \left[ D_{11} \left(\frac{m}{a}\right)^2 + 2(D_{12} + 2D_{66}) \left(\frac{n}{b}\right)^2 + D_{11} \left(\frac{n}{b}\right)^4 \left(\frac{a}{m}\right)^2 \right]}{1 + \left(\frac{N_y}{N_x}\right) \left(\frac{a}{b}\right)^2 \left(\frac{n}{m}\right)^2}$$

and reduced by a constant knock-down factor *K*, derived from buckling coefficients of long isotropic plates:

$$N_{x\,crit\,SSSF} = \frac{K}{3.62} * N_{x\,crit\,SSSS}$$

The D-terms are the bending terms of the plate stiffness matrix. The length of the plate is *a* and the width *b*. The number of buckling half-waves is expressed by *m* in length and *n* in width direction. The equation has to be minimized by selection of the number of integer half-waves (m and n) resulting in the lowest critical load.

### B.1.3 Local Skin-bay Stability

The implemented local stability criterion for isosceles triangular skin-bays under different in-plane loadings is based on the NACA TN-3781. As the NACA guideline is not covering all load combinations the criterion is adapted to FEA studies on stiffened panels.

During this study the implemented method is compared to the semi-analytical results from Weber and FEA results given by HyperSizer. It shows that the Weber buckling values of an unstiffened triangular skin-bay matches well with the HyperSizer FEA results under different loadings.

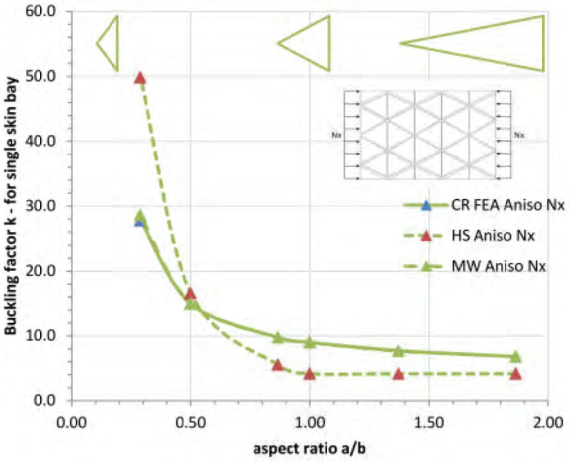

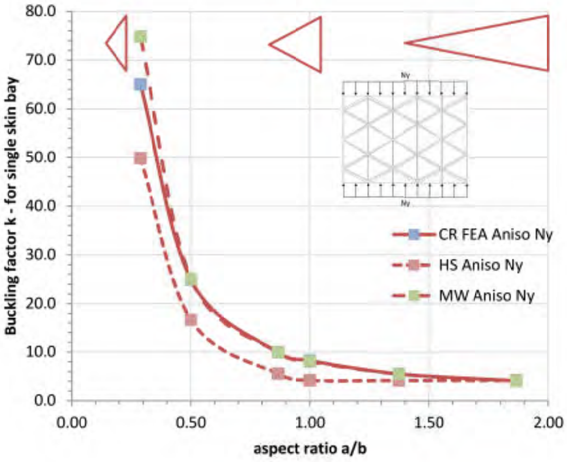

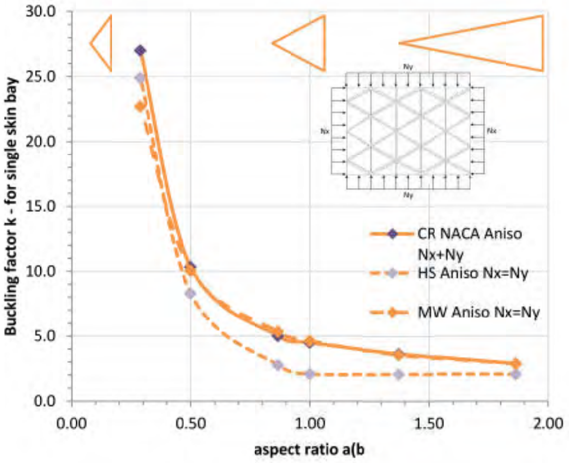

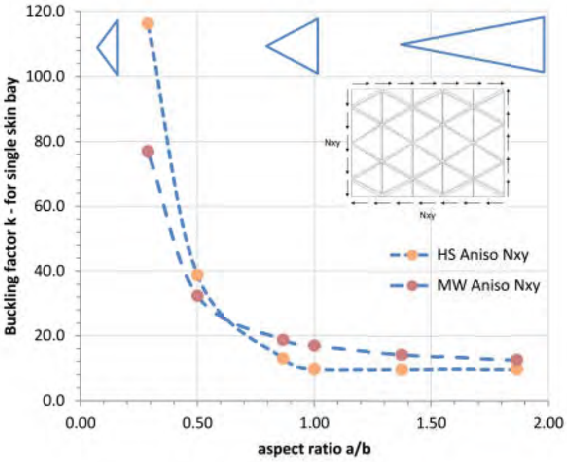

On stiffened panels, it showed that, due to the internal adaptation of the HyperSizer criterion to stiffened panel FE results, the HyperSizer implemented method gives the better correlation even when the fundamental buckling criterion on an unstiffened skin-bay is not matching so well. Accordingly, the study is carried out without implementation of the Weber buckling values as originally intended.

## B.2 Example for Panel Sizing Procedure

The iterative sizing process is shown as an example for the uniaxial compressive load case on the flat panel. In the following table, the results for the Unit weight are listed according to five iteration steps:

| Com Load | Iteration 1 | Iteration 2 | Iteration 3 | Iteration 4 | Iteration 5 |
|---|---|---|---|---|---|
| **50** | 3.153 | 3.040 | 2.924 | 2.854 | 2.816 |
| **100** | 4.671 | 4.262 | 4.020 | 3.963 | 3.898 |
| **150** | 5.784 | 4.872 | 4.926 | 4.776 | 4.723 |
| **200** | 6.201 | 5.516 | 5.508 | 5.409 | 5.409 |
| **250** | 6.441 | 6.226 | 5.987 | 6.027 | 5.993 |
| **300** | 6.821 | 6.763 | 6.665 | 6.486 | 6.484 |
| **350** | 7.236 | 7.154 | 7.037 | 7.009 | 6.956 |
| **400** | 8.088 | 7.711 | 7.526 | 7.477 | 7.443 |
| **450** | 8.474 | 8.190 | 7.942 | 7.843 | 7.825 |
| **500** | 9.018 | 8.345 | 8.400 | 8.221 | 8.254 |
| **550** | 9.511 | 8.862 | 8.662 | 8.658 | 8.647 |
| **600** | 9.807 | 9.100 | 9.144 | 9.006 | 8.904 |
| **650** | 9.867 | 9.774 | 9.506 | 9.344 | 9.368 |
| **700** | 10.052 | 10.017 | 9.819 | 9.699 | 9.633 |
| **750** | 10.411 | 10.411 | 10.074 | 9.916 | 9.919 |
| **800** | 10.411 | 10.411 | 10.390 | 10.235 | 10.194 |
| **850** | 10.955 | 10.806 | 10.653 | 10.579 | 10.496 |
| **900** | 11.321 | 10.988 | 10.913 | 10.882 | 10.765 |
| **950** | 11.445 | 11.324 | 11.230 | 11.084 | 11.090 |
| **1000** | 11.779 | 11.611 | 11.448 | 11.378 | 11.291 |

The percentage change of the unit weight is shown in the following diagram. It can be seen that the unit weight in relation to the last iteration step is achieved relatively fast in 3 iterations within 5%:

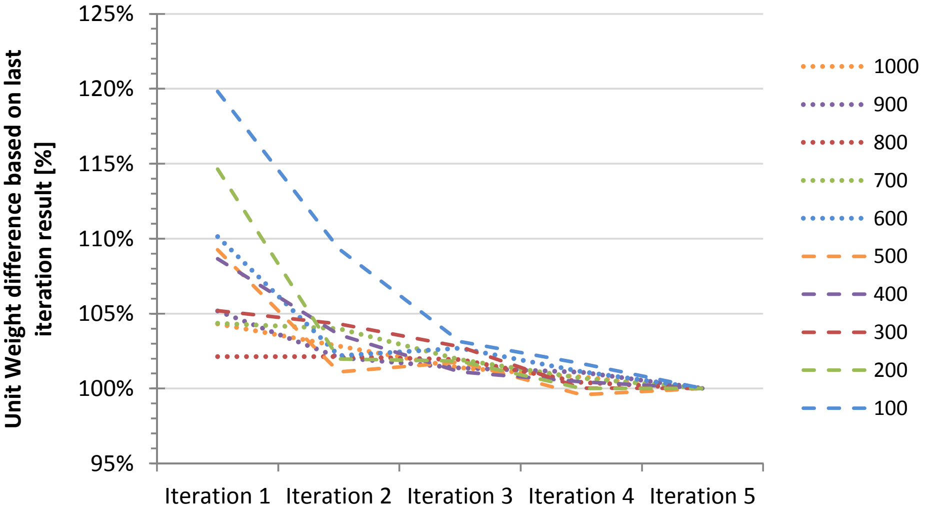

In the following, the inputs (Max and Min values) and results of the first and second iteration step are plotted for all sizing variables. Additionally, the results of the previous iteration step are plotted, which are the basis for the Max/Min values of the active iteration.

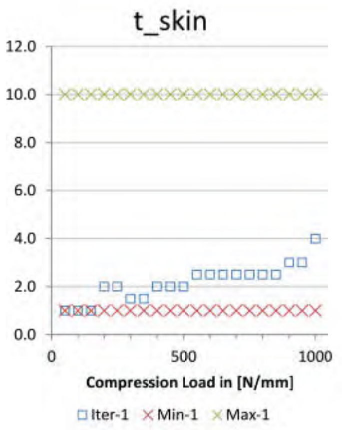
t_skin
12.0
10.0
8.0
6.0
4.0
2.0
0.0
0
500
1000
Compression Load in [N/mm]
□ Iter-1 × Min-1 × Max-1

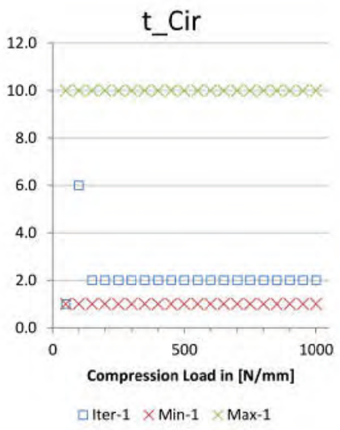
t_Cir
12.0
10.0
8.0
6.0
4.0
2.0
0.0
0
500
1000
Compression Load in [N/mm]
□ Iter-1 × Min-1 × Max-1

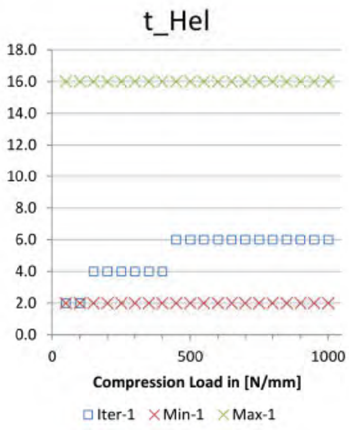
t_Hel
18.0
16.0
14.0
12.0
10.0
8.0
6.0
4.0
2.0
0.0
0
500
1000
Compression Load in [N/mm]
□ Iter-1 × Min-1 × Max-1

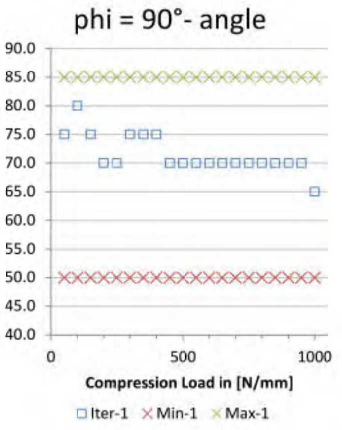
phi = 90°- angle
90.0
85.0
80.0
75.0
70.0
65.0
60.0
55.0
50.0
45.0
40.0
0
500
1000
Compression Load in [N/mm]
□ Iter-1 × Min-1 × Max-1

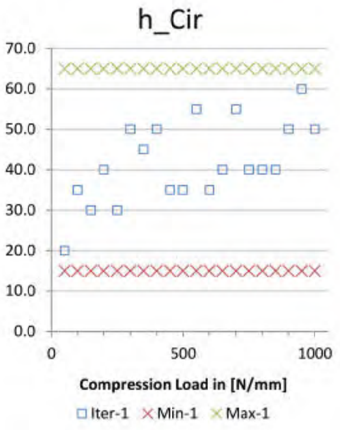
h_Cir
70.0
60.0
50.0
40.0
30.0
20.0
10.0
0.0
0
500
1000
Compression Load in [N/mm]
□ Iter-1 × Min-1 × Max-1

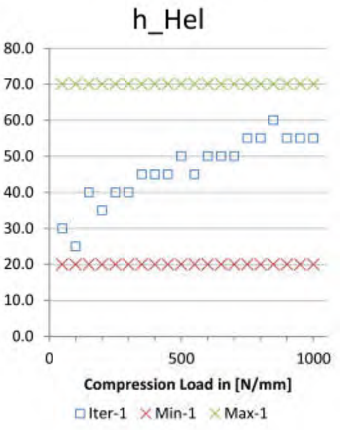
h_Hel
80.0
70.0
60.0
50.0
40.0
30.0
20.0
10.0
0.0
0
500
1000
Compression Load in [N/mm]
□ Iter-1 × Min-1 × Max-1

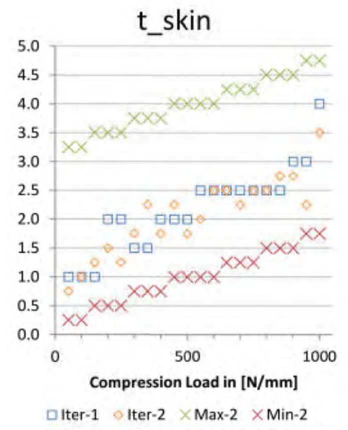
t_skin
5.0
4.5
4.0
3.5
3.0
2.5
2.0
1.5
1.0
0.5
0.0
0
500
1000
Compression Load in [N/mm]
□ Iter-1 ◇ Iter-2 × Max-2 × Min-2

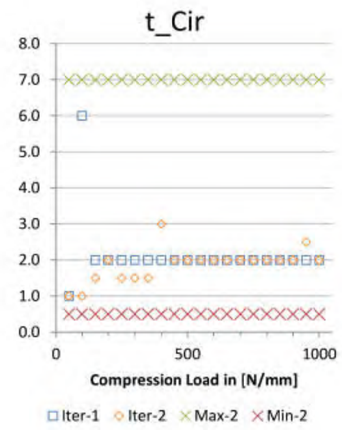
t_Cir
8.0
7.0
6.0
5.0
4.0
3.0
2.0
1.0
0.0
0
500
1000
Compression Load in [N/mm]
□ Iter-1 ◇ Iter-2 × Max-2 × Min-2

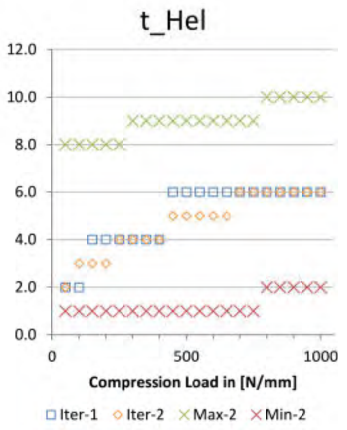
t_Hel
12.0
10.0
8.0
6.0
4.0
2.0
0.0
0
500
1000
Compression Load in [N/mm]
□ Iter-1 ◇ Iter-2 × Max-2 × Min-2

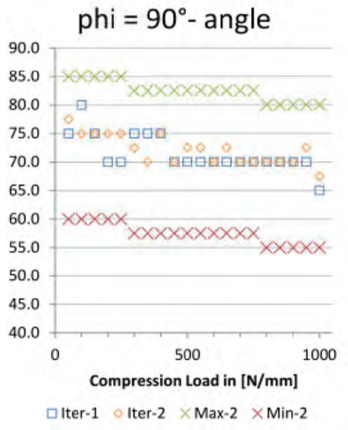
phi = 90°- angle
90.0
85.0
80.0
75.0
70.0
65.0
60.0
55.0
50.0
45.0
40.0
0
500
1000
Compression Load in [N/mm]
□ Iter-1 ◇ Iter-2 × Max-2 × Min-2

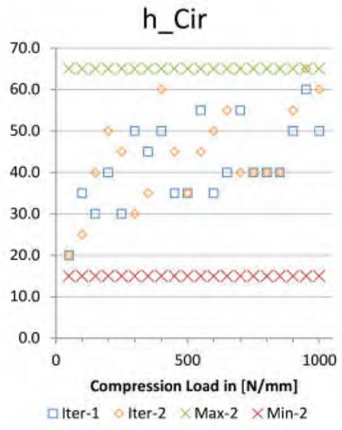
h_Cir
70.0
60.0
50.0
40.0
30.0
20.0
10.0
0.0
0
500
1000
Compression Load in [N/mm]
□ Iter-1 ◇ Iter-2 × Max-2 × Min-2

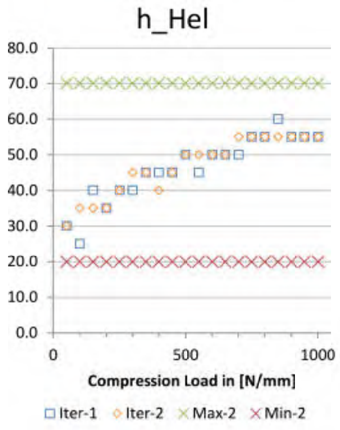
h_Hel
80.0
70.0
60.0
50.0
40.0
30.0
20.0
10.0
0.0
0
500
1000
Compression Load in [N/mm]
□ Iter-1 ◇ Iter-2 × Max-2 × Min-2

## B.3 Results Combination of Compression and Shear

### B.3.1 Anisogrid Panel – flat

***Compression (1:1) Shear - Variables***

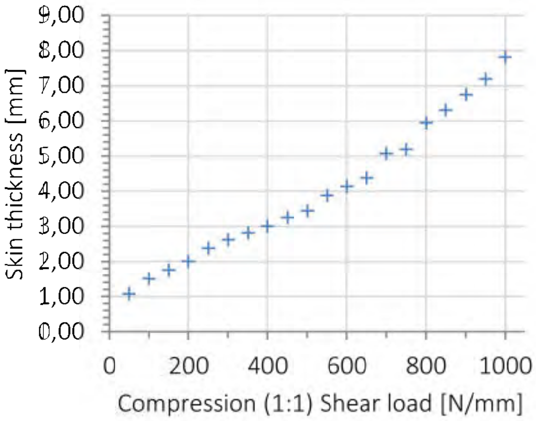

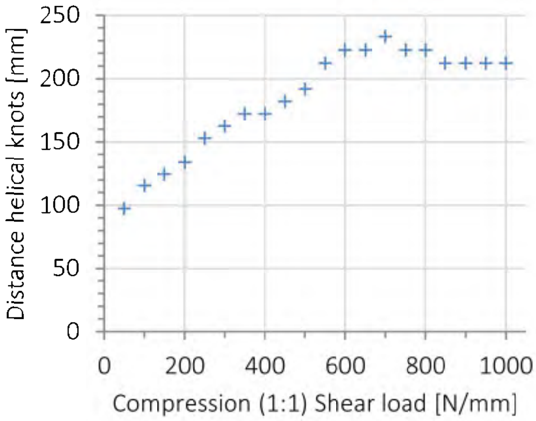

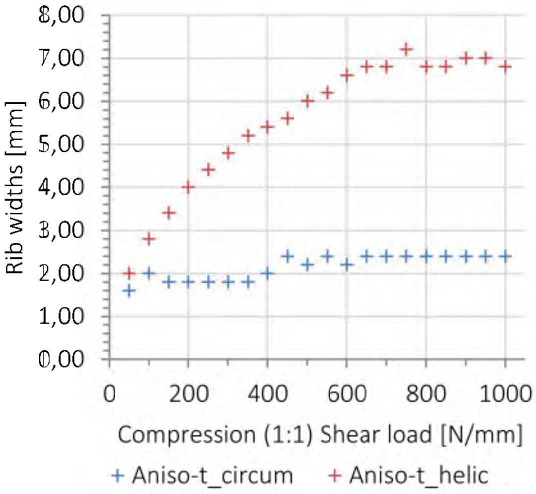

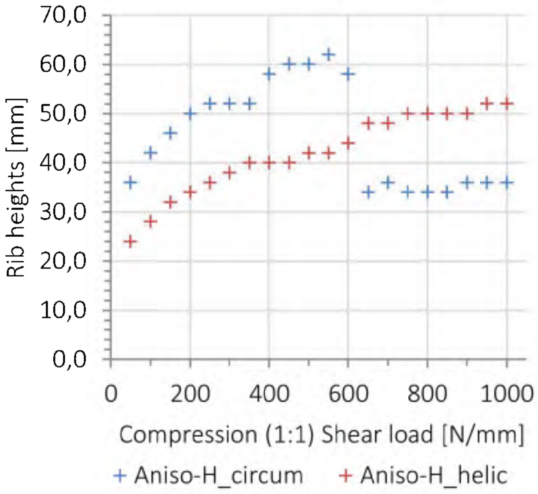

### *Compression (1:0.5) Shear*

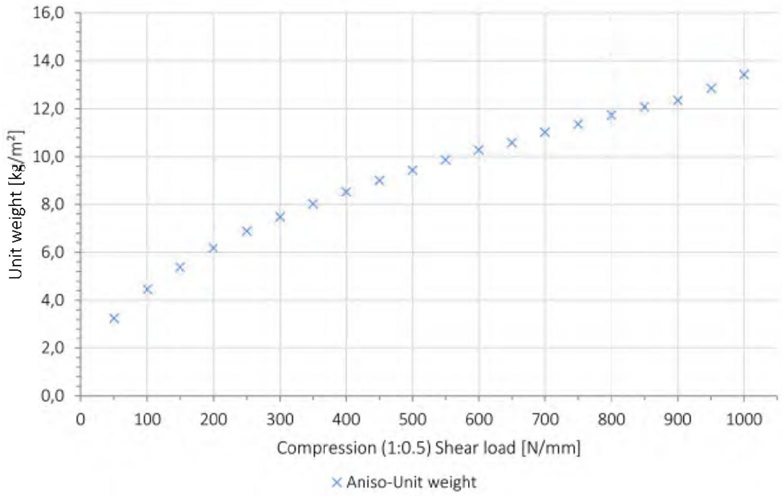

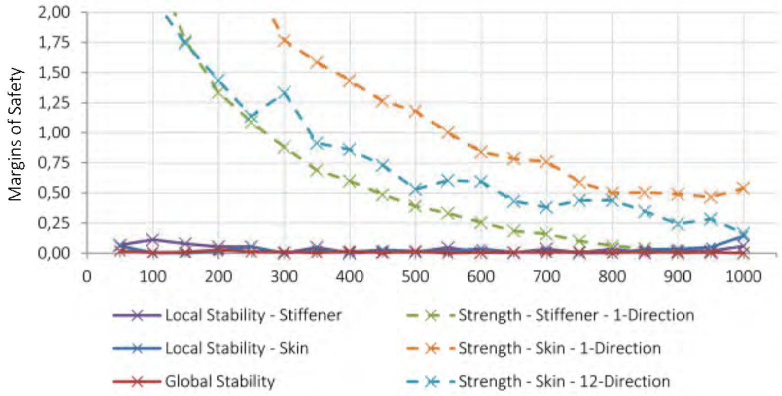

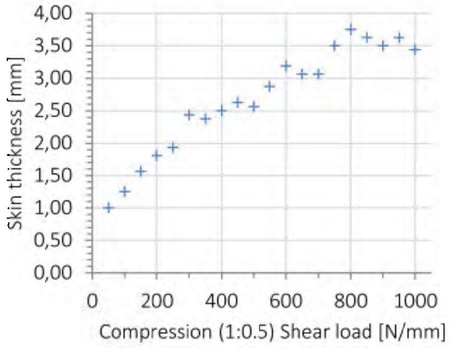

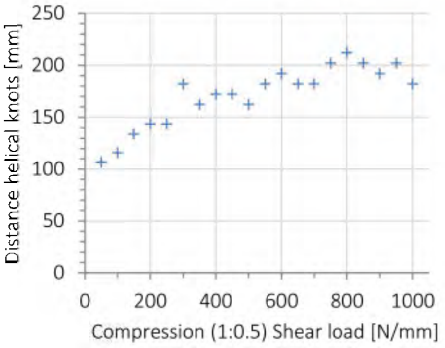

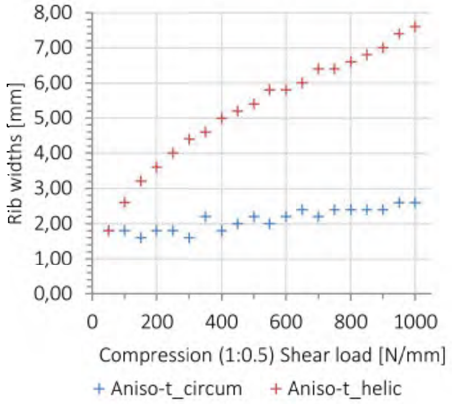

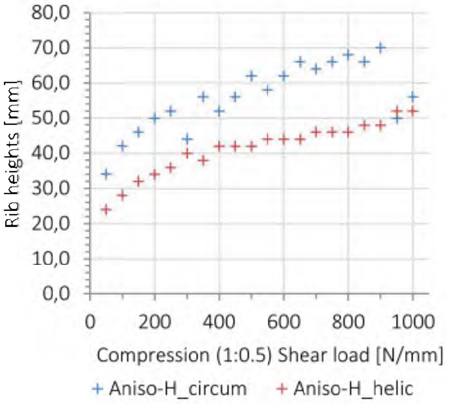

### *Compression (0.5:1) Shear*

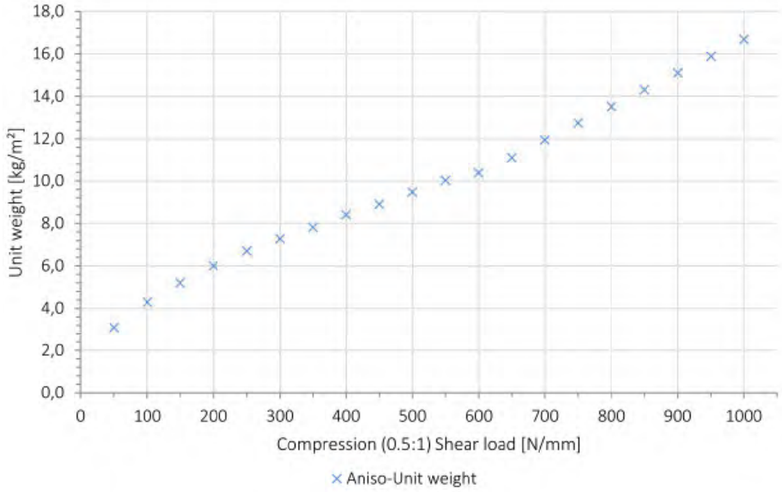

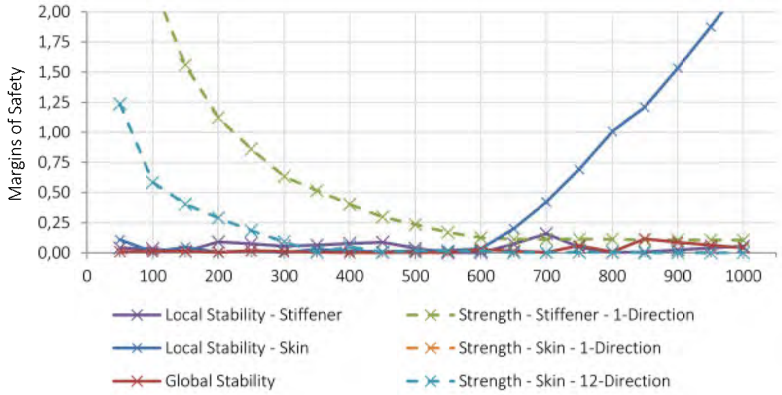

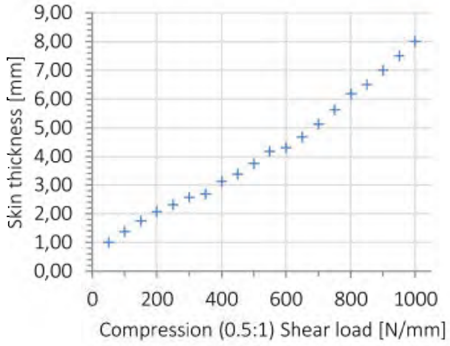

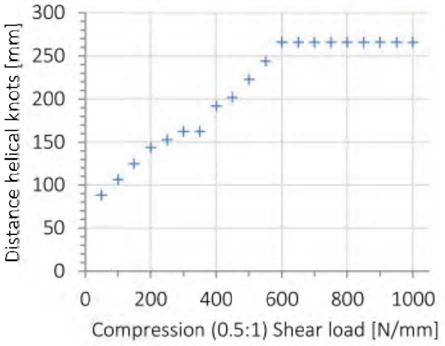

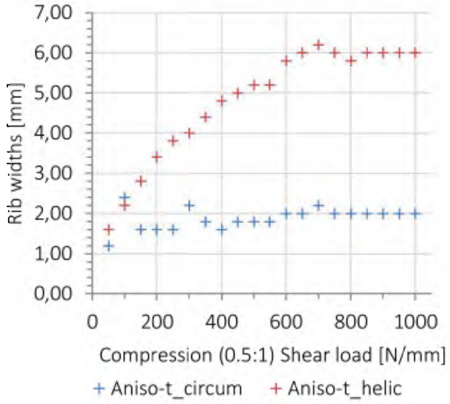

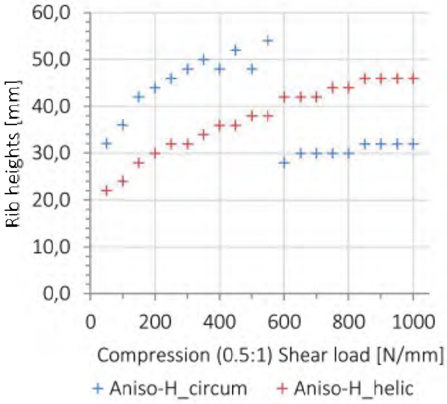

## B.3.2 Anisogrid Panel – curved

### *Compression (1:1) Shear - Variables*

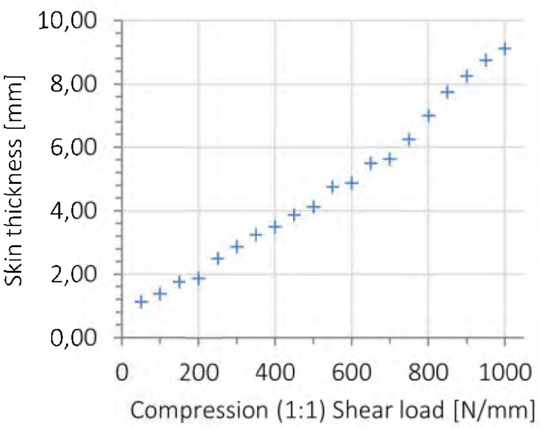

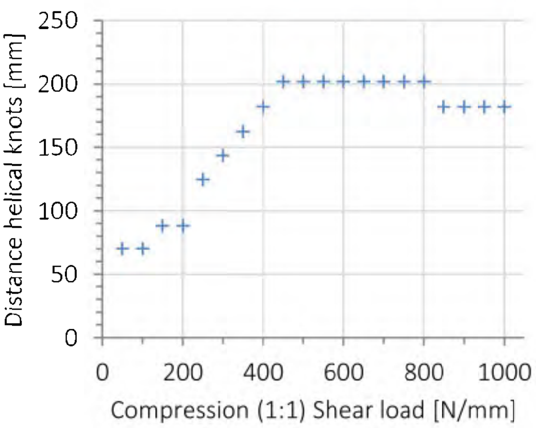

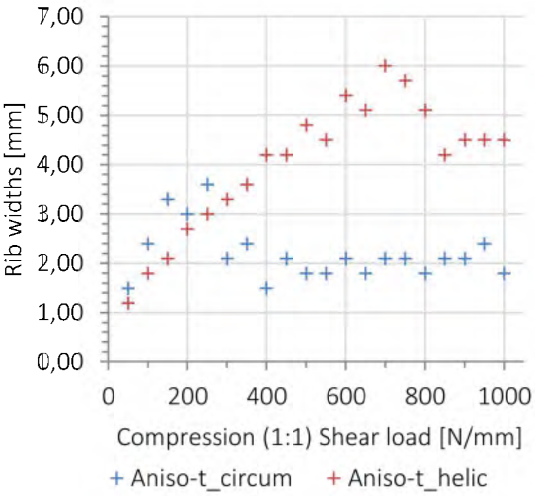

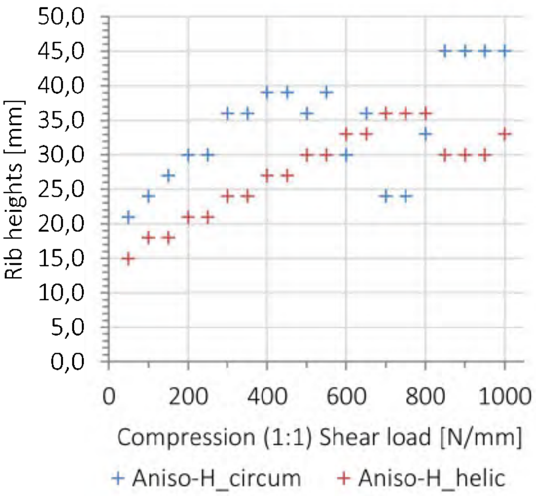

### ***Compression (1:0.5) Shear***

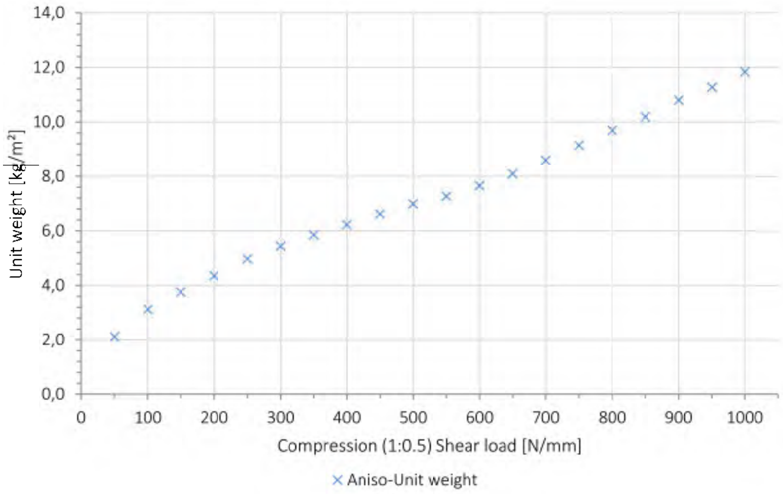

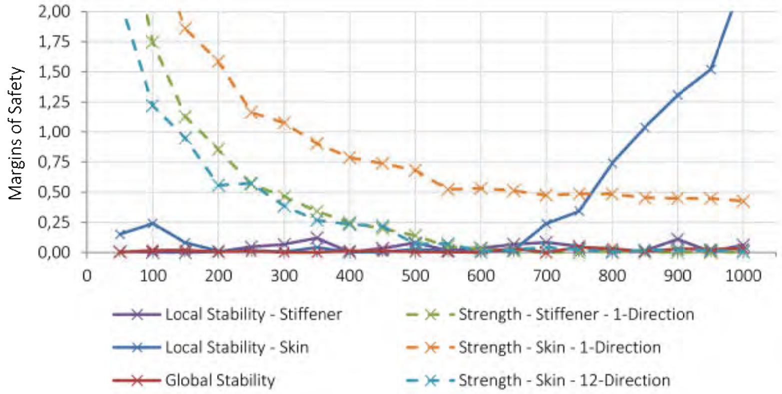

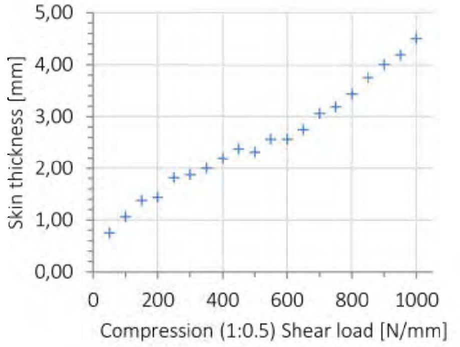

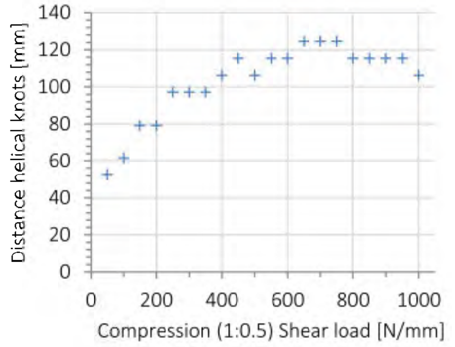

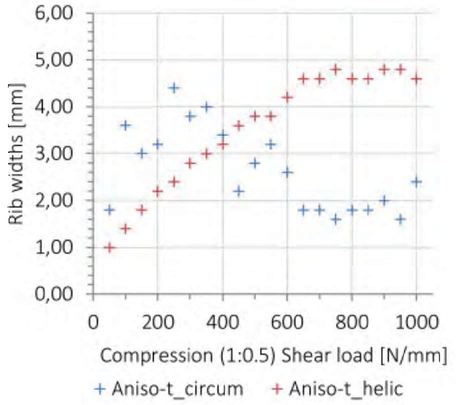

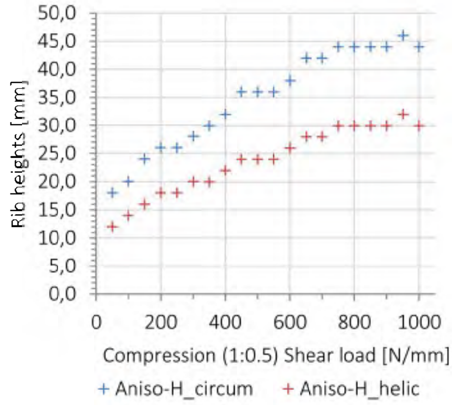

## *Compression (0.5:1) Shear*

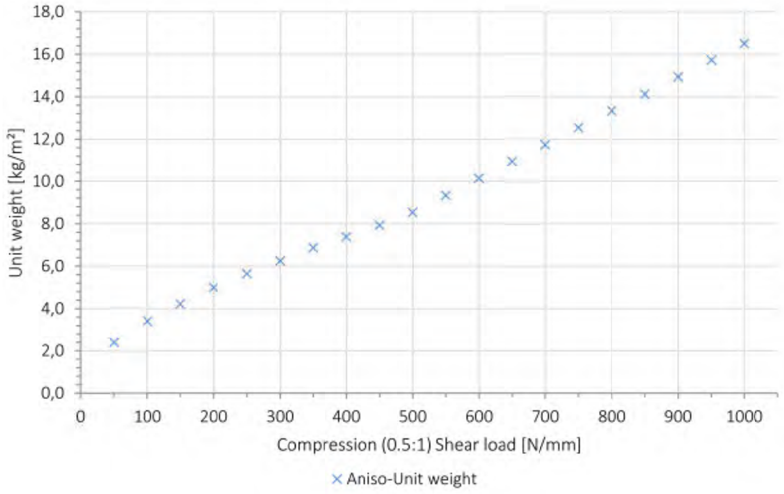

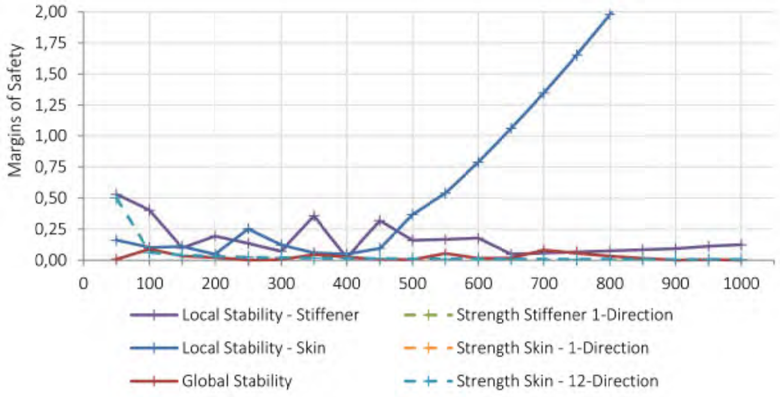

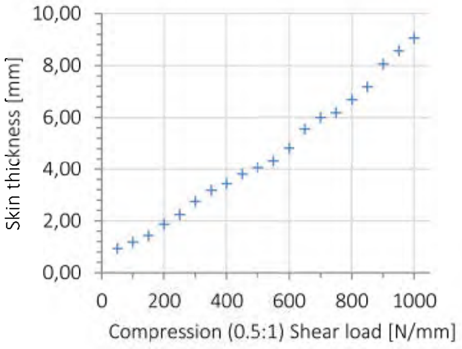

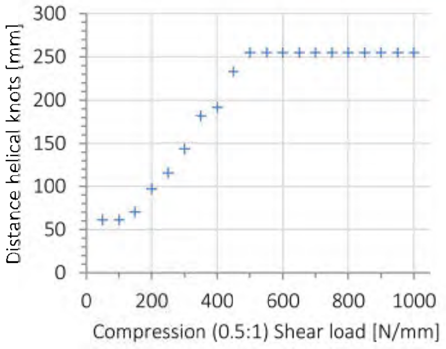

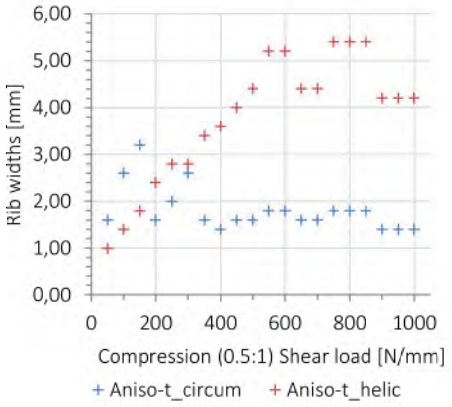

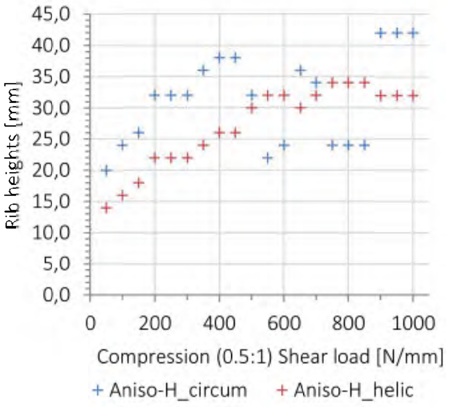

## B.3.3 Orthogrid Panel – flat

### *Compression (1:1) Shear - Variables*

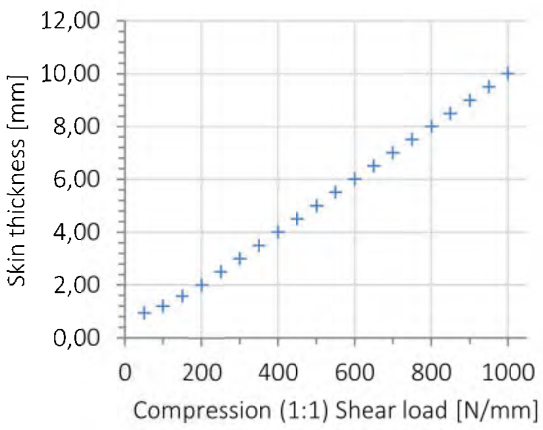

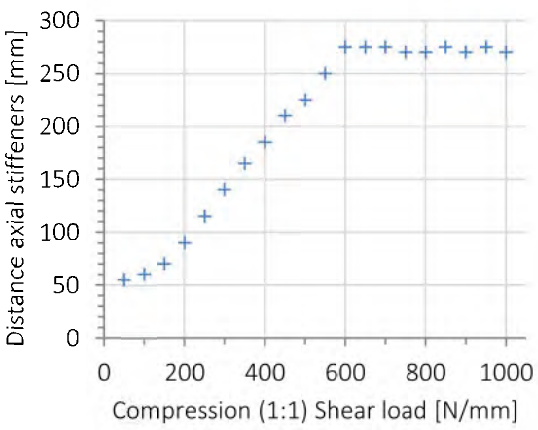

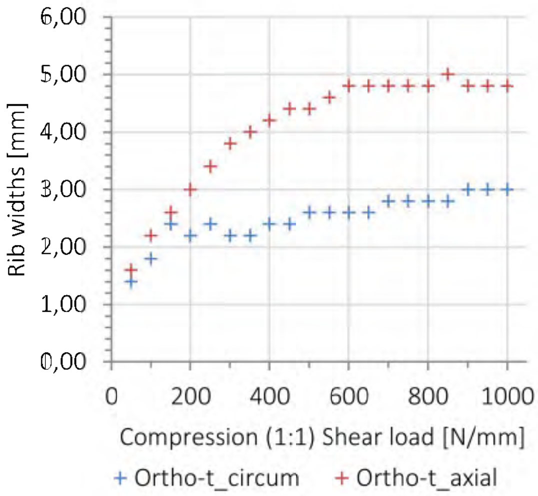

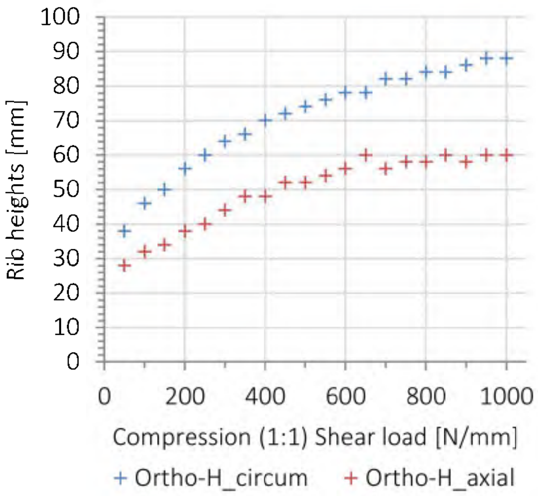

### *Compression (1:0.5) Shear*

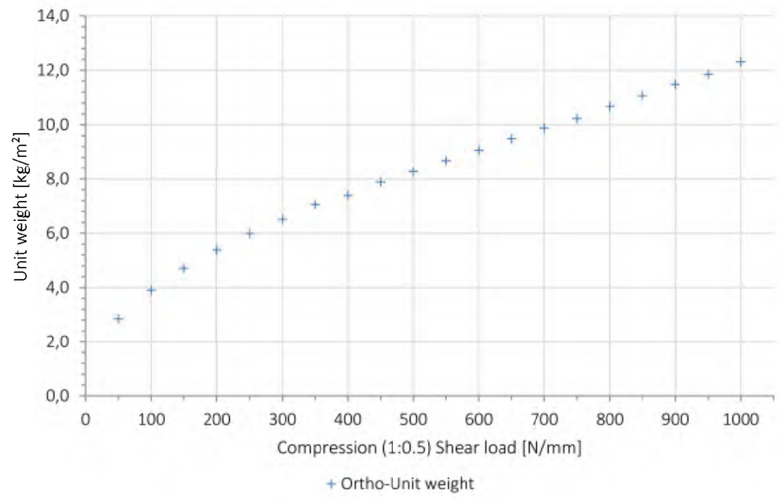

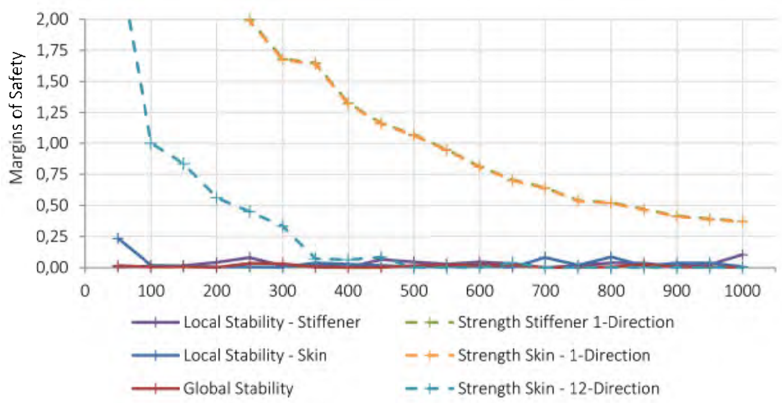

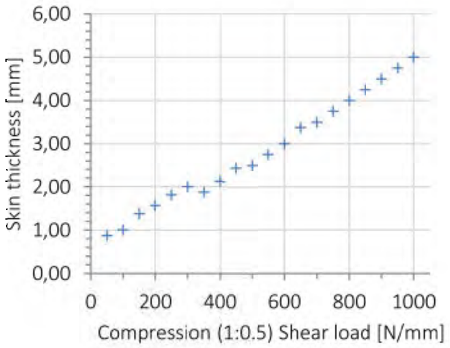

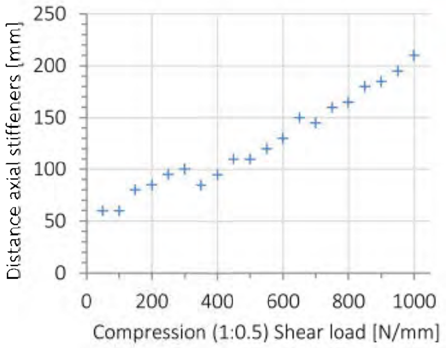

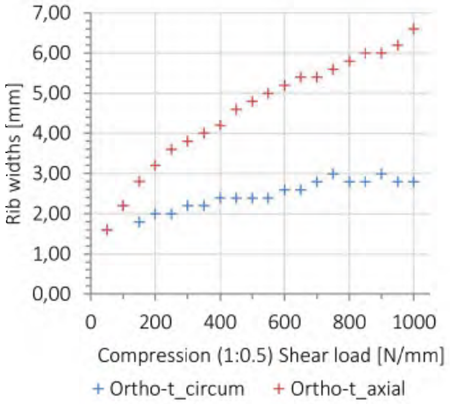

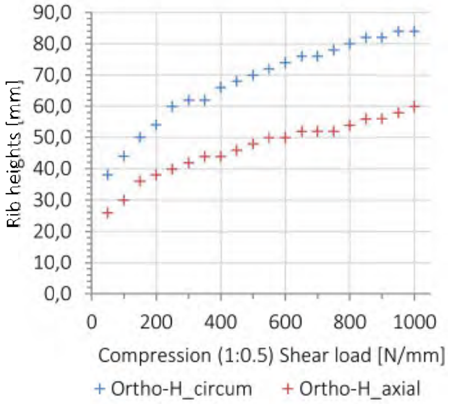

## ***Compression (0.5:1) Shear***

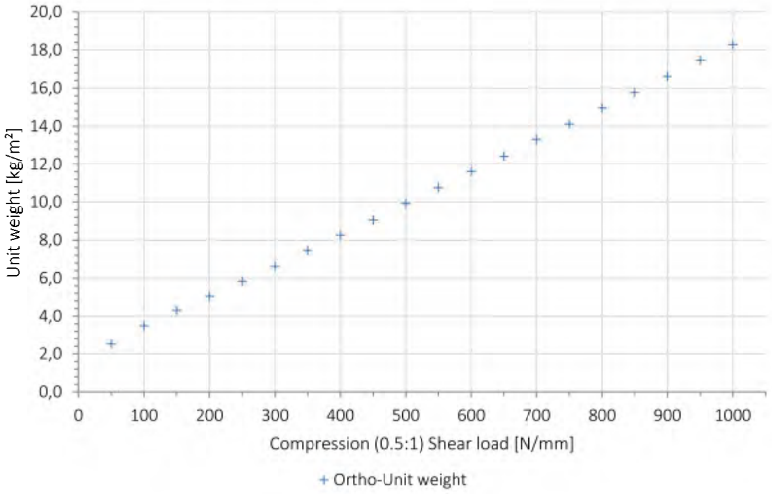

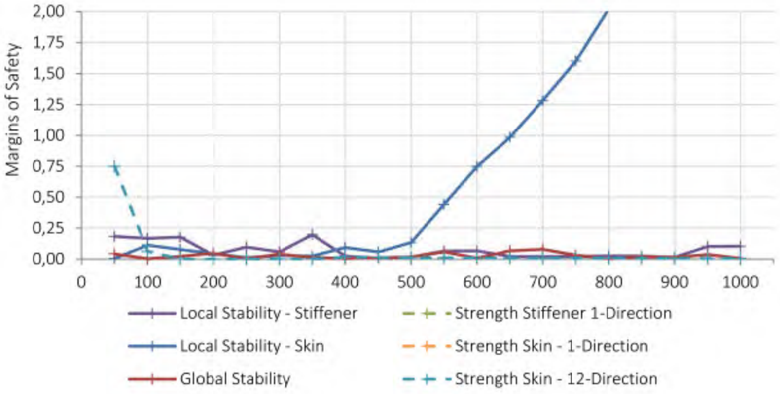

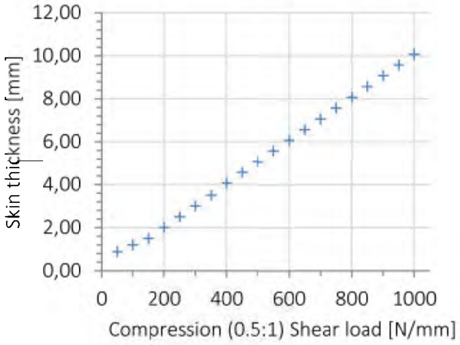

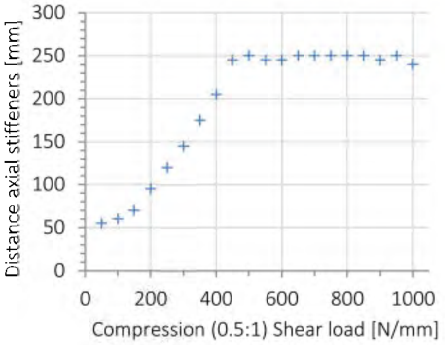

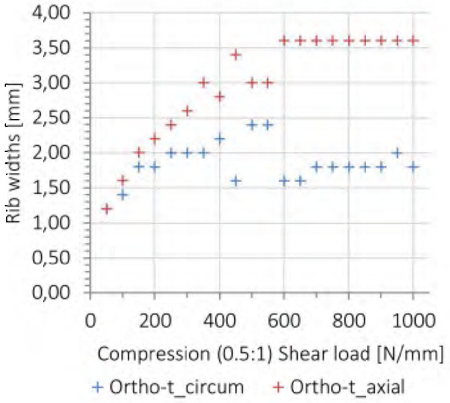

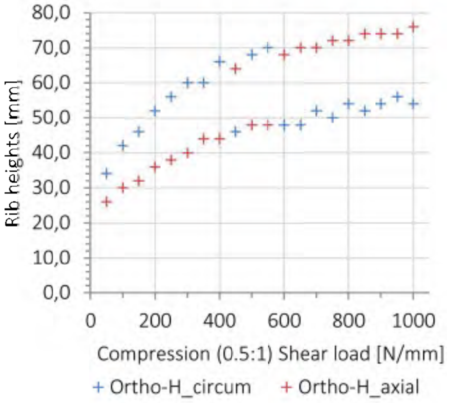

### B.3.4 Orthogrid Panel – curved

***Compression (1:1) Shear - Variables***

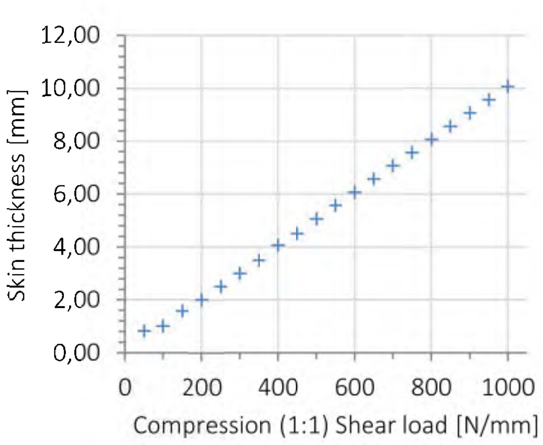

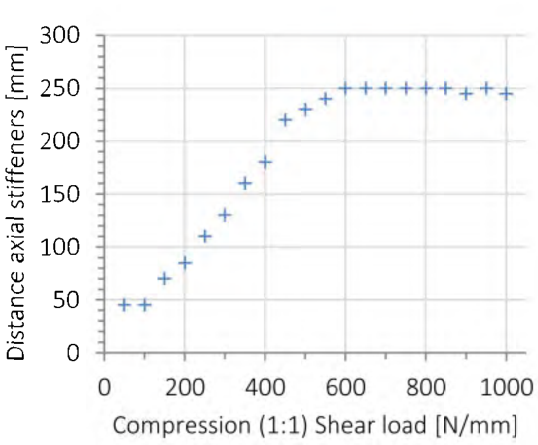

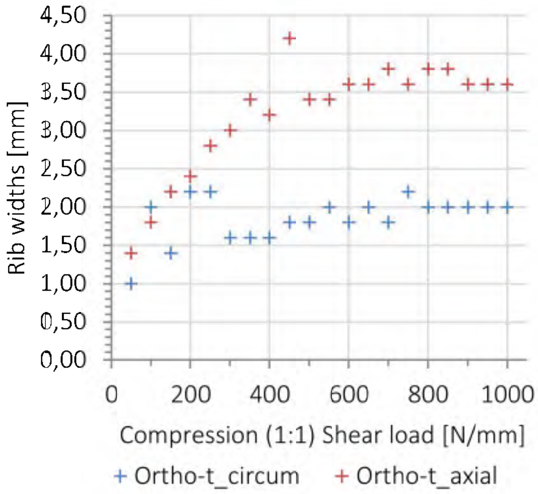

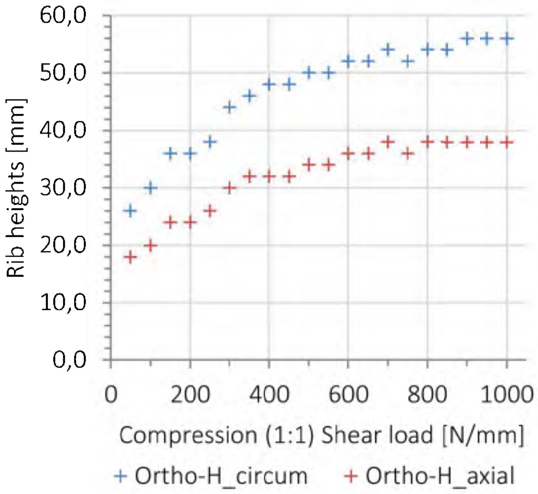

## *Compression (1:0.5) Shear*

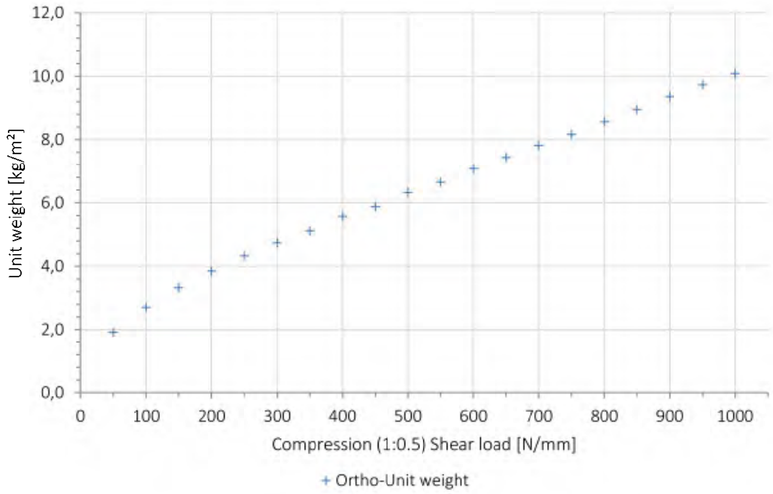

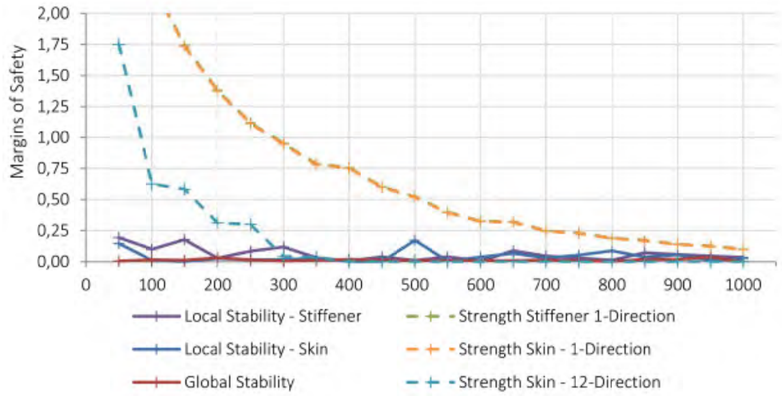

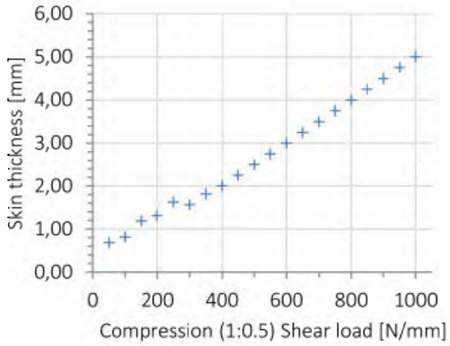

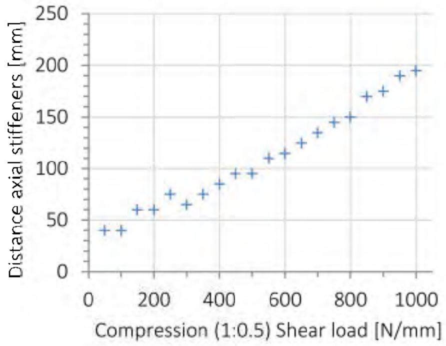

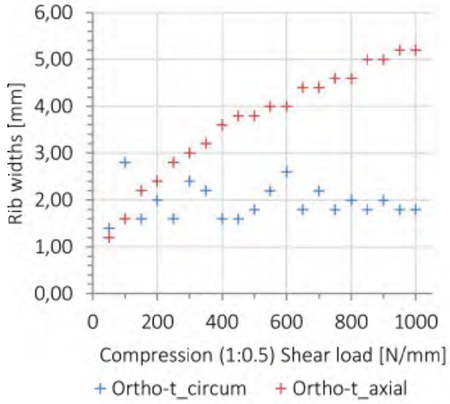

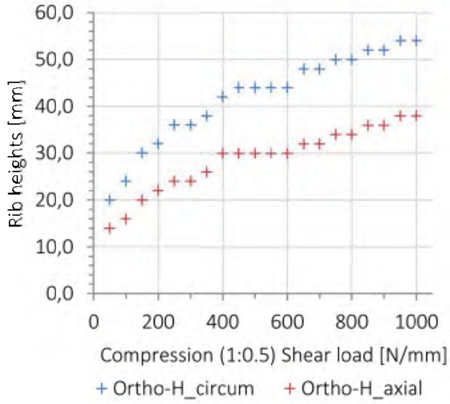

## *Compression (0.5:1) Shear*

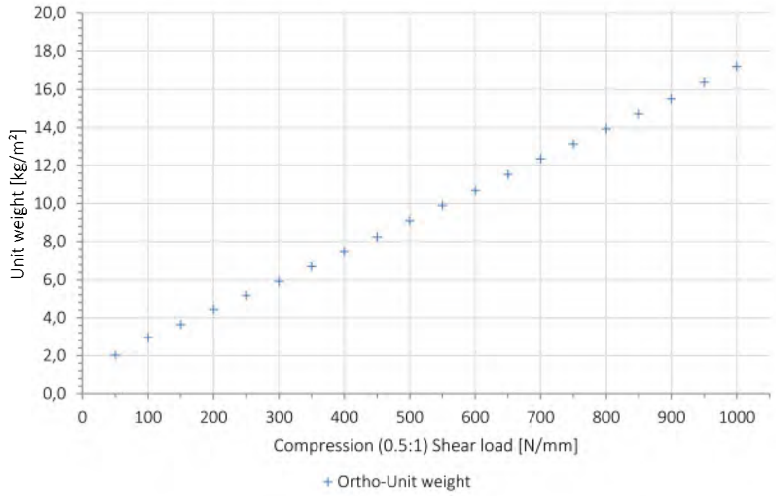

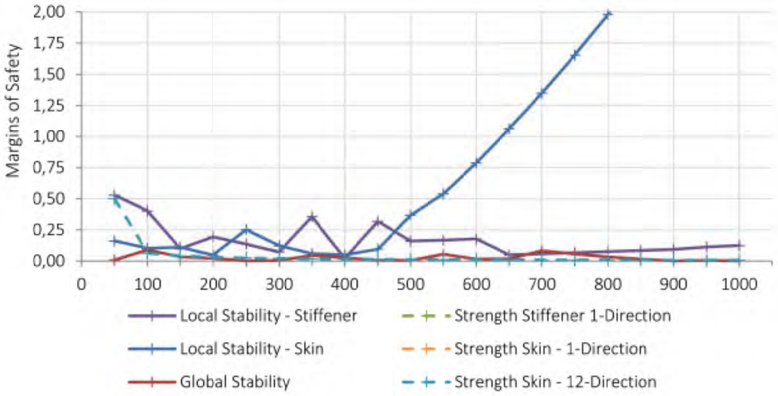

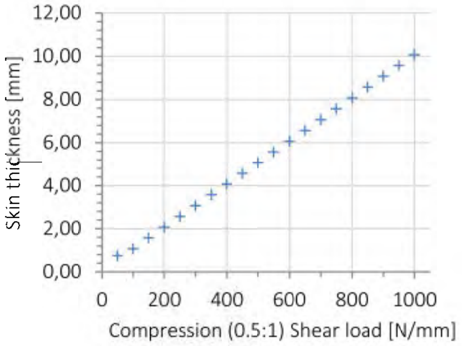

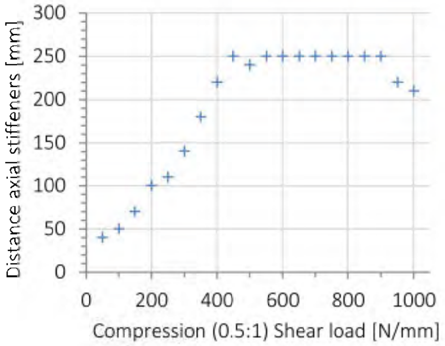

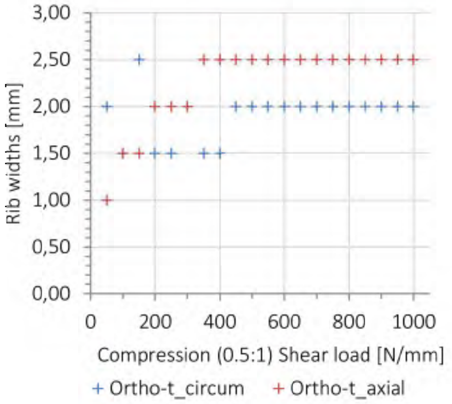

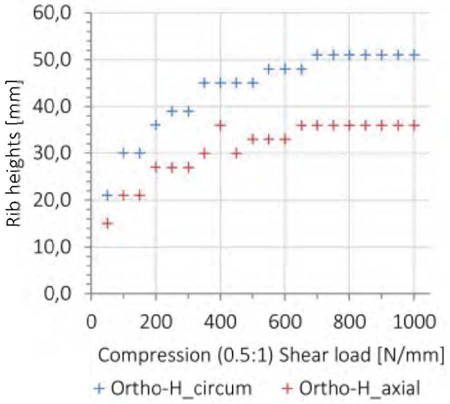

# C – Appendix – Test Panel

## C.1 Test Results Panel Test

In the following, the load-displacement curve of the panel test is shown. These are the values measured directly by the machine during the test:

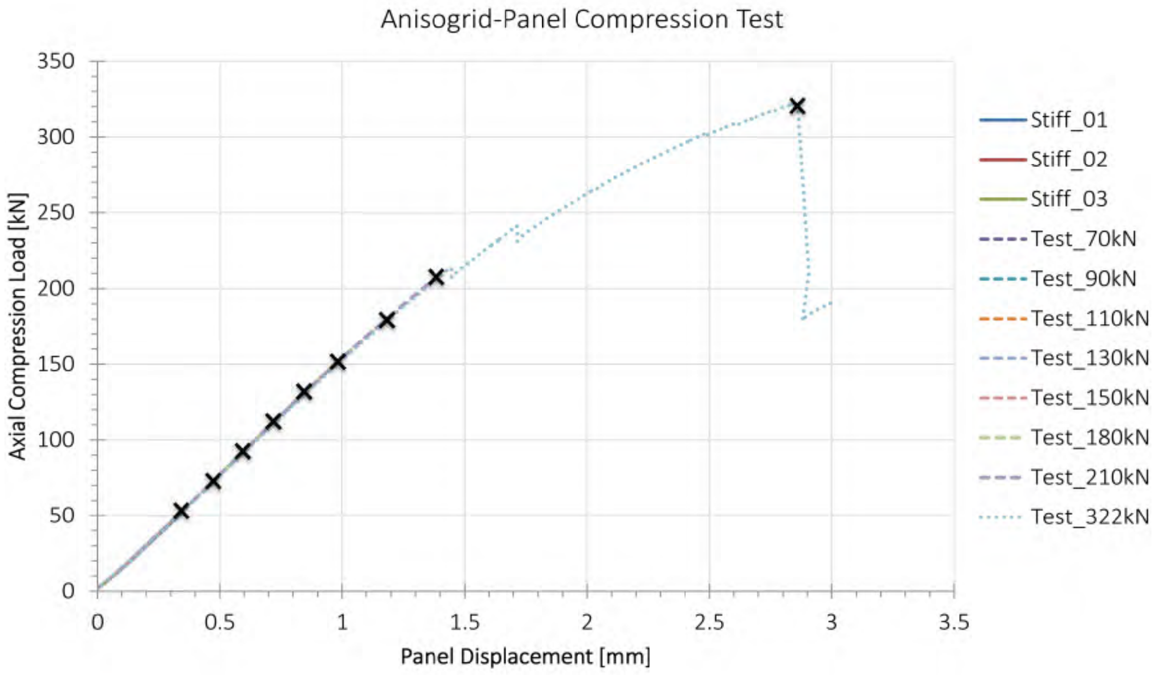

## C.2 Reverse-Calculation of Knot Failure Using Element Test Results

For the reverse-calculation, the maximum strains are used, measured at the rib positions. On the compression side of the panel almost 4000 microstrains are measured. However, this is not the position of maximum bending, which is found directly at the centre knots at the central horizontal rib.

In the grid-knot element tests under compression a maximum compressive strain of 10375 microstrain were obtained in the grid-ribs ($E_{Rib} = 80GPa, \sigma_{com} = 830MPa$). In contrast to the element tests, 8552/AS7 prepreg is used for the grid structure of the test panel, instead of 8552AS4. Under consideration of the slightly higher modulus of the AS7 fibres ($E_{0°\,Tension} = 141\ GPa\ , E_{0°\,Compression} = 141 * 0{,}9 = 130\ GPa$ ), assuming the same maximum strain times the amount of uncut fibres, a maximum compressive stress results of:

$$\sigma_{Rib,compr} = 130\ GPa * 0.010375\ \frac{mm}{mm}\ * 0.3333 = 451MPa$$

Comparing this with the rib modulus of the panel, of 104GPa, and the measured strain:

$$\sigma_{Rib,Panel} = 104\ GPa * 0.004\ \frac{mm}{mm}\ = 416MPa$$

Assuming that in the centre of the panel slightly higher strains occurred in the rib, the brief reverse-calculation show that the knot-failure most likely caused the panel failure.

## C.3 Panel Deformation at Subsequent Test Runs

Out-of-plane deformation each at approx. 0.89 mm global panel displacement for the sequent test runs:

VI

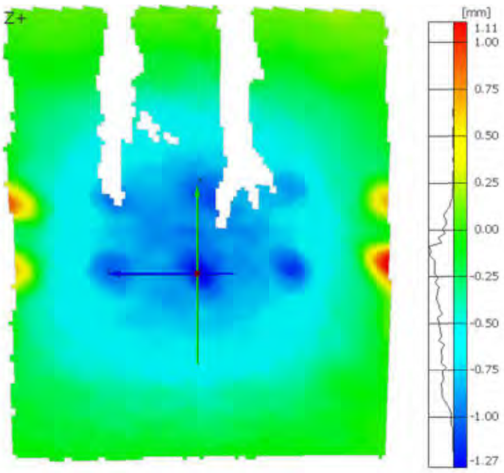

VII

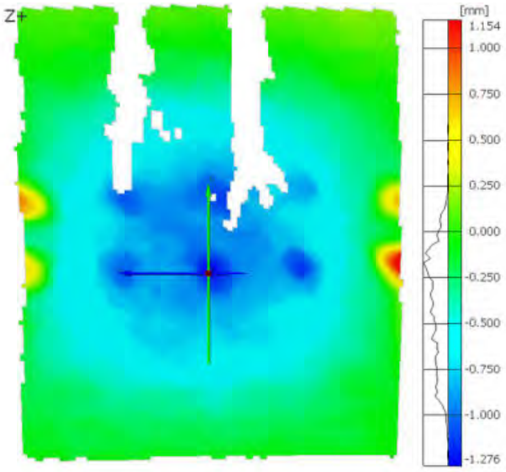

VIII

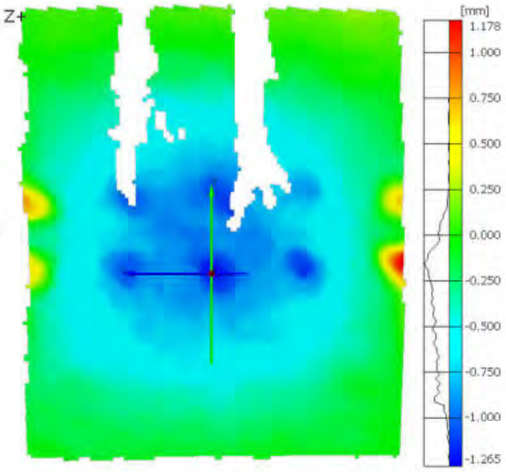

IX

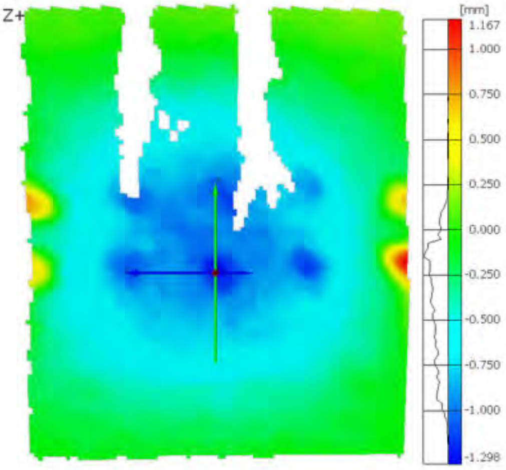

X

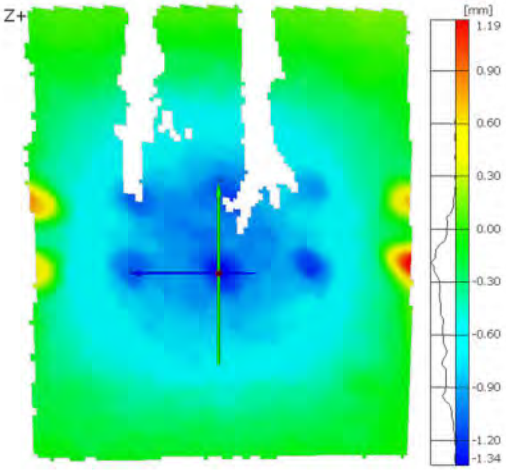

XI

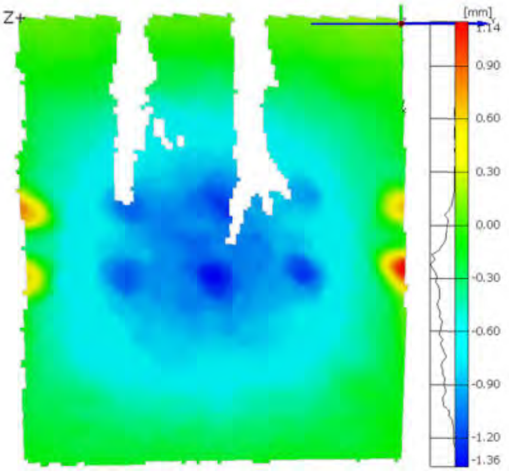

# D Appendix - DIC Measurement System

## D.1 Element tension and compression testing

ARAMIS system – set-up

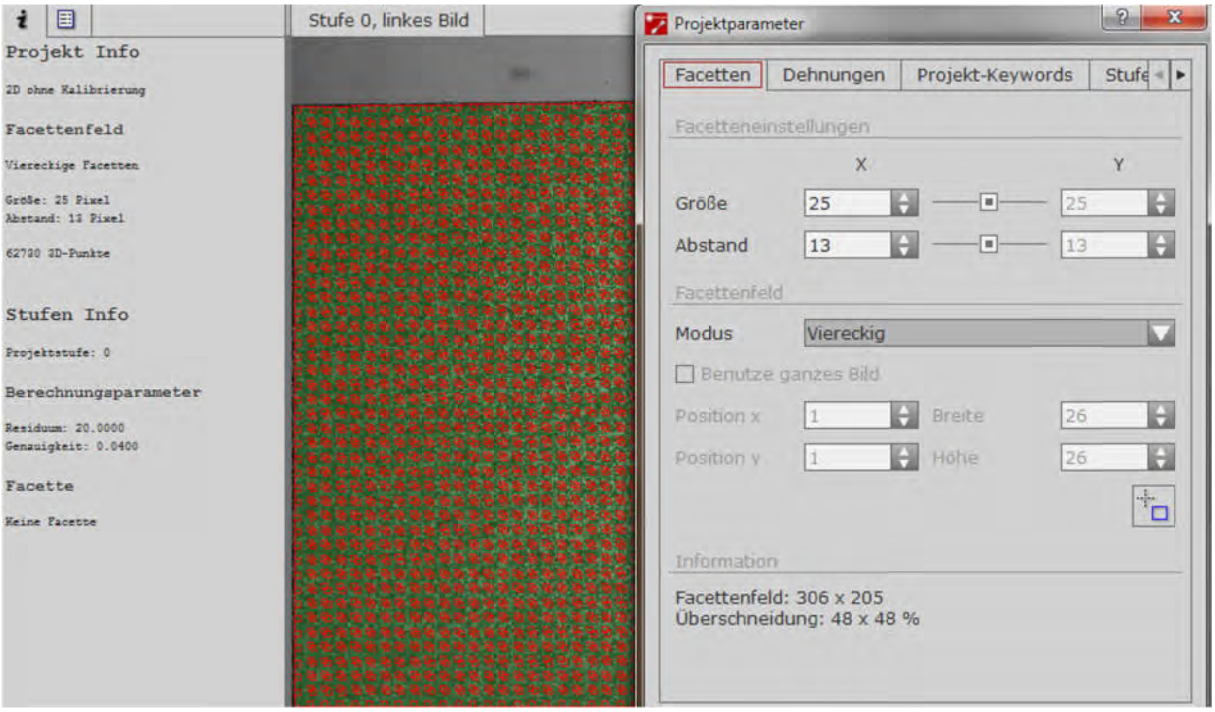

**Projekt Info**

2D ohne Kalibrierung

**Facettenfeld**

Viereckige Facetten

Größe: 25 Pixel
Abstand: 13 Pixel

62730 2D-Punkte

**Stufen Info**

Projektstufe: 0

**Berechnungsparameter**

Residuum: 20.0000
Genauigkeit: 0.0400

**Facette**

Keine Facette

Facetteneinstellungen

| | X | Y |
|---|---|---|
| Größe | 25 | 25 |
| Abstand | 13 | 13 |

Facettenfeld

Modus: Viereckig

☐ Benutze ganzes Bild

| | | | |
|---|---|---|---|
| Position x | 1 | Breite | 26 |
| Position y | 1 | Höhe | 26 |

Information

Facettenfeld: 306 x 205
Überschneidung: 48 x 48 %

## D.2 Panel test

Skin-side: ARAMIS set-up

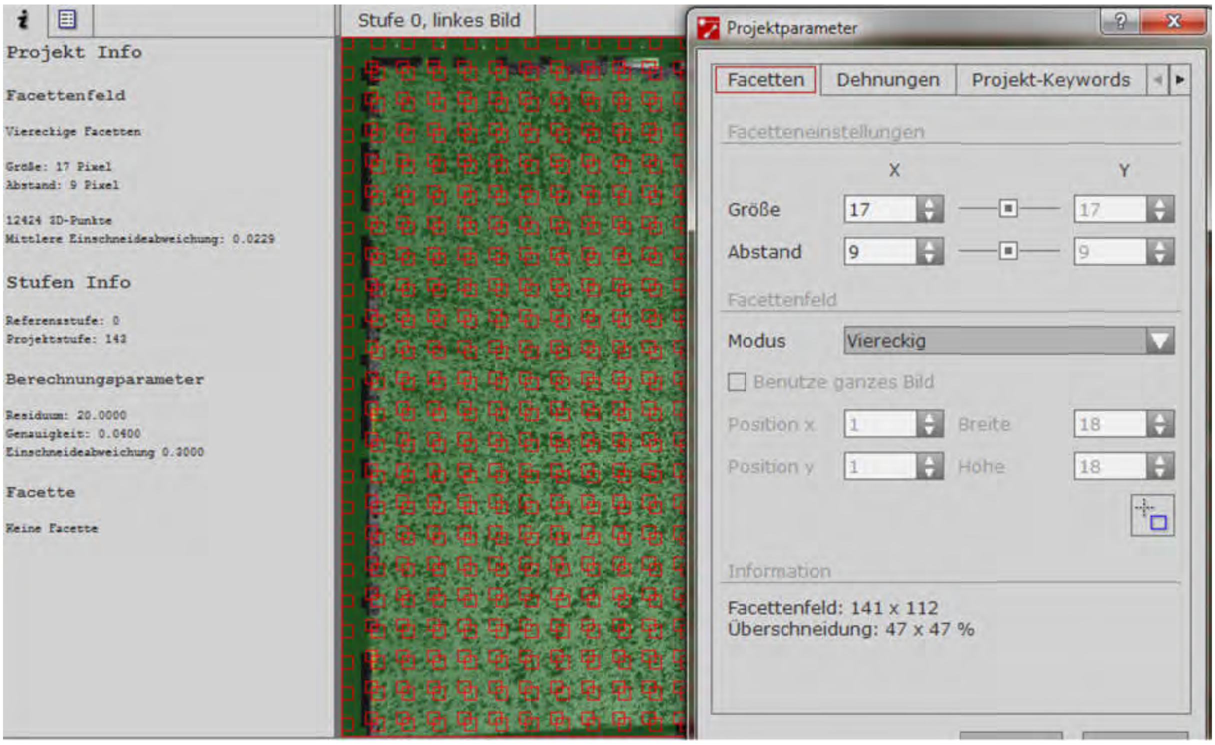

**Projekt Info**

**Facettenfeld**

Viereckige Facetten

Größe: 17 Pixel
Abstand: 9 Pixel

12424 3D-Punkte
Mittlere Einschneideabweichung: 0.0229

**Stufen Info**

Referenzstufe: 0
Projektstufe: 143

**Berechnungsparameter**

Residuum: 20.0000
Genauigkeit: 0.0400
Einschneideabweichung 0.3000

**Facette**

Keine Facette

Facetteneinstellungen

| | X | Y |
|---|---|---|
| Größe | 17 | 17 |
| Abstand | 9 | 9 |

Facettenfeld

Modus: Viereckig

☐ Benutze ganzes Bild

| | | | |
|---|---|---|---|
| Position x | 1 | Breite | 18 |
| Position y | 1 | Höhe | 18 |

Information

Facettenfeld: 141 x 112
Überschneidung: 47 x 47 %